doi.org/10.26434/chemrxiv.8241395.v2

Using Collision Cross Section Distributions to Assess the Distribution of Collision Cross Section Values

Aidan France, Lukasz Migas, Eleanor Sinclair, Bruno Bellina, Perdita Barran

Submitted date: 16/01/2020 • Posted date: 20/01/2020

Citation information: France, Aidan; Migas, Lukasz; Sinclair, Eleanor; Bellina, Bruno; Barran, Perdita (2019): Using Collision Cross Section Distributions to Assess the Distribution of Collision Cross Section Values. ChemRxiv. Preprint. https://doi.org/10.26434/chemrxiv.8241395.v2

In this study we explore the use of collision cross section distributions to allow comparability of IM-MS data for proteins on different instruments. We present measurements on seven standard proteins across three IM-MS configurations, namely an Agilent 6560 IM QToF, a Waters Synapt G2 possessing a TWIMS cell and a modified Synapt G2 possessing an RF confining linear field drift cell. Mobility measurements were taken using both He and N_2 as the drift gases. To aid comparability across instruments and best assess the corresponding gas-phase conformational landscapes of the protein 'standards' we present the data in the form of averaged collision cross section distributions.

Supplementary Information

Using Collision Cross Section Distributions to Assess the Distribution of Collision Cross Section Values

Aidan P. France, Lukasz G. Migas, Eleanor Sinclair, Bruno Bellina and Perdita E. Barran*

Manchester Institute of Biotechnology, University of Manchester,
131 Princess Street, Manchester, M1 7DN, United Kingdom

Table of Contents

Table S1. Analyte sources and final solution conditions.

Protein	Source	Supplier	Catalogue #	Solution conditions
Ubiquitin *(8.6 kDa)*	Bovine erythrocytes	Sigma	U6253	50 mM AmAc pH 7.4
Cytochrome c *(12.4 kDa)*	Horse heart	Sigma	C2506	50 mM AmAc pH 7.4
Myoglobin *(17.6 kDa)*	Horse heart	Sigma	G7882	50 mM AmAc pH 7.4
Avidin *(64 kDa)*	Chicken egg white	Sigma	A9275	200 mM AmAc pH 7.4
Serum albumin (BSA) *(66 kDa)*	Bovine	Bio-rad labs	500-0007	200 mM AmAc pH 7.4
Concanavalin a *(103 kDa)*	Jack bean	Sigma	C2010	200 mM AmAc pH 7.4
Alcohol dehydrogenase *(148 kDa)*	Yeast	Sigma	A7011	200 mM AmAc pH 7.4

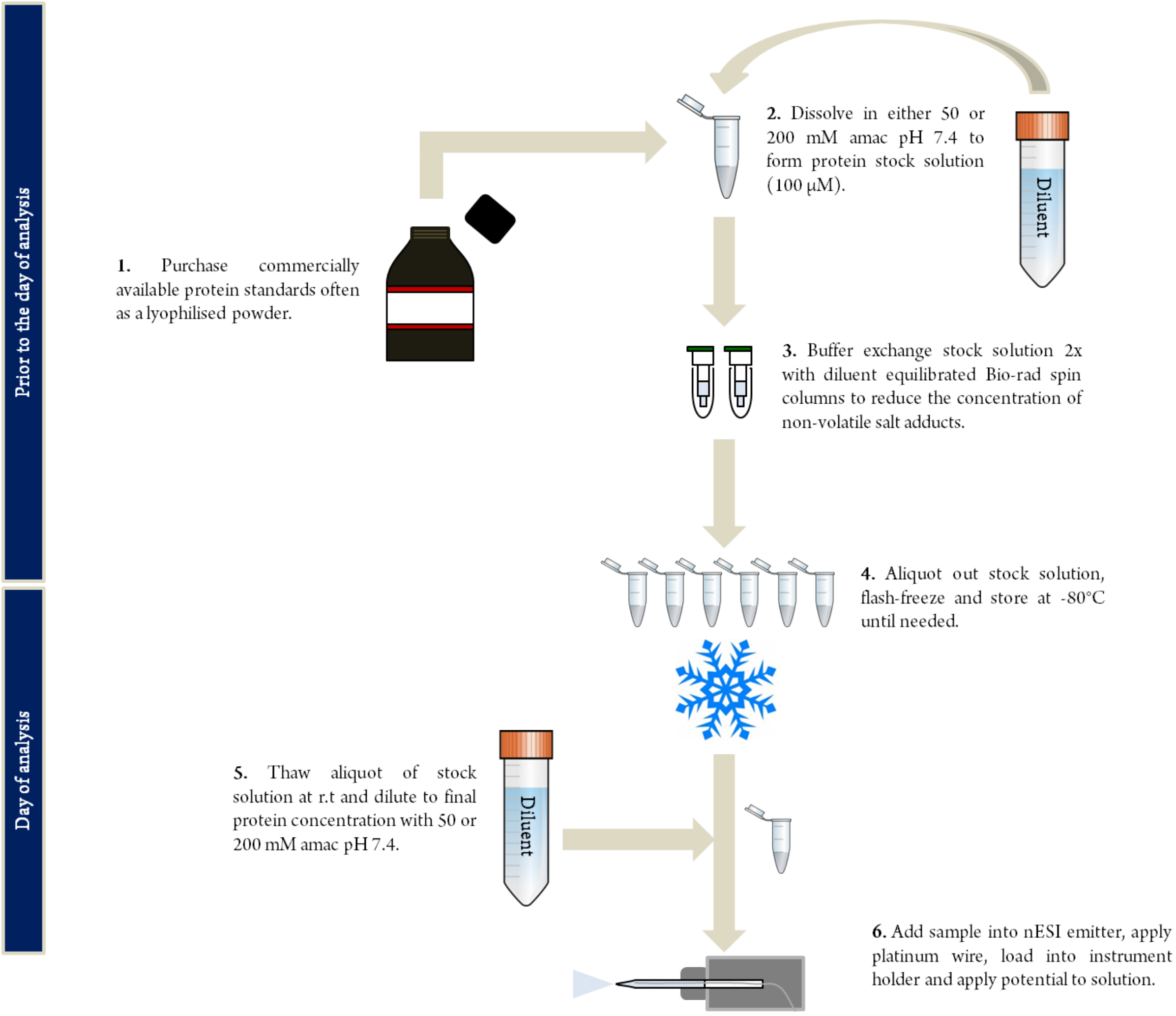

Figure S1. Schematic of standard protein/protein complex preparative procedure. Samples were purchased as lyophilised powders. Samples were then dissolved in 50 mM AmAc (monomeric proteins < 20 kDa) or 200 mM AmAc pH 7.4 (proteins/protein complexes > 20 kDa) to a stock concentration of ~ 100 µM. Stock solutions were then desalted using two equilibrated Bio-rad spin columns. After this process the buffer exchanged stock solutions were aliquoted out, flash-frozen in liquid nitrogen and then stored at -80 °C until the day of analysis. On the day of analysis aliquots were thawed at r.t., diluted to their final concentrations, loaded into nESI borosilicate emitters, centrifuged for 15 seconds and loaded onto an IM-MS holder prior to voltage application. Final analyte concentrations utilised for experiments within this study were between 1.25 – 10 µM.

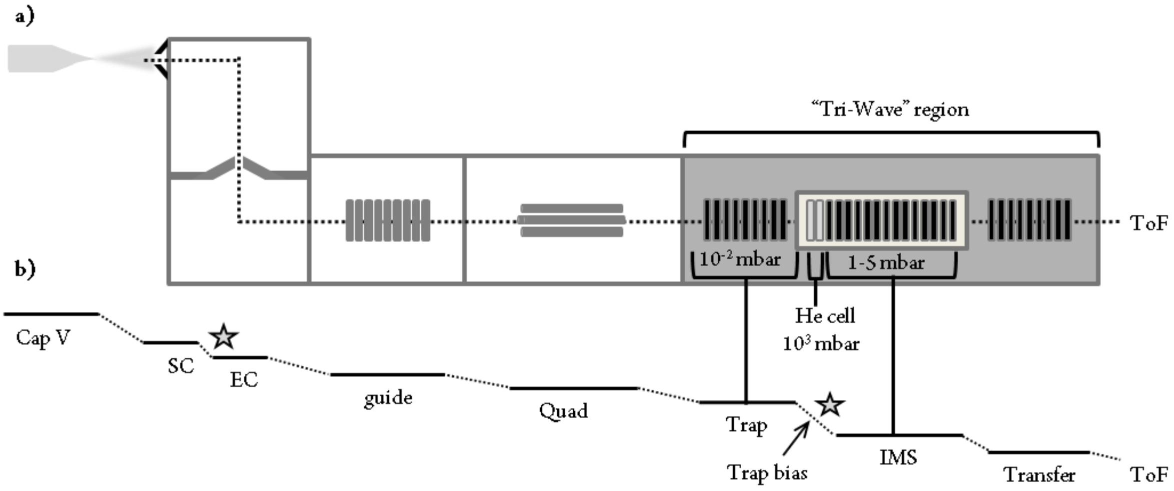

Figure S2. Schematic of the Synapt G2 (TWIMS) and its corresponding potential landscape. a) Schematic of the Synapt G2 (TWIMS). Ions travel through the instrument as follows: 1) droplets produced from nESI undergo continuous evaporation/fission processes whilst navigating a z-spray ion source via a favourable potential gradient and pressure differential, 2) ions are then transferred through a T-wave ion guide into a quadrupole mass analyser (which permits ion selection up to 32,000 m/z), after which they enter the "Tri-wave" region, 3) an argon filled trap cell encompasses the first 9 cm of this region. Within the trap cell ions are "axially focussed" by gas-ion collisions, whilst a transient DC gating field permits regular ion pulses into the next stage of the instrument[1], 4) post gating, the ion pulse travels through a 4 cm travelling wave ion guide into a 7 mm cell pressurised with helium gas. A comparatively high pressure in this region acts to permit the use of greater pressures in the downstream IM region whilst "collisionally cooling" ions prior to IM separation, 5) ions then enter the 25.2 cm long IM region (consisting of 168 stacked ring electrodes) whereby mobility separation is permitted by the application of a DC potential to sequential plate pairs in single plate pair steps. This effectively creates a propagating wave which separates ions based upon their charge and their propensity to interact with the drift gas,[2] 6) following mobility separation, ions traverse a 9 cm transfer region pressurised in the same fashion as the trap cell. The application of low velocity, high amplitude travelling waves in this region acts to ferry ions toward the ToF analyser (for m/z detection) without further activation and IM separation. b) Schematic of the potential gradient along the instrument. Voltages which impart the greatest energy upon ions, thus promoting their gas-phase activation, are highlighted by grey stars. The voltage gradient from the sample cone (SC) to the extractor cone (EC) can be utilised to promote in-source ion activation. Furthermore, the trap bias voltage, which acts to accelerate ions (analogous to an injection voltage in DTIMS) from a comparatively low pressure environment (the trap cell) to a higher pressure one (the Helium and IM cell) can also significantly perturb ion structures if not tuned. Both a) and b) were adapted from Chen *et al.*[3].

Table S2. Synapt G2 (TWIMS) tuning parameters. For proteins/protein complex ions >60 kDa, backing pressure and trap cell pressures were raised to ~4-7 and ~4e-2 mbar respectively in order to maximise ion transmission. Furthermore, larger protein complexes were analysed using higher source and pre-IM voltages which permitted greater transmission without notable structural alteration.

Source voltages (V) and gas flows (mL/min)	
Capillary voltage (kV)	0.7 – 1.2
Source temperature (°C)	40.0
Sample cone	10.0 – 20.0
Extractor cone	1.0
Trap gas flow	2.0
Helium cell gas flow	200
IMS gas flow	75.0
DC voltages	
Trap cell energy (V)	0.0 – 6.0
Trap DC entrance	4.0
Trap DC bias	40.0
Trap DC	-2.2
Trap DC exit	5.0
Trap height (V)	10-15
IMS DC entrance	27.0
Helium cell DC	30.0
Helium cell exit	-5.0
IMS bias	2.0
IMS DC exit	0.0
Transfer cell energy (V)	0.0 – 6.0
Transfer DC entrance	4.0
Transfer DC exit	15.0
RF voltages (V)	
Source	350
Trap	300
IMS	300
IMS mobility	250
Transfer	350
Wave velocities (ms^{-1}) and heights (V)	
Source wave velocity	8
Source wave height	0.0
Trap wave velocity	450
Trap wave height	0.5
IMS wave velocity	100 – 300
IMS wave height	9 – 19.5
Transfer wave velocity	100-600
Transfer wave height	10
Pressures (mbar)	
Backing	2.90
Trap	$2.81e^{-2}$
Helium cell	$1.41e^{3}$
IM cell	4.26
Transfer	$2.96e^{-2}$
ToF	$1.04e^{-6}$

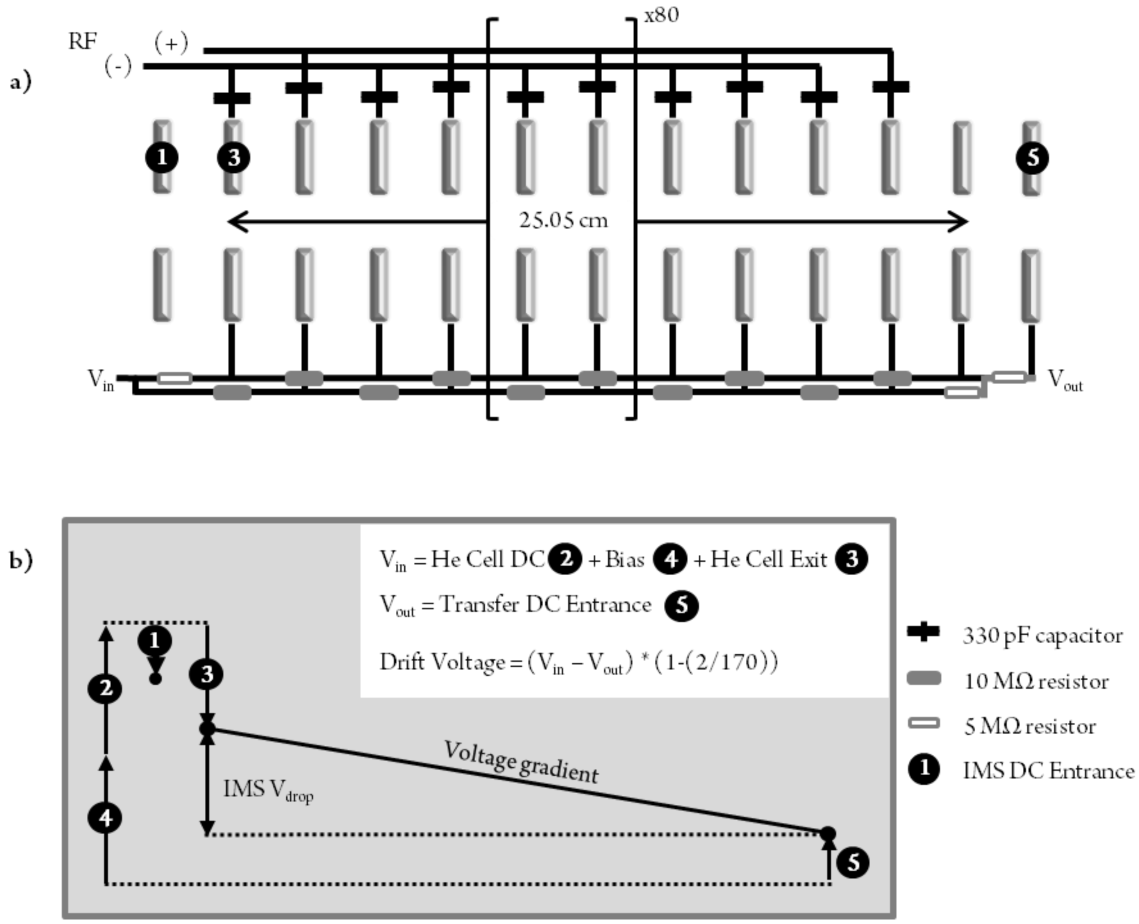

Figure S3. Schematic of the RF cell modification for the G2 and the establishment of the drift voltage within the RF cell. a) Schematic of the RF cell modification for the G2. The DC drift voltage applied across the cell is established by the resistor series which are parallel to one another. The presence of two 330 pF capacitor series running along the length of the cell acts to promote ion transmission via radial confinement of the ion beam. b) Schematic showing how the drift voltage is applied across the RF cell. The entrance drift voltage (V_{in}) is established using the He cell DC (2), IM Bias (4) and He cell exit (3) voltages. The IMS DC entrance (1) controls the helium exit plate and thus does not affect the drift voltage. Within our study (1) was set at approximately a quarter of the value of (3). The effective drift voltage is calculated by subtracting V_{out} from V_{in} and correcting for two individual resistors (one before V_{in} and one between the RF-confining drift cell exit plate and (5)). As such, the effective drift length (25.05 cm) is slightly shorter than the cell length (25.2 cm) as the drift voltage is only applied from the first electrode to the exit plate of the cell. Drift voltages utilised for the experiments described in this study ranged from 325 to 75 V. Both a) and b) were adapted from Allen *et al.*[4].

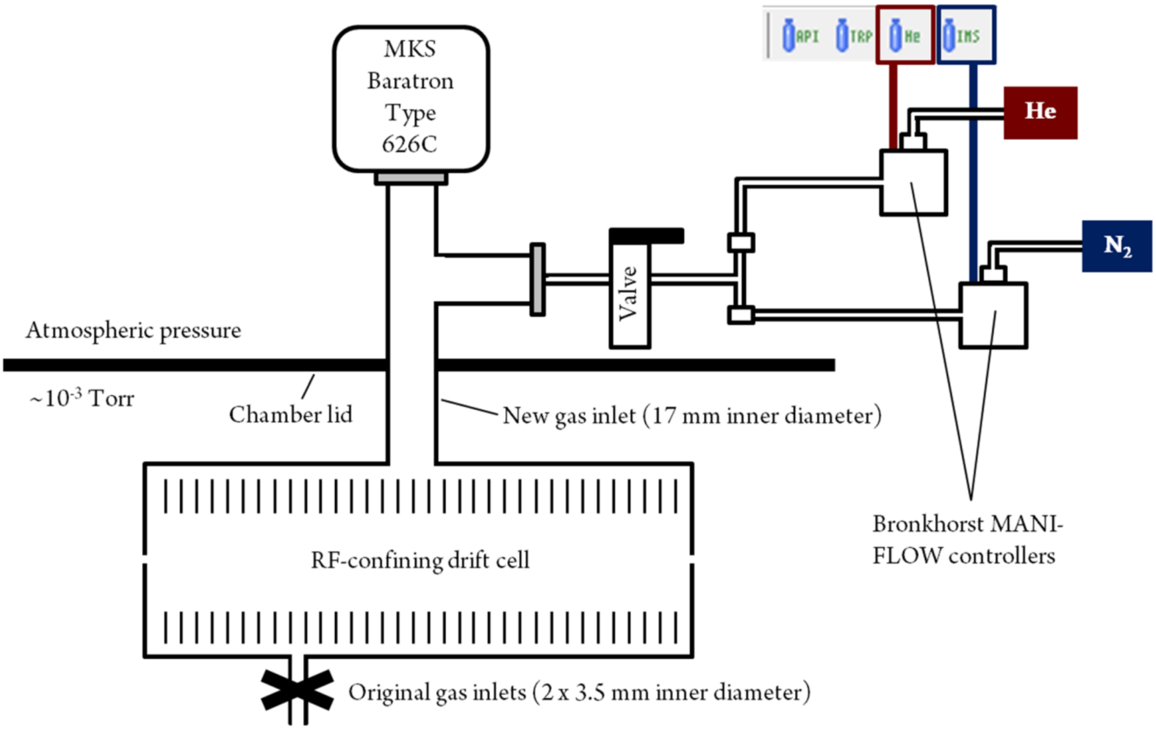

Figure S4. Schematic of the RF cell configuration and gas inlet system. Drift gas composition was controlled using the original MassLynx V4.1 software, where the "IMS" tab permitted nitrogen gas flow and the "He" tab permitted helium gas flow. Gas pressures within the drift cell were controlled via Bronkhorst MANI-FLOW controllers which responded to controls on the original MassLynx V4.1 software, whereby "IMS gas" regulated the amount of nitrogen in the cell and "Helium cell gas" regulated the amount of helium in the cell. Drift gas pressures were measured via a capacitance manometer (MKS Baratron type 626C) placed above the centre of the drift cell which permitted absolute pressure measurements. This figure was adapted from Allen *et al.*[4].

Table S3. Synapt G2 (DTIMS) tuning parameters. For proteins/protein complex ions >60 kDa, the backing pressure and trap cell pressure was raised to ~ 4-7 and ~ 4e-2 mbar respectively in order to maximise ion transmission. Furthermore, larger protein complexes were analysed using higher source and pre-IM voltages as no notable structural alterations occurred whilst significant increases in transmission were observed.

Source voltages (V) and gas flows (mL/min)		
Capillary voltage (kV)	0.7 – 1.2	
Source temperature (°C)	40.0	
Sample cone	10.0 – 20.0	
Extractor cone	1.0	
Trap gas flow	2.0	
Helium gas flow (for experiments in He)	100.0	
Nitrogen gas flow (for experiments in N_2)	41.0	
DC voltages		
Trap cell energy (V)	0.0 – 4.0	
Trap DC entrance	1.0	
Trap DC bias	1.0	
Trap DC	0.0	
Trap DC exit	1.0	
Trap height (V)	10-15	
IMS DC entrance	-6.5	
Helium cell DC	← altered incrementally (25 V steps) to establish Drift Voltages	
Helium cell exit	-40	
IMS bias	← altered incrementally (25 V steps) to establish Drift Voltages	
IMS DC exit	0.0	
Transfer cell energy (V)	0.0 – 6.0	
Transfer DC entrance	4.0	
Transfer DC exit	15.0	
RF voltages (V)		
Source	350	
Trap	300	
IMS	300	
IMS mobility	250	
Transfer	350	
Wave velocities (ms^{-1}) and heights (V)		
Source wave velocity	200	
Source wave height	0.2	
Trap wave velocity	313	
Trap wave height	2.0	
IMS wave velocity	650	
IMS wave height	0	
Transfer wave velocity	300	
Transfer wave height	4	
Pressures		
	He	**N_2**
Backing (mbar)	2.7	2.7
Trap (mbar)	$1.3e^{-2}$	$1.1e^{-2}$
IM (Torr)	1.94	1.98
Transfer (mbar)	$1.4e^{-2}$	$1.1e^{-2}$
ToF (mbar)	$7.4e^{-7}$	$7.5e^{-7}$

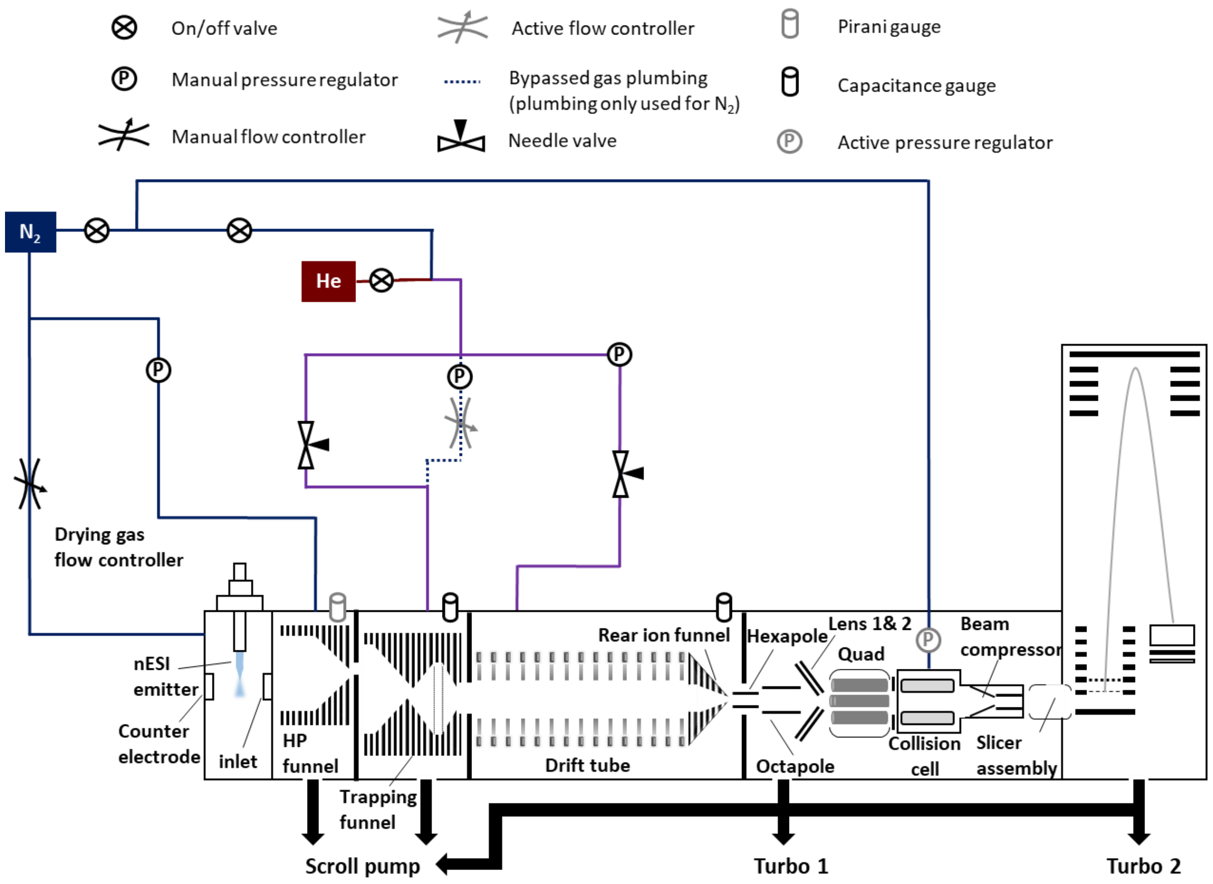

Figure S5. Schematic of the Agilent 6560 IMQToF and gas inlet system. Schematic of the Agilent 6560 IMQToF (with a nESI source) with nitrogen gas inlets (blue), helium gas inlets (red) and inlets which can be configured to allow either nitrogen or helium gas in (purple). In all configurations the internal structure of the instrument remains unchanged. In both configurations nitrogen is pumped into the source (as drying gas), HP funnel region, and collision cell (back end of the instrument post IM). Drying gas flow into the source is regulated by a manually adjustable flow controller (Porter instrument company, USA). For all of the experiments carried out with nitrogen as the drift gas, a mass flow controller (installed as part of the Agilent gas kit upgrade) was utilised to actively regulate the pressure differential between the IM cell and the trapping funnel. In this configuration, manually adjustable pressure regulators prior to the drift cell and HP funnel were also used to help establish the IM pressure and IM-Trap pressure differential. However, for all the experiments done in helium the mass flow controller was bypassed, as pressure stabilisation was not possible. As such, we installed pressure regulators and needle valves which we positioned prior to the IM cell and trap funnel to permit manual control of IM cell and trap funnel pressures. Pressures at the front end of the 6560 are maintained by a single scroll pump (Edwards) whilst at the back end of the instrument the scroll pump works in synergy with two turbo pumps to maintain the low pressures required in the QToF region. Absolute pressure measurements for the trapping funnel and drift tube are recorded by CDG 500 capacitance gauges positioned at the end of the aforementioned regions (black and white cylinders). The HP funnel pressure is recorded via a pirani gauge (grey and white cylinder) which yields a relative pressure measurement. This figure was adapted from May *et al.*[5].

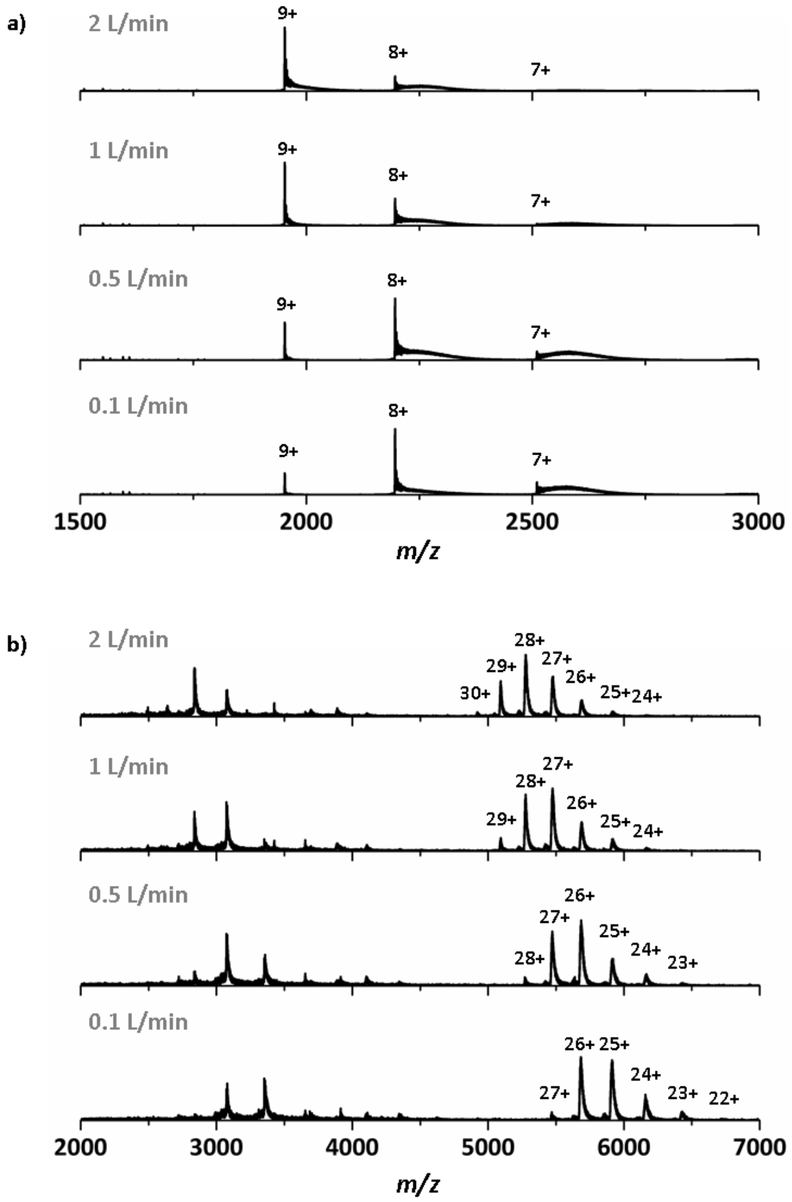

Figure S6. Impact of drying gas flow rates upon protein/protein complex CSDs. Mass spectra of myoglobin and alcohol dehydrogenase obtained using different drying gas flow rates on the Agilent 6560 IMQToF. a) Mass spectra of myoglobin obtained when employing drying gas flow rates of 0.1, 0.5, 1 and 2 L/min. No parameters except drying gas flow rate were altered between the acquisition of the mass spectra. The CSD centres on the 8+ ion of myoglobin at the lowest drying gas flow rate employed and is observed to shift in favour of the 9+ ion as the drying gas flow rate is increased. b) Mass spectra of alcohol dehydrogenase obtained when employing drying gas flow rates of 0.1, 0.5, 1 and 2 L/min. No parameters except drying gas flow rate were altered between the acquisition of the mass spectra. The CSD centres on the 25 and 26+ ions of alcohol dehydrogenase at the lowest drying gas flow rate employed and is observed to shift in favour of higher charge states (eventually centring on the 28+ ion) as the drying gas flow rate is increased. As such, the CSD of protein/protein complex ions can be seen to shift in favour of higher charge states with greater drying gas flow rates. Interestingly, this affect appears to be more significant for larger protein complexes (which present with larger Δz values) in comparison to smaller proteins (which present with smaller Δz values). No parameters except drying gas flow rate were altered between the acquisition of the mass spectra shown above Both myoglobin and alcohol dehydrogenase were sprayed from 50 mM and 200 mM AmAc solutions (pH 7.4) respectively. It is important to note that the associated IM landscape of each ion (peak apexes, ATD morphology and widths) did not noticeably alter with differing drying gas flow rates.

Table S4. Establishing the helium IM-Trap differential on the modified Agilent 6560 IMQToF using Agilent tune mix. a) Average $^{DT}CCS_{He}$ literature values and our experimental $^{DT}CCS_{He}$ values for the 622, 922 & 1222 1+ ions of tune mix obtained under helium IM-Trap differentials of 0.109, 0.130, 0.134, 0.138 & 0.143 Torr. b) Relative differences (%) between the average literature values and our experimental $^{DT}CCS_{He}$ values obtained from the aforementioned helium IM-Trap differentials.

a)

	helium IM-Trap differential (Torr)					
		0.109	**0.130**	**0.134**	**0.138**	**0.143**
Tune mix (m/z)	**Avg of Literature & DTIMS (G2) $^{DT}CCS_{He}$ values**[6,7]	**$^{DT}CCS_{He}$ DTIMS (6560)**	**$^{DT}CCS_{He}$ DTIMS (6560)**	**$^{DT}CCS_{He}$ DTIMS (6560)**	**$^{DT}CCS_{He}$ DTIMS (6560)**	**$^{DT}CCS_{He}$ DTIMS (6560)**
622	138.2	142.4	138.7	137.8	137.2	136.9
922	174.6 ± 1.1	180.2	175.9	176	173.3	173.2
1222	208.2 ± 1.4	214.2	207.4	207.9	205.6	205.3

b)

	helium IM-Trap differential (Torr)				
	0.109	**0.130**	**0.134**	**0.138**	**0.143**
Tune mix (m/z)	**ΔExp vs Ref (%)**	**ΔExp vs Ref (%)**	**ΔExp vs Ref (%)**	**ΔExp vs Ref (%)**	**ΔExp vs Ref (%)**
622	3.04	0.36	-0.29	-0.72	-0.94
922	3.23	0.76	0.82	-0.73	-0.78
1222	2.88	-0.38	-0.14	-1.25	-1.39
Average	3.05 ± 0.17	0.25 ± 0.58	0.13 ± 0.60	-0.90 ± 0.30	-1.04 ± 0.32

Table S5. Establishing the helium IM-Trap differential on the modified Agilent 6560 IMQToF using polyalanine. a) Average ^{DT}CCS$_{He}$ literature values and our experimental ^{DT}CCS$_{He}$ values for a series of 1+, 2+ & 3+ ions of polyalanine obtained under helium IM-Trap differentials of 0.128, 0.132, 0.135 & 0.140 Torr. b) Relative differences (%) between the average literature values and our experimental ^{DT}CCS$_{He}$ values obtained from the aforementioned helium IM-Trap differentials.

a)	**helium IM-Trap differential (Torr)**				
		0.128	**0.132**	**0.135**	**0.140**
Polyalanine	**Avg of Literature ^{DT}CCS$_{He}$ values**[4,8]	**^{DT}CCS$_{He}$ DTIMS (6560)**	**^{DT}CCS$_{He}$ DTIMS (6560)**	**^{DT}CCS$_{He}$ DTIMS (6560)**	**^{DT}CCS$_{He}$ DTIMS (6560)**
z = 1+					
7	140.8 ± 0.4	144.1	142.6	140.3	141.1
8	156.3 ± 1.1	158	157	157.6	156.3
9	169.0 ± 1.5	168.5	169	169.2	168.2
10	178.7 ± 3.3	180.5	179.1	179.4	178.9
11	193.1 ± 1.3	191.6	192.6	190.6	190.6
12	204.2 ± 2.5	202	203.2	203.2	200.4
13	216.0 ± 1.5	215.3	213	220	210.8
14	226.5 ± 2.2	225	221.4	214.1	220.8
z = 2+					
12	208	209.9	207	208.5	206.7
13	220	220.4	221.4	222.5	220
14	232	232.6	232.5	233.6	229.6
15	243	243.4	242.3	242.5	242
16	255	255.7	254.2	254.8	252.5
17	265	267.5	264.4	265.2	264.6
18	276	277.5	273.2	275.8	275.1
19	287	287.9	285.6	285	284.9
20	297	298.7	297.5	295.7	295.3
21	308	306.8	307.1	306.6	305.6
22	317	319.3	314.2	313.3	315.9
23	327	330.2	324.7	326.4	326.2
24	337	336.4	336.8	332.4	334.8
25	348	351.8	347.2	344	346.7
26	358	356.8	359.5	362.2	355.4
z = 3+					
22	373	369.5	371.1	375.2	373.3
23	386	384	388.8	388.4	386.1
24	399	401.6	401.8	400.1	398.6
25	412	415.3	407	410.4	408.7
26	425	427.6	424.9	423.5	424.3
27	438	437.9	436.8	432.6	436.7
28	452	451	449.5	448.4	451.2
29	465	465.4	463.3	460.7	461.7
30	479	475.5	474.8	473.2	473.8
31	490	486	482.6	482.7	487.9
32	502	498.3	495.7	499.2	501.4
33	516	508.5	511.9	503.8	513.3

b)	**helium IM-Trap differential (Torr)**			
	0.128	**0.132**	**0.135**	**0.14**
Polyalanine	**ΔExp vs Ref (%)**	**ΔExp vs Ref (%)**	**ΔExp vs Ref (%)**	**ΔExp vs Ref (%)**
z = 1+				
7	1.31	-0.32	0.25	2.38
8	0.48	0.86	0.03	1.12
9	0.03	0.15	-0.44	-0.27
10	0.25	0.42	0.14	1.04
11	-0.26	-1.29	-1.29	-0.78
12	-0.49	-0.49	-1.86	-1.08
13	-1.37	1.88	-2.38	-0.30
14	-2.23	-5.45	-2.50	-0.64
z = 2+				
12	-0.48	0.24	-0.63	0.91
13	0.64	1.14	0.00	0.18
14	0.22	0.69	-1.03	0.26
15	-0.29	-0.21	-0.41	0.16
16	-0.31	-0.08	-0.98	0.27
17	-0.23	0.08	-0.15	0.94
18	-1.01	-0.07	-0.33	0.54
19	-0.49	-0.70	-0.73	0.31
20	0.17	-0.44	-0.57	0.57
21	-0.29	-0.45	-0.78	-0.39
22	-0.88	-1.17	-0.35	0.73
23	-0.70	-0.18	-0.24	0.98
24	-0.06	-1.36	-0.65	-0.18
25	-0.23	-1.15	-0.37	1.09
26	0.42	1.17	-0.73	-0.34
z = 3+				
22	-0.51	0.59	0.08	-0.94
23	0.73	0.62	0.03	-0.52
24	0.70	0.28	-0.10	0.65
25	-1.21	-0.39	-0.80	0.80
26	-0.02	-0.35	-0.16	0.61
27	-0.27	-1.23	-0.30	-0.02
28	-0.55	-0.80	-0.18	-0.22
29	-0.37	-0.92	-0.71	0.09
30	-0.88	-1.21	-1.09	-0.73
31	-1.51	-1.49	-0.43	-0.82
32	-1.25	-0.56	-0.12	-0.74
33	-0.79	-2.36	-0.52	-1.45
Average	0.12 ± 0.80	-0.34 ± 0.72	-0.42 ± 1.24	-0.58 ± 0.64

Table S6. Establishing the helium IM-Trap differential on the modified Agilent 6560 IMQToF using apo-myoglobin. a) Average $^{DT}CCS_{He}$ literature values and our experimental $^{DT}CCS_{He}$ values for a series of monomorphic ions (18-26+) of apo-myoglobin obtained under helium IM-Trap differentials of 0.125, 0.130, 0.135 & 0.140 Torr. b) Relative differences (%) between the average literature values and our experimental $^{DT}CCS_{He}$ values obtained from the aforementioned helium IM-Trap differentials.

a)	**helium IM-Trap differential (Torr)**				
		0.125	**0.130**	**0.135**	**0.140**
Apo-myoglobin (z)	**Avg of Literature $^{DT}CCS_{He}$ values[9–12]**	**$^{DT}CCS_{He}$ DTIMS (6560)**	**$^{DT}CCS_{He}$ DTIMS (6560)**	**$^{DT}CCS_{He}$ DTIMS (6560)**	**$^{DT}CCS_{He}$ DTIMS (6560)**
18+	3488 ± 38	3534	3487	3499	3476
19+	3578 ± 18	3646	3587	3610	3578
20+	3671 ± 26	3749	3686	3698	3669
21+	3760 ± 27	3824	3770	3774	3733
22+	3816 ± 21	3881	3829	3821	3795
23+	3893 ± 32	3913	3874	3848	3828
24+	3952 ± 45	3936	3897	3881	3847
25+	3995 ± 49	3966	3933	3908	3891
26+	4034 ± 47	4008	3968	3948	3928

b)	**0.125**	**0.130**	**0.135**	**0.140**
Apo-myoglobin (z)	**ΔExp vs Ref (%)**	**ΔExp vs Ref (%)**	**ΔExp vs Ref (%)**	**ΔExp vs Ref (%)**
18+	1.35	-0.02	0.33	-0.34
19+	1.92	0.25	0.92	0.03
20+	2.12	0.40	0.74	-0.04
21+	1.70	0.26	0.38	-0.71
22+	1.70	0.36	0.14	-0.55
23+	0.53	-0.46	-1.14	-1.67
24+	-0.41	-1.38	-1.80	-2.65
25+	-0.71	-1.55	-2.18	-2.60
26+	-0.63	-1.63	-2.11	-2.61
Average	-0.84 ± 1.16	-0.42 ± 0.87	-0.53 ± 1.27	-1.24 ± 1.15

Table S7. Agilent 6560 IMQToF tuning parameters. The Quad AMU was set at 500 for ubiquitin, cytochrome c and myoglobin, at 1000 for Avidin and BSA and 2000 for concanavalin a and alcohol dehydrogenase. These settings were observed to be optimal for the transmission of the different analyte ions analysed during this study. For proteins/protein complexes < 70 kDa, the collision cell flow was maintained at 22. However, for protein complexes > 100 kDa the collision cell flow was increased to 25 in order to aid transmission of these larger ions.

Source voltages (V) and gas flows (L/min)		
Capillary voltage (kV)	0.9 – 1.4	
Source temperature (°C)	50.0	
Drying gas flow	0.1-0.3	
Fragmentor	300-375	
DC voltages		
HP Funnel delta	120-180	
Trap entrance grid delta	1	
Trap entrance grid low	97	
Trap entrance grid high	98	
Trap entrance	91	
Trap exit	90	
Trap exit grid 1 delta	4	
Trap exit grid 1 low	87.6	
Trap exit grid 1 high	91.6	
Trap exit grid 2 delta	7.1	
Trap exit grid 2 low	87.5	
Trap exit grid 2 high	94.6	
Trap Funnel delta	180	
IM Hexapole delta	-8	
IM Hexapole entrance	41	
Rear Funnel entrance	240	
Rear Funnel exit	45	
RF voltages (V)		
Octapole	750	
High Pressure Funnel	100-140	
Trap Funnel	100-160	
IM Hexapole	300	
Rear Funnel	200	
Other parameters		
Trap fill time (µs)	5000	
Trap release time (µs)	150	
Pressures (Torr)		
	He	**N_2**
HP Funnel	4.50-4.80	4.30-4.70
Drift tube	3.89-3.93	3.95
Trap Funnel	3.76-3.80	3.80

Table S8. Calibrants employed for TWIMS experiments and their associated pearson coefficients. Note that for ubiquitin, cytochrome c and myoglobin, there was not a complete selection of calibrant ions with previously published $^{DT}CCS_{N2}$ values. In these instances we utilised our own $^{DT}CCS_{N2}$ values (denoted by *), derived from our RF confining drift cell (to remain consistent with our other literature CCS origins), as calibrant literature CCS for the calibration procedure.

Protein	n	TWIMS calibrants	Calibrant literature Ω source	TWIMS WV (ms^{-1})	TWIMS WH (V)	Average r^2 N$_2$→He	Average r^2 N$_2$
Ubiquitin *(8.6 kDa)*	1	Melittin Insulin (1n) Cytochrome C	Bush *et al.*[4,12,13]	300	18	0.9971 (±0.0003)	*0.9872 (±0.0002)
			*Our RF CCS				
Cytochrome C *(12.4 kDa)*	1	Ubiquitin Lysozyme β-Lactoglobulin A (1n)	Bush *et al.*[4,12]	200	14	0.99317 (±0.0005)	*0.9940 (±0.0035)
			*Our RF CCS				
Myoglobin *(17.6 kDa)*	1	Lysozyme Cytochrome C β-Lactoglobulin A (1n)	Bush *et al.*[4,12]	300	18	0.9824 (±0.0012)	*0.9969 (±0.0011)
			*Our RF CCS				
Avidin *(64 kDa)*	4	TTR Concanavalin A	Bush *et al.*[4,12]	300	19.5	0.9932 (±0.0024)	0.9994 (±0.0005)
Serum albumin (BSA) *(66 kDa)*	1	Avidin Concanavalin A	Bush *et al.*[4,12]	100	9.5	0.9920 (±0.0012)	0.9956 (±0.0014)
Concanavalin A *(103 kDa)*	4	Avidin Alcohol dehydrogenase	Bush *et al.*[4,12]	100	9.5	0.9951 (±0.0036)	0.9706 (±0.0102)
Alcohol dehydrogenase *(148 kDa)*	4	Concanavalin A Pyruvate kinase	Bush *et al.*[4,12]	300	19.5	0.9977 (±0.0004)	0.9851 (±0.0043)

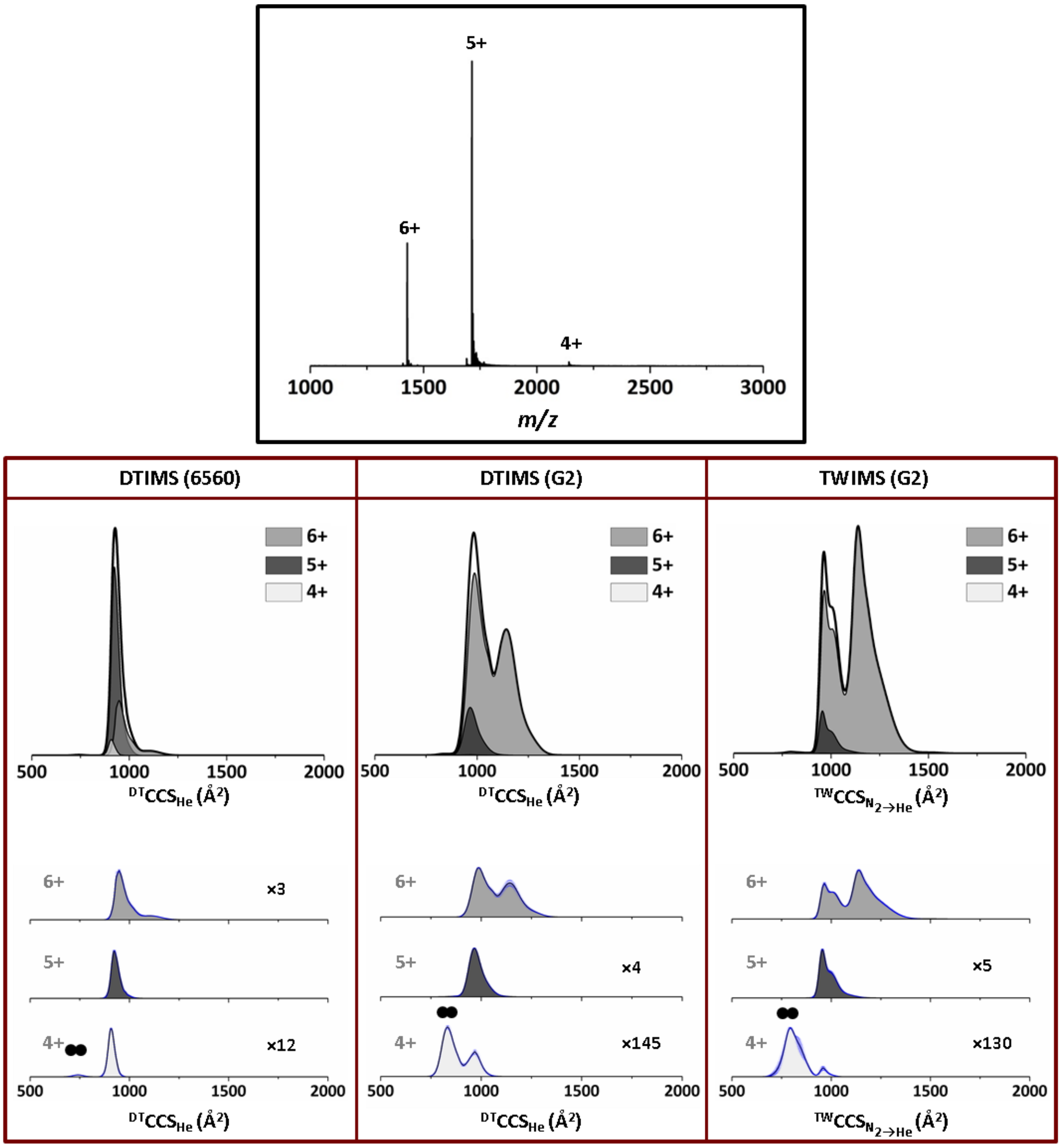

Protein			Helium Drift Gas					
Ubiquitin (8566 Da)			6560-DTIMS		G2-DTIMS		G2-TWIMS	
Z_{Avg}	Species	#	$^{DT}CCS_{He}$ (Å^2)	%RSD	$^{DT}CCS_{He}$ (Å^2)	%RSD	$^{TW}CCS_{He}$ (Å^2)	%RSD
5.41 ± 0.29	$[M+4H]^{4+}$	1	907 ± 2	0.27	963 ± 7	0.72	961 ± 7	0.71
	$[M+5H]^{5+}$	1	924 ± 5	0.51	965 ± 8	0.84	955 ± 2	0.25
		2	-	-	-	-	1003 ± 2	0.22
	$[M+6H]^{6+}$	1	943 ± 8	0.86	987 ± 4	0.37	966 ± 0.2	0.02
		2	1113 ± 10	0.85	1143 ± 2	0.14	1006 ± 9	0.88
		3	-	-	-	-	1143 ± 4	0.35

Figure S7. Ubiquitin helium CCS & CCS distributions. Top) Mass spectrum of Ubiquitin sprayed from 50 mM AmAc solution at pH 7.4, where charge states are denoted by z+. Upper middle) Total CCS distributions of Ubiquitin. Lower middle) Stacked CCS distribution plots for each ion normalised to the same intensity with magnification factors applied. Two black circles denote the presence of coincident dimer. Table) Average CCS_{He} values with replicate (n=3) standard deviations (±) and associated RSDs (%) for Ubiquitin obtained across the instrument platforms utilised.

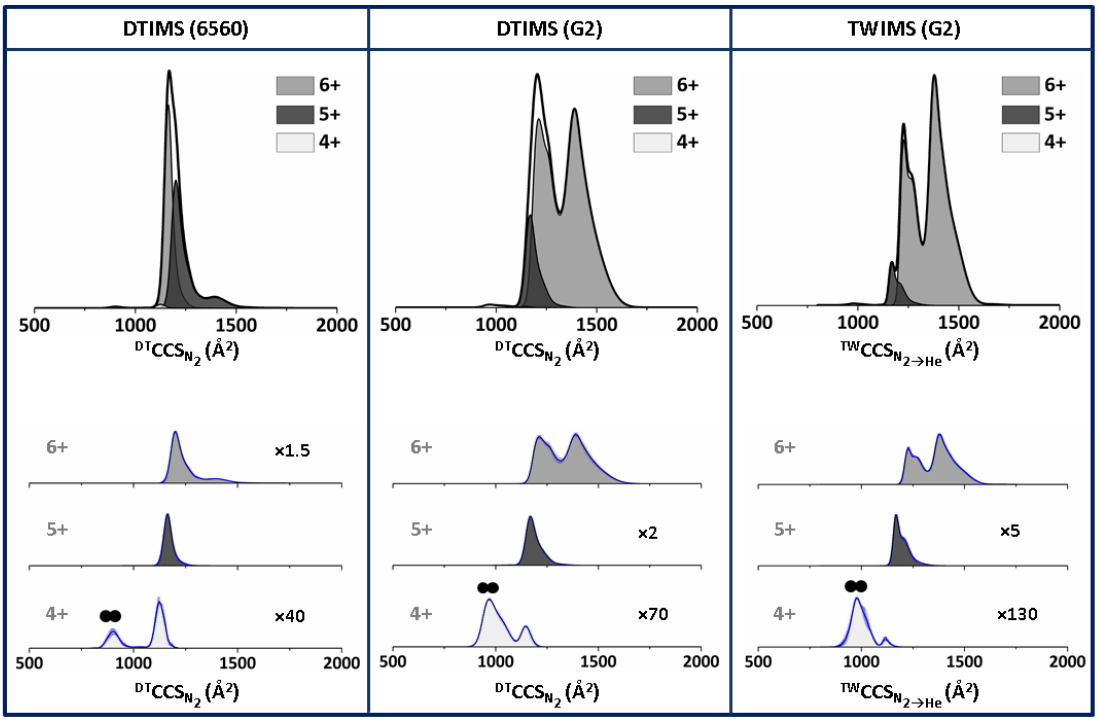

Protein			Nitrogen Drift Gas					
Ubiquitin (8566 Da)			6560-DTIMS		G2-DTIMS		G2-TWIMS	
Z_{Avg}	Species	#	$^{DT}CCS_{N_2}$ (Å²)	%RSD	$^{DT}CCS_{N_2}$ (Å²)	%RSD	$^{TW}CCS_{N_2}$ (Å²)	%RSD
5.43 ± 0.18	$[M+4H]^{4+}$	1	1128 ± 13	1.15	1148 ± 10	0.90	1118 ± 3	0.45
	$[M+5H]^{5+}$	1	1163 ± 4	0.31	1166 ± 6	0.54	1167 ± 1	0.08
		2	-	-	1208 ± 4	0.35	1208 ± 3	0.28
	$[M+6H]^{6+}$	1	1199 ± 5	0.38	1209 ± 13	1.05	1229 ± 0.3	0.03
		2	1401 ± 2	0.11	1386 ± 4	0.32	1268 ± 2	0.15
		3	-	-	1466 ± 13	0.91	1382 ± 1.4	0.10

Figure S8. Ubiquitin nitrogen CCS & CCS distributions. Upper) Total CCS distributions of Ubiquitin. Lower) Stacked CCS distribution plots for each ion normalised to the same intensity with magnification factors applied. Two black circles denote the presence of coincident dimer. Table) Average CCS_{N_2} values with replicate (n=3) standard deviations (±) and associated RSDs (%) for Ubiquitin obtained across the instrument platforms utilised. Interactive versions of Figures S7 & S8 are available online at https://france-ccs-2019.netlify.com/assets/ubi_s7&s8.

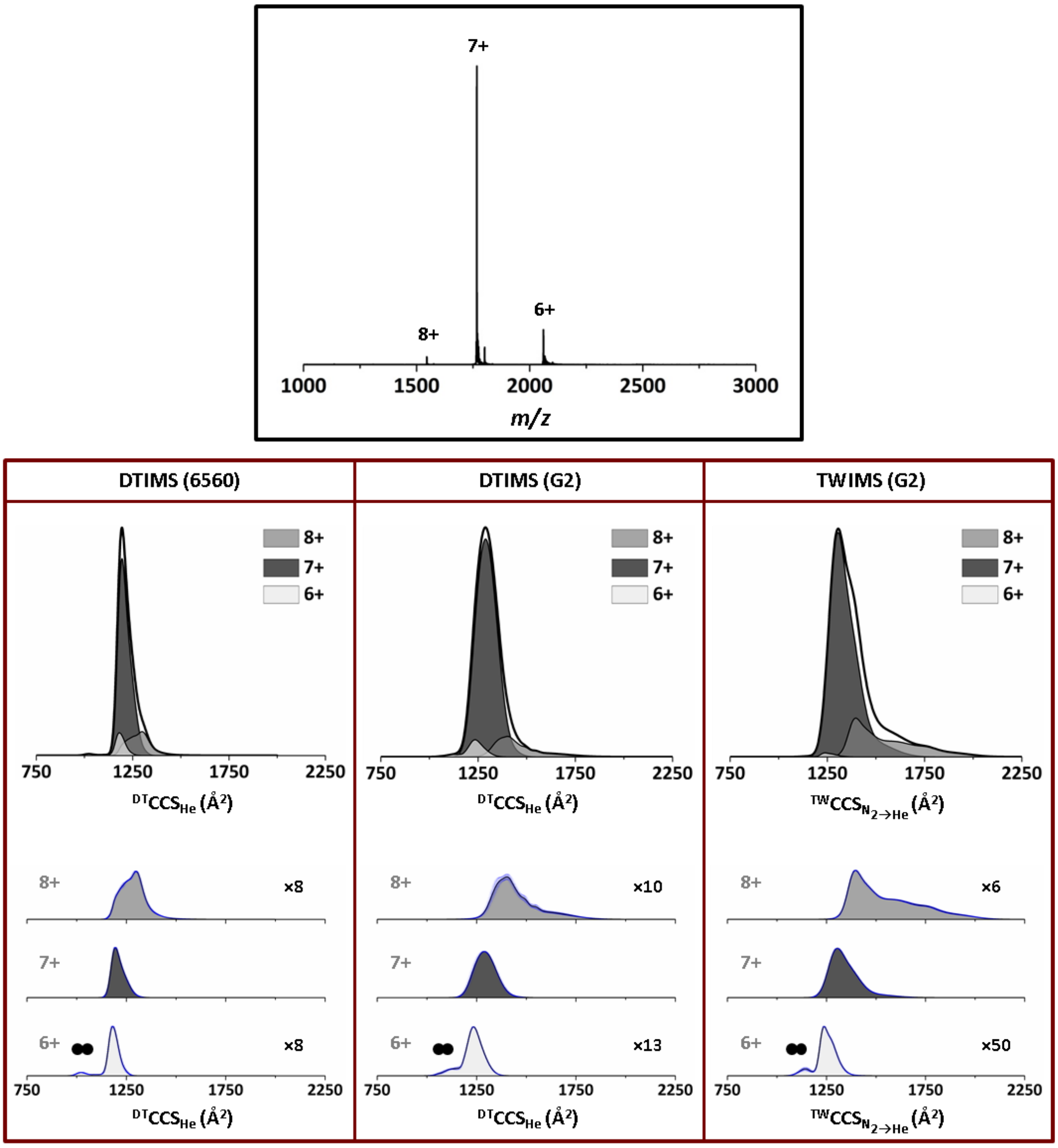

Protein			Helium Drift Gas					
Cytochrome c (12,358 Da)			6560-DTIMS		G2-DTIMS		G2-TWIMS	
Z_{Avg}	Species	#	$^{DT}CCS_{He}$ (Å^2)	%RSD	$^{DT}CCS_{He}$ (Å^2)	%RSD	$^{TW}CCS_{He}$ (Å^2)	%RSD
6.96 ± 0.01	$[M+6H]^{6+}$	1	1182 ± 4	0.33	1234 ± 5	0.41	1238 ± 6	0.48
	$[M+7H]^{7+}$	1	1196 ± 1	0.09	1286 ± 12	0.93	1304 ± 6	0.49
		2	-	-	-	-	-	
	$[M+8H]^{8+}$	1	1258 ± 19	1.47	1373 ± 34	2.49	1399 ± 6	0.46
		2	1297 ± 2	0.14	1540 ± 17	1.12	1625 ± 11	0.67
		3	-	-	-	-	1768 ± 6	0.36
		4	-	-	-	-	1918 ± 12	0.62

Figure S9. Cytochrome c helium CCS & CCS distributions. Top) Mass spectrum of cytochrome c sprayed from 50 mM AmAc solution at pH 7.4, where charge states are denoted by z+. Upper middle) Total CCS distributions of Ubiquitin. Lower middle) Stacked CCS distribution plots for each ion normalised to the same intensity with magnification factors applied. Two black circles denote the presence of coincident dimer. Table) Average CCS_{He} values with replicate (n=3) standard deviations (±) and associated RSDs (%) for cytochrome c obtained across the instrument platforms utilised.

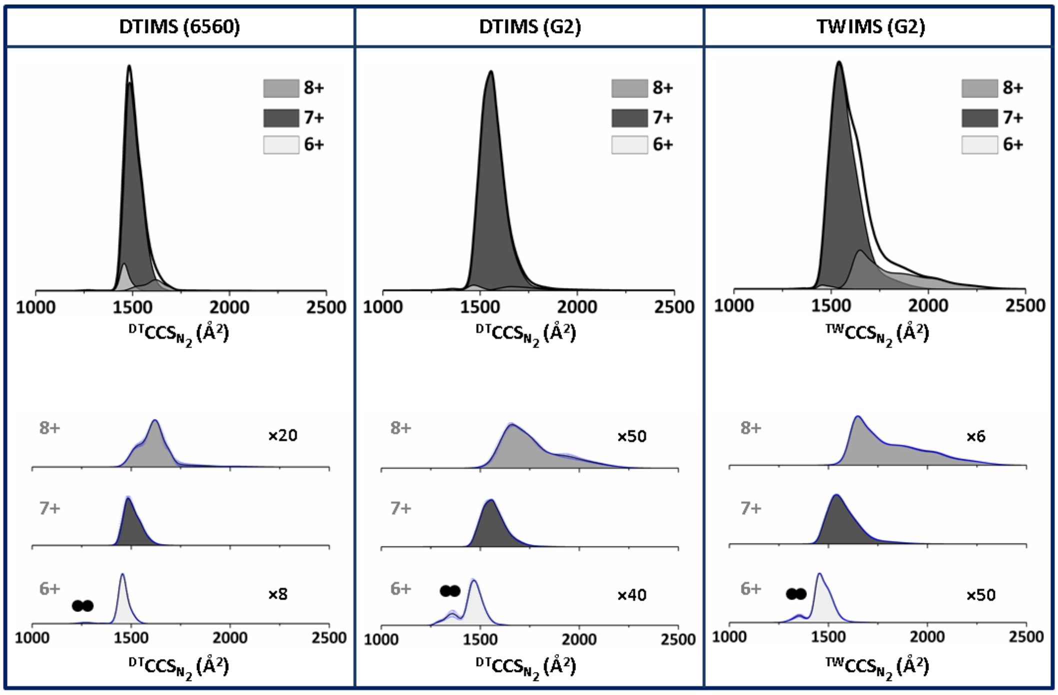

Protein			Nitrogen Drift Gas					
Cytochrome c (12,358 Da)			6560-DTIMS		G2-DTIMS		G2-TWIMS	
Z_{Avg}	Species	#	$^{DT}CCS_{N_2}$ (Å^2)	%RSD	$^{DT}CCS_{N_2}$ (Å^2)	%RSD	$^{TW}CCS_{N_2}$ (Å^2)	%RSD
6.94 ± 0.04	[M+6H]$^{6+}$	1	1456 ± 7	0.47	1465 ± 9	0.63	1454 ± 6	0.43
	[M+7H]$^{7+}$	1	1481 ± 18	1.23	1561 ± 11	0.71	1537 ± 7	0.46
		2	1540 ± 19	1.23	-	-	-	-
	[M+8H]$^{8+}$	1	1519 ± 21	1.41	1654 ± 8	0.50	1654 ± 9	0.54
		2	1629 ± 9	0.57	1915 ± 8	0.40	1887 ± 11	0.61
		3	-	-	-	-	2043 ± 7	0.34
		4	-	-	-	-	2201 ± 13	0.58

Figure S10. Cytochrome c nitrogen CCS & CCS distributions. Upper) Total CCS distributions of cytochrome c. Lower) Stacked CCS distribution plots for each ion normalised to the same intensity with magnification factors applied. Two black circles denote the presence of coincident dimer. Table) Average CCS_{N_2} values with replicate (n=3) standard deviations (±) and associated RSDs (%) for cytochrome c obtained across the instrument platforms utilised. Interactive versions of Figures S9 & S10 are available online at https://france-ccs-2019.netlify.com/assets/cytc_s9&s10.

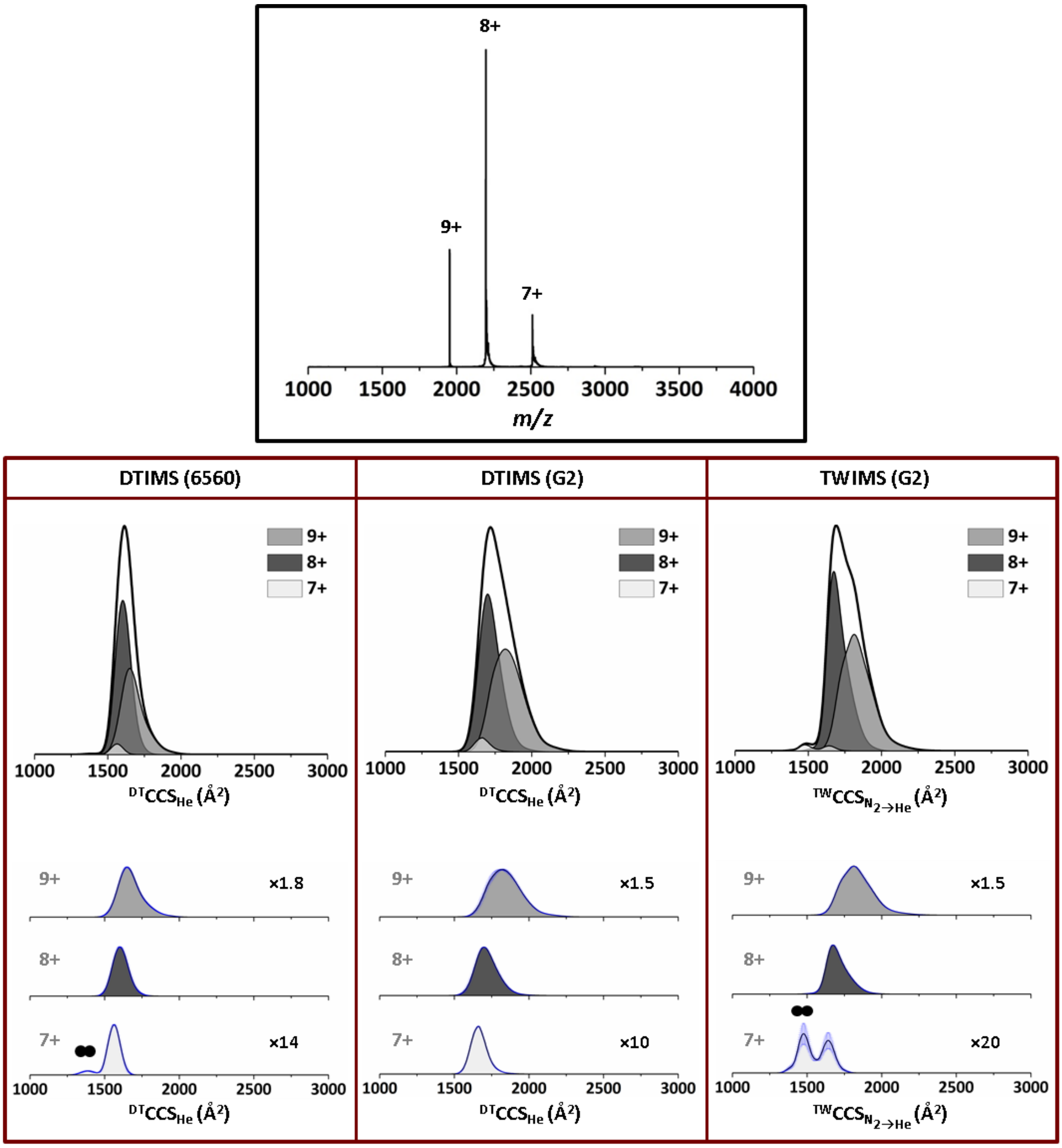

Protein			Helium Drift Gas					
Myoglobin (17,567 Da)			**6560-DTIMS**		**G2-DTIMS**		**G2-TWIMS**	
Z_{Avg}	**Species**	**#**	$^{DT}CCS_{He}$ (Å^2)	**%RSD**	$^{DT}CCS_{He}$ (Å^2)	**%RSD**	$^{TW}CCS_{He}$ (Å^2)	**%RSD**
8.13 ± 0.10	$[M+7H]^{7+}$	1	1566 ± 6	0.25	1664 ± 1	0.07	1641 ± 2	0.14
	$[M+8H]^{8+}$	1	1604 ± 5	0.33	1704 ± 4	0.21	1674 ± 12	0.71
	$[M+9H]^{9+}$	1	1649 ± 4	0.39	1832 ± 30	1.63	1713 ± 17	0.72
		2	-	-	-	-	1818 ± 13	0.98

Figure S11. Myoglobin helium CCS & CCS distributions. Top) Mass spectrum of myoglobin sprayed from 50 mM AmAc solution at pH 7.4, where charge states are denoted by z+. Upper middle) Total CCS distributions of myoglobin. Lower middle) Stacked CCS distribution plots for each ion normalised to the same intensity with magnification factors applied. Two black circles denote the presence of coincident dimer. Table) Average CCS_{He} values with replicate (n=3) standard deviations (±) and associated RSDs (%) for myoglobin obtained across the instrument platforms utilised.

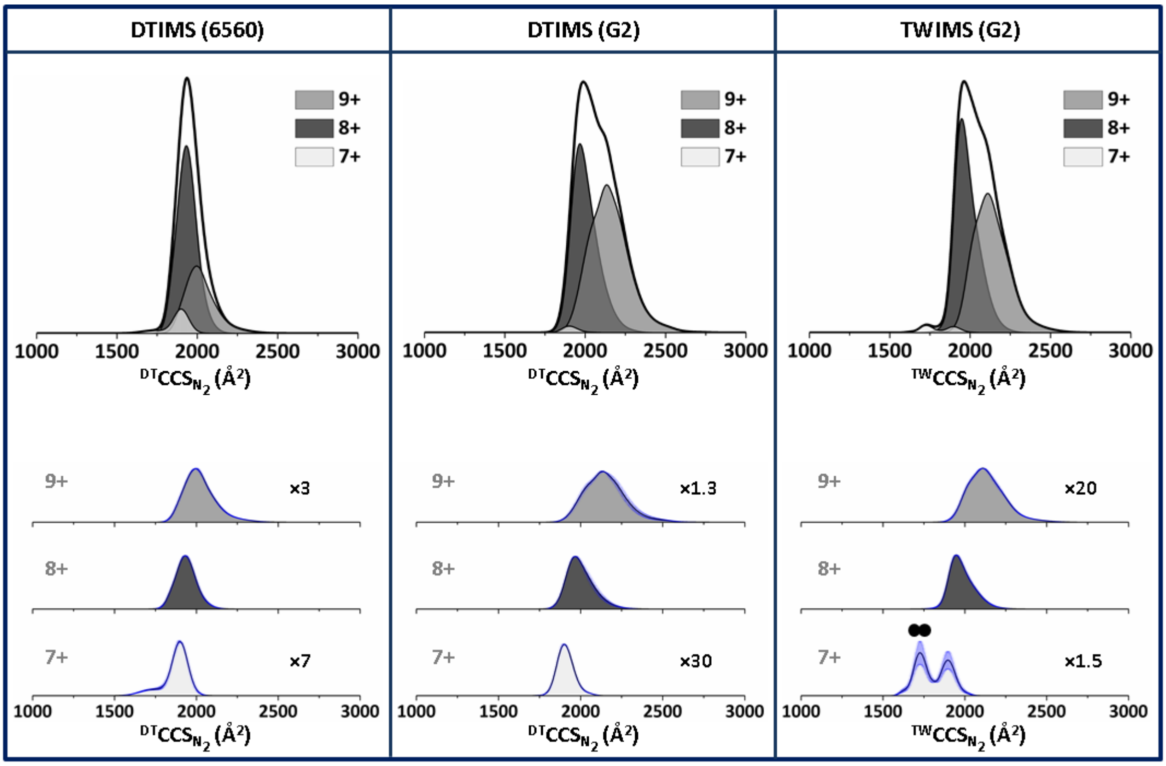

Protein			Nitrogen Drift Gas					
Myoglobin (17,567 Da)			6560-DTIMS		G2-DTIMS		G2-TWIMS	
Z_{Avg}	Species	#	$^{DT}CCS_{N_2}$ (Å^2)	%RSD	$^{DT}CCS_{N_2}$ (Å^2)	%RSD	$^{TW}CCS_{N_2}$ (Å^2)	%RSD
8.11 ± 0.09	$[M+7H]^{7+}$	1	1899 ± 12	0.62	1903 ± 8	0.40	1896 ± 3	0.17
	$[M+8H]^{8+}$	1	1934 ± 2	0.11	1972 ± 9	0.44	1949 ± 10	0.51
	$[M+9H]^{9+}$	1	1995 ± 13	0.63	2040 ± 17	0.85	2003 ± 16	0.43
		2	-	-	2149 ± 26	1.19	2114 ± 14	0.94

Figure S12. Myoglobin nitrogen CCS & CCS distributions. Upper) Total CCS distributions of myoglobin. Lower) Stacked CCS distribution plots for each ion normalised to the same intensity with magnification factors applied. Two black circles denote the presence of coincident dimer. Table) Average CCS_{N_2} values with replicate (n=3) standard deviations (±) and associated RSDs (%) for myoglobin obtained across the instrument platforms utilised. Interactive versions of Figures S11 & S12 are available online at https://france-ccs-2019.netlify.com/assets/myo_s11&s12.

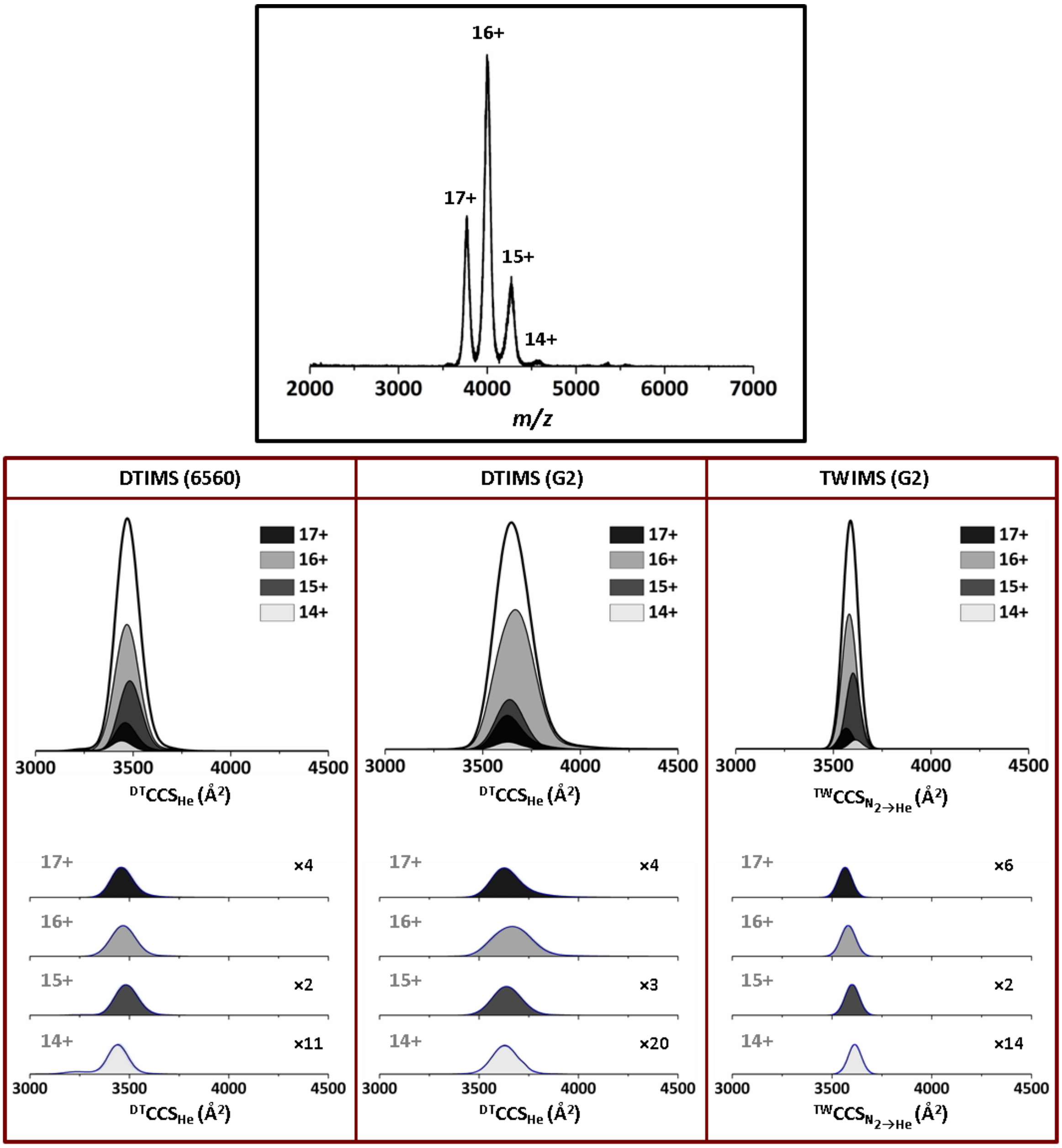

Protein			Helium Drift Gas					
Avidin (4n = 63,933 Da)			6560-DTIMS		G2-DTIMS		G2-TWIMS	
Z_{avg}	Species	#	$^{DT}CCS_{He}$ (Å^2)	%RSD	$^{DT}CCS_{He}$ (Å^2)	%RSD	$^{TW}CCS_{He}$ (Å^2)	%RSD
15.75 ± 0.07	$[4M+14H]^{14+}$	1	3441 ± 16	0.45	3633 ± 3	0.35	3614 ± 5	0.13
	$[4M+15H]^{15+}$	1	3485 ± 14	0.39	3640 ± 9	0.25	3601 ± 2	0.07
	$[4M+16H]^{16+}$	1	3471 ± 5	0.14	3665 ± 14	0.38	3581 ± 3	0.08
	$[4M+17H]^{17+}$	1	3467 ± 12	0.35	3633 ± 13	0.35	3566 ± 2	0.06

Figure S13. Avidin helium CCS & CCS distributions. Top) Mass spectrum of avidin sprayed from 200 mM AmAc solution at pH 7.4, where charge states are denoted by z+. Upper middle) Total CCS distributions of avidin. Lower middle) Stacked CCS distribution plots for each ion normalised to the same intensity with magnification factors applied. Table) Average CCS_{He} values with replicate (n=3) standard deviations (±) and associated RSDs (%) for avidin obtained across the instrument platforms utilised.

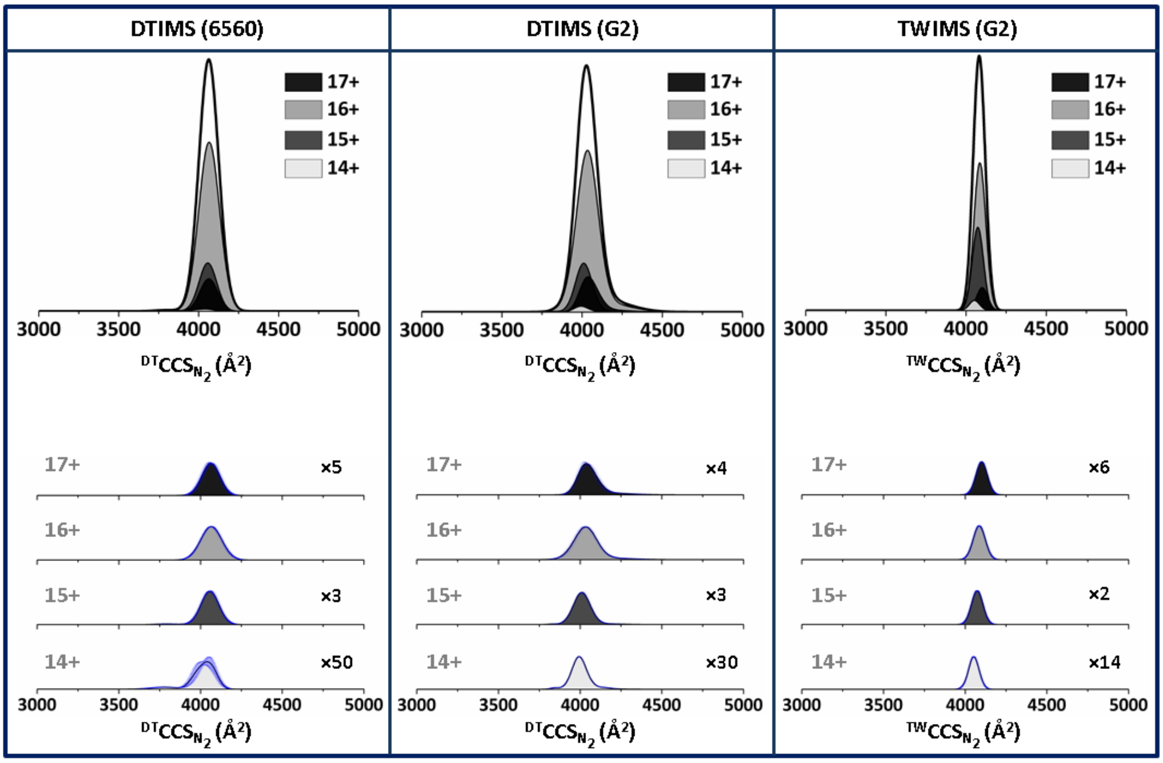

Protein			Nitrogen Drift Gas					
Avidin (4n = 63,933 Da)			6560-DTIMS		G2-DTIMS		G2-TWIMS	
Z_{avg}	Species	#	$^{DT}CCS_{N_2}$ (Å^2)	%RSD	$^{DT}CCS_{N_2}$ (Å^2)	%RSD	$^{TW}CCS_{N_2}$ (Å^2)	%RSD
15.83 ± 0.12	$[4M+14H]^{14+}$	1	4029 ± 46	1.14	3996 ± 6	0.15	4053 ± 5	0.12
	$[4M+15H]^{15+}$	1	4057 ± 13	0.33	4008 ± 14	0.34	4073 ± 2	0.05
	$[4M+16H]^{16+}$	1	4066 ± 11	0.26	4038 ± 14	0.34	4086 ± 3	0.07
	$[4M+17H]^{17+}$	1	4063 ± 23	0.56	4041 ± 31	0.77	4101 ± 2	0.06

Figure S14. Avidin nitrogen CCS & CCS distributions. Upper) Total CCS distributions of avidin. Lower) Stacked CCS distribution plots for each ion normalised to the same intensity with magnification factors applied. Table) Average CCS_{N_2} values with replicate (n=3) standard deviations (±) and associated RSDs (%) for avidin obtained across the instrument platforms utilised. Interactive versions of Figures S13 & S14 are available online at https://france-ccs-2019.netlify.com/assets/avi_s13&s14.

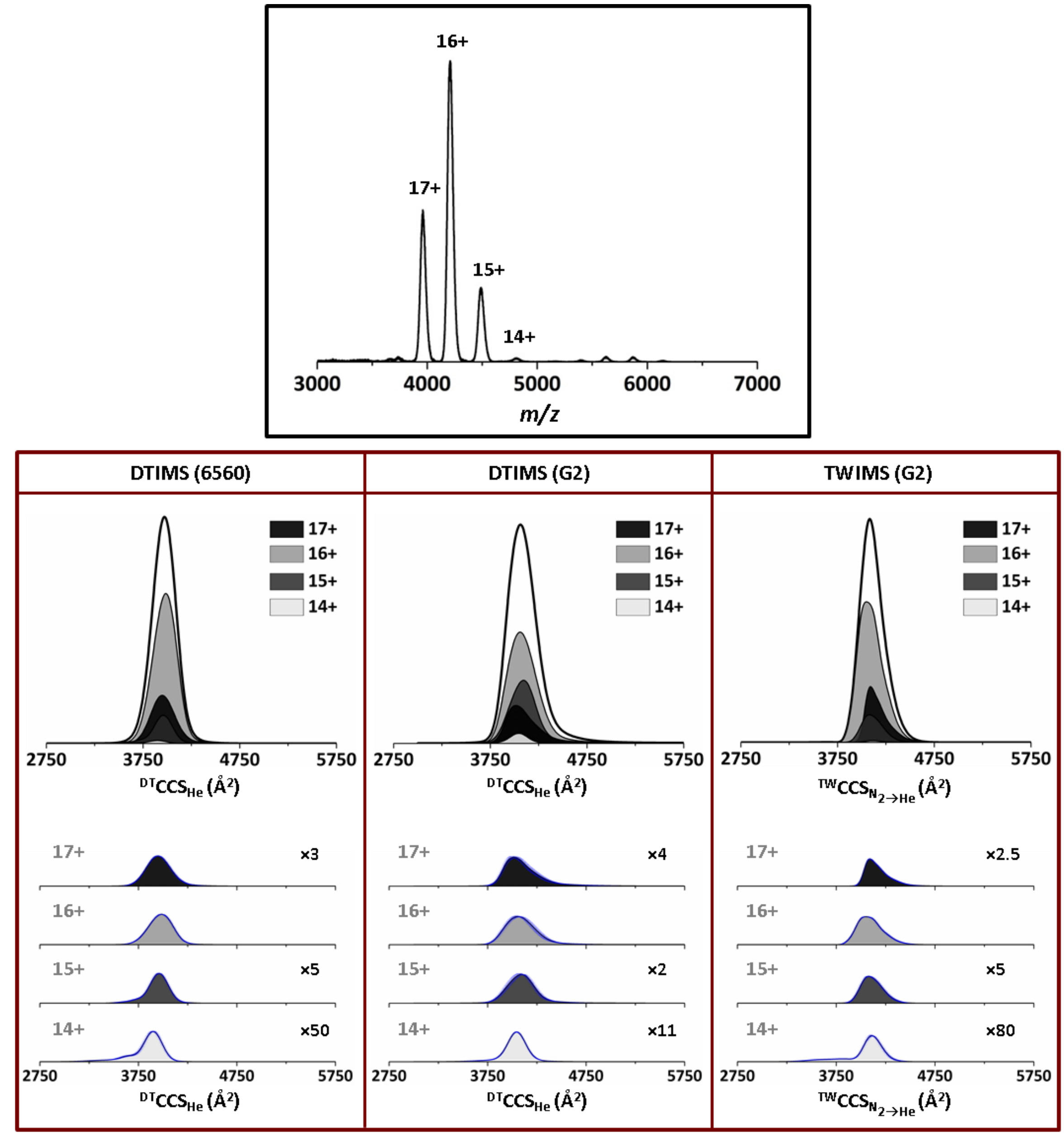

Protein			Helium Drift Gas					
BSA (66,433 Da)			6560-DTIMS		G2-DTIMS		G2-TWIMS	
Z_{avg}	Species	#	$^{DT}CCS_{He}$ (Å^2)	%RSD	$^{DT}CCS_{He}$ (Å^2)	%RSD	$^{TW}CCS_{He}$ (Å^2)	%RSD
15.95 ± 0.22	$[4M+14H]^{14+}$	1	3891 ± 28	0.73	4041 ± 4	0.11	4108 ± 24	0.59
	$[4M+15H]^{15+}$	1	3956 ± 22	0.56	4093 ± 55	1.35	4087 ± 31	0.76
	$[4M+16H]^{16+}$	1	3989 ± 15	0.36	4084 ± 63	1.53	4051 ± 16	0.39
	$[4M+17H]^{17+}$	1	3956 ± 15	0.39	4026 ± 59	1.44	4094 ± 11	0.26

Figure S15. BSA helium CCS & CCS distributions. Top) Mass spectrum of BSA sprayed from 200 mM AmAc solution at pH 7.4, where charge states are denoted by z+. Upper middle) Total CCS distributions of BSA. Lower middle) Stacked CCS distribution plots for each ion normalised to the same intensity with magnification factors applied. Table) Average CCS_{He} values with replicate (n=3) standard deviations (±) and associated RSDs (%) for BSA obtained across the instrument platforms utilised.

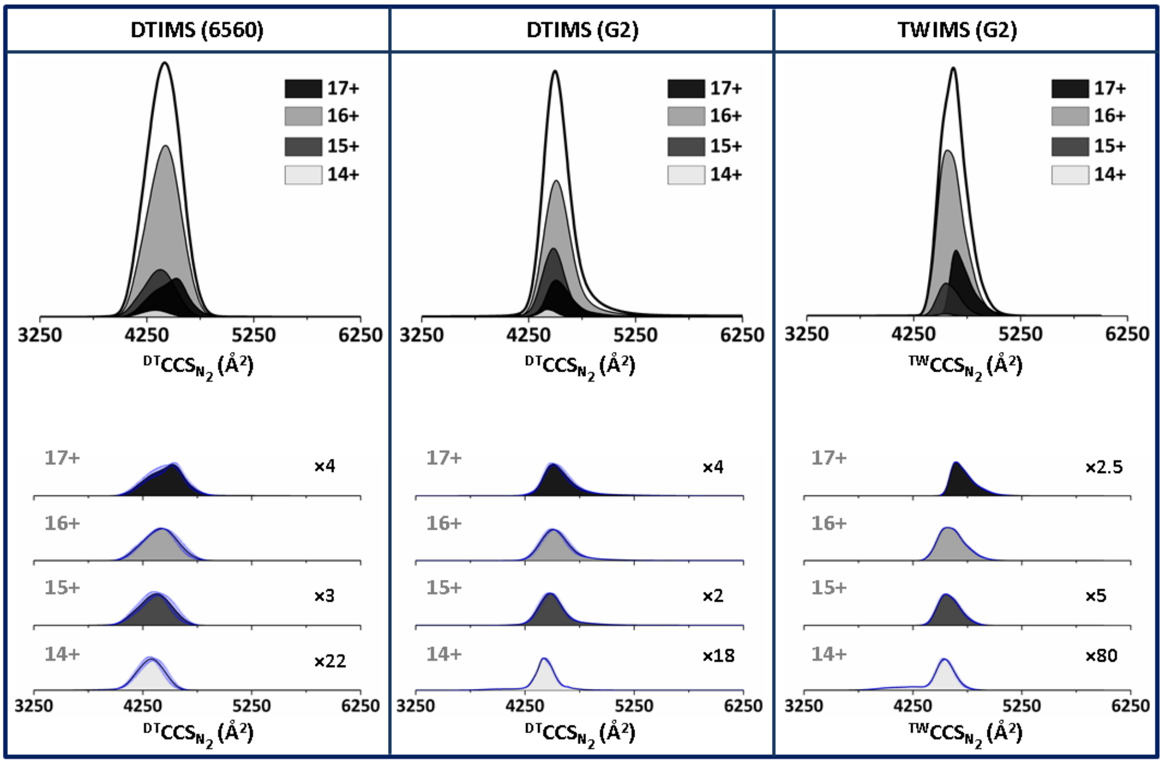

Protein			Nitrogen Drift Gas					
BSA (66,433 Da)			6560-DTIMS		G2-DTIMS		G2-TWIMS	
Z_{avg}	Species	#	$^{DT}CCS_{N_2}$ (Å²)	%RSD	$^{DT}CCS_{N_2}$ (Å²)	%RSD	$^{TW}CCS_{N_2}$ (Å²)	%RSD
15.85 ± 0.12	$[M+14H]^{14+}$	1	4349 ± 74	1.70	4425 ± 19	0.43	4535 ± 23	0.50
	$[M+15H]^{15+}$	1	4392 ± 96	2.18	4478 ± 35	0.79	4548 ± 20	0.44
	$[M+14H]^{16+}$	1	4445 ± 68	1.53	4514 ± 51	1.14	4567 ± 18	0.40
	$[M+17H]^{17+}$	1	4506 ± 80	1.77	4523 ± 54	1.18	4648 ± 10	0.22

Figure S16. BSA nitrogen CCS & CCS distributions. Upper) Total CCS distributions of BSA. Lower) Stacked CCS distribution plots for each ion normalised to the same intensity with magnification factors applied. Table) Average CCS_{N_2} values with replicate (n=3) standard deviations (±) and associated RSDs (%) for BSA obtained across the instrument platforms utilised. Interactive versions of Figures S15 & S16 are available online at https://france-ccs-2019.netlify.com/assets/bsa_s15&s16.

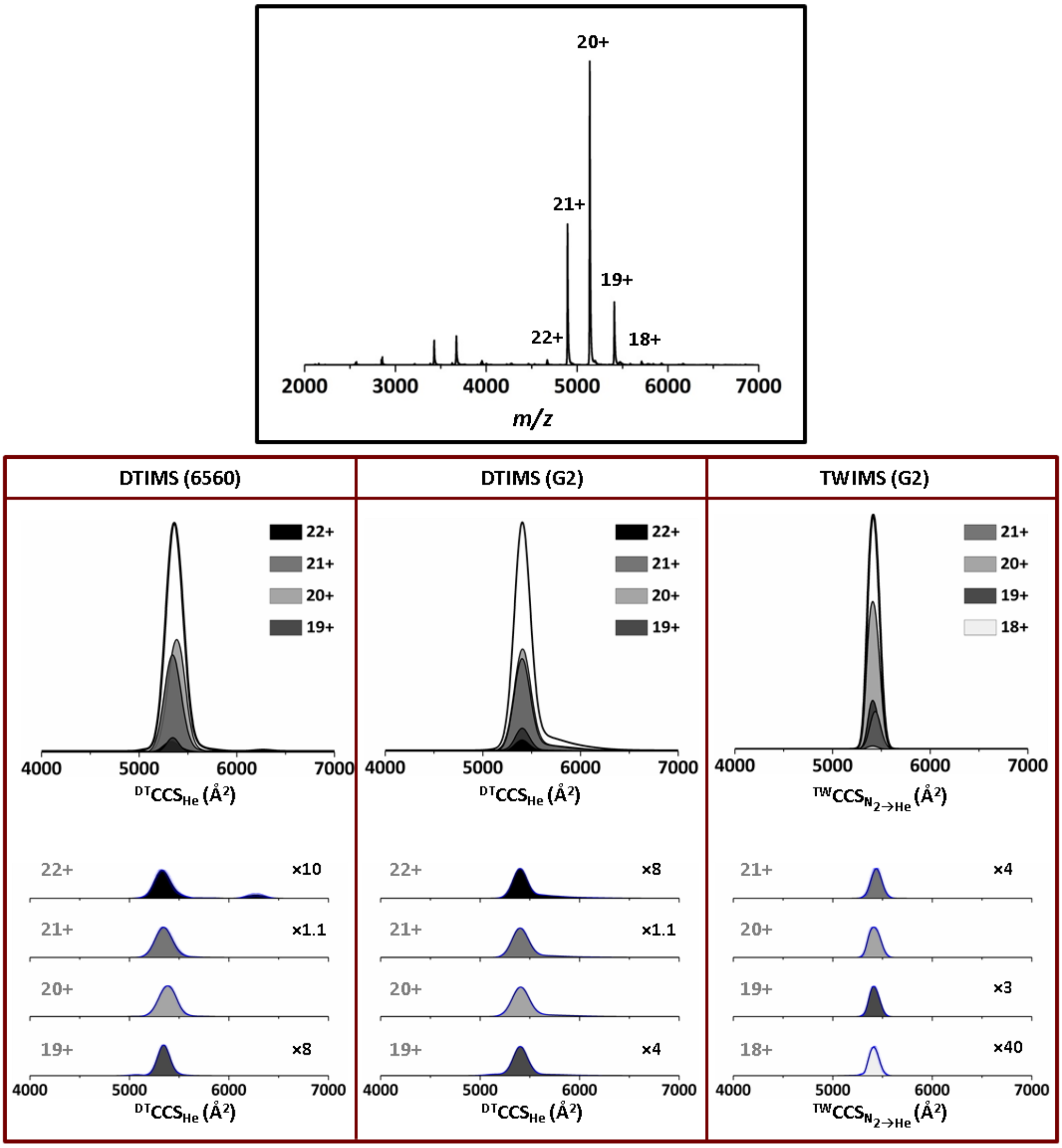

Protein			Helium Drift Gas					
Concanavalin A (4n = 102,393 Da)			6560-DTIMS		G2-DTIMS		G2-TWIMS	
Z_{avg}	Species	#	$^{DT}CCS_{He}$ (Å²)	%RSD	$^{DT}CCS_{He}$ (Å²)	%RSD	$^{TW}CCS_{He}$ (Å²)	%RSD
20.20 ± 0.30	$[4M+18H]^{18+}$	1	-	-	-	-	5412 ± 16	0.30
	$[4M+19H]^{19+}$	1	5340 ± 15	0.28	5399 ± 2	0.04	5409 ± 8	0.14
	$[4M+20H]^{20+}$	1	5384 ± 20	0.38	5397 ± 1	0.03	5412 ± 14	0.27
	$[4M+21H]^{21+}$	1	5345 ± 29	0.53	5401 ± 1	0.01	5434 ± 18	0.33
	$[4M+22H]^{22+}$	1	5335 ± 23	0.45	5405 ± 1	0.01	-	-
		2	6285 ± 24	0.38	-	-	-	-

Figure S17. Concanavalin a helium CCS & CCS distributions. Top) Mass spectrum of concanavalin a sprayed from 200 mM AmAc solution at pH 7.4, where charge states are denoted by z+. Upper middle) Total CCS distributions of concanavalin a. Lower middle) Stacked CCS distribution plots for each ion normalised to the same intensity with magnification factors applied. Table) Average CCS_{He} values with replicate (n=3) standard deviations (±) and associated RSDs (%) for concanavalin a obtained across the instrument platforms utilised.

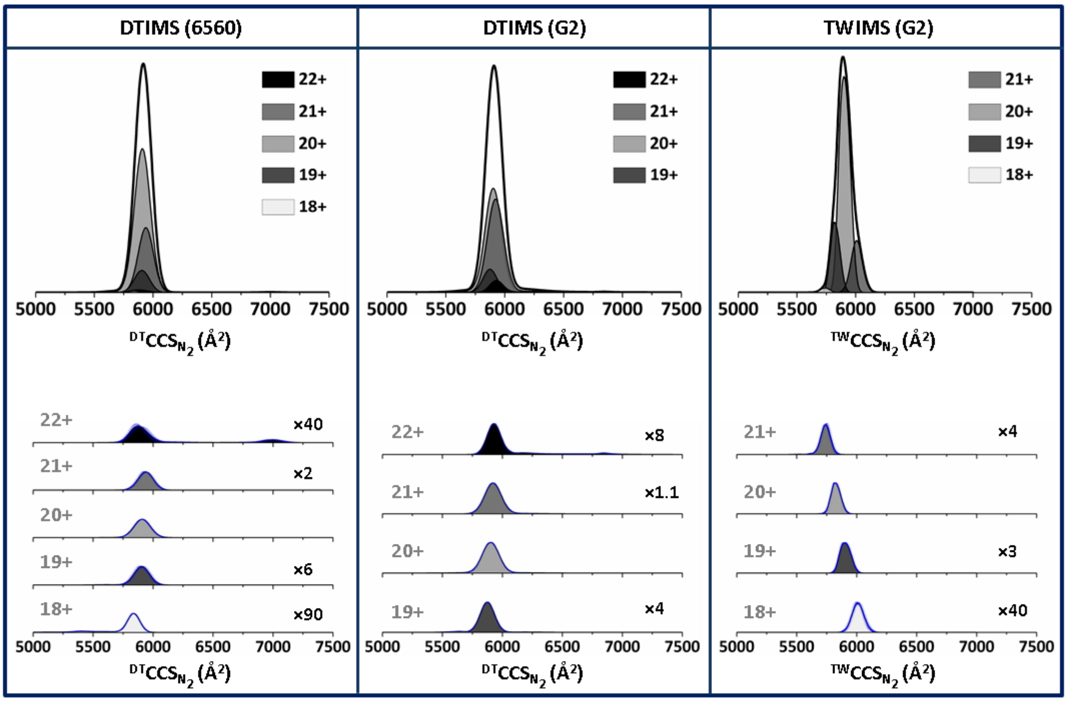

Protein			Nitrogen Drift Gas					
Concanavalin A (4n = 102,393 Da)			6560-DTIMS		G2-DTIMS		G2-TWIMS	
Z_{avg}	Species	#	$^{DT}CCS_{N_2}$ (Å^2)	%RSD	$^{DT}CCS_{N_2}$ (Å^2)	%RSD	$^{TW}CCS_{N_2}$ (Å^2)	%RSD
20.13 ± 0.25	$[4M+18H]^{18+}$	1	5838 ± 7	0.11	-	-	5740 ± 15	0.27
	$[4M+19H]^{19+}$	1	5905 ± 32	0.54	5879 ± 13	0.22	5820 ± 5	0.09
	$[4M+20H]^{20+}$	1	5913 ± 5	0.09	5902 ± 9	0.15	5900 ± 11	0.18
	$[4M+21H]^{21+}$	1	5937 ± 25	0.42	5921 ± 9	0.16	5997 ± 14	0.24
	$[4M+22H]^{22+}$	1	5890 ± 34	0.58	5930 ± 9	0.16	-	
		2	7011 ± 38	0.55	6846 ± 36	0.52	-	

Figure S18. Concanavalin a nitrogen CCS & CCS distributions. Upper) Total CCS distributions of concanavalin a. Lower) Stacked CCS distribution plots for each ion normalised to the same intensity with magnification factors applied. Table) Average CCS_{N_2} values with replicate (n=3) standard deviations (±) and associated RSDs (%) for concanavalin a obtained across the instrument platforms utilised. Interactive versions of Figures S17 & S18 are available online at https://france-ccs-2019.netlify.com/assets/cona_s17&s18.

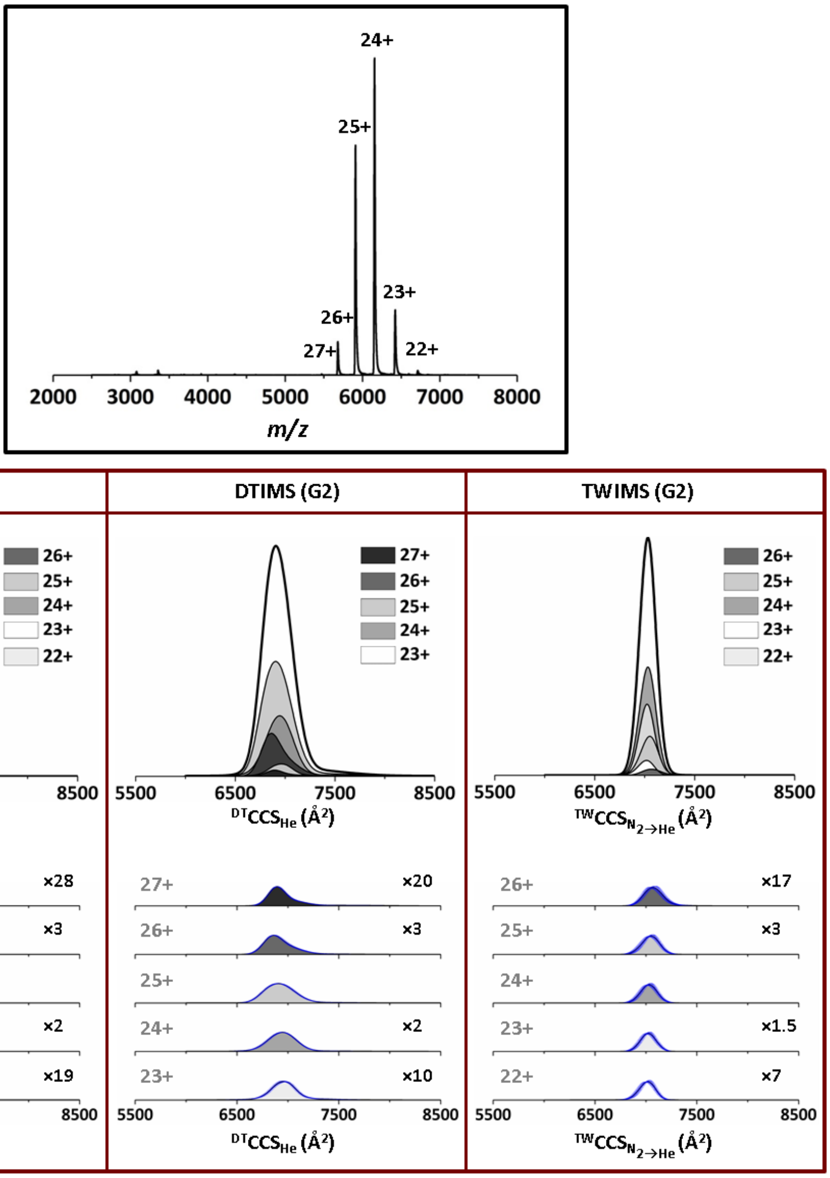

Protein			Helium Drift Gas					
Alcohol Dehydrogenase (4n = 147,659 Da)			6560-DTIMS		G2-DTIMS		G2-TWIMS	
Z_{Avg}	Species	#	$^{DT}CCS_{He}$ (Å^2)	%RSD	$^{DT}CCS_{He}$ (Å^2)	%RSD	$^{TW}CCS_{He}$ (Å^2)	%RSD
24.20 ± 0.54	$[4M+22H]^{22+}$	1	6579 ± 45	0.69	-	-	7015 ± 47	0.66
	$[4M+23H]^{23+}$	1	6584 ± 35	0.53	6968 ± 48	0.68	7020 ± 42	0.60
	$[4M+24H]^{24+}$	1	6606 ± 16	0.24	6943 ± 17	0.24	7027 ± 46	0.65
	$[4M+25H]^{25+}$	1	6588 ± 16	0.23	6914 ± 22	0.32	7045 ± 51	0.72
	$[4M+26H]^{26+}$	1	6557 ± 36	0.54	6879 ± 12	0.17	7069 ± 49	0.70
	$[4M+27H]^{27+}$	1	-	-	6908 ± 5	0.05	-	-

Figure S19. Alcohol dehydrogenase helium CCS & CCS distributions. Top) Mass spectrum of alcohol dehydrogenase sprayed from 200 mM AmAc solution at pH 7.4, where charge states are denoted by z+. Upper middle) Total CCS distributions of alcohol dehydrogenase. Lower middle) Stacked CCS distribution plots for each ion normalised to the same intensity with magnification factors applied. Table) Average CCS_{He} values with replicate (n=3) standard deviations (±) and associated RSDs (%) for alcohol dehydrogenase obtained across the instrument platforms utilised.

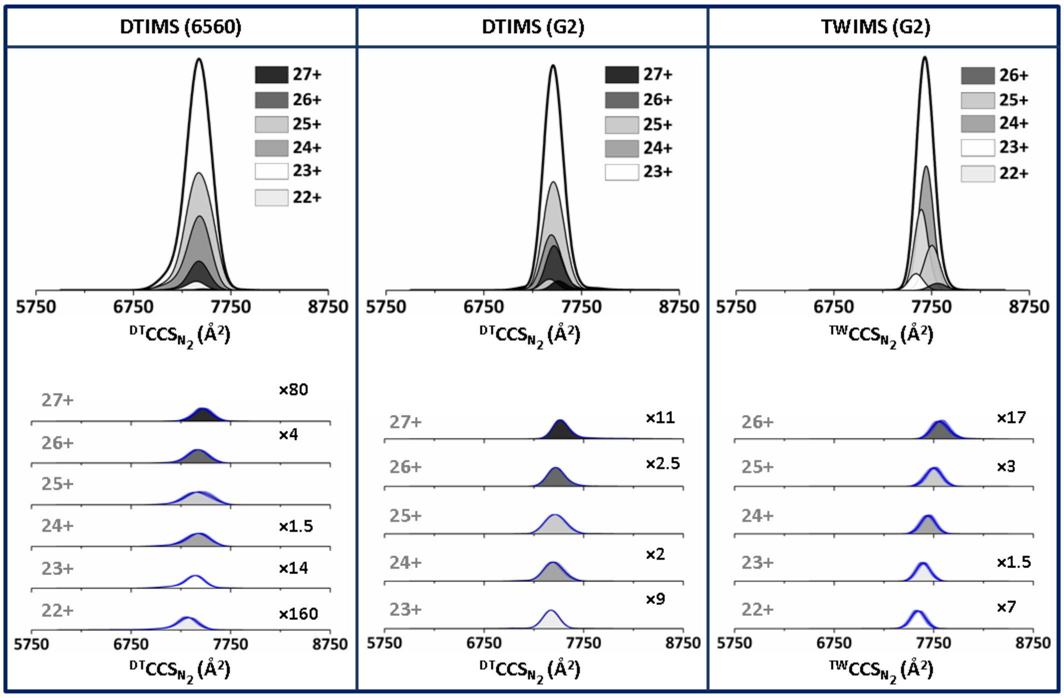

Protein			Nitrogen Drift Gas					
Alcohol Dehydrogenase (4n = 147,659 Da)			6560-DTIMS		G2-DTIMS		G2-TWIMS	
Z_{avg}	Species	#	$^{DT}CCS_{N_2}$ (Å²)	%RSD	$^{DT}CCS_{N_2}$ (Å²)	%RSD	$^{TW}CCS_{N_2}$ (Å²)	%RSD
24.45 ± 0.62	$[4M+22H]^{22+}$	1	7330 ± 70	0.70	-	-	7594 ± 44	0.58
	$[4M+23H]^{23+}$	1	7399 ± 32	0.43	7422 ± 4	0.06	7640 ± 33	0.44
	$[4M+24H]^{24+}$	1	7427 ± 52	0.71	7447 ± 37	0.50	7693 ± 41	0.54
	$[4M+25H]^{25+}$	1	7429 ± 70	0.94	7465 ± 22	0.30	7750 ± 47	0.60
	$[4M+26H]^{26+}$	1	7424 ± 36	0.49	7473 ± 16	0.21	7814 ± 45	0.58
	$[4M+27H]^{27+}$	1	7470 ± 51	0.68	7520 ± 18	0.24	-	-

Figure S20. Alcohol dehydrogenase nitrogen CCS & CCS distributions. Upper) Total CCS distributions of alcohol dehydrogenase. Lower) Stacked CCS distribution plots for each ion normalised to the same intensity with magnification factors applied. Table) Average CCS_{N_2} values with replicate (n=3) standard deviations (±) and associated RSDs (%) for alcohol dehydrogenase obtained across the instrument platforms utilised. Interactive versions of Figures S19 & S20 are available online at https://france-ccs-2019.netlify.com/assets/alcdehy_s19&s20.

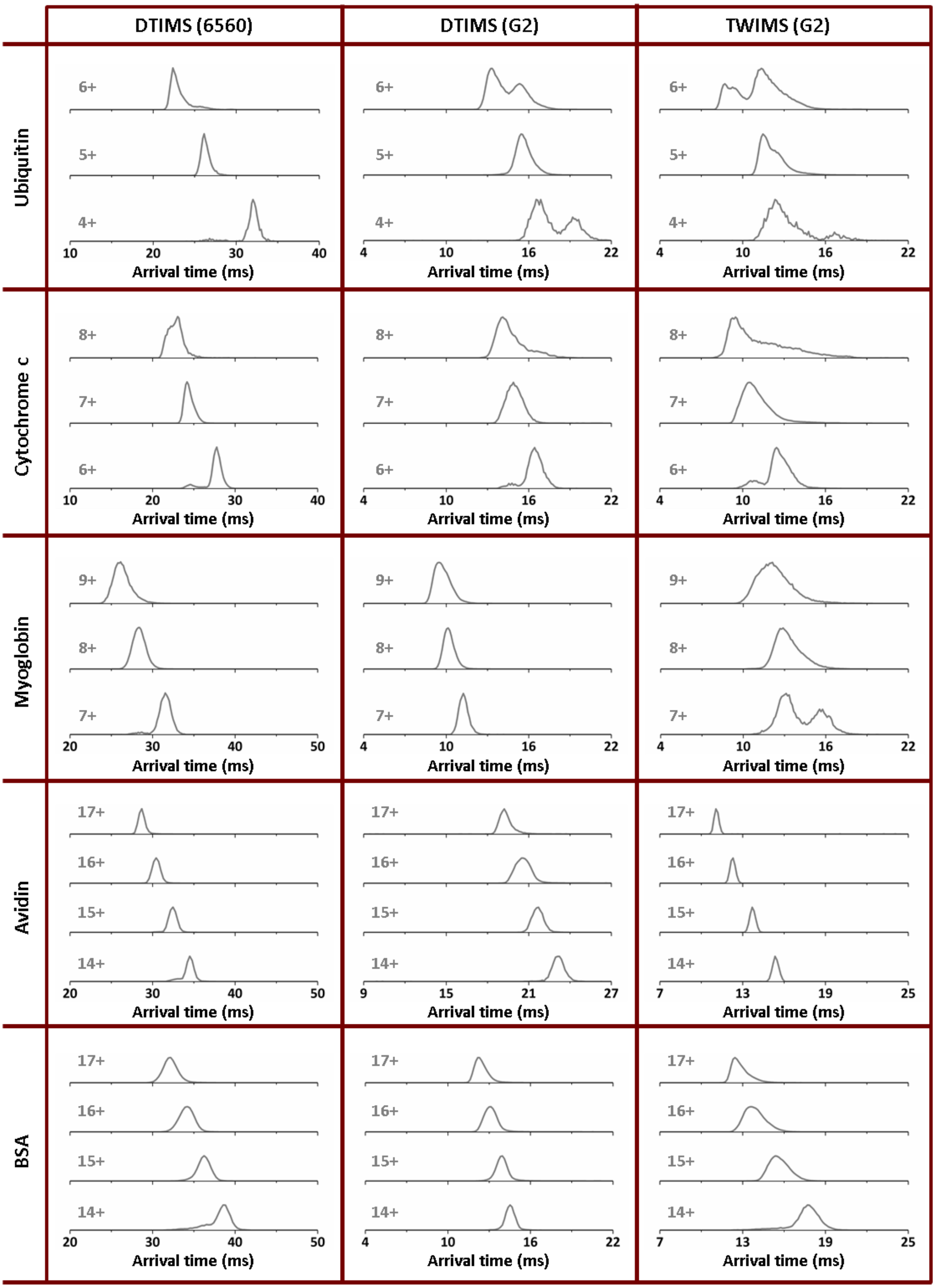
DTIMS (6560)
DTIMS (G2)
TWIMS (G2)
Ubiquitin
6+
5+
4+
10 20 30 40
4 10 16 22
Arrival time (ms)
Cytochrome c
8+
7+
6+
10 20 30 40
4 10 16 22
Arrival time (ms)
Myoglobin
9+
8+
7+
20 30 40 50
4 10 16 22
Arrival time (ms)
Avidin
17+
16+
15+
14+
20 30 40 50
9 15 21 27
7 13 19 25
Arrival time (ms)
BSA
17+
16+
15+
14+
20 30 40 50
4 10 16 22
7 13 19 25
Arrival time (ms)

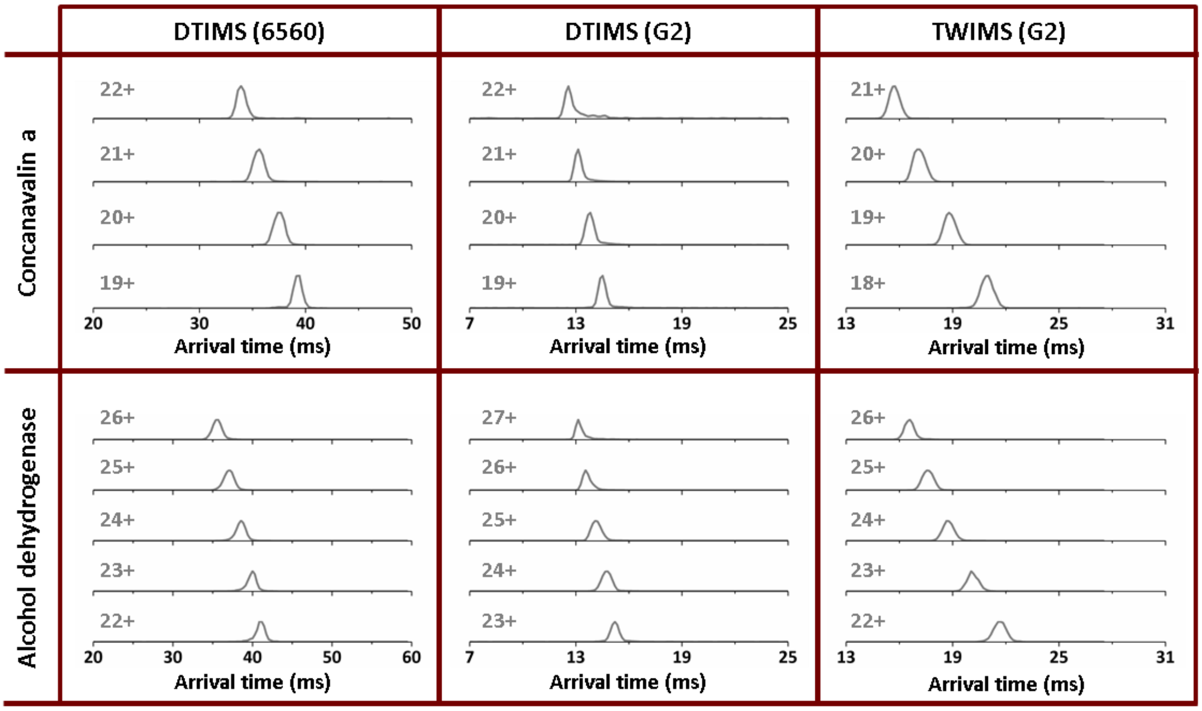

Figure 21. Raw ATDs (He).Raw single replicate ATDs, obtained with He as the drift gas, for all of the protein/protein complex ions analysed across the instruments utilised within this study.

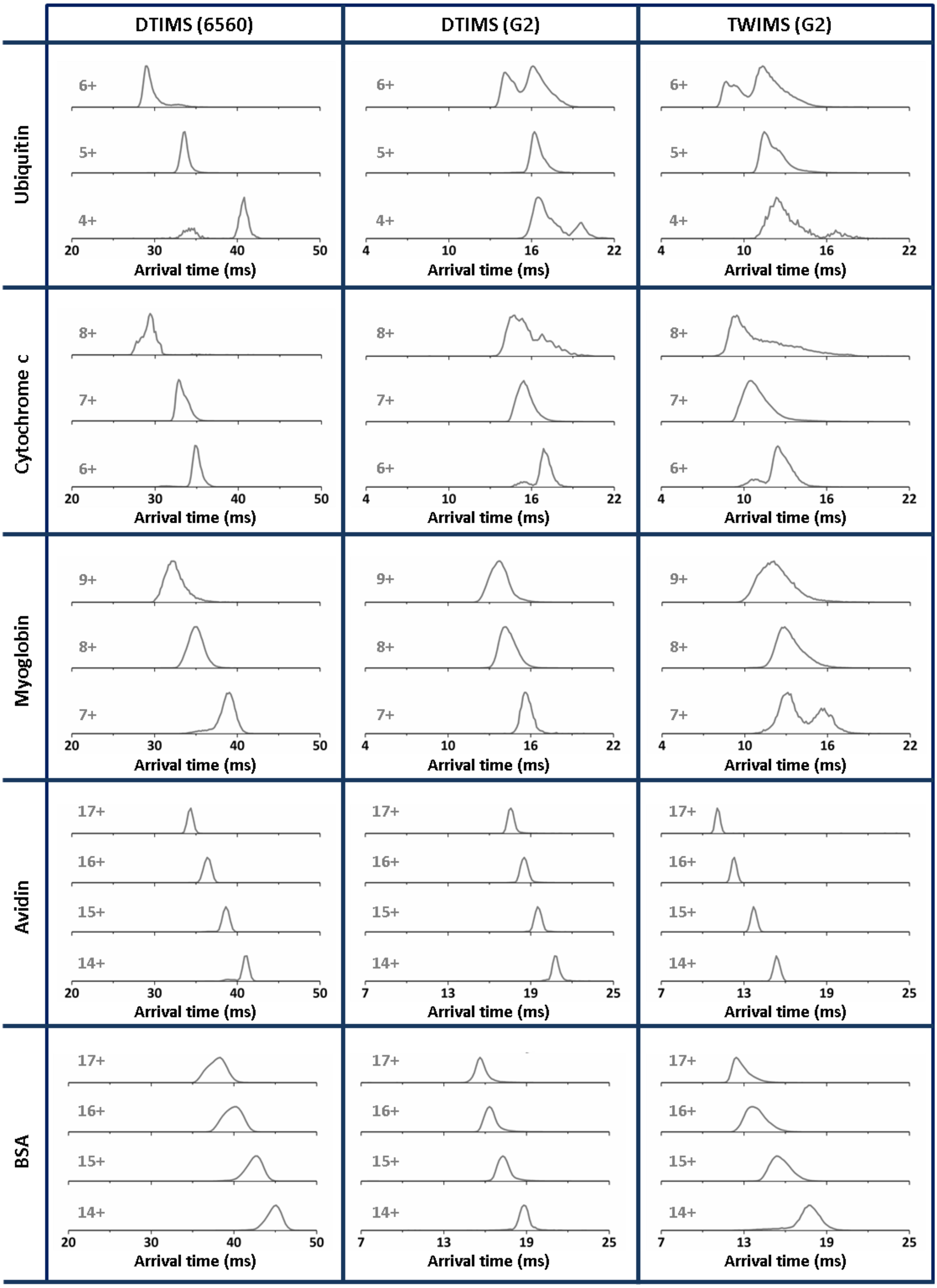
DTIMS (6560)
DTIMS (G2)
TWIMS (G2)
Ubiquitin
6+
5+
4+
Cytochrome c
8+
7+
6+
Myoglobin
9+
8+
7+
Avidin
17+
16+
15+
14+
BSA
17+
16+
15+
14+
20
30
40
50
4
10
16
22
7
13
19
25
Arrival time (ms)

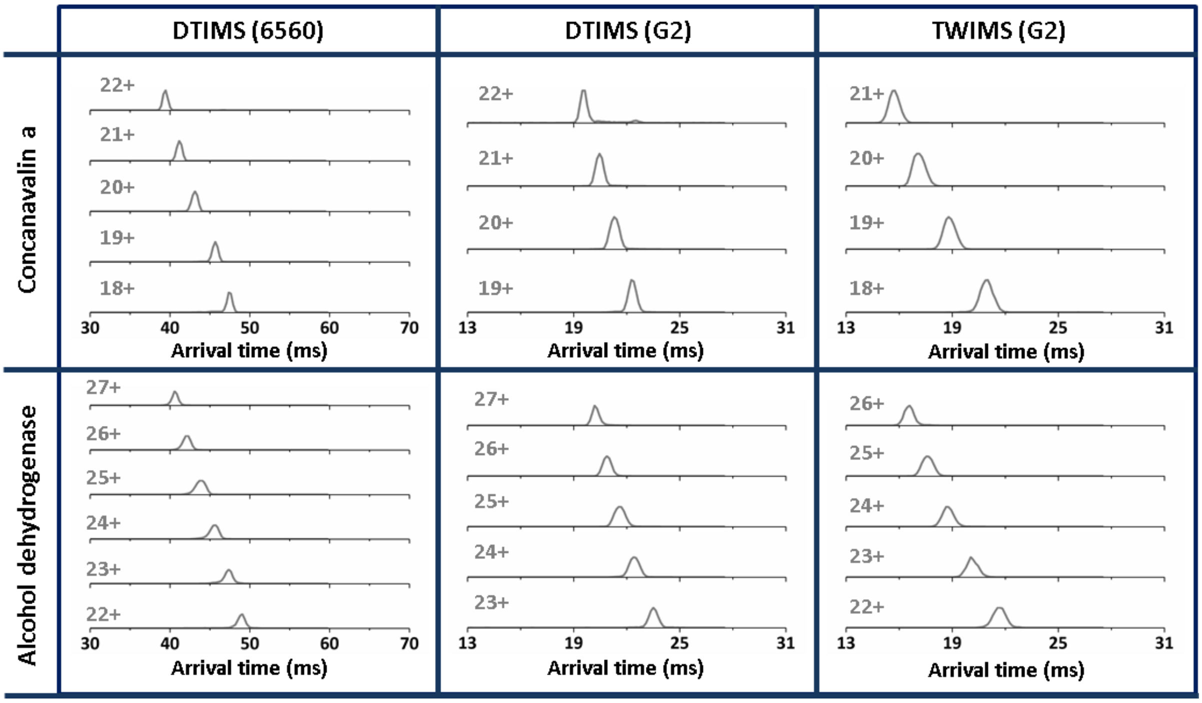

Figure S22. ATDs (N_2). Raw single replicate ATDs, obtained with N_2 as the drift gas, for all of the protein/protein complex ions analysed across the instruments utilised within this study. Interactive versions of Figures S21 & S22 are available online at: 1) https://france-ccs-2019.netlify.com/assets/ubi_s21&s22, 2) https://france-ccs-2019.netlify.com/assets/cytc_s21&s22, 3) https://france-ccs-2019.netlify.com/assets/myo_s21&s22, 4) https://france-ccs-2019.netlify.com/assets/avi_s21&s22, 5) https://france-ccs-2019.netlify.com/assets/bsa_s21&s22, 6) https://france-ccs-2019.netlify.com/assets/cona_s21&s22, 7) https://france-ccs-2019.netlify.com/assets/alcdehy_s21&s22.

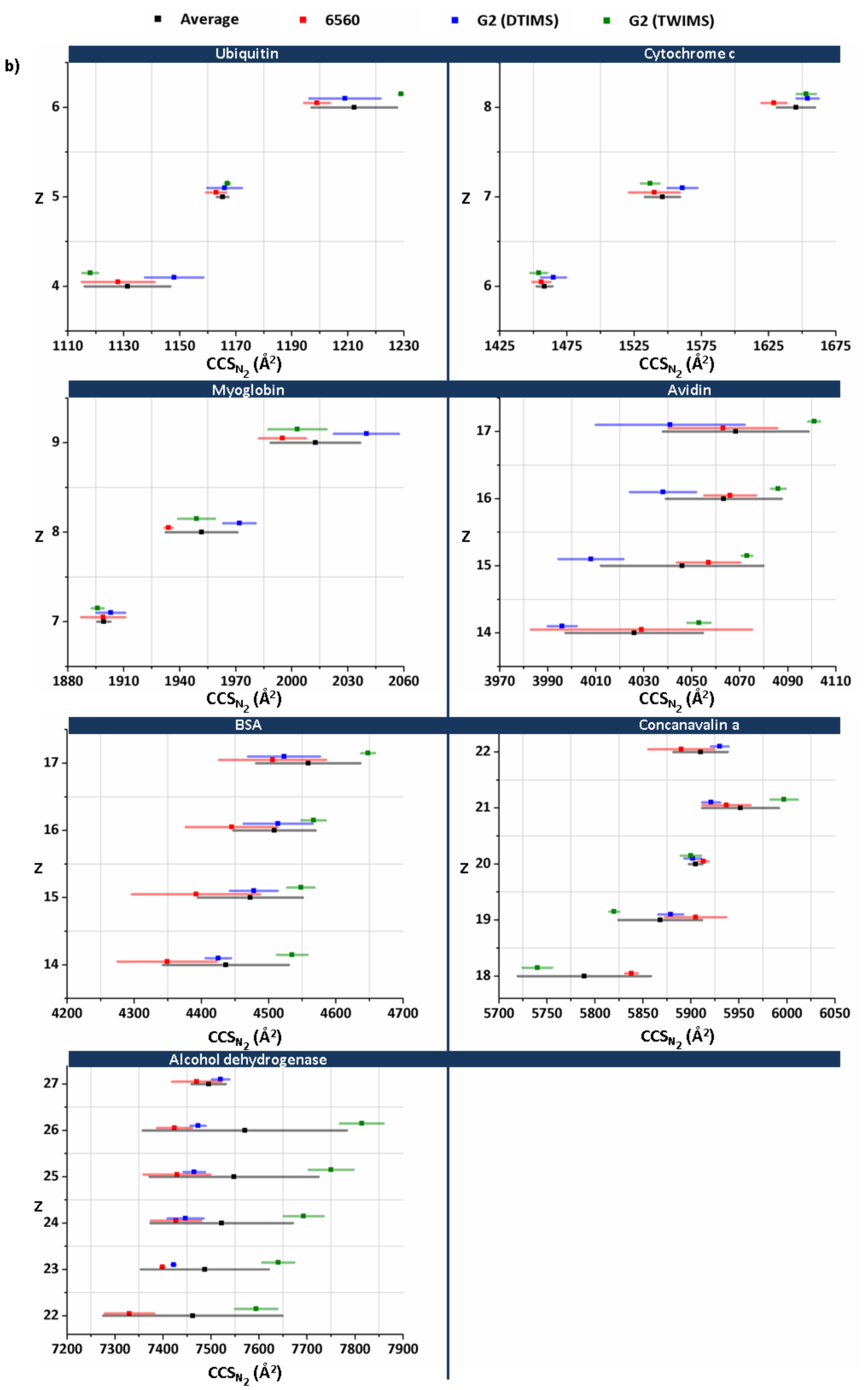

Figure S23. Scatter plots showing the range of CCS_{N_2} values taken for the protein/protein complexes analysed within this study across the instrumental platforms utilised. In all cases the CCS for the single most abundant conformation for each charge state was compared across the three instruments. The black, red, blue and green squares represent the average CCS_{N_2} values obtained for single conformations as an average across all the instruments, on the 6560, the G2 (DTIMS) and the G2 (TWIMS) respectively. The associated coloured bars show the standard deviation across the experimental replicates.

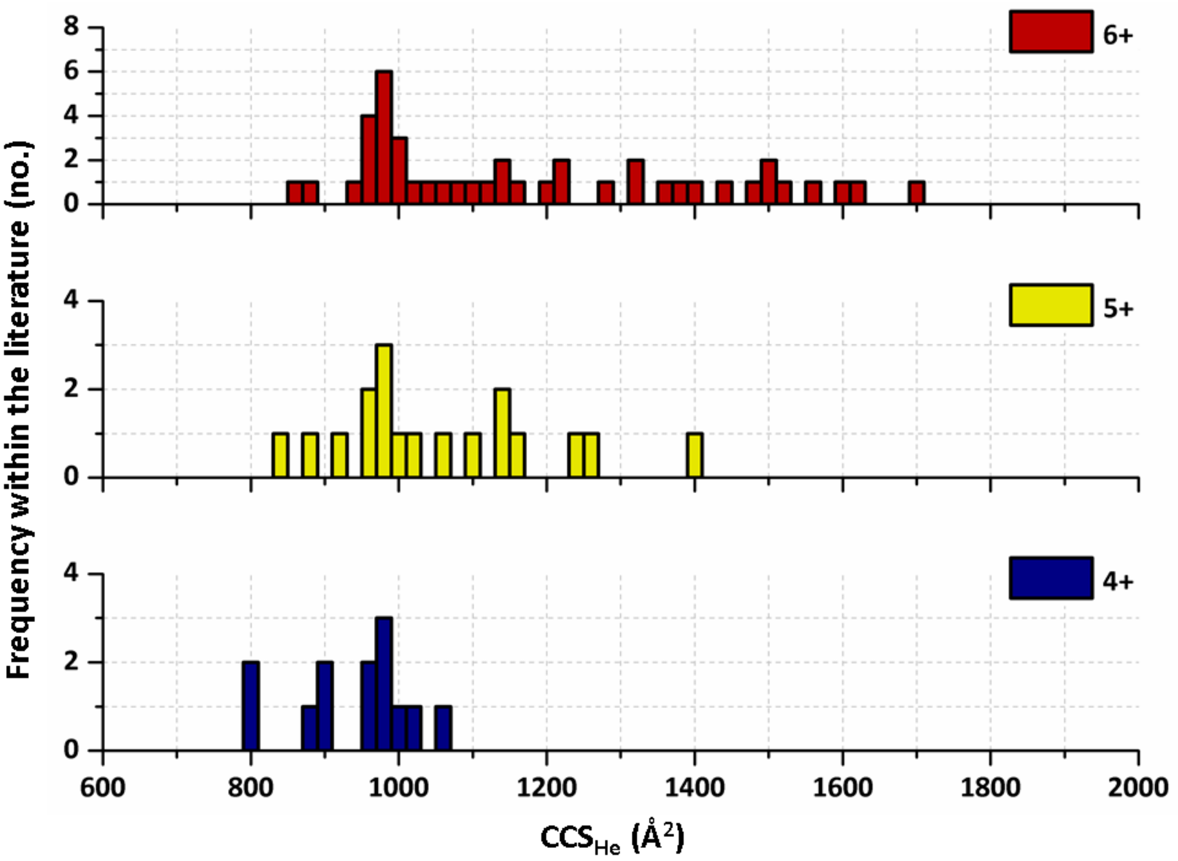

Figure S24. Global CCS_{He} histogram plots for the charge states of ubiquitin observed across the experiments outlined in this study. Literature as well as our own experimentally obtained CCS were grouped into 20 Å^2 bins, whereby the frequency of CCS to the nearest 20 Å^2 increment were summed and represented as solid bars within the histogram plots. Within these stacked histogram plots, blue, yellow and red bars represent the frequency and size of CCS values for the 4+, 5+ and 6+ ions of ubiquitin respectively.

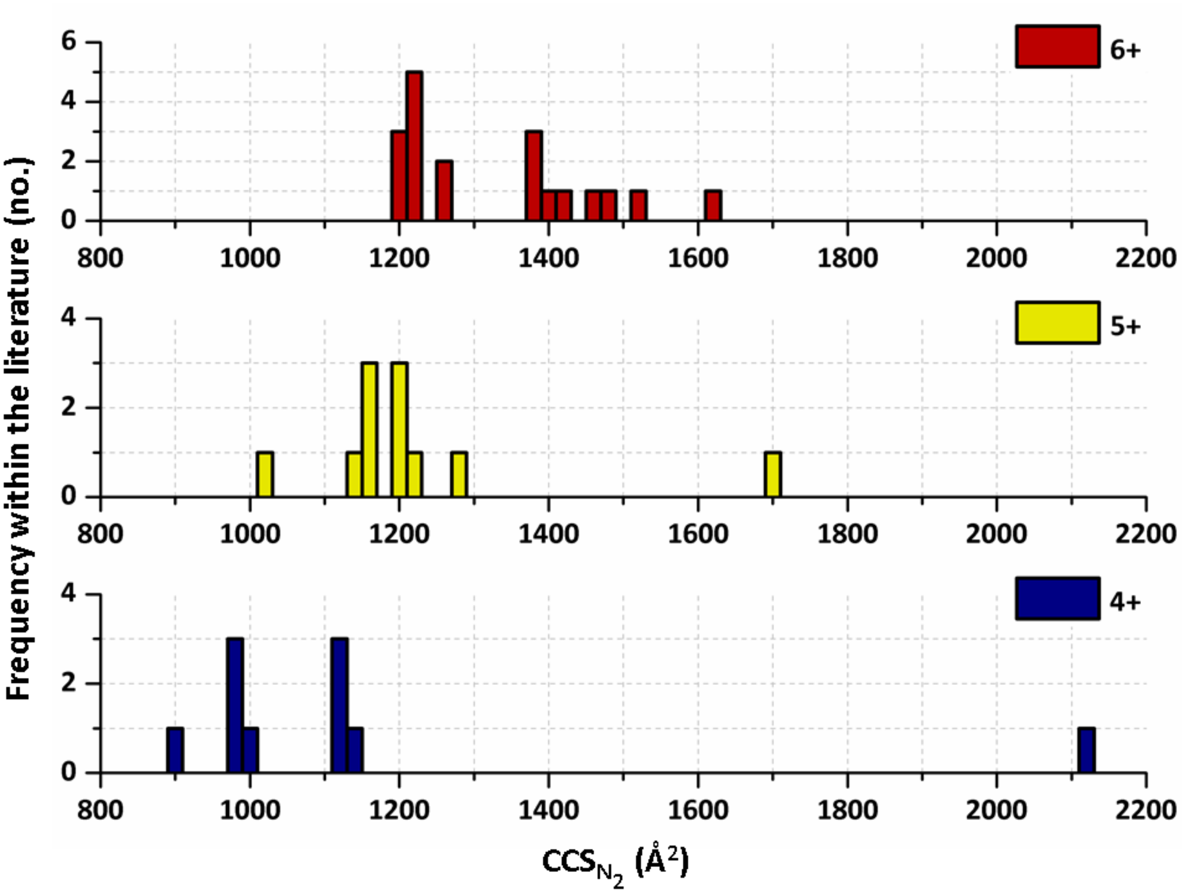

Figure S25. Global CCS$_{N_2}$ histogram plots for the charge states of ubiquitin observed across the experiments outlined in this study. Literature as well as our own experimentally obtained CCS were grouped into 20 Å^2 bins, whereby the frequency of CCS to the nearest 20 Å^2 increment were summed and represented as solid bars within the histogram plots. Within these stacked histogram plots, blue, yellow and red bars represent the frequency and size of CCS values for the 4+, 5+ and 6+ ions of ubiquitin respectively.

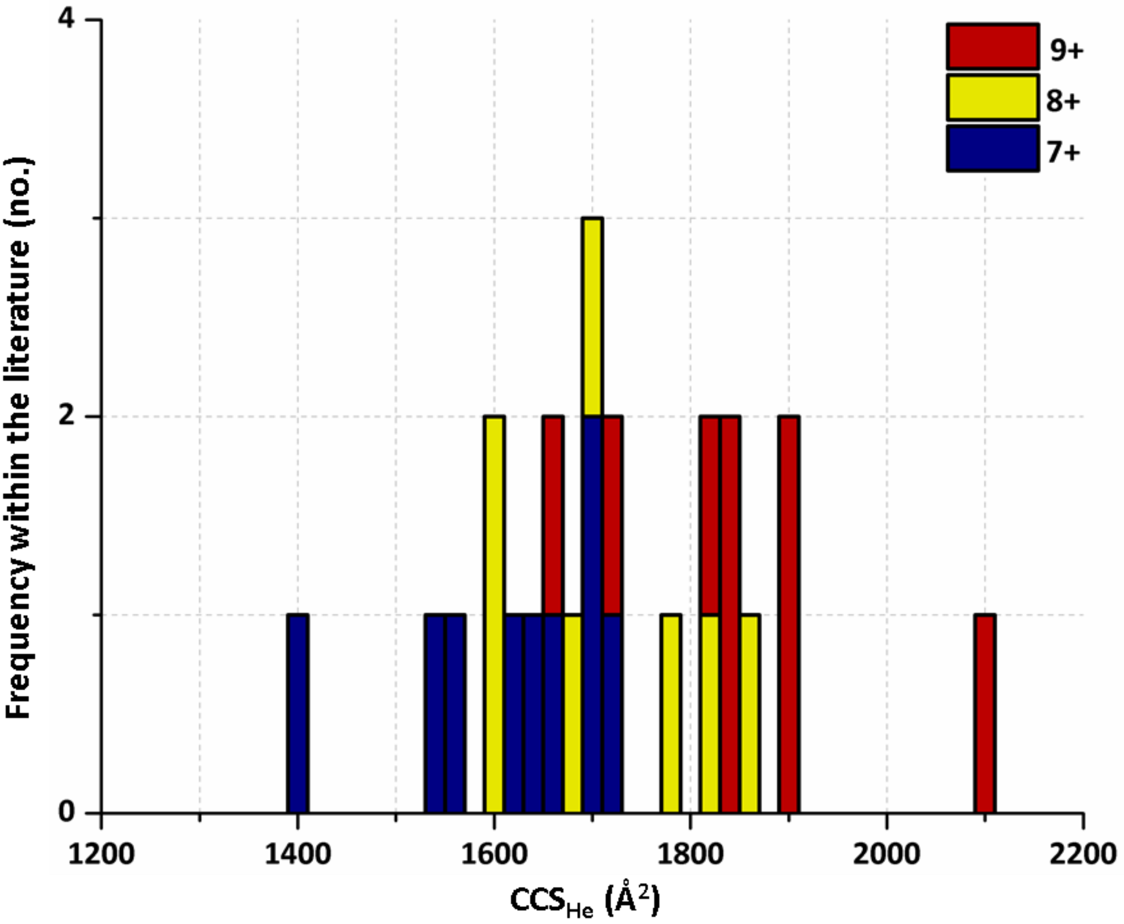

Figure S26. Global CCS$_{He}$ histogram plot for the charge states of myoglobin observed across the experiments outlined in this study. Literature as well as our own experimentally obtained CCS were grouped into 20 Å^2 bins, whereby the frequency of CCS to the nearest 20 Å^2 increment were summed and represented as solid bars within the histogram plot. Within the histogram plot, blue, yellow and red bars represent the frequency and size of CCS values for the 7+, 8+ and 9+ ions of myoglobin respectively.

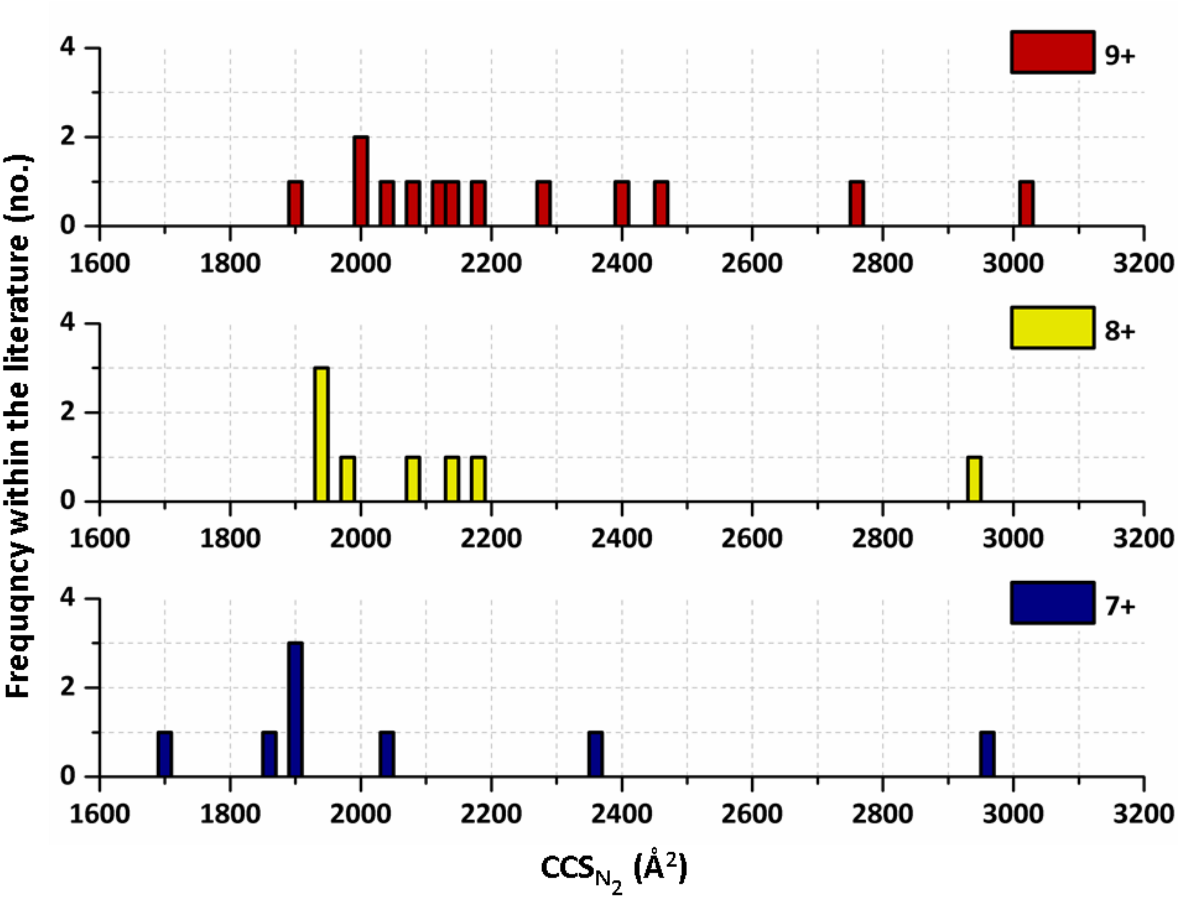

Figure S27. Global CCS_{N_2} histogram plots for the charge states of myoglobin observed across the experiments outlined in this study. Literature as well as our own experimentally obtained CCS were grouped into 20 Å^2 bins, whereby the frequency of CCS to the nearest 20 Å^2 increment were summed and represented as solid bars within the histogram plots. Within these stacked histogram plots, blue, yellow and red bars represent the frequency and size of CCS values for the 7+, 8+ and 9+ ions of myoglobin respectively.

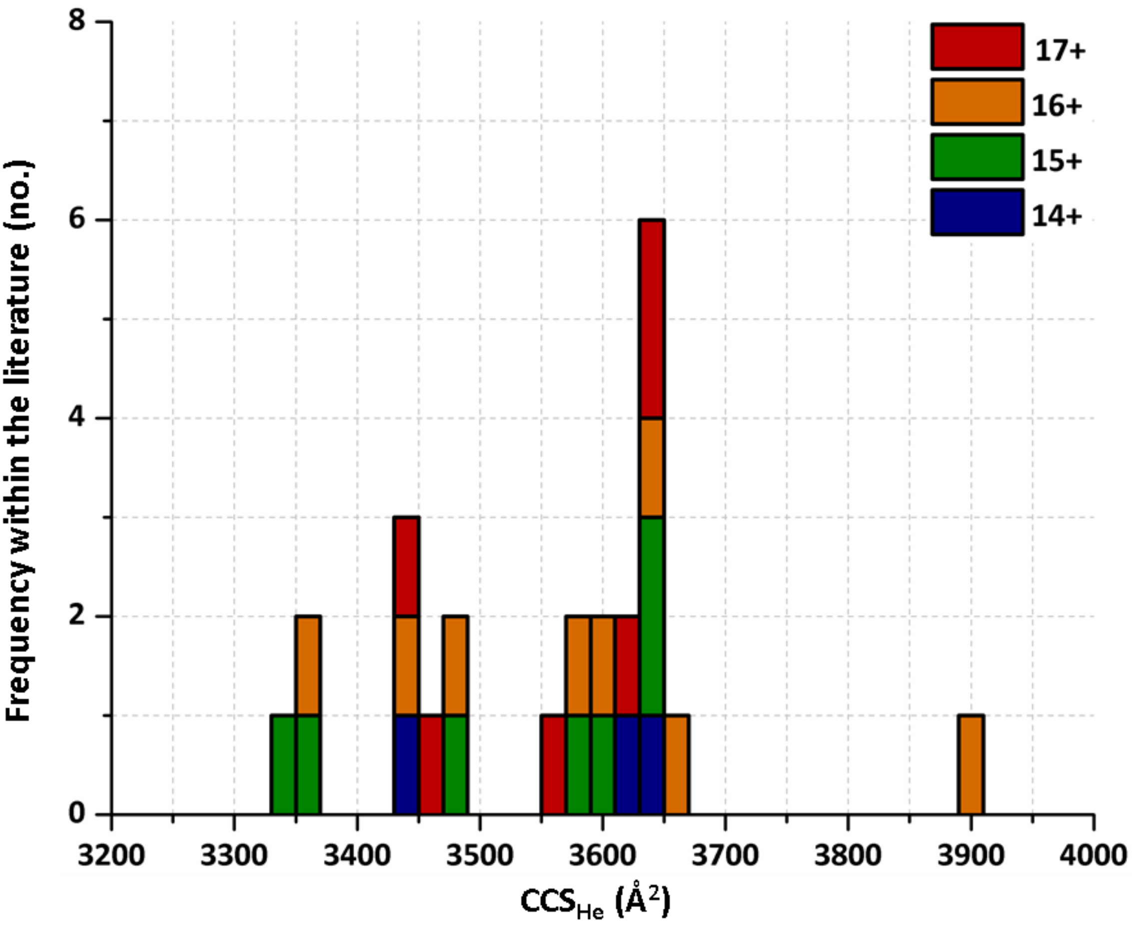

Figure S28. Global CCS_{He} histogram plot for the charge states of avidin observed across the experiments outlined in this study. Literature as well as our own experimentally obtained CCS were grouped into 40 Å^2 bins, whereby the frequency of CCS to the nearest 40 Å^2 increment were summed and represented as solid bars within the histogram plot. Within the histogram plot, blue, green, orange and red bars represent the frequency and value of CCS for the 14+, 15+, 16+ and 17+ ions of avidin respectively.

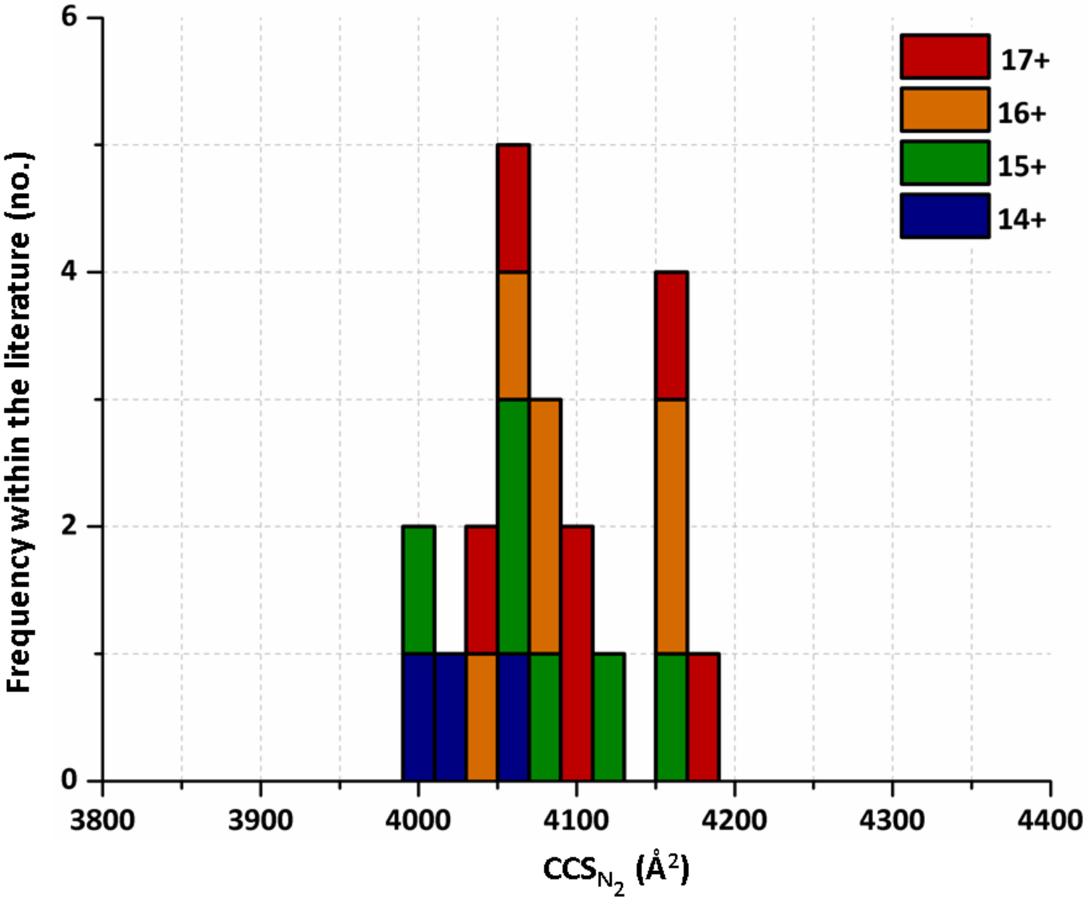

Figure S29. Global CCS_{N_2} histogram plot for the charge states of avidin observed across the experiments outlined in this study. Literature as well as our own experimentally obtained CCS were grouped into 40 Å^2 bins, whereby the frequency of CCS to the nearest 40 Å^2 increment were summed and represented as solid bars within the histogram plot. Within the histogram plot, blue, green, orange and red bars represent the frequency and value of CCS for the 14+, 15+, 16+ and 17+ ions of avidin respectively.

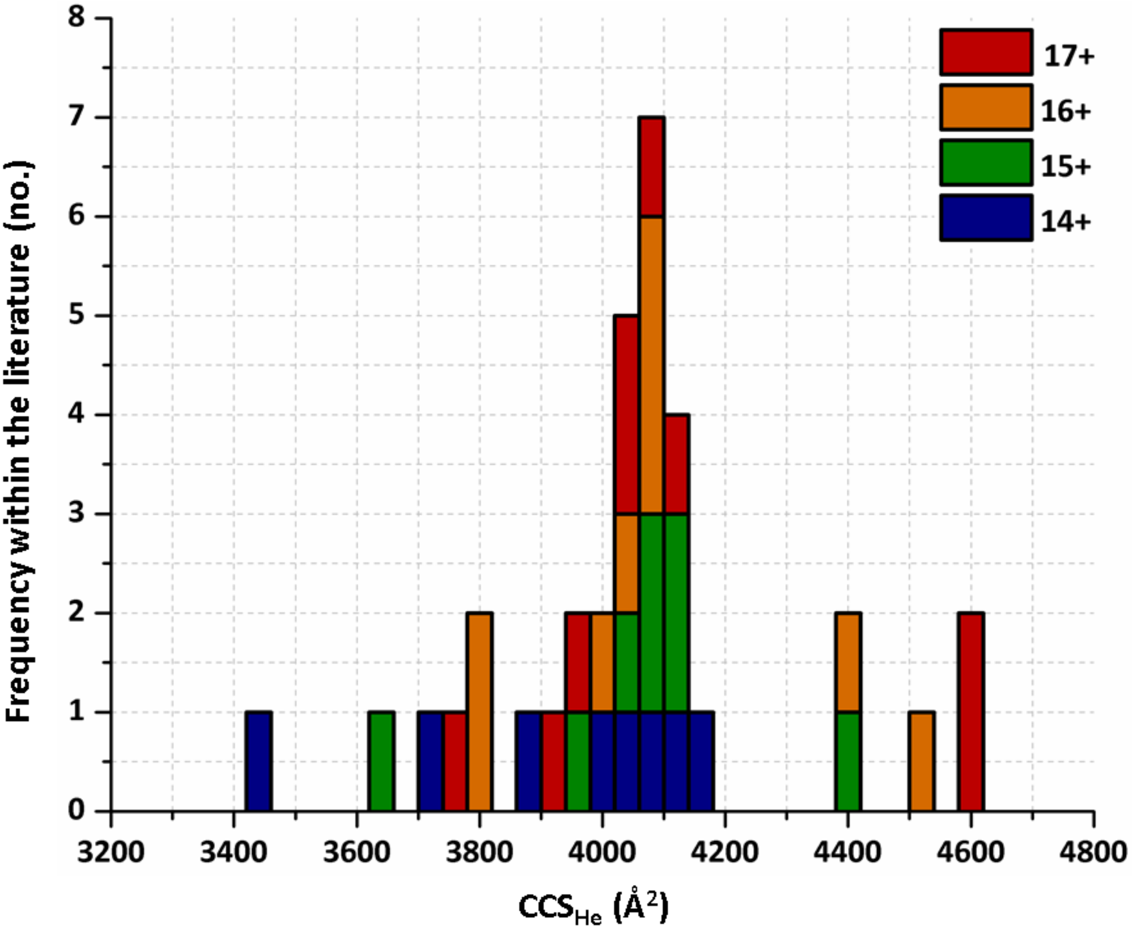

Figure S30. Global CCS$_{He}$ histogram plot for the charge states of BSA observed across the experiments outlined in this study. Literature as well as our own experimentally obtained CCS were grouped into 40 Å^2 bins, whereby the frequency of CCS to the nearest 40 Å^2 increment were summed and represented as solid bars within the histogram plot. Within the histogram plot, blue, green, orange and red bars represent the frequency and value of CCS for the 14+, 15+, 16+ and 17+ ions of BSA respectively.

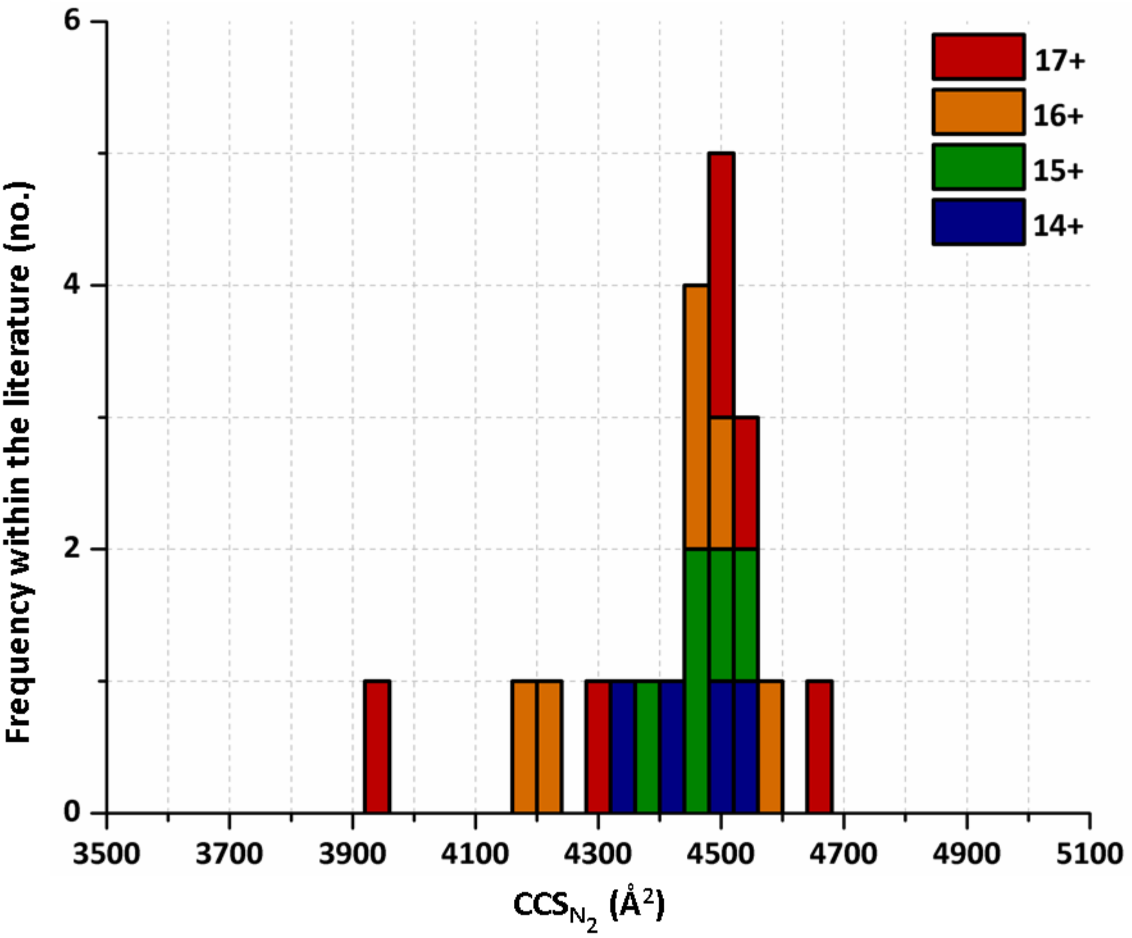

Figure 31. Global CCS$_{N_2}$ histogram plot for the charge states of BSA observed across the experiments outlined in this study. Literature as well as our own experimentally obtained CCS were grouped into 40 Å^2 bins, whereby the frequency of CCS to the nearest 40 Å^2 increment were summed and represented as solid bars within the histogram plot. Within the histogram plot, blue, green, orange and red bars represent the frequency and value of CCS for the 14+, 15+, 16+ and 17+ ions of BSA respectively.

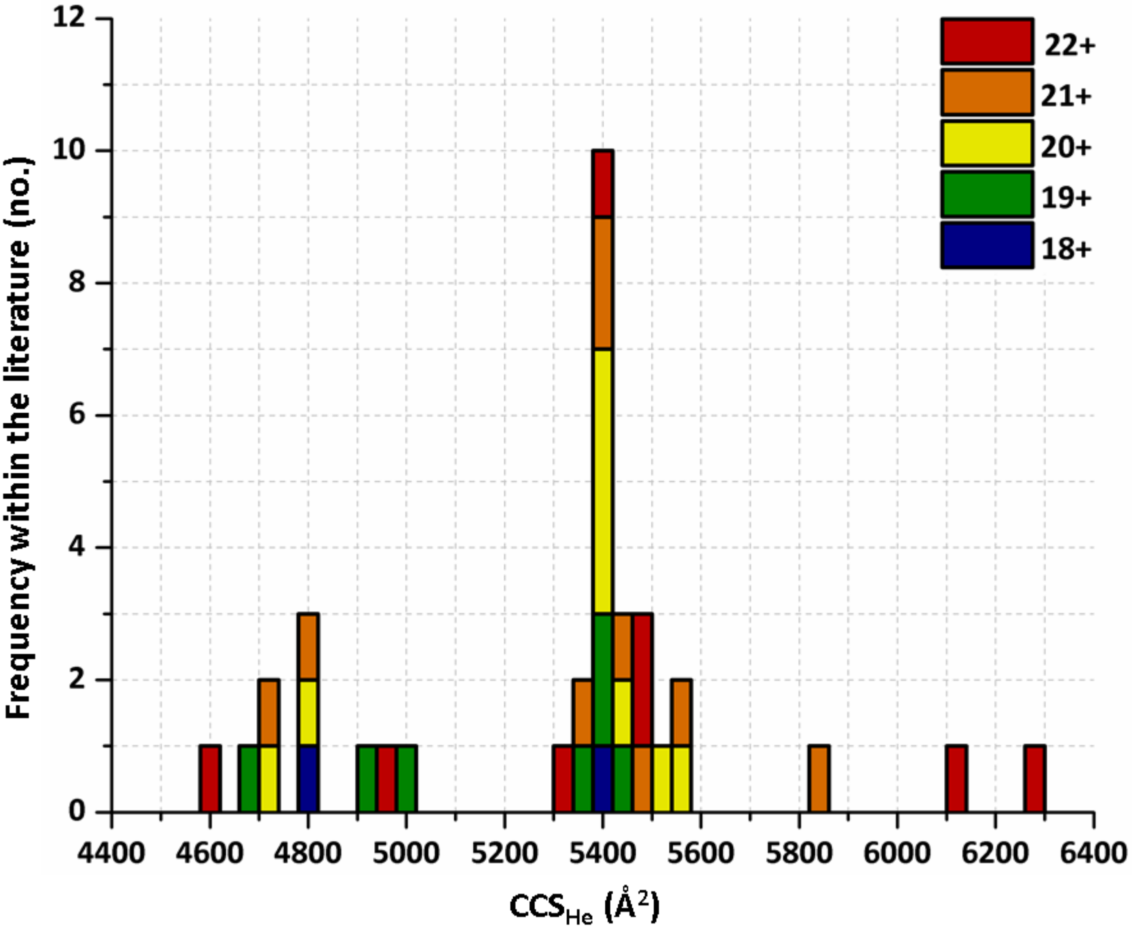

Figure S32. Global CCS$_{He}$ histogram plot for the charge states of concanavalin a observed across the experiments outlined in this study. Literature as well as our own experimentally obtained CCS were grouped into 40 Å^2 bins, whereby the frequency of CCS to the nearest 40 Å^2 increment were summed and represented as solid bars within the histogram plot. Within the histogram plot, blue, green, yellow, orange and red bars represent the frequency and value of CCS for the 18+, 19+, 20+, 21+ and 22+ ions of concanavalin a respectively.

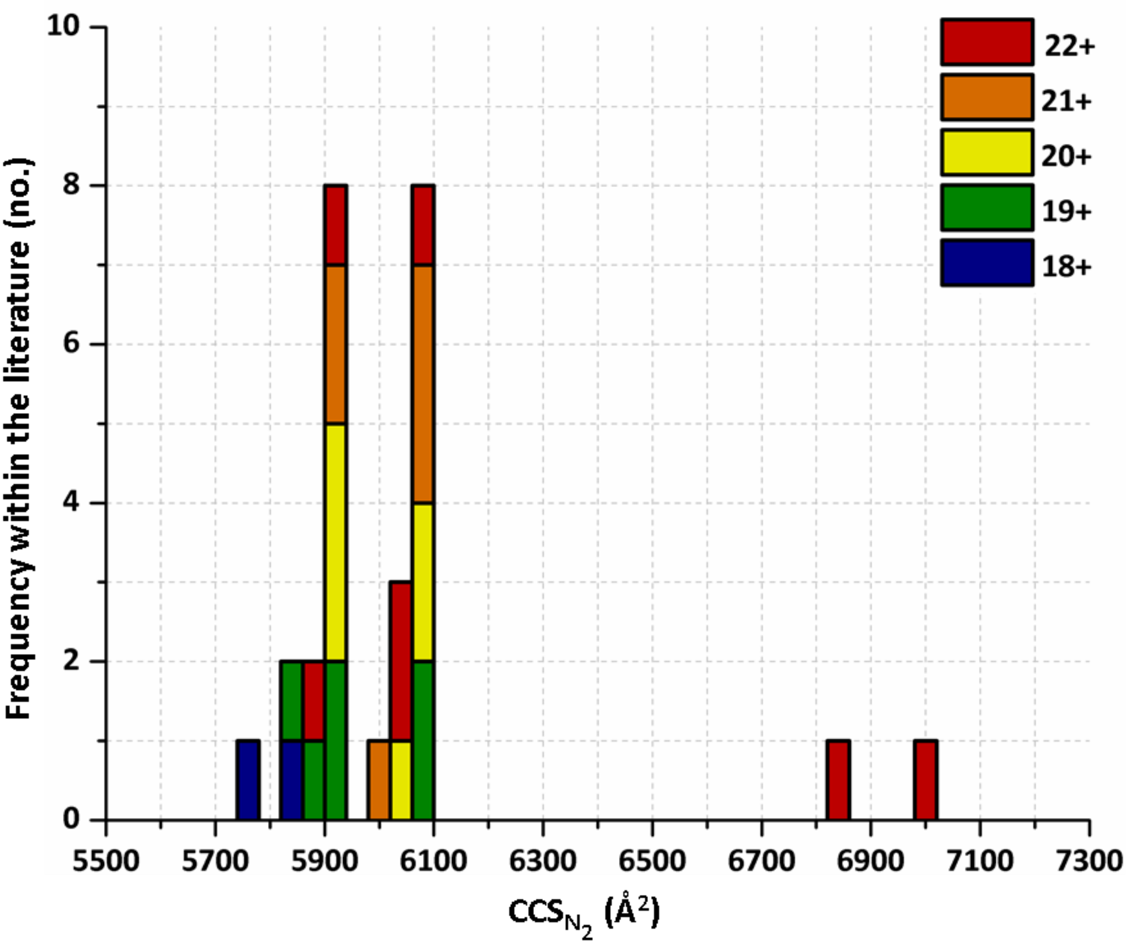

Figure S33. Global CCS_{N_2} histogram plot for the charge states of concanavalin a observed across the experiments outlined in this study. Literature as well as our own experimentally obtained CCS were grouped into 40 Å^2 bins, whereby the frequency of CCS to the nearest 40 Å^2 increment were summed and represented as solid bars within the histogram plot. Within the histogram plot, blue, green, yellow, orange and red bars represent the frequency and value of CCS for the 18+, 19+, 20+, 21+ and 22+ ions of concanavalin a respectively.

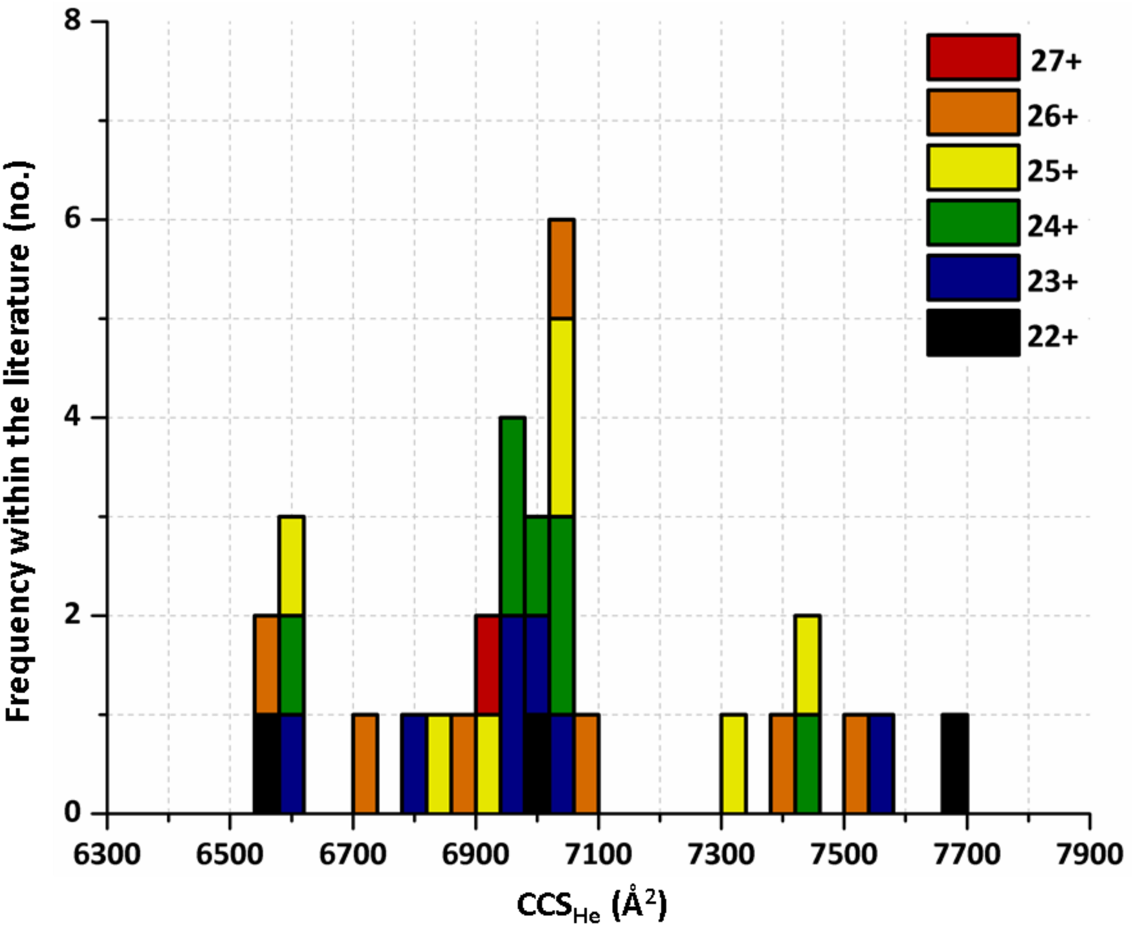

Figure S34. Global CCS$_{He}$ histogram plot for the charge states of alcohol dehydrogenase observed across the experiments outlined in this study. Literature as well as our own experimentally obtained CCS were grouped into 40 Å^2 bins, whereby the frequency of CCS to the nearest 40 Å^2 increment were summed and represented as solid bars within the histogram plot. Within the histogram plot, black, blue, green, yellow, orange and red bars represent the frequency and value of CCS for the 22+, 23+, 24+, 25+, 26+ and 27+ ions of alcohol dehydrogenase respectively.

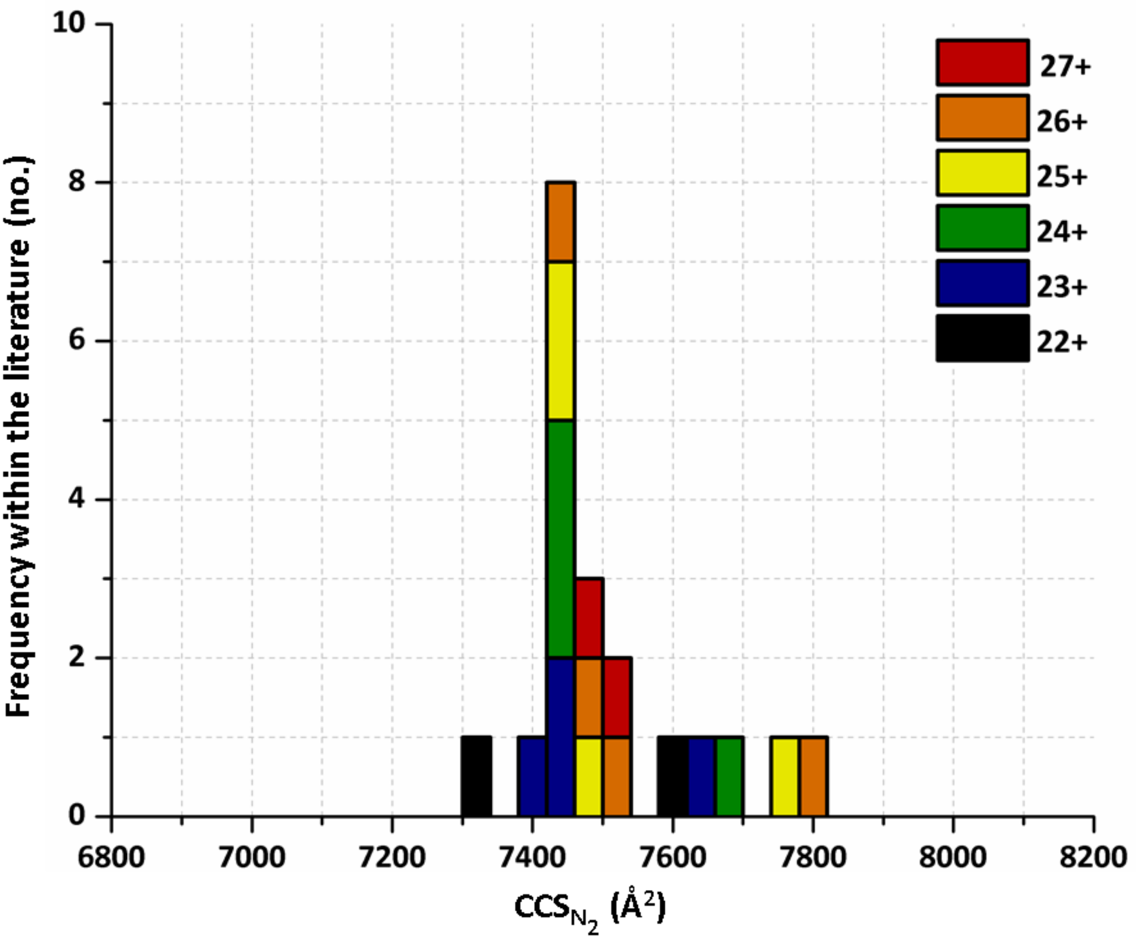

Figure S35. Global CCS_{N_2} histogram plot for the charge states of alcohol dehydrogenase observed across the experiments outlined in this study. Literature as well as our own experimentally obtained CCS were grouped into 40 Å^2 bins, whereby the frequency of CCS to the nearest 40 Å^2 increment were summed and represented as solid bars within the histogram plot. Within the histogram plot, black, blue, green, yellow, orange and red bars represent the frequency and value of CCS for the 22+, 23+, 24+, 25+, 26+ and 27+ ions of alcohol dehydrogenase respectively.

Table S9. Literature and experimentally determined CCS$_{He}$ values obtained for the protein/protein complex ions described within this study. Within this table 'n' represents the multimeric state of the protein, 'z' denotes the protein charge state and the 'Source' column highlights the references from which the CCS$_{He}$ values were found, where the '#' denotes CCS$_{He}$ values that were obtained experimentally within this study. Abbreviated versions of the IM techniques employed to obtain the corresponding CCS$_{He}$ values are noted in the 'IM technique' column. CCS$_{He}$ values highlighted in red were obtained from graphs within the associated references and as such will likely not be completely accurate. The '**' after some CCS denotes the high likelihood that these values actually correspond to misidentified coincident dimer species and not more compact monomeric conformations.

Analyte	**n**	**Z (+)**	**CCS$_{He}$**	**IM technique**	**Source**
Ubiquitin	1	4	791	TWIMS	[14]
			800	TWIMS	[15]
			889**	DTIMS	[9]
			904	DTIMS	[16]
			907	DTIMS	#
			961	TWIMS	#
			963	DTIMS	#
			971	DTIMS	[9]
			972	DTIMS	[4]
			972	DTIMS	[13]
			1004	DTIMS	[17]
			1020	DTIMS	[18]
			1059	DTIMS	[17]
	1	5	840	TWIMS	[15]
			872	DTIMS	[16]
			924	DTIMS	#
			955	TWIMS	#
			965	DTIMS	#
			979	DTIMS	[16]
			982	DTIMS	[4]
			983	DTIMS	[13]
			1003	TWIMS	#
			1027	DTIMS	[17]
			1053	DTIMS	[9]
			1100	TWIMS	[19]
			1135	TWIMS	[20]
			1137	DTIMS	[17]
			1150	DTIMS	[18]
			1239	DTIMS	[17]
			1260	TWIMS	[19]
			1390	ROMIAC	[21]
	1	6	863	DTIMS	[16]
			870	TWIMS	[15]
			943	DTIMS	#
			950	TWIMS	[15]
			950	DTIMS	[22]
			950	TWIMS	[3]
			966	TWIMS	#
			970	DTIMS	[23]
			970	DTIMS	[24]
			970	DTIMS	[25]
			980	TWIMS	[3]

			980	TWIMS	[26]
			987	DTIMS	#
			1000	DTIMS	[13]
			1000	DTIMS	[22]
			1006	TWIMS	#
			1020	DTIMS	[18]
			1041	DTIMS	[17]
			1056	DTIMS	[16]
			1080	FAIMS	[27]
			1103	DTIMS	[9]
			1110	TWIMS	[3]
			1113	DTIMS	#
			1143	DTIMS	#
			1143	TWIMS	#
			1160	FAIMS	[27]
			1200	TWIMS	[3]
			1220	DTIMS	[17]
			1220	DTIMS	[18]
			1280	FAIMS	[27]
			1311	TWIMS	[19]
			1314	DTIMS	[16]
			1368	DTIMS	[9]
			1380	FAIMS	[27]
			1400	TWIMS	[3]
			1440	FAIMS	[27]
			1480	FAIMS	[27]
			1500	DTIMS	[18]
			1500	TWIMS	[3]
			1525	DTIMS	[17]
			1553	TWIMS	[20]
			1590	FAIMS	[27]
			1613	ROMIAC	[21]
			1700	TWIMS	[19]
Cytochrome C	1	6	1050	TWIMS	[15]
			1080**	DTIMS	[28]
			1120	TWIMS	[29]
			1130	TWIMS	[30]
			1150	TWIMS	[29]
			1182	DTIMS	#
			1190	TWIMS	[29]
			1230	DTIMS	[28]
			1230	TWIMS	[29]
			1234	DTIMS	#
			1238	TWIMS	#
			1238	DTIMS	[9]
			1240	DTIMS	[4]
			1240	DTIMS	[12]
			1240	TWIMS	[14]
			1240	DTIMS	[28]
			1243	DTIMS	[31]
			1244	DTIMS	[32]
			1254	DTIMS	[33] (found in [28])

			1270	TWIMS	[29]
			1270	TWIMS	[30]
			1280	TWIMS	[29]
			1290	TWIMS	[14]
			1360	TWIMS	[34]
			1393	DTIMS	[32]
			1400	DTIMS	[33] (found in [28])
			1402	DTIMS	[9]
			1530	TWIMS	[29]
			1571	TWIMS	[35]
			1602	DTIMS	[32]
			1611	DTIMS	[33] (found in [28])
			1880	DTIMS	[28]
	1	7	1000	DTIMS	[36]
			1100	TWIMS	[15]
			1170	TWIMS	[30]
			1196	DTIMS	#
			1230	TWIMS	[29]
			1247	DTIMS	[32]
			1250	TWIMS	[29]
			1257	DTIMS	[33] (found in [28])
			1280	DTIMS	[12]
			1286	DTIMS	#
			1290	TWIMS	[30]
			1300	DTIMS	[4]
			1304	TWIMS	#
			1338	DTIMS	[37]
			1380	DTIMS	[28]
			1418	DTIMS	[9]
			1426	DTIMS	[33] (found in [28])
			1500	TWIMS	[29]
			1520	TWIMS	[30]
			1520	TWIMS	[14]
			1546	DTIMS	[31]
			1550	TWIMS	[29]
			1579	TWIMS	[35]
			1580	TWIMS	[14]
			1600	DTIMS	[36]
			1620	DTIMS	[32]
			1629	DTIMS	[33] (found in [28])
			1640	TWIMS	[29]
			1650	DTIMS	[28]
			1650	TWIMS	[29]
			1650	TWIMS	[30]
			1650	TWIMS	[34]
			1660	DTIMS	[28]
			1670	TWIMS	[14]
			1680	TWIMS	[29]
			1685	DTIMS	[9]
			1720	TWIMS	[35]
			1785	DTIMS	[32]
			1790	TWIMS	[34]

			1792	DTIMS	[33] (found in [28])
			1826	DTIMS	[9]
			1870	TWIMS	[30]
			1900	DTIMS	[28]
			2007	DTIMS	[32]
			2018	DTIMS	[33] (found in [28])
			2120	TWIMS	[35]
	1	8	1250	DTIMS	[32]
			1250	TWIMS	[15]
			1250	TWIMS	[29]
			1258	DTIMS	#
			1260	DTIMS	[33] (found in [28])
			1297	DTIMS	#
			1370	TWIMS	[15]
			1373	DTIMS	#
			1399	TWIMS	#
			1430	TWIMS	[15]
			1450	TWIMS	[30]
			1477	DTIMS	[33] (found in [28])
			1540	DTIMS	#
			1583	DTIMS	[9]
			1625	TWIMS	#
			1670	TWIMS	[29]
			1680	TWIMS	[29]
			1700	TWIMS	[30]
			1702	DTIMS	[32]
			1709	DTIMS	[33] (found in [28])
			1710	TWIMS	[14]
			1768	TWIMS	#
			1796	DTIMS	[9]
			1802	TWIMS	[35]
			1820	TWIMS	[34]
			1845	DTIMS	[32]
			1854	DTIMS	[33] (found in [28])
			1863	DTIMS	[31]
			1875	TWIMS	[35]
			1918	TWIMS	#
			1940	TWIMS	[29]
			1940	TWIMS	[30]
			1980	TWIMS	[14]
			2000	TWIMS	[14]
			2020	TWIMS	[29]
			2020	TWIMS	[14]
			2040	TWIMS	[29]
			2053	DTIMS	[9]
			2061	DTIMS	[32]
			2071	DTIMS	[33] (found in [28])
			2114	DTIMS	[9]
			2150	TWIMS	[35]
			2230	TWIMS	[34]
Myoglobin	1	7	1398	TWIMS	[35]
			1546**	DTIMS	[9]

			1566	DTIMS	#
			1613	TWIMS	35
			1641	TWIMS	#
			1664	DTIMS	#
			1695	DTIMS	38
			1700	TWIMS	34
			1716	DTIMS	9
	1	8	1593	TWIMS	35
			1604	DTIMS	#
			1674	TWIMS	#
			1704	DTIMS	#
			1788	DTIMS	38
			1824	DTIMS	9
			1850	TWIMS	34
	1	9	1650	DTIMS	#
			1713	TWIMS	#
			1818	TWIMS	#
			1832	DTIMS	#
			1835	DTIMS	38
			1900	TWIMS	34
			1907	DTIMS	9
			2106	DTIMS	38
Avidin	4	14	3441	DTIMS	#
			3614	TWIMS	#
			3633	DTIMS	#
	4	15	3347	DTIMS	39
			3350	DTIMS	40
			3485	DTIMS	#
			3570	DTIMS	4
			3601	TWIMS	#
			3640	DTIMS	#
			3640	DTIMS	12
	4	16	3350	DTIMS	40
			3434	DTIMS	39
			3471	DTIMS	#
			3581	TWIMS	#
			3590	DTIMS	4
			3640	DTIMS	12
			3665	DTIMS	#
			3900	DTIMS	40
	4	17	3446	DTIMS	39
			3467	DTIMS	#
			3566	TWIMS	#
			3610	DTIMS	4
			3633	DTIMS	#
			3640	DTIMS	12
BSA	1	14	3433	DTIMS	39
			3700	TWIMS	30
			3891	DTIMS	#
			4010	DTIMS	4
			4041	DTIMS	#
			4090	DTIMS	12

			4108	TWIMS	#
			4167	DTIMS	39
	1	15	3653	DTIMS	39
			3956	DTIMS	#
			4030	DTIMS	4
			4087	TWIMS	#
			4093	DTIMS	#
			4100	DTIMS	12
			4100	TWIMS	30
			4419	DTIMS	39
	1	16	3788	DTIMS	39
			3800	TWIMS	15
			3989	DTIMS	#
			4051	TWIMS	#
			4060	DTIMS	12
			4070	DTIMS	4
			4084	DTIMS	#
			4400	TWIMS	30
			4535	DTIMS	39
	1	17	3766	DTIMS	39
			3900	TWIMS	15
			3956	DTIMS	#
			4026	DTIMS	#
			4040	DTIMS	12
			4094	TWIMS	#
			4110	DTIMS	4
			4600	TWIMS	30
			4613	DTIMS	39
Concanavalin A	4	18	4800	TWIMS	30
			5412	TWIMS	#
	4	19	4681	DTIMS	39
			4900	DTIMS	40
			5000	TWIMS	30
			5340	DTIMS	#
			5399	DTIMS	#
			5409	TWIMS	#
			5440	DTIMS	4
	4	20	4713	DTIMS	39
			4800	DTIMS	40
			5384	DTIMS	#
			5397	DTIMS	#
			5400	DTIMS	6
			5412	TWIMS	#
			5450	DTIMS	4
			5500	TWIMS	30
			5550	DTIMS	12
	4	21	4700	DTIMS	40
			4804	DTIMS	39
			5345	DTIMS	#
			5401	DTIMS	#
			5434	TWIMS	#
			5460	DTIMS	4

			5550	DTIMS	12
			5850	TWIMS	30
	4	22	4600	DTIMS	40
			4977	DTIMS	39
			5335	DTIMS	#
			5405	DTIMS	#
			5460	DTIMS	4
			5480	DTIMS	12
			6100	TWIMS	30
			6285	DTIMS	#
Alcohol Dehydrogenase	4	22	6579	DTIMS	#
			7015	TWIMS	#
			7696	TWIMS	41
	4	23	6584	DTIMS	#
			6800	TWIMS	30
			6940	DTIMS	12
			6968	DTIMS	#
			6990	DTIMS	4
			7020	TWIMS	#
			7545	TWIMS	41
	4	24	6606	DTIMS	#
			6940	DTIMS	12
			6943	DTIMS	#
			7000	TWIMS	30
			7020	DTIMS	4
			7027	TWIMS	#
			7457	TWIMS	41
	4	25	6588	DTIMS	#
			6830	DTIMS	12
			6914	DTIMS	#
			7020	DTIMS	4
			7045	TWIMS	#
			7300	TWIMS	30
			7428	TWIMS	41
	4	26	6557	DTIMS	#
			6720	DTIMS	12
			6879	DTIMS	#
			7020	DTIMS	4
			7069	TWIMS	#
			7388	TWIMS	41
			7500	TWIMS	30
	4	27	6908	DTIMS	#

Table S10. Literature and experimentally determined $\mathrm{CCS_{N_2}}$ values obtained for the protein/protein complex ions described within this study. Within this table 'n' represents the multimeric state of the protein, 'z' denotes the protein charge state and the 'Source' column highlights the references from which the $\mathrm{CCS_{N_2}}$ values were found, where the '#' denotes $\mathrm{CCS_{N_2}}$ values that were obtained experimentally within this study. Abbreviated versions of the IM techniques employed to obtain the corresponding $\mathrm{CCS_{N_2}}$ values are noted in the 'IM technique' column. $\mathrm{CCS_{N_2}}$ values highlighted in red were obtained from graphs within the associated references and as such will likely not be completely accurate. The '**' after some CCS denotes the high likelihood that these values actually correspond to misidentified coincident dimer species and not more compact monomeric conformations.

Analyte	n	Z (+)	$\mathrm{CCS_{N_2}}$	IM technique	Source
Ubiquitin	1	4	949**	DTIMS	[9]
			967	DTIMS	[42]
			1116	DTIMS	[9]
			1118	TWIMS	#
			1128	DTIMS	#
			1148	DTIMS	#
			2125	TIMS	[43]
	1	5	1011	DTIMS	[9]
			1116	DTIMS	[42]
			1139	DTIMS	[42]
			1149	TIMS	[43]
			1163	DTIMS	#
			1166	DTIMS	#
			1167	TWIMS	#
			1204	SLIM	[44]
			1208	DTIMS	#
			1208	TWIMS	#
			1221	DTIMS	[9]
			1271	OrbiCCS	[45]
			1700	TIMS	[43]
	1	6	1196	DTIMS	[42]
			1199	DTIMS	#
			1200	DTIMS	[25]
			1209	DTIMS	#
			1217	TIMS	[46]
			1222	DTIMS	[9]
			1229	TIMS	[43]
			1229	TWIMS	#
			1258	SLIM	[44]
			1268	TWIMS	#
			1380	DTIMS	[25]
			1382	TWIMS	#
			1386	DTIMS	#
			1401	DTIMS	#
			1417	TIMS	[43]
			1466	DTIMS	#
			1474	DTIMS	[9]
			1517	OrbiCCS	[45]
			1628	DTIMS	[9]
Cytochrome C	1	6	1289	TIMS	[43]

			1330	DTIMS	[42]
			1360**	DTIMS	[9]
			1398	TWIMS	[42]
			1413	OrbiCCS	[45]
			1438	TIMS	[43]
			1449	DTIMS	[42]
			1450	SLIM	[44]
			1454	TWIMS	#
			1456	DTIMS	#
			1465	DTIMS	#
			1477	DTIMS	[9]
			1490	DTIMS	[12]
			1590	DTIMS	[44]
			1769	TIMS	[43]
	1	7	1030	TMIMS	[47] interpolated from [32]
			1307	TIMS	[43]
			1481	DTIMS	#
			1508	DTIMS	[42]
			1533	TWIMS	[42]
			1536	DTIMS	[9]
			1537	TWIMS	#
			1540	DTIMS	#
			1540	TMIMS	[47] interpolated from [31]
			1548	TIMS	[43]
			1550	SLIM	[48]
			1560	SLIM	[44]
			1561	DTIMS	#
			1574	TIMS	[43]
			1590	DTIMS	[12]
			1636	TMIMS	[47] interpolated from [32]
			1810	OrbiCCS	[45]
			1922	TIMS	[43]
			1948	TMIMS	[47] interpolated from [32]
			1970	DTIMS	[44]
			2083	TIMS	[43]
			2115	DTIMS	[9]
			2326	TMIMS	[47] interpolated from [32]
	1	8	1036	TMIMS	[47] interpolated from [32]
			1053	TMIMS	[47] interpolated from [49]
			1519	DTIMS	#
			1629	DTIMS	#
			1654	TWIMS	#
			1654	DTIMS	#
			1686	TIMS	[43]
			1793	DTIMS	[9]
			1806	TMIMS	[47] interpolated from [32]
			1887	TWIMS	#
			1915	DTIMS	#
			1925	TIMS	[43]
			2043	TWIMS	#

			2050	TMIMS	[47] interpolated from [32]
			2084	TMIMS	[47] interpolated from [31]
			2114	DTIMS	[9]
			2146	OrbiCCS	[45]
			2201	TWIMS	#
			2249	TIMS	[43]
			2418	TMIMS	[47] interpolated from [32]
			2441	DTIMS	[9]
			2468	TIMS	[43]
			2496	TIMS	[43]
			2528	DTIMS	[9]
			2543	TMIMS	[47] interpolated from [49]
Myoglobin	1	7	1697**	DTIMS	[9]
			1709	DTIMS	[42]
			1788	TWIMS	[42]
			1863	DTIMS	[9]
			1896	TWIMS	#
			1899	DTIMS	#
			1903	DTIMS	#
			1908	DTIMS	[42]
			2037	DTIMS	[38]
			2353	DTIMS	[38]
			2952	DTIMS	[38]
	1	8	1839	TWIMS	[42]
			1934	DTIMS	#
			1937	DTIMS	[9]
			1949	TWIMS	#
			1953	DTIMS	[42]
			1972	DTIMS	#
			2089	OrbiCCS	[45]
			2147	TIMS	[43]
			2187	TIMS	[50]
			2939	DTIMS	[38]
	1	9	1908	TIMS	[43]
			1995	DTIMS	#
			2003	TWIMS	#
			2010	TWIMS	[42]
			2038	DTIMS	[42]
			2040	DTIMS	#
			2085	DTIMS	[9]
			2114	TWIMS	#
			2149	DTIMS	#
			2187	TIMS	[43]
			2280	OrbiCCS	[45]
			2399	TIMS	[50]
			2465	TIMS	[50]
			2756	DTIMS	[38]
			3027	DTIMS	[38]
Avidin	4	14	3996	DTIMS	#
			4029	DTIMS	#
			4053	TWIMS	#

	4	15	4008	DTIMS	#
			4057	DTIMS	#
			4060	DTIMS	[44]
			4073	TWIMS	#
			4120	SLIM	[44]
			4150	DTIMS	[12]
	4	16	4038	DTIMS	#
			4066	DTIMS	#
			4080	DTIMS	[44]
			4086	TWIMS	#
			4150	SLIM	[44]
			4150	DTIMS	[12]
	4	17	4041	DTIMS	#
			4063	DTIMS	#
			4100	DTIMS	[44]
			4101	TWIMS	#
			4160	DTIMS	[12]
			4170	SLIM	[44]
BSA	1	14	4349	DTIMS	#
			4425	DTIMS	#
			4490	DTIMS	[12]
			4535	TWIMS	#
	1	15	4392	DTIMS	#
			4467	TIMS	[43]
			4478	DTIMS	#
			4490	DTIMS	[12]
			4548	TWIMS	#
	1	16	4188	TIMS	[43]
			4200	TIMS	[43]
			4445	DTIMS	#
			4470	DTIMS	[12]
			4514	DTIMS	#
			4567	TWIMS	#
	1	17	3941	TIMS	[43]
			4291	TIMS	[43]
			4490	DTIMS	[12]
			4506	DTIMS	#
			4523	DTIMS	#
			4648	TWIMS	#
Concanavalin A	4	18	5740	TWIMS	#
			5838	DTIMS	#
	4	19	5820	TWIMS	#
			5879	DTIMS	#
			5905	DTIMS	#
			5920	SLIM	[44]
			6060	DTIMS	[12]
			6060	DTIMS	[44]
	4	20	5900	TWIMS	#
			5902	DTIMS	#
			5913	DTIMS	#
			6020	SLIM	[44]
			6060	DTIMS	[44]

			6080	DTIMS	[12]
	4	21	5921	DTIMS	#
			5937	DTIMS	#
			5997	TWIMS	#
			6060	DTIMS	[44]
			6070	SLIM	[44]
			6090	DTIMS	[12]
	4	22	5890	DTIMS	#
			5930	DTIMS	#
			6030	SLIM	[44]
			6050	DTIMS	[12]
			6070	DTIMS	[44]
			6846	DTIMS	#
			7011	DTIMS	#
Alcohol Dehydrogenase	4	22	7330	DTIMS	#
			7594	DTIMS	#
	4	23	7399	DTIMS	#
			7420	DTIMS	[12]
			7422	DTIMS	#
			7640	TWIMS	#
	4	24	7427	DTIMS	#
			7447	DTIMS	#
			7450	DTIMS	[12]
			7693	TWIMS	#
	4	25	7429	DTIMS	#
			7440	DTIMS	[12]
			7465	DTIMS	#
			7750	TWIMS	#
	4	26	7424	DTIMS	#
			7473	DTIMS	#
			7500	DTIMS	[12]
			7814	TWIMS	#
	4	27	7470	DTIMS	#
			7520	DTIMS	#

(1) Zhong, Y.; Hyung, S.-J.; Ruotolo, B. T. Characterizing the Resolution and Accuracy of a Second-Generation Traveling-Wave Ion Mobility Separator for Biomolecular Ions. *Analyst* **2011**, *136* (17), 3534. https://doi.org/10.1039/c0an00987c.

(2) Giles, K.; Williams, J. P.; Campuzano, I. D. G. Enhancements in Travelling Wave Ion Mobility Resolution. In *Rapid Communications in Mass Spectrometry*; 2011; Vol. 25, pp 1559–1566. https://doi.org/10.1002/rcm.5013.

(3) Chen, S. H.; Russell, D. H. How Closely Related Are Conformations of Protein Ions Sampled by IM-MS to Native Solution Structures? *J. Am. Soc. Mass Spectrom.* **2015**, *26* (9), 1433–1443. https://doi.org/10.1007/s13361-015-1191-1.

(4) Allen, S. J.; Giles, K.; Gilbert, T.; Bush, M. F. Ion Mobility Mass Spectrometry of Peptide, Protein, and Protein Complex Ions Using a Radio-Frequency Confining Drift Cell. *Analyst* **2016**, *141* (3), 884–891. https://doi.org/10.1039/C5AN02107C.

(5) May, J. C.; Goodwin, C. R.; Lareau, N. M.; Leaptrot, K. L.; Morris, C. B.; Kurulugama, R. T.; Mordehai, A.; Klein, C.; Barry, W.; Darland, E.; et al. Conformational Ordering of Biomolecules in the Gas Phase: Nitrogen Collision Cross Sections Measured on a Prototype High Resolution Drift Tube Ion Mobility-Mass Spectrometer. *Anal. Chem.* **2014**, *86* (4), 2107–2116. https://doi.org/10.1021/ac4038448.

(6) Ujma, J.; Giles, K.; Morris, M.; Barran, P. E. New High Resolution Ion Mobility Mass Spectrometer Capable of Measurements of Collision Cross Sections from 150 to 520 K. *Anal. Chem.* **2016**, *88* (19), 9469–9478. https://doi.org/10.1021/acs.analchem.6b01812.

(7) Kurulugama, R. T.; Darland, E.; Kuhlmann, F.; Stafford, G.; Fjeldsted, J. Evaluation of Drift Gas Selection in Complex Sample Analyses Using a High Performance Drift Tube Ion Mobility-QTOF Mass Spectrometer. *Analyst* **2015**, *140* (20), 6834–6844. https://doi.org/10.1039/c5an00991j.

(8) Henderson, S. C.; Li, J.; Counterman, A. E.; Clemmer, D. E. Intrinsic Size Parameters for Val, Ile, Leu, Gln, Thr, Phe, and Trp Residues from Ion Mobility Measurements of Polyamino Acid Ions. *J. Phys. Chem. B* **1999**, *103*, 8780–8785. https://doi.org/10.1021/jp991783h.

(9) May, J. C.; Jurneczko, E.; Stow, S. M.; Kratochvil, I.; Kalkhof, S.; McLean, J. A. Conformational Landscapes of Ubiquitin, Cytochrome c, and Myoglobin: Uniform Field Ion Mobility Measurements in Helium and Nitrogen Drift Gas. *Int. J. Mass Spectrom.* **2017**, 1–16. https://doi.org/10.1016/j.ijms.2017.09.014.

(10) Baker, E. S.; Clowers, B. H.; Li, F.; Tang, K.; Tolmachev, A. V.; Prior, D. C.; Belov, M. E.; Smith, R. D. Ion Mobility Spectrometry-Mass Spectrometry Performance Using Electrodynamic Ion Funnels and Elevated Drift Gas Pressures. *J. Am. Soc. Mass Spectrom.* **2007**, *18* (7), 1176–1187. https://doi.org/10.1016/j.jasms.2007.03.031.

(11) Hoaglund-Hyzer, C. S.; Counterman, A. E.; Clemmer, D. E. Anhydrous Protein Ions. *Chem. Rev.* **2002**, *99* (10), 3037–3080. https://doi.org/10.1021/cr980139g.

(12) Bush, M. F.; Hall, Z.; Giles, K.; Hoyes, J.; Robinson, C. V.; Ruotolo, B. T. Collision Cross Sections of Proteins and Their Complexes: A Calibration Framework and Database for Gas-Phase Structural Biology. *Anal. Chem.* **2010**, *82* (22), 9557–9565. https://doi.org/10.1021/ac1022953.

(13) Salbo, R.; Bush, M. F.; Naver, H.; Campuzano, I.; Robinson, C. V.; Pettersson, I.; Jørgensen, T. J. D.; Haselmann, K. F. Traveling-Wave Ion Mobility Mass Spectrometry of Protein Complexes: Accurate Calibrated Collision Cross-Sections of Human Insulin Oligomers. *Rapid Commun. Mass Spectrom.* **2012**, *26* (10), 1181–1193. https://doi.org/10.1002/rcm.6211.

(14) Smith, D.; Knapman, T.; Campuzano, I.; Malham, R.; Berryman, J.; Radford, S.; Ashcroft, A. Deciphering Drift Time Measurements from Travelling Wave Ion Mobility Spectrometry-Mass Spectrometry Studies. *Eur. J. Mass Spectrom.* **2009**, *15* (5), 113. https://doi.org/10.1255/ejms.947.

(15) Zhong, Y.; Han, L.; Ruotolo, B. T. Collisional and Coulombic Unfolding of Gas-Phase Proteins: High Correlation to Their Domain Structures in Solution. *Angew. Chemie Int. Ed.* **2014**, *53* (35), 9209–9212. https://doi.org/10.1002/anie.201403784.

(16) Zhao, Q.; Soyk, M. W.; Schieffer, G. M.; Fuhrer, K.; Gonin, M. M.; Houk, R. S.; Badman, E. R. An Ion Trap-Ion Mobility-Time of Flight Mass Spectrometer with Three Ion Sources for Ion/Ion Reactions. *J. Am. Soc. Mass Spectrom.* **2009**, *20* (8), 1549–1561. https://doi.org/10.1016/j.jasms.2009.04.014.

(17) Valentine, S. J.; Counterman, A. E.; Clemmer, D. E. Conformer-Dependent Proton-Transfer Reactions of Ubiquitin Ions. *J. Am. Soc. Mass Spectrom.* **1997**, *8* (9), 954–961. https://doi.org/10.1016/S1044-0305(97)00085-8.

(18) Guo, Y.; Wang, J.; Javahery, G.; Thomson, B. A.; Siu, K. W. M. Ion Mobility Spectrometer with Radial Collisional Focusing. *Anal. Chem.* **2005**, *77* (1), 266–275. https://doi.org/10.1021/ac048974n.

(19) Merenbloom, S. I.; Flick, T. G.; Williams, E. R. How Hot Are Your Ions in TWAVE Ion Mobility Spectrometry? *J. Am. Soc. Mass Spectrom.* **2012**, *23* (3), 553–562. https://doi.org/10.1007/s13361-011-0313-7.

(20) Shrestha, B.; Vertes, A. High-Throughput Cell and Tissue Analysis with Enhanced Molecular Coverage by Laser Ablation Electrospray Ionization Mass Spectrometry Using Ion Mobility Separation. *Anal. Chem.* **2014**, *86* (9), 4308–4315. https://doi.org/10.1021/ac500007t.

(21) Mui, W.; Thomas, D. A.; Downard, A. J.; Beauchamp, J. L.; Seinfeld, J. H.; Flagan, R. C. Ion Mobility-Mass Spectrometry with a Radial Opposed Migration Ion and Aerosol Classifier (ROMIAC). *Anal. Chem.* **2013**, *85* (13), 6319–6326. https://doi.org/10.1021/ac400580u.

(22) Li, J.; Taraszka, J. A.; Counterman, A. E.; Clemmer, D. E. Influence of Solvent Composition and Capillary Temperature on the Conformations of Electrosprayed Ions: Unfolding of Compact Ubiquitin Conformers from Pseudonative and Denatured Solutions. *Int. J. Mass Spectrom.* **1999**, *185*, 37–47. https://doi.org/10.1016/S1387-3806(98)14135-0.

(23) El-Baba, T. J.; Woodall, D. W.; Raab, S. A.; Fuller, D. R.; Laganowsky, A.; Russell, D. H.; Clemmer, D. E. Melting Proteins: Evidence for Multiple Stable Structures upon Thermal Denaturation of Native Ubiquitin from Ion Mobility Spectrometry-Mass Spectrometry Measurements. *J. Am. Chem. Soc.* **2017**, *139* (18), 6306–6309. https://doi.org/10.1021/jacs.7b02774.

(24) Wyttenbach, T.; Bowers, M. T. Structural Stability from Solution to the Gas Phase: Native Solution Structure of Ubiquitin Survives Analysis in a Solvent-Free Ion Mobility-Mass Spectrometry Environment. *J. Phys. Chem. B* **2011**, *115* (42), 12266–12275. https://doi.org/10.1021/jp206867a.

(25) Bleiholder, C.; Johnson, N. R.; Contreras, S.; Wyttenbach, T.; Bowers, M. T. Molecular Structures and Ion Mobility Cross Sections: Analysis of the Effects of He and N2 Buffer Gas. *Anal. Chem.* **2015**, *87* (14), 7196–7203. https://doi.org/10.1021/acs.analchem.5b01429.

(26) Wagner, N. D.; Kim, D.; Russell, D. H. Increasing Ubiquitin Ion Resistance to Unfolding in the Gas Phase Using Chloride Adduction: Preserving More “Native-Like” Conformations Despite Collisional Activation. *Anal. Chem.* **2016**, *88* (11), 5934–5940. https://doi.org/10.1021/acs.analchem.6b00871.

(27) Shvartsburg, A. A.; Li, F.; Tang, K.; Smith, R. D. Distortion of Ion Structures by Field Asymmetric Waveform Ion Mobility Spectrometry. *Anal. Chem.* **2007**, *79* (4), 1523–1528. https://doi.org/10.1021/ac061306c.

(28) Zhao, Q.; Schieffer, G. M.; Soyk, M. W.; Anderson, T. J.; Houk, R. S.; Badman, E. R. Effects of Ion/Ion Proton Transfer Reactions on Conformation of Gas-Phase Cytochrome c Ions. *J. Am. Soc. Mass Spectrom.* **2010**, *21* (7), 1208–1217. https://doi.org/10.1016/j.jasms.2010.03.032.

(29) Knapman, T. W.; Valette, N. M.; Warriner, S. L.; Ashcroft, a E. Ion Mobility Spectrometry-Mass Spectrometry of Intrinsically Unfolded Proteins: Trying to Put Order into Disorder. *Curr. Anal. Chem.*

2013, *9* (0), 181–191. https://doi.org/10.2174/1573411011309020004.

(30) Sivalingam, G. N.; Yan, J.; Sahota, H.; Thalassinos, K. Amphitrite: A Program for Processing Travelling Wave Ion Mobility Mass Spectrometry Data. *Int. J. Mass Spectrom.* **2013**, *345–347*, 54–62. https://doi.org/10.1016/j.ijms.2012.09.005.

(31) Faull, P. A.; Korkeila, K. E.; Kalapothakis, J. M.; Gray, A.; McCullough, B. J.; Barran, P. E. Gas-Phase Metalloprotein Complexes Interrogated by Ion Mobility-Mass Spectrometry. *Int. J. Mass Spectrom.* **2009**, *283* (1–3), 140–148. https://doi.org/10.1016/j.ijms.2009.02.024.

(32) Shelimov, K. B.; Clemmer, D. E.; Hudgins, R. R.; Jarrold, M. F. Protein Structure in Vacuo: Gas-Phase Conformations of BPTI and Cytochrome C. *J. Am. Chem. Soc.* **1997**, *119* (9), 2240–2248. https://doi.org/10.1021/ja9619059.

(33) Badman, E. R.; Hoaglund-Hyzer, C. S.; Clemmer, D. E. Monitoring Structural Changes of Proteins in an Ion Trap over 10 - 200 Ms: Unfolding Transitions in Cytochrome c Ions. *Anal. Chem.* **2001**, *73* (24), 6000–6007.

(34) Scarff, C. A.; Thalassinos, K.; Hilton, G. R.; Scrivens, J. H. Travelling Wave Ion Mobility Mass Spectrometry Studies of Protein Structure: Biological Significance and Comparison with X-Ray Crystallography and Nuclear Magnetic Resonance Spectroscopy Measurements. *Rapid Commun. Mass Spectrom.* **2008**, *22*, 3297–3304. https://doi.org/10.1002/rcm.3737.

(35) Jhingree, J. R.; Beveridge, R.; Dickinson, E. R.; Williams, J. P.; Brown, J. M.; Bellina, B.; Barran, P. E. Electron Transfer with No Dissociation Ion Mobility–Mass Spectrometry (ETnoD IM-MS). The Effect of Charge Reduction on Protein Conformation. *Int. J. Mass Spectrom.* **2017**, *413*, 43–51. https://doi.org/10.1016/j.ijms.2016.08.006.

(36) Dickinson, E. R.; Jurneczko, E.; Pacholarz, K. J.; Clarke, D. J.; Reeves, M.; Ball, K. L.; Hupp, T.; Campopiano, D.; Nikolova, P. V.; Barran, P. E. Insights into the Conformations of Three Structurally Diverse Proteins: Cytochrome c, P53, and MDM2, Provided by Variable-Temperature Ion Mobility Mass Spectrometry. *Anal. Chem.* **2015**, *87* (6), 3231–3238. https://doi.org/10.1021/ac503720v.

(37) Jarrold, M. F. Unfolding, Refolding, and Hydration of Proteins in the Gas Phase. *Acc. Chem. Res.* **1999**, *32* (4), 360–367. https://doi.org/10.1021/ar960081x.

(38) Jurneczko, E.; Kalapothakis, J.; Campuzano, I. D. G.; Morris, M.; Barran, P. E. Effects of Drift Gas on Collision Cross Sections of a Protein Standard in Linear Drift Tube and Traveling Wave Ion Mobility Mass Spectrometry. *Anal. Chem.* **2012**, *84* (20), 8524–8531. https://doi.org/10.1021/ac301260d.

(39) Beveridge, R.; Covill, S.; Pacholarz, K. J.; Kalapothakis, J. M. D.; Macphee, C. E.; Barran, P. E. A Mass-Spectrometry-Based Framework to Define the Extent of Disorder in Proteins. *Anal. Chem.* **2014**, *86* (22), 10979–10991. https://doi.org/10.1021/ac5027435.

(40) Pacholarz, K. J.; Barran, P. E. Distinguishing Loss of Structure from Subunit Dissociation for Protein Complexes with Variable Temperature Ion Mobility Mass Spectrometry. *Anal. Chem.* **2015**, *87* (12), 6271–6279. https://doi.org/10.1021/acs.analchem.5b01063.

(41) Campuzano, I. Gas Phase Protein Structure Is Consistent with Structural Measurements Made by X-Ray Crystallography. *Waters, Tech. Note* **2008**, 1–4.

(42) Harrison, J. A.; Kelso, C.; Pukala, T. L.; Beck, J. L. Conditions for Analysis of Native Protein Structures Using Uniform Field Drift Tube Ion Mobility Mass Spectrometry and Characterization of Stable Calibrants for TWIM-MS. *J. Am. Soc. Mass Spectrom.* **2018**. https://doi.org/10.1007/s13361-018-2074-z.

(43) Benigni, P.; Marin, R.; Molano-Arevalo, J. C.; Garabedian, A.; Wolff, J. J.; Ridgeway, M. E.; Park, M. A.; Fernandez-Lima, F. Towards the Analysis of High Molecular Weight Proteins and Protein Complexes Using TIMS-MS. *Int. J. Ion Mobil. Spectrom.* **2016**, *19* (2–3), 95–104. https://doi.org/10.1007/s12127-

016-0201-8.

(44) Allen, S. J.; Eaton, R. M.; Bush, M. F. Analysis of Native-Like Ions Using Structures for Lossless Ion Manipulations. *Anal. Chem.* **2016**, *88* (18), 9118–9126. https://doi.org/10.1021/acs.analchem.6b02089.

(45) Sanders, J. D.; Grinfeld, D.; Aizikov, K.; Makarov, A. A.; Holden, D. D.; Brodbelt, J. S. Determination of Collision Cross Sections of Protein Ions in an Orbitrap Mass Analyzer. *Anal. Chem.* **2018**, acs.analchem.8b00724. https://doi.org/10.1021/acs.analchem.8b00724.

(46) Liu, F. C.; Kirk, S. R.; Bleiholder, C. On the Structural Denaturation of Biological Analytes in Trapped Ion Mobility Spectrometry – Mass Spectrometry. *Analyst* **2016**, *141* (12), 3722–3730. https://doi.org/10.1039/C5AN02399H.

(47) Meyer, N. A.; Root, K.; Zenobi, R.; Vidal-De-Miguel, G. Gas-Phase Dopant-Induced Conformational Changes Monitored with Transversal Modulation Ion Mobility Spectrometry. *Anal. Chem.* **2016**, *88* (4), 2033–2040. https://doi.org/10.1021/acs.analchem.5b02750.

(48) Allen, S. J.; Eaton, R. M.; Bush, M. F. Structural Dynamics of Native-Like Ions in the Gas Phase: Results from Tandem Ion Mobility of Cytochrome C. *Anal. Chem.* **2017**, *89* (14), 7527–7534. https://doi.org/10.1021/acs.analchem.7b01234.

(49) Valentine, S. J.; Clemmer, D. E. H/D Exchange Levels of Shape-Resolved Cytochrome c Conformers in the Gas Phase. *J. Am. Chem. Soc.* **1997**, *119* (15), 3558–3566. https://doi.org/10.1021/ja9626751.

(50) Schenk, E. R.; Almeida, R.; Miksovska, J.; Ridgeway, M. E.; Park, M. A.; Fernandez-Lima, F. Kinetic Intermediates of Holo-and Apo-Myoglobin Studied Using Hdx-Tims-Ms and Molecular Dynamic Simulations. *J. Am. Soc. Mass Spectrom.* **2015**, *26* (4), 555–563. https://doi.org/10.1007/s13361-014-1067-9.

Using Collision Cross Section Distributions to Assess the Distribution of Collision Cross Section Values

Aidan P. France, Lukasz G. Migas, Eleanor Sinclair, Bruno Bellina and Perdita E. Barran*

Michael Barber Centre for Collaborative Mass Spectrometry, Manchester Institute of Biotechnology and Photon Science Institute, University of Manchester, 131 Princess Street, Manchester, M1 7DN, UK

Abstract

Careful transfer of ions into the gas-phase permits the measurement of protein structures, with ion mobility-mass spectrometry, which provides shape and stoichiometry information. Collision cross sections (CCS) can be obtained from measurements made of the proteins mobility through a given gas, and such structural information once obtained should also permit inter-lab comparisons. However, until recently there was not a recommended standard form for the reporting of such measurements. In this study we explore the use of collision cross section distributions to allow comparability of IM-MS data for proteins on different instruments. We present measurements on seven standard proteins across three IM-MS configurations, namely an Agilent 6560 IM QToF, a Waters Synapt G2 possessing a TWIMS cell and a modified Synapt G2 possessing an RF confining linear field drift cell. Mobility measurements were taken using both He and N_2 as the drift gases. To aid comparability across instruments and best assess the corresponding gas-phase conformational landscapes of the protein 'standards' we present the data in the form of averaged collision cross section distributions. For experiments carried out in N_2, CCS values for the most compact ion conformations have an inter-instrument variability of ≤ 3%, and the total CCS distributions are similar across platforms. For experiments carried out in He, we observe the total CCS distributions to follow the same trend as observed in N_2, whilst CCS for the most compact ion conformations sampled on the 6560, are systematically smaller by up to 10%, than those observed on the G2. From this study, we observe the applied protein calibration procedure (for TWIMS) to yield ^{TW}CCS for native-like proteins which are largely similar to those obtained on DTIMS instruments. However, when considering the ease by which unintentional protein structural activation *in vacuo* can occur and the broad range of ^{DT}CCS within the literature from which to calibrate drift times against, we advise caution when calibrating sample protein drift times against protein 'standards' in order to obtain CCS values and recommend the use of CCS distributions.

1. Background & Motivation

Ion mobility spectrometry (IMS) coupled with mass spectrometry (IM-MS) permits the characterisation of an ions structure from its mobility in a gas (IM) as well providing its mass (MS).[1] IM-MS is now established as a method to interrogate the structure of proteins, and under gentle ionisation conditions ESI can produce ions which retain aspects of their solution-phase structure.[2–7] IM-MS approaches have been exploited to permit the structural and functional characterisation of many types of biomolecules, including peptides;[8,9] small monomeric proteins;[5,10] cytosolic and membrane bound protein complexes;[11,12] protein-protein and protein-ligand interactions;[13–16] Nucleic acids[17,18] and amyloidogenic proteins.[19,20] Regardless of the molecular species to be analysed there are features or constraints that are common to all IM-MS experiments. These have recently been well outlined for all the prevalent forms of IM-MS.[21] Protein measurements have in the main utilised a form of ion mobility which can be generally described by a common process. In this, packets of ions are focussed to traverse a drift cell filled with an inert buffer gas at a known temperature and pressure (1mbar to atmospheric) whereby weak electric fields act to axially propel them through a drift cell/region. As they traverse this gas filled cell, the "frictional" force of gas-ion collisional events retards their motion, thus permitting the temporal separation of ions based upon their size, shape and charge.[22,23] IM-MS experiments record the arrival time (t_A) of m/z selected ions and this data can be used to determine their rotationally averaged collision cross sections (CCS).[24] Leading a wide community effort Gabelica recently recommended how to report IM-MS measurements to better facilitate inter-lab comparability and in this work we take this as the basis by which we can compare the data obtained on well-studied proteins.[21]

In so called, 'native' mass spectrometry experiments, a protein of interest is infused from an aqueous solution along with volatile salts such as ammonium acetate buffered to appropriate physiological pHs (~6-8).[2,25] In order to retain solvated structures *in vacuo*, careful optimisation of source parameters is necessary to minimise collisional heating and subsequent structural rearrangement.[26] Such effects can also occur on the injection of desolvated ions into the ion mobility drift tube.[27] Foundational studies from Clemmer and Jarrold demonstrated that minimising the energy of ions prior to IM separation permits the retention of native-like conformations for the monomeric proteins ubiquitin and cytochrome c.[10,28] In addition, Williams and Russell, using a 2nd generation Waters Synapt G2 ion mobility-mass spectrometer, demonstrated how voltages and trapping conditions prior to the drift cell can substantially affect the conformational landscapes of ubiquitin and metallothionein-2A.[26,29] Furthermore, Gabelica *et al*. defined tuning parameters on an Agilent 6560 IMQToF which allowed the preservation of a compact so called "N state" of Ubiquitin as well as the ammonium-bound states of a fragile nucleic acid complex.[30] Such efforts to establish optimal gentle transfer of biomolecules via careful tuning of ion optics across homemade and commercially available IM-MS instruments, have been used to support arguments about the preservation of solution-like biomolecular structures *in vacuo*, although it is evident that the ESI process also plays a major role.

Despite the body of work that reports the conditions required to 'least perturb' the structure of proteins for IM-MS measurements, there has been less focus on the reproducibility of CCS, with exceptions being studies on small biomolecule CCS on single vendor platforms.[31–33] To our knowledge, there have only been a handful of publications in which protein CCS have been compared across different platforms.[34,35] That being said, none of these studies have employed the use of CCS distributions to probe the conformational landscape of the systems under analysis. Visualising these ion conformational landscapes for malleable systems has great utility in defining optimal tuning parameters for native IM-MS experiments and as such, is commonly employed within many labs including our own.

In this study we establish "starting point" operational parameters which minimise the gas-phase activation of proteins across three instrumental platforms. We report CCS distribution/CCS across three ion mobility-mass spectrometers: the Synapt G2 (TWIMS & RF DTIMS configurations) and the Agilent 6560, in helium and nitrogen drift gases, to ascertain the degree of differentiation between protein structures sampled across different IM-MS platforms under "soft" tuning conditions. In addition, we provide interactive representations of CCS distributions to augment traditionally numerical CCS datasets. Furthermore, we present global CCS histogram distributions for compiled literature CCS values of our chosen systems, in order to facilitate a better understanding of where individual “native IM-MS” CCS lie relative to previously published values.

2. Methods and Materials

2.1. Sample preparation and ionisation

Seven commercially available protein/protein complex standards were utilised for the experiments outlined in this study. Sample identities, sources, suppliers, catalogue numbers and final solution conditions are detailed in SI Table S1.

Ammonium acetate solutions were made by dissolving ammonium acetate (Sigma) in ultrapure water (Merck Milli-Q) to yield ionic buffer concentrations of 50 or 200 mM (SI Table S1). All of these solutions were then adjusted to a pH of 7.4 using ammonium hydroxide solution (Sigma).

All seven samples were purchased as lyophilised powders which were dissolved in either 50 or 200 mM ammonium acetate solution, pH 7.4, to form protein stock solutions (typically 100 µM protein concentrations). These stocks were then de-salted twice using Biospin-6 columns (BioRad, USA), aliquoted out, flash frozen and stored at -80 °C until the day of analysis. On the day of analysis, aliquots were thawed at r.t and diluted to their final concentration prior to experimentation (SI Figure S1).

A mixture of commercially available phosphazine salts pre-dissolved in a acetonitrile/water solution (95:5, % v:v) (G1969-85020) known as “tunemix” (Agilent technologies, Santa Clara, CA), as well as poly-DL-alanine (Sigma, P9003) and myoglobin (Sigma, G7882) dissolved in water/methanol/formic acid (50:50:0.1, % v:v) were used to optimise the helium IM-Trap differential on the modified Agilent 6560 IMQToF.

All experiments were performed using nano-electrospray ionisation (nESI) in positive ionisation mode. Samples were infused into emitters prepared in-house from thin walled (O.D. 1.2 mm, I.D. 0.9 mm; WPI, UK) and thick walled (O.D. 1.2 mm, I.D. 0.69 mm; Sutter Instrument Company, USA) fire polished borosilicate glass capillaries using either a Flaming/Brown P-97, Sutter P1000 or P2000/F micropipette puller (Sutter Instrument Company, USA). In order to facilitate more facile spraying, all solution loaded emitters were centrifuged at 5000 rpm for 15 seconds prior to loading into the instrument tip holder. Platinum wire (diamater 0.125 mm, Goodfellow Cambridge Ltd, UK), was inserted into the capillaries to permit efficient ionisation. In order to compensate for the reduction in ion transmission which typically accompanies native IM-MS instrument optimisation, all experiments were carried out in sensitivity mode.

2.2 Instrumentation

2.2.1. Waters Synapt G2 (TWIMS)

Travelling wave derived CCS distributions/CCS were obtained on a Synapt G2 (Waters, UK) with nitrogen as the drift gas (SI Figure S2). Within this instrumental configuration, ions can be mass selected in the quadrupole prior to IMS. After navigating the quadrupole, ions enter the “Tri-wave” region which encompasses: 1) an argon filled trap cell, where ions are periodically stored and gated into the helium cell, 2) a helium cell held at a comparatively high pressure to the trap cell, where ions experience "collisional cooling" prior to IM separation, 3) an ~25 cm long TWIMS cell filled with nitrogen, whereby propagating DC waves enable the mobility separation of ions based upon their size, charge and conformation and 4) a transfer cell which acts to ferry ions toward the ToF analyser for *m/z* quantitation. For all the TWIMS experiments within this study, IM wave velocities of 100-300 ms^{-1} and wave heights of 9.5-19.5 V were employed. General parameters employed for native TWIMS experiments are outlined in Table S2. For a more detailed description of the Synapt G2 (TWIMS), see Giles *et al.*[36].

2.2.2. Waters Synapt G2 (DTIMS)

The Synapt G2 was modified *via* substitution of the travelling-wave IM cell (incorporating the helium cell) with an ~25 cm long RF-confining drift cell (Waters, UK) (SI Figure S3).[37] Helium/nitrogen gas was introduced into the RF cell using a gas inlet system positioned in the centre of the cell to promote pressure homogeneity (SI Figure S4). Absolute IM cell pressure readouts were enabled by the installation of a baratron (model 626C, MKS, UK). Drift gases could be switched by toggling the "He" (for helium) or "IMS" (for nitrogen) tabs, whilst the RF confining drift cell could also be operated using the original instrument software (MassLynx V4.1) (SI Figure S4). The static potential gradient required for IMS was applied across the RF cell using a combination of four DC voltages (SI Figure S3). For all the experiments outlined in this study, six drift voltages separated by 25 V increments were employed to obtain ion dead times (t_0) and subsequent CCS/CCS distributions. It is important to note that the RF cell pressure was left to equilibrate for >30 minutes after gas initiation/switching prior to data acquisition. General parameters employed for native DTIMS experiments performed on the modified G2 are outlined in SI Table S3. For a more detailed description of the modified Synapt G2 (DTIMS), see Allen *et al.*[37].

2.2.3. Agilent 6560 IMQToF

The setup employed for helium and nitrogen experiments carried out on the 6560 is described in SI Figure S5. For experiments undertaken on the 6560, an orthogonally configured nESI source (G1988-60000 Nanospray, Agilent) was utilised. The source drying gas flow (nitrogen), which was observed to have a large impact upon the observed analyte charge state distributions (CSDs) (SI Figure S6), was adjusted to below 2 L min^{-1} by a manual flow controller (Porter instrument company, USA) fitted to the drying gas outlet and source inlet. Post source, ions were transferred through a heated capillary into a two-stage ion funnel, the first of which focuses ions *via* the use of elevated pressures, whilst the latter operates as an ion funnel trap which enables the release of discrete ion pulses into the IM cell. The IM region comprises an ~78 cm long static field drift tube with an absolute pressure capacitance gauge (CDG 500, Agilent) positioned at the far end of the cell and a thermocouple (Type K, Omega engineering) positioned above the middle of the cell. The instrument configuration employed for measurements taken with nitrogen and helium drift gases is depicted in SI Figure S5. For measurements taken in nitrogen, a positive IM cell pressure differential of 0.15 Torr relative to the preceding trapping funnel was utilised, as described previously.[38] The pressure differential was maintained within 0.01 Torr *via* the inclusion of a drift gas kit (G2582A, Agilent) fitted with a precision flow controller (640B 10 Torr range, MKS) which regulated drift tube pressure by responding to the absolute pressure capacitance gauge (CDG 500, Agilent). However, we found the precision flow controller to be unable to maintain pressure differentials when the instrument was operated with helium as the drift gas. As such, we modified the gas inlets into the trap and IM cell so as to bypass the flow controller and permit manual control of the gas pressures using needle valves (Swagelok) (See SI Figure S5). After carrying out pressure differential optimisation experiments in helium using tunemix (SI Table S4), polyalanine (SI Table S5) and myoglobin (SI Table S6), we settled on an optimum helium IM-Trap differential of ~0.13 Torr. This differential prevented nitrogen contamination in the IM cell, resulting in $^{DT}CCS_{He}$ values closest to those previously published. It is important to note that all gases pass through a gas purifier trap (nitrogen and helium; RMSN and RMSH, Agilent) prior to entering the instrument in both of the instrumental configurations employed. Data was recorded using the MassHunter Data Acquisition software (Agilent) using the stepped-field method, whereby incremental variation of the electric field (five 100 V steps) across the drift cell permitted enumeration of the CCS distributions for a given ion. General parameters employed for native experiments performed on the 6560 IMQToF are outlined in SI Table S7. For a more detailed description of the 6560 IMQToF, see May *et al.*[39].

2.3. Data Analysis and CCS distribution production

All experimental data obtained from the Synapt G2 (with TWIMS/DTIMS configurations) was analysed using MassLynx V4.1 software (Waters, UK). Arrival time distributions (ATDs) encompassing a drift time axis (x-axis) and an associated ion intensity axis (y-axis) were extracted for the desired *m/z* region (Figure 1 a. ii). The drift time axis was transformed to a CCS axis by employing suitable calibrant ions (SI Table S8) following an approach described previously for TWIMS,[11,40,41] or DTIMS data (Figure 1 a & b iii & iv).[23,42] Data acquired on the 6560 IM-QToF was analysed using MassHunter IM-MS Browser software (Agilent). Drift times and their corresponding ion intensities were extracted for the desired *m/z* regions (Figure 1 b. ii), as for data acquired on the Synapt G2. However, unlike MassLynx software, the MassHunter IM-MS browser records all IMS parameters, these can then be extracted as tabulated data and applied to the Mason-Schamp equation to convert the x-axis from drift time to CCS units (Figure 1 b. iii & iv).

Each replicate yielded a single CCS distribution plot with slightly different x-axis CCS binning increments (due to different A and X values from TWIMS experiments and different dead times in DTIMS experimental replicates) (Figure 1 b. iv. Top). In order to produce averaged CCS distribution plots from individual CCS distribution replicates, Gaussian fits were made to the experimental data using a consistent number of data points (e.g. 1000) across a fixed CCS range (e.g. 2500-4500 $Å^2$). After fitting all CCS distribution replicates for a single ion across the same CCS range and number of data points, the average CCS distribution plot was constructed as follows: 1) The range employed for the CCS distribution replicate was extracted and used to form the x-axis of the averaged CCS distribution plot. 2) The ion intensity across the CCS range of each replicate was averaged whereby standard deviations denote the variation between replicates. 3) The constructed x-axis, y-axis and y-axis standard deviation were combined to obtain averaged CCS distributions (Figure 1 b. iv. Bottom). Ion CCS were obtained *via* averaging apex values from Gaussian fitted CCS distribution replicates. Associated CCS errors (±) came from the standard deviation of these values. Total CCS distribution plots for protein/protein complexes were obtained by combining averaged ion CCS distribution plots (normalised for mass spectral peak intensity and CCS distribution area). All CCS distributions produced within this study were constructed using OriginPro 2015/2017 software.

2.4. Interactive figures

A number of main text and SI figures presented in this article were recreated in an interactive format to enable in-depth interrogation of the presented results. These are deposited online at https://france-ccs-2019.netlify.com/.

The interactive figures were created using ORIGAMI^{ANALYSE} and require the use of a modern internet browser and access to the internet.[43]

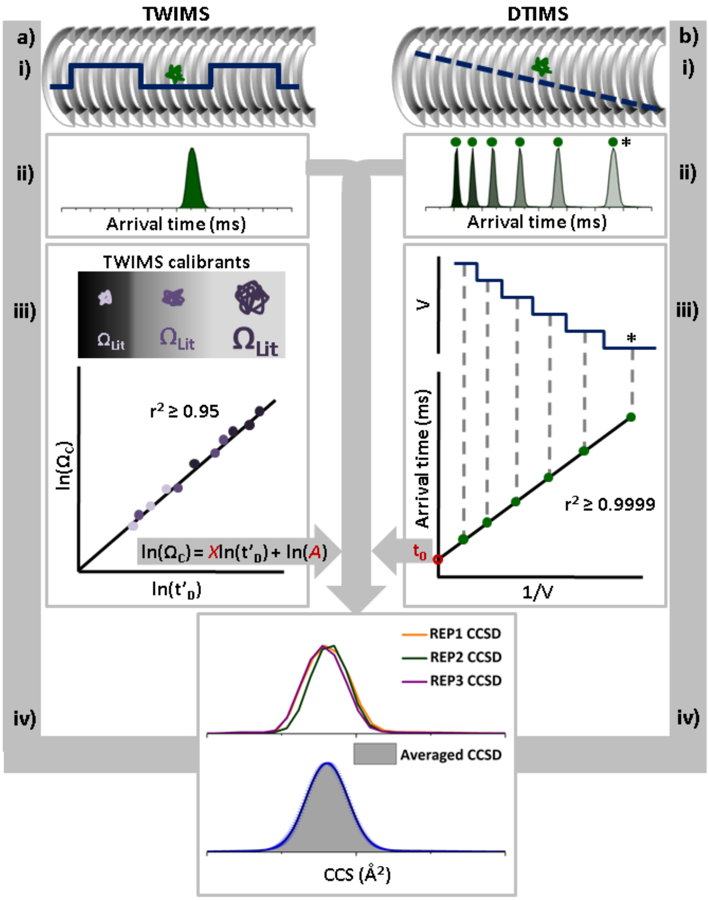

Figure 1. Schematic showing how TWIMS (LHS) & DTIMS (RHS) data yields averaged ion CCS and CCS distributions. a) i) Schema for the trajectories of ions in each type of IM experiment. ii) Example ATDs required to determine CCS distributions. For DTIMS data (RHS) the ATD corresponding to the lowest DV is marked by (*). iii) LHS: Drift times from calibrant ions with previously measured ^{DT}CCS which bracket the mass of the ion of interest are corrected for their charge, time spent outside the drift cell post IM and reduced mass, yielding a plot that converts experimental corrected drift times (t'_D) to CCS (Ω_C). From the plot of $\ln(\Omega_C)$ vs $\ln(t'_D)$, the exponential factor (X) and fit-determined constant (A) can be obtained for conversion of ATDs into CCS distributions. RHS: The arrival time apex of ions obtained from each DV are plotted against a reciprocal of the DVs (1/V), where the y-intercept of this plot yields the ion 'dead time' (t_0), which is the time spent outside of the drift cell. Additionally, the slope of the plot represents the ions mobility. iv) CCS axes are not the same across CCS distribution replicates, so interpolation of the data yields an averaged CCS distribution wherein error bars (blue) represent the deviation between replicates.

3. Results and Discussion

3.1 Tuning ion transmission to preserve structure

Native IM-MS workflows are dependent upon the solvation of biomolecules within non-denaturing, MS compatible solutions which adequately reflect the electrolytic milieu of the cell.[25,44,45] Accordingly, aqueous ammonium acetate adjusted to pH (~7) is the most commonly employed solution for native IM-MS experiments.[25,44,45] In order to sample macromolecular structures which most closely resemble those found in physiological solutions, IM-MS instrumentation has to be carefully tuned so as to reduce lab frame energies and in turn, ion internal energies (E_{int}) which promote gas-phase restructuring.[26] Perturbations in protein conformation, *via* ion heating, often have minimal effects upon the observed CSD (Figure 2a insets);[26] as a result, structural conclusions derived solely from protein charge state signatures (i.e CSDs) observed *via* native MS should be addressed with caution.[46,47]

To ascertain the degree to which a set of instrument parameters promote ion activation, we use the observed ATD of selected proteins as a measure of transmission 'softness', analogous to the use of fragments from thermometer ions.[29,48,49] Given this approach, suitable ions are those with a well-documented "native" globular state and defined unfolding pathway previously observed with IM-MS. Accordingly, we recommend the $[\text{Ubiquitin+6H}]^{6+}$ and $[\text{Cytochrome c+7H}]^{7+}$ ions as suitable (Figure 2a).

Post ionisation, optimisation for 'soft' ion transmission is dependent upon: 1) the reduction of accelerating voltages and 2) the modulation of gas pressures, both of which act in synergy to minimise the energy of ion-neutral collisions. In the instance where desirable 'soft' tuning has been achieved, the ATD of the thermometer ion (cytochrome c in this instance) should present with a comparatively narrow, Gaussian-like peak (indicative of a single conformational population) observed at low arrival times (Figure 2a, Top). These observations would likely point to the retention of a folded form of the protein which effectively is a dehydrated solution-phase structure; this hypothesis can be confirmed *via* CCS determination.[50] The associated mass spectrum (Figure 2a, Top, inset) presents with a dominant 7+ peak and a small amount of the 6+ ion. This mass spectrum is typical for cytochrome c sprayed from non-denaturing solutions.[51] Critical to our workflow is the observation that when certain ions undergo collisional heating, they first anneal into highly collapsed structures prior to unfolding. These collapsed structures will present in much the same manner as the native-like dehydrated ion, except with lower CCS values. Subsequently, in situations where gas-phase annealing to collapsed structures is suspected, it is instructive to compare the associated CCS with those found within the literature.[52]

For many commercial mass spectrometers the default settings employ greater accelerating voltages in tandem with gas pressures which permit increased gains in ion transmission (~5 fold) and detection efficiency. Often these gains in signal intensity are concomitant with a reduction in salt adducts (observed *via* MS). Under default settings a protein will undergo a degree of gas-phase restructuring, typically yielding more complicated ATDs (Figure 2a, Middle). Interestingly, within the corresponding MS (Figure 2a, Middle, Inset), under such conditions we observe an slight increase in the relative abundance of lower charge states (6 & 5+) when compared to the soft tune, perhaps attributed to the loss of counterions. If accelerating potentials within the instrument are increased further still, then the intermediary conformations largely re-organise to an extended gas-phase form which tends to have one conformer.[10,53] This capability to manipulate the structure of a given ion *in vacuo* is exploited in activated ion mobility (aIM)/ collision induced unfolding (CIU) experiments, which describe the gas-phase restructuring of an ion, often induced by high energy gas-ion collisions, monitored via IM-MS.[43] aIM/CIU has played a pivotal role in the interrogation of protein unfolding mechanisms as well as the effect of ligand/co-factor binding upon protein stability.[26,54,55]

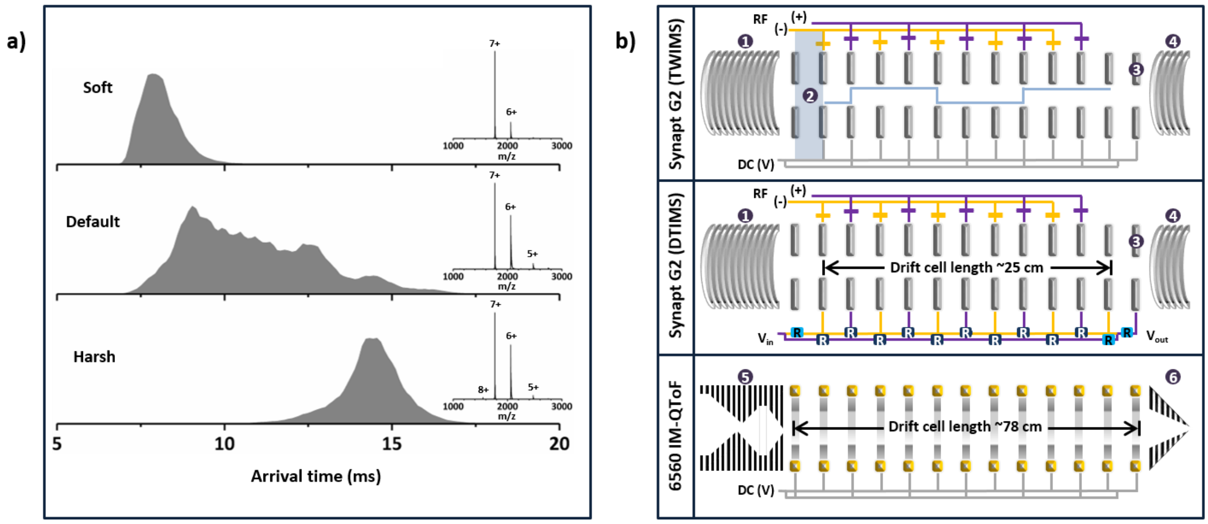

Figure 2. a) IM conformational landscapes of [cytochrome c +7H]$^{7+}$ obtained from the Synapt G2 (TWIMS) under different tuning conditions. Top) 7+ ATD observed under 'soft' settings. Middle) 7+ ATD observed under 'Default' settings. Bottom) 7+ ATD observed under 'Harsh' settings. Insets) Mass spectra corresponding to each set of tuning conditions. b) Schematic of the three IM-MS configurations employed within this study illustrating the differences in the trapping regions prior to injection to the drift cells. Top) G2-TWIMS configuration - Ions are gated from the trap region (1) into the He cell (2) where they are 'collisionally cooled' prior to reaching the IM cell. Upon entering the IM cell, ions are separated by propagating DC waves (blue line) which propel ions through the stacked ring ion guide (SRIG) filled with an inert drift gas. Ions then reach the transfer DC entrance (3) after which they enter the transfer cell (4) prior to entering the ToF-MS for *m/z* quantitation. Middle) G2-DTIMS configuration - In this setup, the helium cell entrance plate & TWIMS cell have been replaced by a linear drift cell.[37] RF-confinement of the ion beam within this configuration is established by a dual series of 330 pF capacitors. Ions traverse a uniform DC voltage gradient established via a network of resistors ('R' Boxes). Bottom) 6560 IMQToF – The trapping funnel (5) permits the temporal release of ions into the drift cell where they drift under the influence of a shallow DC potential (without RF confinement). After which the ion beam is axially refocused by the rear funnel (6) at the exit of the drift cell prior to entering the post-IM optics.

To least perturb the ions structure, its kinetic energies must be kept at or near the minimum threshold required for successful transmission. On the Synapt G2, parameters such as the trap cell gas flow, trap bias DC (which acts as an injection voltage) and Trap CE, are critical determinants of transmission 'softness' (Figure 2b, Top & Middle). The trap cell gas flow, when tuned with voltages within the trap cell, permits effective trapping of ions prior to gating into the IM region. In addition, this gas collisionally focuses ions by dampening their axial and radial velocities, which in turn increases overall ion transmission. That being said, if the trap cell flow is too high, then structural perturbation can occur due to the increased ion-gas collision frequency. In the G2 TWIMS configuration, the addition of a gas cell before the drift region (2) which acts to permit higher IM resolution, offers another parameter to alter, that of the helium gas within it.[36]

Raising the trap bias DC increases the potential difference between the trap and IM region of the G2 instrument which effectively imbues ions with greater kinetic energies as they enter the IM cell (SI Figure S2 b). Raising the Trap

CE, as with aIM experiments, acts in much the same way. Even for stable protein complexes, for example the tetrameric alcohol dehydrogenase, large potential differences applied between the trap and IM regions result in individual subunit unfolding (Figure 3a) prior to the ejection of highly charged monomers.[56,57] When modulating the trap bias DC it is crucial that a compromise between transmission 'softness' and signal intensity/MS resolution is struck, as this parameter significantly effects MS resolution and ion transmission. Surprisingly for the Synapt G2 (DTIMS configuration), we also found the trap wave height (WH) has an observable impact upon the conformational landscape sampled for monomeric protein ions. We believe this affect to be due to the increased kinetic energy imparted upon ions within the trap when higher trap WHs are employed. Interestingly, we did not observe this effect on the Synapt G2 (TWIMS configuration). In agreement with Williams *et al.*[29], we did not observe TWIMS wave velocity or wave height to have any observable effect upon the conformational landscape sampled for any of the ions analysed. Voltages at the beginning of the IM cell, namely the IMS entrance voltage and the He cell DC (Figure 3a), were also observed to have a 'fine tuning' effect on the observed ion ATD (for monomeric proteins), with the latter only impacting the ATD when the G2 was configured for TWIMS.

In contrast to the aforementioned pre-IM DC voltages, variation of RF voltages within both instrument configurations were not observed to have any significant effects upon ion ATDs, although they did have a notable impact upon ion transmission.[58] To offset reductions in ion transmission which occur under native IM-MS settings, the IM bias DC, transfer CE and transfer wave velocity can be raised. Increasing the IM bias DC and/or the transfer CE, raises the potential energy difference between the IM and transfer region and thus raises ion kinetic energies post-IMS (SI Figure S2b). Optimisation of these three parameters permit favourable gains in ion transmission concomitant with the dissociation of non-volatile salt adducts.

Tuning for 'soft' ion transmission on the Agilent 6560 IMQToF, like the Synapt G2, is largely dependent upon the application of voltages within the trapping region (Figure 2b, Bottom). Most importantly the trap entrance grid delta, which is the potential difference between the trap during filling (low) and during storage and release (high), had a significant effect upon ion activation. This effect was most notable for small monomeric proteins such as cytochrome c (Figure 3b) and was in corroboration with findings from Gabelica *et al*.[30]. Unlike the Synapt G2, we observed tuning of the RF voltages within the 6560 to have a noticeable effect upon ion activation (Figure 2b). The most significant of these was the trapping funnel RF which acts to radially confine ions within the trapping funnel prior to gating into the IM cell. In contrast to Gabelica *et al*.[30] and Mclean *et al*.[51], we found that maintaining the trap DC voltages employed across both N_2 and He drift gases (SI Table S7) did not yield any observable differences in protein conformation (See SI Figures S7-20, LHS column). Within the source region of the instrument we observed minor effects on the conformation of monomeric proteins when the fragmentor voltage, was altered within the 300-400 V range. Lower fragmentor voltages led to losses in signal transmission without gains in transmission 'softness', whilst higher fragmentor voltages did not permit gains in signal intensity yet began to promote ion activation.[30]

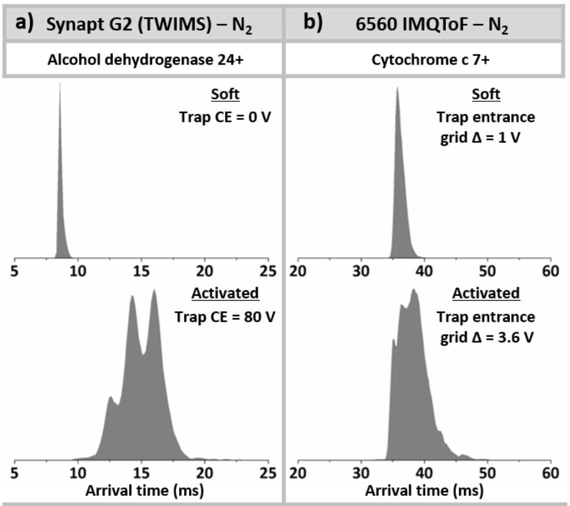

Tuning parameters which affect gas-phase protein structure						
SC	Trap bias	Trap CE		Trap entrance grid Δ		
He cell flow*	IM DC Ent	Trap WH		Fragmentor	RFs	DCs

Figure 3. The use of alcohol dehydrogenase and cytochrome c (200 mM and 50 mM AmAc solutions respectively) to illustrate the effect of altering instrument parameters a) [Alcohol dehydrogenase + 24H]$^{24+}$, Synapt G2, Top) soft tuning, whereby no trap collision energy is applied. Bottom) activating tuning: trap collision energy has been raised to 80 V. b) [Cytochrome c + 7H]$^{7+}$ 6560 IM-QToF, Top) soft tuning parameters: gating height of the trap entrance is +1V. Bottom) using activating tuning parameters: whereby the gating height of the trap entrance is +3.6V. The table describes the parameters which we have found to have substantial (grey & bold) and lesser (just grey) affects upon ion activation on the Synapt G2 (LHS) and 6560 IMQToF (RHS). (*) G2-TWIMS configuration only. SC = source cone potential for the G2.

3.2 Assessing inter-instrument variation in the CCS distributions for proteins and protein complexes

After ‘soft’ and comparable ion transmission parameters were defined across the three instrumental platforms, we focused upon the IM-MS analysis of a range of protein analytes that are readily available and have been much studied before (Table S1). We sought to compare analyte gas-phase CCS distributions with both He and N$_2$ as drift gases (SI Figure S7-20). In Figure 4 we compare the data obtained for tetrameric concanavalin a with cytochrome c. Concanavalin a presents with a CSD centring on the 20+ species and a Δz of 5 (although the charge states at either end of the CSD are often barely visible). Across all three instruments, the CCS distributions for the tetrameric species of concanavalin a largely present as unimodal Gaussian-like peaks which yield CCS$_{He}$ values (replicable to within ~0.5%) that differ by ~0.1-0.9% across charge states and <2% across instruments (when comparing like charge states).

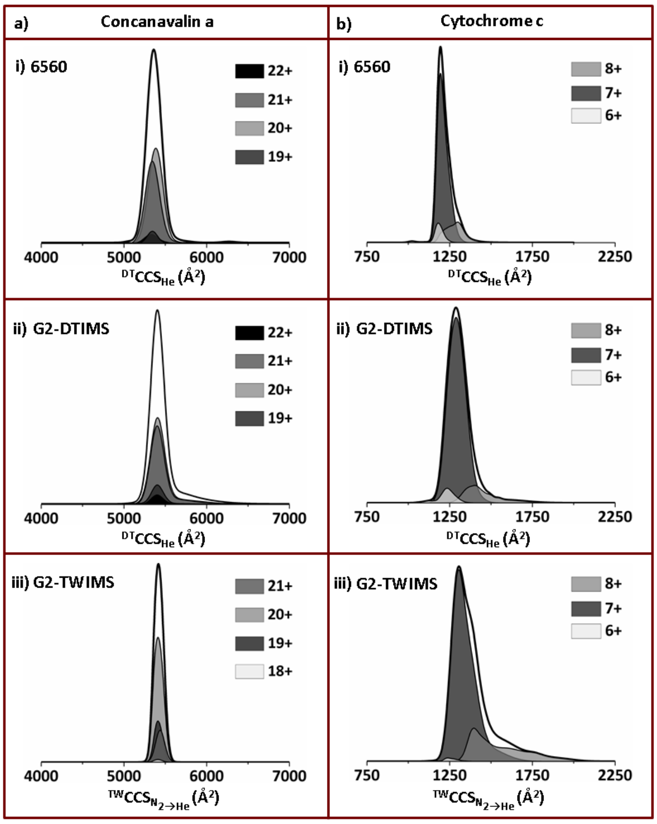

Helium CCS values (Å²) across all platforms

Concanavalin a			
Z (+)	6560	G2-DTIMS	G2-TWIMS
18	-	-	5412 ± 16
19	5340 ± 15	5399 ± 2	5409 ± 8
20	5384 ± 20	5397 ± 1	5412 ± 14
21	5345 ± 29	5401 ± 1	5434 ± 18
22	5335 ± 23 6285 ± 24	5405 ± 1	-

Cytochrome c			
Z (+)	6560	G2-DTIMS	G2-TWIMS
6	1182 ± 4	1234 ± 5	1238 ± 6
7	1196 ± 1	1286 ± 12	1304 ± 6
8	1258 ± 19 1297 ± 2	1373 ± 34 1540 ± 17	1399 ± 6 1625 ± 11 1768 ± 6 1918 ± 12

Figure 4. Total CCS distribution for a flexible protein and rigid protein complex obtained across all instrumental platforms utilised within this study with helium as the drift gas. a) Total CCS distributions obtained when analysing monomeric cytochrome c using parameters tuned for native IM-MS on the i) Agilent 6560 IMQToF, ii) Synapt G2 (TWIMS) and iii) Synapt G2 (DTIMS). b) Total CCS distributions obtained when analysing tetrameric concanavalin a using parameters tuned for native IM-MS on the i) Agilent 6560 IMQToF, ii) Synapt G2 (TWIMS) and iii) Synapt G2 (DTIMS). The total CCS distribution trace encompassing the averaged CCS distributions for each analyte charge state are represented by the thick black lines. The colours of the CCS distributions for each charge state observed correspond to the key at the RHS of each total CCS distribution. The table underneath the total CCS distributions describes the average CCS_{He} values obtained for the observed conformations of concanavalin a (LHS) and cytochrome c (RHS) across the three instrumental configurations employed. The (±) values represent the standard deviations across replicates. For all of these experiments concanavalin a and cytochrome c were sprayed from 200 mM and 50 mM AmAc solution (pH 7.4) respectively.

Our findings suggest that we are probably sampling a single conformational population which is retained across the charge states analysed, as might be expected for a well-structured protein complex. The only exception to this is the

$[M+22H]^{22+}$ species which presents as a bimodal CCS distribution with a larger conformer observed at ~6300 Å^2 (SI Figure S17). Previous aIM experiments on concanavalin a, showed a larger species with a drift time which was ~25% higher than the structure sampled prior to activation.[43,59] Regarding the CCS distribution for concanavalin a analysed in He, the charge states sampled on a given instrument possess almost identical widths (with the exception of the 19+ species sampled on the 6560 which is notably narrower) (SI Figure S17). However, across instruments there are observable differences in CCS distribution width. Most notably the CCS distributions obtained from the G2 (TWIMS), both for $N_2 \rightarrow He$ (SI Figure S17) and N_2 (SI Figure S18) are ~50% narrower than the corresponding CCS distributions obtained from the 6560 and G2 (DTIMS) respectively, which themselves are very similar to one another (Figure 4a). With nitrogen as the drift gas, we observe predominantly unimodal Gaussian-like CCS distributions (as in He) but with CCS (replicable to within ~0.5%) that differ more significantly across charge states (~0.9-4.3%) but not instruments (<2%) (SI Figure S18). For clarity we have provided representative raw ATDs to show the unprocessed gas-phase conformational landscapes we observe by IM in both He (SI Figure S21) and N_2 (SI Figure S22), within this study. The most notable variation across CCS_{N_2} values is observed on the G2-TWIMS, where the highest charge state (21+) is ~4.3% bigger than the lowest charge state (18+). This difference is most likely due to the Ω_{Lit} values employed for the $^{TW}CCS_{N_2}$ calibration procedure. In accordance with this hypothesis, a significantly smaller CCS variation across charge states is observed (~0.5%) for the same raw data set calibrated to yield $^{TW}CCS_{N_2 \rightarrow He}$ values. In contrast, the range of CCS_{N_2} values obtained for concanavalin a on the G2 (DTIMS) and 6560 do not vary to the same degree, at ~1.7 and 0.9% respectively.

Cytochrome c also presents as a narrow CSD, with a Δz = 2-3, centring on the $[M+7H]^{7+}$ species (Figure 2 and SI Figure S9). Across all three instruments, the ATDs for the $[M+6H]^{6+}$ are bimodal, but here the earlier arriving species corresponds to a concentration specific coincident dimer whilst the $[M+7H]^{7+}$ ATD is unimodal. Slight tailing toward higher CCS is observed for the $[M+6H]^{6+}$ on the G2 (TWIMS) and the 7+ ion analysed on the 6560 and G2. The CCS distribution of the 7+ ion, analysed on the G2 is comparatively broad (Figure 4 & SI Figure S9). This tailing and broader CCS distribution (7+, G2) may be indicative of a lowly populated, partially unfolded conformer which we were unable to resolve. In contrast to the highest charge states of concanavalin a, the 8+ species of cytochrome c when sampled on the G2 presents as a broad unresolved peak with one dominant, partially resolved apex with a notable tail. This tail likely constitutes numerous unresolved, closely related intermediate conformations resulting from differing degrees of structural activation. On the other hand, the 8+ ion sampled on the 6560 presents as a far narrower, albeit partially resolved peak with minimal tailing. Across the three instruments, the CCS_{He} values for the most compact ion conformations observed vary by ~0.3-9%, with the variation increasing with increasing charge (Figure 4 & Figure 5). However, most of this variation is due to the CCS_{He} values obtained on the 6560 which are ~4-9% smaller than those obtained on the G2 platform. When comparing CCS_{He} values obtained on the 6560 and G2 we observe the same trend (to differing degrees) for all analytes within this study, except for concanavalin a (Figure 5). Interestingly, the systematic reduction in measured CCS on the 6560 relative to the G2 is not observed with nitrogen as the drift gas (SI Figures S7-S20 & S23). Comparing the total CCS distribution plots for cytochrome c across the three instruments employed, we see that the CCS distribution widths, particularly for the 7+ and 8+ ion, are considerably wider on the G2 platform (~50%) than on the 6560. This finding is inconsistent with the total CCS distributions of concanavalin a, where the opposite is observed.

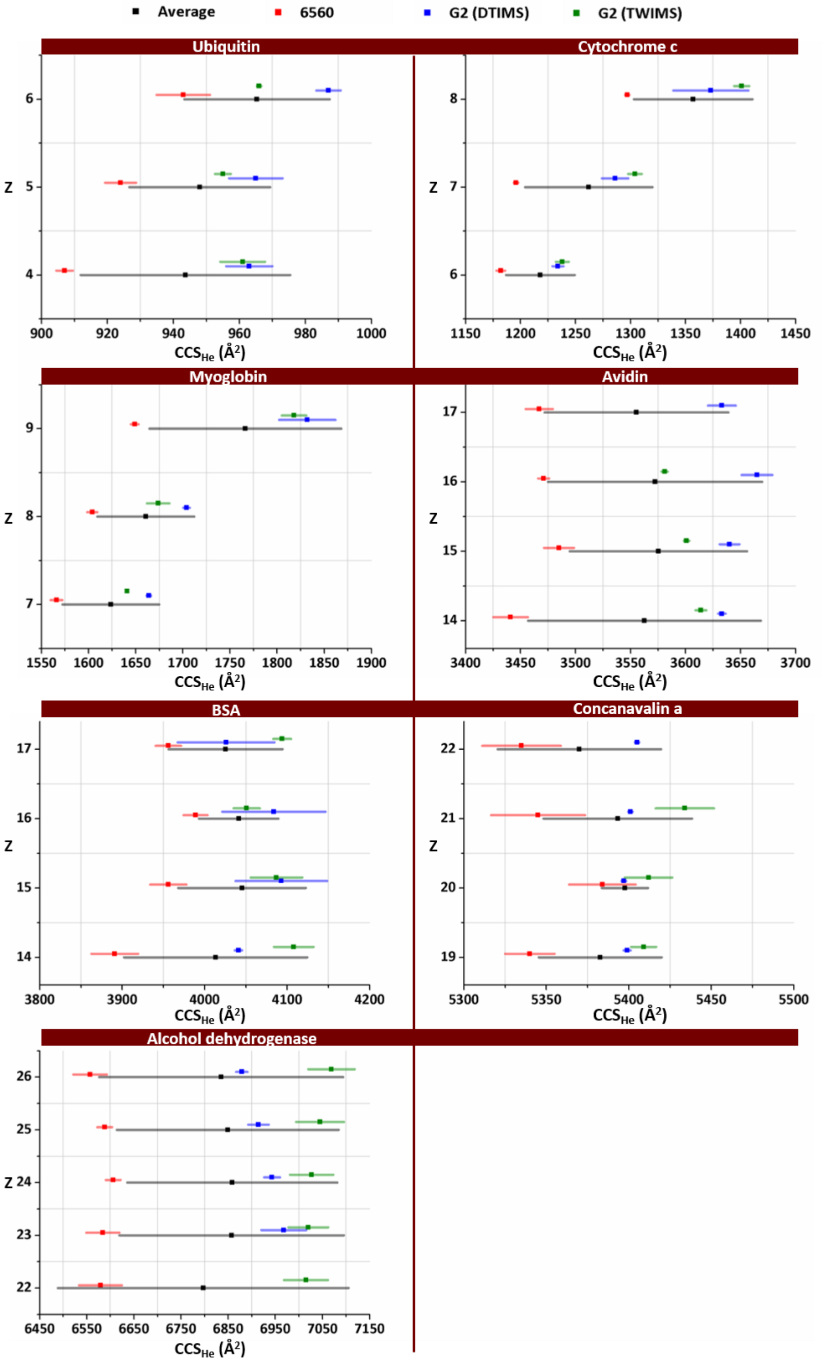

Figure 5. Scatter plots showing the range of CCS$_{He}$ values obtained for the protein/protein complexes analysed within this study across the instrumental platforms utilised. In all cases the CCS for the single most abundant conformation for each charge state was compared across the three instruments. The black, red, blue and green squares represent the average CCS$_{He}$ values obtained for single conformations as an average across all the instruments, on the 6560, the G2 (DTIMS) and the G2 (TWIMS) respectively. The associated coloured bars show the standard deviation across the experimental replicates.

3.4 Comparisons with literature

In order to visualise the general spread of conformations for proteins/protein complexes across the literature, as well as this study (as discussed above), we have plotted all of the CCS values we could find, for all the analytes and their charge states observed in this study, as global CCS frequency histogram plots (see Figure 6 for cytochrome c [He & N_2] and SI Figures S24-S35 and Tables S9 & S10 for all of the analytes). These plots, along with their associated tabulated CCS should act as a rough guide for future native IM-MS analyses of the analytes discussed within this study.

The CCS_{He} values obtained for the 6+ and 7+ ions of cytochrome c within our study are ~6% smaller to 5% larger than the most compact conformations sampled by Clemmer and co-workers on their 50.6 cm and 7.6 cm long drift tube instruments (Figure 6a & Table S9).[10,60,61] Additionally, our CCS_{He} values are ~ 8 % smaller to 2 % larger than those measured by Bush *et al*. on a modified Synapt G2 with an RF confining linear cell (Figure 6a & Table S9).[37,41] Regarding the most compact conformations of the 8+ ion sampled on the G2 our CCS_{He} values are ~9-12% larger than those reported by Clemmer, whilst the values obtained from the 6560 are <1% larger than the most compact conformation sampled by Clemmer (Figure 6a & Table S9).[10,60,61] Furthermore, our measurements for the most compact conformations of the 6+, 7+ and 8+ ions range from 5-21% smaller than the most compact conformations sampled by Mclean *et al*. on a 6560 IMQToF (Figure 6a & Table S9).[51] Importantly, our measurements on the 6560 in He, are seen to provide the largest source of variation when comparing our CCS_{He} values with those found in the literature.

The CCS_{He} values measured for concanavalin a within this study are in good agreement (~0.5-3% smaller) with those obtained on a modified Synapt G2 (RF confining linear cell) by Bush *et al*.[37,41], and those measured on a home built VT-IM-MS instrument by Barran *et al*. (SI Figure 32 & Table S9).[62] That being said, Barran *et al*. also recorded CCS, on a home-built IMQToF, which were ~8-18% smaller than those observed in our study (SI Figure S32 & Table S9).[52,63] Regarding the small body of published CCS_{N_2} measurements, the values we have obtained within this study are systematically smaller (~0.5-4%) than those measured by Bush and coworkers on a 1st and 2nd gen RF confining drift cell and on a SLIM system (SI Figure S33 & Table S10).[41,64]

When comparing our CCS_{N_2} values with those obtained in the literature, our values for the 6+ and 7+ ions of cytochrome c are systematically smaller than the most compact conformers obtained in a series of studies by Bush *et al*. by anywhere from ~1 up to 25% (Figure 6b & Table S10).[41,64] In comparison to measurements by Mclean *et al*. on a 6560 IMQToF, our measurements range from 5-13% smaller for the 8+, 4 % smaller to 2% larger for the 7+ and 7-8% larger for the 6+ ion (Figure 6b & Table S10).[51] We reason that the most compact conformation measured for the 6+ ion by Mclean *et al*. corresponds to a trace amount of coincident dimer, which, if we were to measure as a compact conformer of the 6+ ion (as an average across the three instruments utilised), does yield a CCS_{N_2} of 1326 ± 48 Å^2 which is in close agreement with their published CCS_{N_2} value of 1360 ± 13 Å^2.[51] Accordingly, our measurements for the 6+ ion are <1-2% smaller than the measurement given for the most abundant conformer they observe, making it more likely that this species is indeed the most compact conformation of the 6+ ion which they sampled. The above information, together with prior EHSS and PSA models (in He) for the native fold of cytochrome c, suggest that for the 6+, 7+ (on all instruments) and 8+ ion (measured on the 6560), we are sampling dehydrated, partially collapsed, native-like structures of cytochrome c.[10,51,65] Regarding the 8+ ion, the conformations sampled on the G2 likely represent different intermediates along the gas-phase unfolding pathway toward more extended structures, as seen previously.[10,66] In contrast, concanavalin a does not show the same degree of charge/instrument dependent CCS distribution variation and CCS increase, likely due to its more rigid structure.

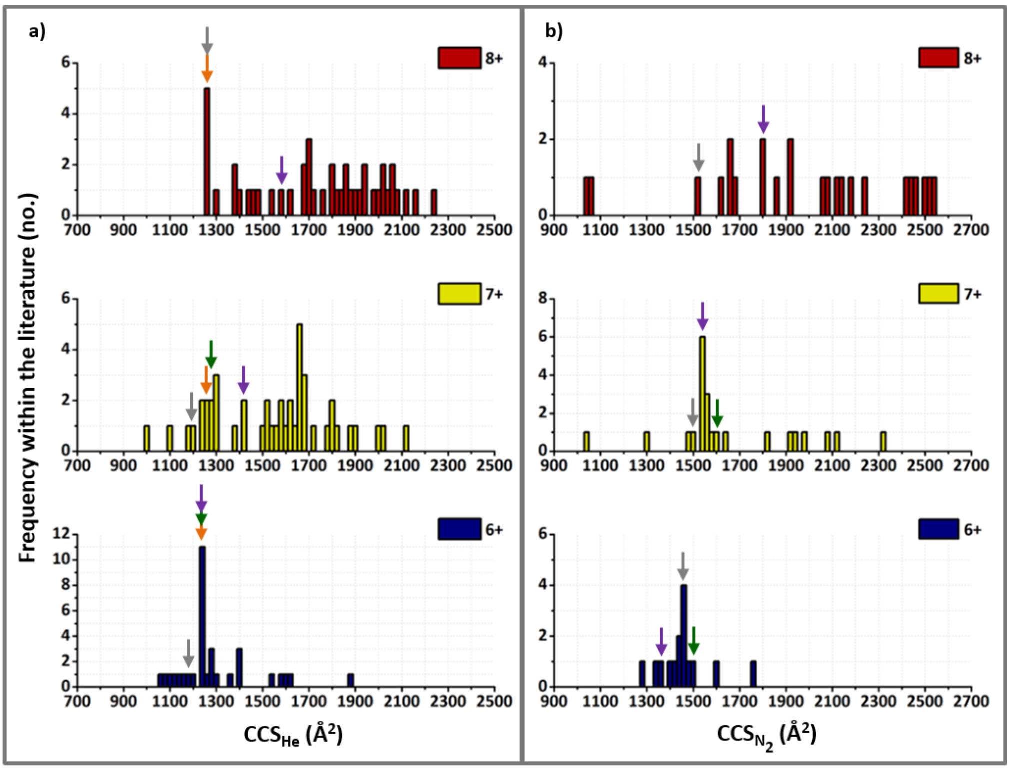

Figure 6. Global histogram plots of cytochrome c. a) Global CCS_{He} histogram plots, b) Global CCS_{N_2} histogram plots, for all the experimentally observed charge states of cytochrome c. Literature as well as our own experimentally obtained CCS values were grouped into 20 Å^2 bins, whereby the frequency of CCS values to the nearest 20 Å^2 increment were summed and represented as solid bars within the histogram plots. Within these stacked histogram plots, blue, yellow and red bars represent the frequency and size of CCS values for the 6+, 7+ and 8+ ions of cytochrome c respectively. Grey, orange, green and purple arrows represent the smallest CCS values measured from this study, and the literature values of Clemmer *et al*., Bush *et al*. and McLean *et al*. respectively.[10,41,51,60,61,64]

Across all of the protein/protein complexes analysed, we present CCS_{N_2} values which are reproducible to within <3 % across the 6560 and G2 (TWIMS and DTIMS) configurations. Similarly, this degree of variation was observed when comparing CCS_{He} values obtained across both configurations of the G2. However, CCS_{He} values derived from the Agilent 6560 proved significantly different to those obtained on the Synapt G2 platform, with the (notable) exception of concanavalin a. If this difference in CCS was a result of applying an incorrect IM-Trap pressure Δ, then we would expect 1) The CCS_{He} values obtained for the monomorphic test systems utilised to be significantly different from their published values and 2) all of the CCS_{He} values to be systematically larger on the 6560 relative to the G2, as the drift cell would be contaminated with nitrogen gas (if the IM-Trap pressure Δ was too low), which would retard ion motion more than helium, leading to comparatively longer drift times and thus larger CCS.[51] Instead, at a

Δ of ~0.13 Torr, we observe the CCS_{He} values for the monomorphic systems to be in close agreement with the average helium CCS derived from previously published data (<0.5%).[27,37,51,67–70] In addition, the CCS_{He} values for the analytes under test were systematically smaller than those observed on the G2, by an average of 4.3% and a maximum of ~ 10 %. As we employed the same trapping DC voltages across both N_2 and He gas experiments we thought it possible that analyte ions injected into the IM cell filled with helium might be introduced with such force (due to the relative differences in mass between He and N_2) that they do not immediately begin to 'drift' within the IM cell, thus shortening their effective drift length, which would lead to a systematic reduction in CCS_{He} values. However, this effect was not observed for the monomorphic test systems and concanavalin a, which were analysed using identical pre-IM DC voltages to those employed for the other analytes studied.

4. Conclusion and Outlook

Native IM-MS is used to measure a host of protein/protein complexes across many instrumental platforms. Within this study we have shown that, when parameters are tuned to minimise gas-phase activation via the employment of suitable thermometer ions, compact conformations and highly similar structural landscapes can be sampled across three common platforms. These findings in tandem with the body of literature for CCS_{He} values suggests things: 1) that the instrument parameters employed on the 6560 (when operating in He) permit access to native-like dehydrated solution-phase like structures that are notably smaller than those obtained on the G2, or 2) that the instrument parameters employed on the 6560 (when operating in He) promote gas-phase annealing of all but the most rigid structural conformations. When comparing our 6560 CCS_{He} values with the smallest values from the literature (SI Table S9), we observe that our measurements are not systematically smaller, and actually range from ~16% larger to 11% smaller than the smallest $^{DT}CCS_{He}$ values published. As such, we conclude that the smallest CCS_{He} values we observe on the 6560 are most probably dehydrated, native-like solution-phase structures sampled *in vacuo*. Our findings in combination with the broad range of accessed CCS observed within our global CCS frequency histogram plots (and their associated tables) show that proteins/protein complexes are often conformationally flexible, dynamic structures which can easily undergo unintentional gas-phase restructuring to yield non-native conformations. As such, regarding the future of CCS calibration procedures (as utilised to obtain ^{TW}CCS) we propose that the ideal set of calibrants would be monomorphic (and therefore impervious to gas-phase ion activation), unlike proteins. But similar to the array of protein 'standards', these calibrants would span a wide range of masses, mobilities, Δz's and effective densities (thus mimicking the breadth of potential protein samples) whilst being readily available, highly stable and easily sprayed. This version of a calibration approach will be the focus of future studies.

Acknowledgements

This research was supported by the BBSRC (awards: BB/L015048/1, BB/K017802/1 and BB/H013636/1 and the BBSRC/EPSRC-funded Manchester Synthetic Biology Research Centre, SYNBIOCHEM (BB/M017702/1)). MRC, BBSRC, EPSRC, Waters Corp. Agilent and the Universities of Edinburgh and Manchester are thanked for their support of studentships to AF, LGM, and ES.

(1) Smith, D.; Knapman, T.; Campuzano, I.; Malham, R.; Berryman, J.; Radford, S.; Ashcroft, A. Deciphering Drift Time Measurements from Travelling Wave Ion Mobility Spectrometry-Mass Spectrometry Studies. *Eur. J. Mass Spectrom.* **2009**, *15* (5), 113. https://doi.org/10.1255/ejms.947.

(2) Li, J.; Taraszka, J. A.; Counterman, A. E.; Clemmer, D. E. Influence of Solvent Composition and Capillary Temperature on the Conformations of Electrosprayed Ions: Unfolding of Compact Ubiquitin Conformers from Pseudonative and Denatured Solutions. *Int. J. Mass Spectrom.* **1999**, *185*, 37–47. https://doi.org/10.1016/S1387-3806(98)14135-0.

(3) Hudgins, R. R.; Woenckhaus, J.; Jarrold, M. F. High Resolution Ion Mobility Measurements for Gas Phase Proteins: Correlation between Solution Phase and Gas Phase Conformations. *Int. J. Mass Spectrom. Ion Process.* **1997**, *165–166*, 497–507. https://doi.org/10.1016/S0168-1176(97)00182-1.

(4) Breuker, K.; McLafferty, F. W. Stepwise Evolution of Protein Native Structure with Electrospray into the Gas Phase, 10-12 to 102 S. *Proc. Natl. Acad. Sci.* **2008**, *105* (47), 18145–18152. https://doi.org/10.1073/pnas.0807005105.

(5) Wyttenbach, T.; Bowers, M. T. Structural Stability from Solution to the Gas Phase: Native Solution Structure of Ubiquitin Survives Analysis in a Solvent-Free Ion Mobility-Mass Spectrometry Environment. *J. Phys. Chem. B* **2011**, *115* (42), 12266–12275. https://doi.org/10.1021/jp206867a.

(6) Lee, S. W.; Freivogel, P.; Schindler, T.; Beauchamp, J. L. Freeze-Dried Biomolecules: FT-ICR Studies of the Specific Solvation of Functional Groups and Clathrate Formation Observed by the Slow Evaporation of Water from Hydrated Peptides and Model Compounds in the Gas Phase. *J. Am. Chem. Soc.* **1998**, *120* (45), 11758–11765. https://doi.org/10.1021/ja982075x.

(7) McAllister, R. G.; Metwally, H.; Sun, Y.; Konermann, L. Release of Native-like Gaseous Proteins from Electrospray Droplets via the Charged Residue Mechanism: Insights from Molecular Dynamics Simulations. *J. Am. Chem. Soc.* **2015**, *137* (39), 12667–12676. https://doi.org/10.1021/jacs.5b07913.

(8) Wyttenbach, T.; Von Helden, G.; Bowers, M. T. Gas-Phase Conformation of Biological Molecules: Bradykinin. *J. Am. Chem. Soc.* **1996**, *118* (35), 8355–8364. https://doi.org/10.1021/ja9535928.

(9) Florance, H. V.; Stopford, A. P.; Kalapothakis, J. M.; McCullough, B. J.; Bretherick, A.; Barran, P. E. Evidence for α-Helices in the Gas Phase: A Case Study Using Melittin from Honey Bee Venom. *Analyst* **2011**, *136* (17), 3446. https://doi.org/10.1039/c1an15291b.

(10) Shelimov, K. B.; Clemmer, D. E.; Hudgins, R. R.; Jarrold, M. F. Protein Structure in Vacuo: Gas-Phase Conformations of BPTI and Cytochrome C. *J. Am. Chem. Soc.* **1997**, *119* (9), 2240–2248. https://doi.org/10.1021/ja9619059.

(11) Ruotolo, B. T.; Benesch, J. L. P.; Sandercock, A. M.; Hyung, S.-J.; Robinson, C. V. Ion Mobility–Mass Spectrometry Analysis of Large Protein Complexes. *Nat. Protoc.* **2008**, *3* (7), 1139–1152.

https://doi.org/10.1038/nprot.2008.78.

(12) Wang, S. C.; Politis, A.; Di Bartolo, N.; Bavro, V. N.; Tucker, S. J.; Booth, P. J.; Barrera, N. P.; Robinson, C. V. Ion Mobility Mass Spectrometry of Two Tetrameric Membrane Protein Complexes Reveals Compact Structures and Differences in Stability and Packing. *J. Am. Chem. Soc.* **2010**, *132* (44), 15468–15470. https://doi.org/10.1021/ja104312e.

(13) Ruotolo, B. T.; Giles, K.; Campuzano, I. D. G.; Sandercock, A. M.; Bateman, R. H.; Robinson, C. V. Biochemistry: Evidence for Macromolecular Protein Rings in the Absence of Bulk Water. *Science (80-.).* **2005**, *310* (5754), 1658–1661. https://doi.org/10.1126/science.1120177.

(14) Schiffrin, B.; Calabrese, A. N.; Devine, P. W. A.; Harris, S. A.; Ashcroft, A. E.; Brockwell, D. J.; Radford, S. E. Skp Is a Multivalent Chaperone of Outer-Membrane Proteins. *Nat. Struct. Mol. Biol.* **2016**, *23* (9), 786–793. https://doi.org/10.1038/nsmb.3266.

(15) Beveridge, R.; Migas, L. G.; Payne, K. A. P.; Scrutton, N. S.; Leys, D.; Barran, P. E. Mass Spectrometry Locates Local and Allosteric Conformational Changes That Occur on Cofactor Binding. *Nat. Commun.* **2016**, *7*, 1–9. https://doi.org/10.1038/ncomms12163.

(16) Laganowsky, A.; Reading, E.; Allison, T. M.; Ulmschneider, M. B.; Degiacomi, M. T.; Baldwin, A. J.; Robinson, C. V. Membrane Proteins Bind Lipids Selectively to Modulate Their Structure and Function. *Nature* **2014**, *510* (7503), 172–175. https://doi.org/10.1038/nature13419.

(17) Baker, E. S.; Bernstein, S. L.; Gabelica, V.; De Pauw, E.; Bowers, M. T. G-Quadruplexes in Telomeric Repeats Are Conserved in a Solvent-Free Environment. *Int. J. Mass Spectrom.* **2006**, *253* (3), 225–237. https://doi.org/10.1016/j.ijms.2006.03.016.

(18) Gabelica, V.; Baker, E. S.; Teulade-Fichou, M. P.; De Pauw, E.; Bowers, M. T. Stabilization and Structure of Telomeric and C-Myc Region Intramolecular G-Quadruplexes: The Role of Central Cations and Small Planar Ligands. *J. Am. Chem. Soc.* **2007**, *129* (4), 895–904. https://doi.org/10.1021/ja065989p.

(19) Bernstein, S. L.; Dupuis, N. F.; Lazo, N. D.; Wyttenbach, T.; Condron, M. M.; Bitan, G.; Teplow, D. B.; Shea, J. E.; Ruotolo, B. T.; Robinson, C. V.; et al. Amyloid-β 2 Protein Oligomerization and the Importance of Tetramers and Dodecamers in the Aetiology of Alzheimer's Disease. *Nat. Chem.* **2009**, *1* (4), 326–331. https://doi.org/10.1038/nchem.247.

(20) Dupuis, N. F.; Wu, C.; Shea, J. E.; Bowers, M. T. The Amyloid Formation Mechanism in Human IAPP: Dimers Have β-Strand Monomer-Monomer Interfaces. *J. Am. Chem. Soc.* **2011**, *133* (19), 7240–7243. https://doi.org/10.1021/ja1081537.

(21) Gabelica, V.; Shvartsburg, A. A.; Afonso, C.; Barran, P.; Benesch, J. L. P.; Bleiholder, C.; Bowers, M. T.; Bilbao, A.; Bush, M. F.; Campbell, J. L.; et al. Recommendations for Reporting Ion Mobility Mass Spectrometry Measurements. *Mass Spectrom. Rev.* **2019**, 1–30. https://doi.org/10.1002/mas.21585.

(22) Verbeck, G. F.; Ruotolo, B. T.; Gillig, K. J.; Russell, D. H. Resolution Equations for High-Field Ion Mobility. *J. Am. Soc. Mass Spectrom.* **2004**, *15* (9), 1320–1324. https://doi.org/10.1016/j.jasms.2004.06.005.

(23) Mason, E. A.; McDaniel, E. W. *Transport Properties of Ions in Gases*; Wiley: New York, 1988.

(24) Jurneczko, E.; Barran, P. E. How Useful Is Ion Mobility Mass Spectrometry for Structural Biology? The Relationship between Protein Crystal Structures and Their Collision Cross Sections in the Gas Phase.

Analyst **2011**, *136* (1), 20–28. https://doi.org/10.1039/C0AN00373E.

(25) Hernández, H.; Robinson, C. V. Determining the Stoichiometry and Interactions of Macromolecular Assemblies from Mass Spectrometry. *Nat. Protoc.* **2007**, *2* (3), 715–726. https://doi.org/10.1038/nprot.2007.73.

(26) Chen, S. H.; Russell, D. H. How Closely Related Are Conformations of Protein Ions Sampled by IM-MS to Native Solution Structures? *J. Am. Soc. Mass Spectrom.* **2015**, *26* (9), 1433–1443. https://doi.org/10.1007/s13361-015-1191-1.

(27) Jurneczko, E.; Kalapothakis, J.; Campuzano, I. D. G.; Morris, M.; Barran, P. E. Effects of Drift Gas on Collision Cross Sections of a Protein Standard in Linear Drift Tube and Traveling Wave Ion Mobility Mass Spectrometry. *Anal. Chem.* **2012**, *84* (20), 8524–8531. https://doi.org/10.1021/ac301260d.

(28) Valentine, S. J.; Counterman, A. E.; Clemmer, D. E. Conformer-Dependent Proton-Transfer Reactions of Ubiquitin Ions. *J. Am. Soc. Mass Spectrom.* **1997**, *8* (9), 954–961. https://doi.org/10.1016/S1044-0305(97)00085-8.

(29) Merenbloom, S. I.; Flick, T. G.; Williams, E. R. How Hot Are Your Ions in TWAVE Ion Mobility Spectrometry? *J. Am. Soc. Mass Spectrom.* **2012**, *23* (3), 553–562. https://doi.org/10.1007/s13361-011-0313-7.

(30) Gabelica, V.; Livet, S.; Rosu, F.; Bordeaux, U. De; Européen, I.; Chimie, D.; Iecb, B. Optimizing Native Ion Mobility Q-TOF in Helium and Nitrogen for Very Fragile Noncovalent Interactions. **2018**. https://doi.org/10.1007/s13361-018-2029-4.

(31) Paglia, G.; Williams, J. P.; Menikarachchi, L.; Thompson, J. W.; Tyldesley-Worster, R.; Halldórsson, S.; Rolfsson, O.; Moseley, A.; Grant, D.; Langridge, J.; et al. Ion Mobility Derived Collision Cross Sections to Support Metabolomics Applications. *Anal. Chem.* **2014**, *86* (8), 3985–3993. https://doi.org/10.1021/ac500405x.

(32) Paglia, G.; Angel, P.; Williams, J. P.; Richardson, K.; Olivos, H. J.; Thompson, J. W.; Menikarachchi, L.; Lai, S.; Walsh, C.; Moseley, A.; et al. Ion Mobility-Derived Collision Cross Section as an Additional Measure for Lipid Fingerprinting and Identification. *Anal. Chem.* **2015**, *87* (2), 1137–1144. https://doi.org/10.1021/ac503715v.

(33) Stow, S. M.; Causon, T. J.; Zheng, X.; Kurulugama, R. T.; Mairinger, T.; May, J. C.; Rennie, E. E.; Baker, E. S.; Smith, R. D.; McLean, J. A.; et al. An Interlaboratory Evaluation of Drift Tube Ion Mobility-Mass Spectrometry Collision Cross Section Measurements. *Anal. Chem.* **2017**, *89* (17), 9048–9055. https://doi.org/10.1021/acs.analchem.7b01729.

(34) Harrison, J. A.; Kelso, C.; Pukala, T. L.; Beck, J. L. Conditions for Analysis of Native Protein Structures Using Uniform Field Drift Tube Ion Mobility Mass Spectrometry and Characterization of Stable Calibrants for TWIM-MS. *J. Am. Soc. Mass Spectrom.* **2018**. https://doi.org/10.1007/s13361-018-2074-z.

(35) Salbo, R.; Bush, M. F.; Naver, H.; Campuzano, I.; Robinson, C. V.; Pettersson, I.; Jørgensen, T. J. D.; Haselmann, K. F. Traveling-Wave Ion Mobility Mass Spectrometry of Protein Complexes: Accurate Calibrated Collision Cross-Sections of Human Insulin Oligomers. *Rapid Commun. Mass Spectrom.* **2012**,

26 (10), 1181–1193. https://doi.org/10.1002/rcm.6211.

(36) Giles, K.; Williams, J. P.; Campuzano, I. D. G. Enhancements in Travelling Wave Ion Mobility Resolution. In *Rapid Communications in Mass Spectrometry*; 2011; Vol. 25, pp 1559–1566. https://doi.org/10.1002/rcm.5013.

(37) Allen, S. J.; Giles, K.; Gilbert, T.; Bush, M. F. Ion Mobility Mass Spectrometry of Peptide, Protein, and Protein Complex Ions Using a Radio-Frequency Confining Drift Cell. *Analyst* **2016**, *141* (3), 884–891. https://doi.org/10.1039/C5AN02107C.

(38) May, J. C.; Dodds, J. N.; Kurulugama, R. T.; Stafford, G. C.; Fjeldsted, J. C.; McLean, J. A. Broadscale Resolving Power Performance of a High Precision Uniform Field Ion Mobility-Mass Spectrometer. *Analyst* **2015**, *140* (20), 6824–6833. https://doi.org/10.1039/C5AN00923E.

(39) May, J. C.; Goodwin, C. R.; Lareau, N. M.; Leaptrot, K. L.; Morris, C. B.; Kurulugama, R. T.; Mordehai, A.; Klein, C.; Barry, W.; Darland, E.; et al. Conformational Ordering of Biomolecules in the Gas Phase: Nitrogen Collision Cross Sections Measured on a Prototype High Resolution Drift Tube Ion Mobility-Mass Spectrometer. *Anal. Chem.* **2014**, *86* (4), 2107–2116. https://doi.org/10.1021/ac4038448.

(40) Shvartsburg, A. A.; Smith, R. D. Fundamentals of Traveling Wave Ion Mobility Spectrometry. *Anal. Chem.* **2008**, *80* (24), 9689–9699. https://doi.org/10.1021/ac8016295.

(41) Bush, M. F.; Hall, Z.; Giles, K.; Hoyes, J.; Robinson, C. V.; Ruotolo, B. T. Collision Cross Sections of Proteins and Their Complexes: A Calibration Framework and Database for Gas-Phase Structural Biology. *Anal. Chem.* **2010**, *82* (22), 9557–9565. https://doi.org/10.1021/ac1022953.

(42) Wyttenbach, T.; Bowers, M. T. Gas-Phase Conformations: The Ion Mobility/Ion Chromatography Method. *Top. Curr. Chem.* **2003**, *225*, 207–232. https://doi.org/10.1007/b10470.

(43) Migas, L. G.; France, A. P.; Bellina, B.; Barran, P. E. ORIGAMI: A Software Suite for Activated Ion Mobility Mass Spectrometry (AIM-MS) Applied to Multimeric Protein Assemblies. *Int. J. Mass Spectrom.* **2018**, *427*, 20–28. https://doi.org/10.1016/j.ijms.2017.08.014.

(44) Konermann, L. Addressing a Common Misconception: Ammonium Acetate as Neutral PH “Buffer” for Native Electrospray Mass Spectrometry. *J. Am. Soc. Mass Spectrom.* **2017**, *28* (9), 1827–1835. https://doi.org/10.1007/s13361-017-1739-3.

(45) Heck, A. J. R. Native Mass Spectrometry: A Bridge between Interactomics and Structural Biology. *Nat. Methods* **2008**, *5* (11), 927–933. https://doi.org/10.1038/nmeth.1265.

(46) Natalello, A.; Santambrogio, C.; Grandori, R. Are Charge-State Distributions a Reliable Tool Describing Molecular Ensembles of Intrinsically Disordered Proteins by Native MS? *J. Am. Soc. Mass Spectrom.* **2017**, *28* (1), 21–28. https://doi.org/10.1007/s13361-016-1490-1.

(47) Hall, Z.; Robinson, C. V. Do Charge State Signatures Guarantee Protein Conformations? *J. Am. Soc. Mass Spectrom.* **2012**, *23* (7), 1161–1168. https://doi.org/10.1007/s13361-012-0393-z.

(48) Morsa, D.; Gabelica, V.; De Pauw, E. Fragmentation and Isomerization Due to Field Heating in Traveling Wave Ion Mobility Spectrometry. *J. Am. Soc. Mass Spectrom.* **2014**, *25* (8), 1384–1393. https://doi.org/10.1007/s13361-014-0909-9.

(49) Gabellca, V.; De Pauw, E. Internal Energy and Fragmentation of Ions Produced in Electrospray Sources.

Mass Spectrom. Rev. **2005**, *24* (4), 566–587. https://doi.org/10.1002/mas.20027.

(50) Jarrold, M. F. Unfolding, Refolding, and Hydration of Proteins in the Gas Phase. *Acc. Chem. Res.* **1999**, *32* (4), 360–367. https://doi.org/10.1021/ar960081x.

(51) May, J. C.; Jurneczko, E.; Stow, S. M.; Kratochvil, I.; Kalkhof, S.; McLean, J. A. Conformational Landscapes of Ubiquitin, Cytochrome c, and Myoglobin: Uniform Field Ion Mobility Measurements in Helium and Nitrogen Drift Gas. *Int. J. Mass Spectrom.* **2017**, 1–16. https://doi.org/10.1016/j.ijms.2017.09.014.

(52) Beveridge, R.; Covill, S.; Pacholarz, K. J.; Kalapothakis, J. M. D.; Macphee, C. E.; Barran, P. E. A Mass-Spectrometry-Based Framework to Define the Extent of Disorder in Proteins. *Anal. Chem.* **2014**, *86* (22), 10979–10991. https://doi.org/10.1021/ac5027435.

(53) Valentine, S. J.; Counterman, A. E.; Clemmer, D. E. A Database of 660 Peptide Ion Cross Sections: Use of Intrinsic Size Parameters for Bona Fide Predictions of Cross Sections. *J. Am. Soc. Mass Spectrom.* **1999**, *10* (11), 1188–1211. https://doi.org/10.1016/S1044-0305(99)00079-3.

(54) Niu, S.; Ruotolo, B. T. Collisional Unfolding of Multiprotein Complexes Reveals Cooperative Stabilization upon Ligand Binding. *Protein Sci.* **2015**, *24* (8), 1272–1281. https://doi.org/10.1002/pro.2699.

(55) Zhao, Y.; Singh, A.; Xu, Y.; Zong, C.; Zhang, F.; Boons, G. J.; Liu, J.; Linhardt, R. J.; Woods, R. J.; Amster, I. J. Gas-Phase Analysis of the Complex of Fibroblast GrowthFactor 1 with Heparan Sulfate: A Traveling Wave Ion Mobility Spectrometry (TWIMS) and Molecular Modeling Study. *J. Am. Soc. Mass Spectrom.* **2017**, *28* (1), 96–109. https://doi.org/10.1007/s13361-016-1496-8.

(56) Light-Wahl, K. J.; Schwartz, B. L.; Smith, R. D. Observation of the Noncovalent Quaternary Associations of Proteins by Electrospray Ionization Mass Spectrometry. *J. Am. Chem. Soc.* **1994**, *116* (12), 5271–5278. https://doi.org/10.1021/ja00091a035.

(57) Ruotolo, B. T.; Hyung, S. J.; Robinson, P. M.; Giles, K.; Bateman, R. H.; Robinson, C. V. Ion Mobility-Mass Spectrometry Reveals Long-Lived, Unfolded Intermediates in the Dissociation of Protein Complexes. *Angew. Chemie - Int. Ed.* **2007**, *46* (42), 8001–8004. https://doi.org/10.1002/anie.200702161.

(58) Allen, S. J.; Bush, M. F. Radio-Frequency (Rf) Confinement in Ion Mobility Spectrometry: Apparent Mobilities and Effective Temperatures. *J. Am. Soc. Mass Spectrom.* **2016**, *27* (12), 2054–2063. https://doi.org/10.1007/s13361-016-1479-9.

(59) Han, L.; Ruotolo, B. T. Traveling-Wave Ion Mobility-Mass Spectrometry Reveals Additional Mechanistic Details in the Stabilization of Protein Complex Ions through Tuned Salt Additives. *Int. J. Ion Mobil. Spectrom.* **2013**, *16* (1), 41–50. https://doi.org/10.1007/s12127-013-0121-9.

(60) Badman, E. R.; Hoaglund-Hyzer, C. S.; Clemmer, D. E. Monitoring Structural Changes of Proteins in an Ion Trap over 10 - 200 Ms: Unfolding Transitions in Cytochrome c Ions. *Anal. Chem.* **2001**, *73* (24), 6000–6007.

(61) Zhao, Q.; Schieffer, G. M.; Soyk, M. W.; Anderson, T. J.; Houk, R. S.; Badman, E. R. Effects of Ion/Ion Proton Transfer Reactions on Conformation of Gas-Phase Cytochrome c Ions. *J. Am. Soc. Mass Spectrom.* **2010**, *21* (7), 1208–1217. https://doi.org/10.1016/j.jasms.2010.03.032.

(62) Ujma, J.; Giles, K.; Morris, M.; Barran, P. E. New High Resolution Ion Mobility Mass Spectrometer

Capable of Measurements of Collision Cross Sections from 150 to 520 K. *Anal. Chem.* **2016**, *88* (19), 9469–9478. https://doi.org/10.1021/acs.analchem.6b01812.

(63) Pacholarz, K. J.; Barran, P. E. Distinguishing Loss of Structure from Subunit Dissociation for Protein Complexes with Variable Temperature Ion Mobility Mass Spectrometry. *Anal. Chem.* **2015**, *87* (12), 6271–6279. https://doi.org/10.1021/acs.analchem.5b01063.

(64) Allen, S. J.; Eaton, R. M.; Bush, M. F. Analysis of Native-Like Ions Using Structures for Lossless Ion Manipulations. *Anal. Chem.* **2016**, *88* (18), 9118–9126. https://doi.org/10.1021/acs.analchem.6b02089.

(65) Sun, Y.; Vahidi, S.; Sowole, M. A.; Konermann, L. Protein Structural Studies by Traveling Wave Ion Mobility Spectrometry: A Critical Look at Electrospray Sources and Calibration Issues. *J. Am. Soc. Mass Spectrom.* **2016**, *27* (1), 31–40. https://doi.org/10.1007/s13361-015-1244-5.

(66) Jhingree, J. R.; Beveridge, R.; Dickinson, E. R.; Williams, J. P.; Brown, J. M.; Bellina, B.; Barran, P. E. Electron Transfer with No Dissociation Ion Mobility–Mass Spectrometry (ETnoD IM-MS). The Effect of Charge Reduction on Protein Conformation. *Int. J. Mass Spectrom.* **2017**, *413*, 43–51. https://doi.org/10.1016/j.ijms.2016.08.006.

(67) Henderson, S. C.; Li, J.; Counterman, A. E.; Clemmer, D. E. Intrinsic Size Parameters for Val, Ile, Leu, Gln, Thr, Phe, and Trp Residues from Ion Mobility Measurements of Polyamino Acid Ions. *J. Phys. Chem. B* **1999**, *103*, 8780–8785. https://doi.org/10.1021/jp991783h.

(68) Bush, M. F.; Campuzano, I. D. G.; Robinson, C. V. Ion Mobility Mass Spectrometry of Peptide Ions: Effects of Drift Gas and Calibration Strategies. *Anal. Chem.* **2012**, *84* (16), 7124–7130. https://doi.org/10.1021/ac3014498.

(69) Baker, E. S.; Clowers, B. H.; Li, F.; Tang, K.; Tolmachev, A. V.; Prior, D. C.; Belov, M. E.; Smith, R. D. Ion Mobility Spectrometry-Mass Spectrometry Performance Using Electrodynamic Ion Funnels and Elevated Drift Gas Pressures. *J. Am. Soc. Mass Spectrom.* **2007**, *18* (7), 1176–1187. https://doi.org/10.1016/j.jasms.2007.03.031.

(70) Liu, Y.; Valentine, S. J.; Clemmer, D. E. (unpublished results) http://www.indiana.edu/~clemmer.

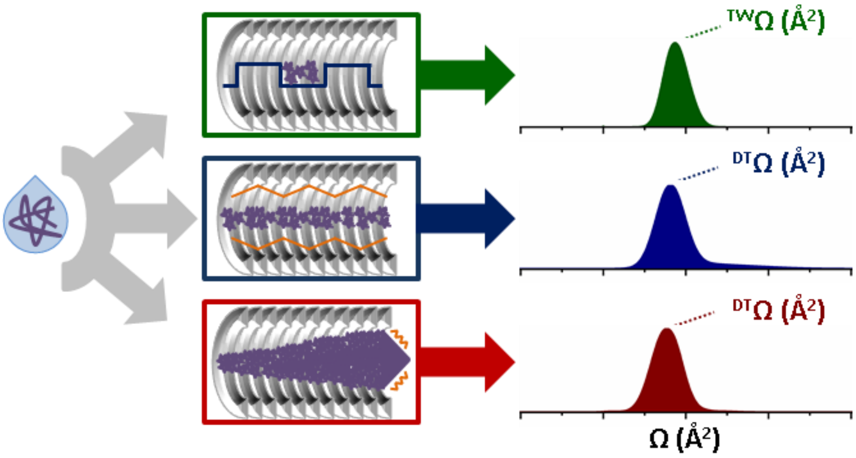

For TOC only

Using Collision Cross Section Distributions to Assess the Distribution of Collision Cross Section Values

Aidan P. France, Lukasz G. Migas, Eleanor Sinclair, Bruno Bellina and Perdita E. Barran*

Michael Barber Centre for Collaborative Mass Spectrometry, Manchester Institute of Biotechnology and Photon Science Institute, University of Manchester, 131 Princess Street, Manchester, M1 7DN, UK

Careful transfer of ions into the gas-phase permits the measurement of protein structures, with ion mobility-mass spectrometry, which provides shape and stoichiometry information. Collision cross sections (CCS) can be obtained from measurements made of the ions mobility through a given gas, and such structural information once obtained should also permit inter-lab comparisons. However, until recently there was not a recommended standard form for the reporting of such measurements. In this study we explore the use of collision cross section distributions to allow comparisons of IM-MS data for commonly analysed proteins. We present measurements from seven proteins across three IM-MS configurations, namely an Agilent 6560 IMQToF, a Waters Synapt G2 possessing a TWIMS cell and a modified Synapt G2 possessing an RF confining linear field drift cell. Mobility measurements were taken using He and N_2 as the drift gases. To aid comparability across instruments and best assess the corresponding gas-phase conformational landscapes of the protein 'standards', we present the data in the form of averaged CCS distributions. For experiments carried out in N_2, CCS values for the most compact ion conformations have an inter-instrument variability of $\leq 3\%$, and the total CCS distributions are generally similar across platforms. For experiments carried out in He, we observe the total CCS distributions to follow the same trend as observed in N_2, whilst CCS for the most compact ion conformations sampled on the 6560 are systematically smaller by up to 10% than those observed on the G2. The calibration procedure (for TWIMS) yields ^{TW}CCS for native-like proteins which are largely similar to those obtained on DTIMS instruments. We collate previously reported values of CCS for these proteins in the form of histograms which bear a remarkable similarity to the CCS distributions, reflecting the conformational heterogeneity of proteins and also how conformer populations can be altered on transfer from solution to the detector. This gives concern for some caution when calibrating sample protein drift times simply with single numeric CCS values.

1. Background & Motivation

Ion mobility spectrometry (IMS) coupled with mass spectrometry (IM-MS) permits the characterisation of an ions structure from its mobility in a gas (IM) as well as providing its mass (MS).[1] IM-MS is established as a method to determine structure, and under gentle ionisation conditions ESI can produce ions which retain aspects of their solution-phase structure.[2,3] IM-MS approaches have been exploited to permit the structural and functional characterisation of many types of biomolecules, including peptides;[4] small monomeric proteins;[5,6] cytosolic and membrane-bound protein complexes;[7,8] protein-protein and protein-ligand interactions;[9,10] Nucleic acids[11,12] and amyloidogenic proteins.[13,14] Regardless of the molecular species to be analysed, there are features or constraints that are common to all IM-MS experiments. These have recently been well outlined for all the predominant forms of IM-MS.[15] Protein measurements have in the main utilised a form of ion mobility which can be generally described by a common process. Within this process, packets of ions are focussed to traverse a drift cell filled with an inert buffer gas at a known temperature and pressure (1mbar to atmospheric), whereby weak electric fields act to axially propel them through a drift cell/region. As they traverse this gas-filled cell, the "frictional" force of gas-ion collisional events retards their motion, thus permitting the temporal separation of ions based upon their size, shape and charge.[16] IM-MS experiments record the arrival time (t_A) of m/z selected ions and this data can be used to determine their rotationally averaged collision cross sections (CCS).[17] As part of a wide community effort Gabelica and co-authors recently recommended how to report IM-MS measurements to better facilitate inter-lab comparability and in this study we take this as the basis by which we can compare the data obtained on well-studied proteins.[15]

In so-called, 'native' mass spectrometry experiments, a protein of interest is infused from an aqueous solution, containing volatile salts such as ammonium acetate, buffered to appropriate physiological pHs (~6-8).[18] In order to retain solvated structures *in vacuo*, careful optimisation of source parameters is necessary to minimise collisional heating and subsequent structural rearrangement.[19] Such effects can also occur on the injection of desolvated ions into the drift tube.[20] Foundational studies from Clemmer and Jarrold demonstrated that minimising the energy of ions prior to IM separation permits the retention of native-like conformations for the monomeric proteins ubiquitin and cytochrome c.[5,21] In addition, Williams and Russell, using a 2nd generation Waters Synapt G2 ion mobility-mass spectrometer, demonstrated how voltages and trapping conditions prior to the drift cell can substantially affect the conformational landscapes of ubiquitin and metallothionein-2A.[19,22] Furthermore, Gabelica *et al.* defined tuning parameters on an Agilent 6560 IMQToF which allowed the preservation of a compact so-called "N state" of ubiquitin as well as the ammonium-bound states of a fragile nucleic acid complex.[23] Such efforts to establish optimal gentle transfer of biomolecules *via* careful tuning of ion optics across homemade and commercially available IM-MS instruments, have been used to support arguments about the preservation of solution-like biomolecular structures *in vacuo*, although it is evident that the ESI process and solution conditions are also integral.

Despite the body of work that reports the conditions required to 'least perturb' the structure of proteins for IM-MS measurements, there has been less focus on the reproducibility of CCS, with exceptions being studies on small biomolecule CCS on single vendor platforms.[24–26] To our knowledge, there have only been a handful of publications in which protein CCS have been compared across different platforms,[27,28] and none of these studies have employed the use of CCS distributions to probe the conformational landscape of the systems under analysis. Visualising these ion conformational landscapes for malleable systems has great utility in defining optimal tuning parameters for native IM-MS experiments and as such, is commonly employed within many labs including our own.

In this study we establish "starting point" operational parameters which minimise the gas-phase activation of proteins across three instrumental platforms. We report CCS/CCS distributions across three ion mobility-mass spectrometers: the Synapt G2 (TWIMS & RF DTIMS configurations) and the Agilent 6560, in helium and nitrogen drift gases, to ascertain the degree of differentiation between protein structures sampled across different IM-MS platforms under "soft" tuning conditions. In addition, we provide interactive representations of CCS distributions to augment traditionally numerical CCS datasets. Furthermore, we present global CCS histogram distributions for compiled literature CCS for our chosen systems, in order to facilitate a better understanding of where individual "native IM-MS" CCS lie relative to previously published values.

2. Methods and Materials

2.1. Sample preparation and ionisation

Seven commercially available proteins were used. The preparation of samples, their identities, sources, suppliers, catalogue numbers and final solution conditions are detailed in SI 1.1-1.2, Table S1 & Figure S1.

2.2 Ion Mobility Mass Spectrometry Measurements

Ion mobility mass spectrometry data was acquired on each of the three platforms (See SI 2.1-2.3, Figures S2-5 for more information). Acquisition conditions to obtain arrival time distributions (across platforms), and pressure differential optimisation (for the Agilent 6560 IMQToF) are available in the supplementary dataset (Tables S2-7).

2.3. Data Analysis and CCS distribution production

All experimental data obtained from the Synapt G2 (with either TWIMS/DTIMS configurations) was analysed using MassLynx V4.1 software (Waters, UK). Arrival time distributions (ATDs) encompassing a drift time axis (x-axis) and an associated ion intensity axis (y-axis) were extracted for the desired *m/z* region (Figure 1. ii). The drift time axis was transformed to a CCS axis by employing suitable calibrant ions (Table S8 and supplementary calibrant data set) following an approach described previously for TWIMS,[7,29,30] or using the stepped field-method for DTIMS (Figure 1a & b iii & iv).[16,31] Data acquired on the 6560 IMQToF was analysed using MassHunter IM-MS Browser software (Agilent). Drift times and their corresponding ion intensities were extracted for the desired *m/z* regions (Figure 1b. ii), as for data acquired on the Synapt G2. The MassHunter IM-MS browser records all IMS parameters, these can then be extracted and applied to the Mason-Schamp equation to convert the x-axis from drift time to CCS units (Figure 1b. iii & iv). Each replicate yields a single CCS distribution plot with slightly different x-axis CCS binning increments (due to different A and X values from TWIMS experiments and different dead times in DTIMS experimental replicates) (Figure 1b. iv.).

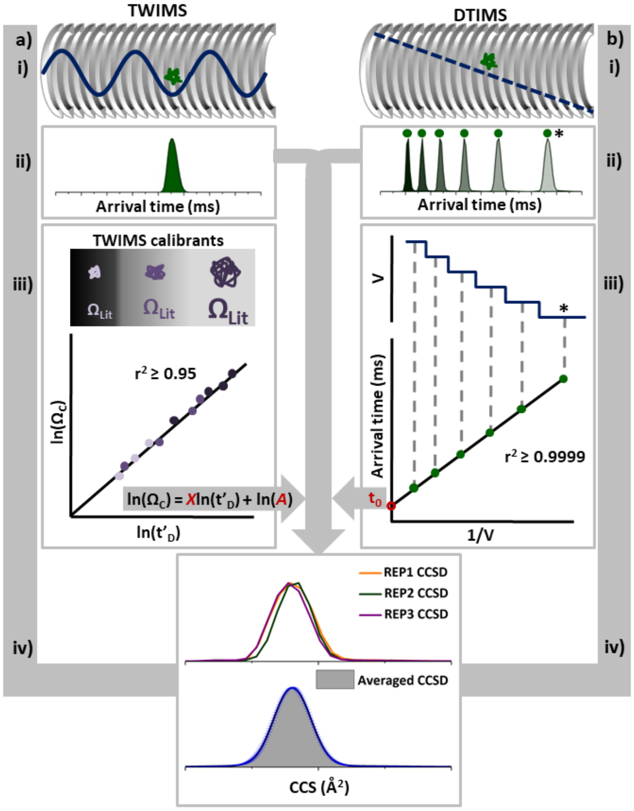

Figure 1. Schematic showing how a) TWIMS & b) DTIMS data yields averaged ion CCS and CCS distributions. i) Schema for the trajectories of ions in each type of IM experiment. ii) Example ATDs required to determine CCS distributions. For DTIMS data (RHS) the ATD corresponding to the lowest DV is marked by (*). iii) LHS: Drift times from calibrant ions with previously measured ^{DT}CCS which bracket the mass of the ion of interest are corrected for their charge, time spent outside the drift cell post IM and reduced mass, yielding a plot that converts experimental corrected drift times (t'_D) to CCS (Ω_C). From the plot of $\ln(\Omega_C)$ vs $\ln(t'_D)$, the exponential factor (X) and fit-determined constant (A) can be obtained for conversion of ATDs into CCS distributions. RHS: The arrival time apex of ions obtained from each DV are plotted against a reciprocal of the DVs (1/V), where the y-intercept of this plot yields the ion 'dead time' (t_0), which is the time spent outside of the drift cell. Additionally, the slope of the plot represents the ions mobility. iv) CCS axes are not the same across CCS distribution replicates, so interpolation of the data yields an averaged CCS distribution wherein error bars (blue halo) represent the deviation between replicates.

In order to produce averaged CCS distribution plots from individual CCS distribution replicates, Gaussian fits were made to the experimental data using a consistent number of data points (e.g. 1000) across a fixed CCS range (e.g. 2500-4500 Å^2) (See SI 3). After fitting all CCS distribution replicates for a single ion across the same CCS range and number of data points, the average CCS distribution plot was constructed as follows: 1) The range employed for the CCS distribution replicates was extracted and used to form the x-axis of the averaged CCS distribution plot. 2) The ion intensity across the CCS range of each replicate was averaged whereby standard deviations denote the variation between replicates. 3) The constructed x-axis, y-axis and y-axis standard deviation were combined to obtain averaged CCS distributions (Figure 1b. iv. Bottom). Ion CCS were obtained *via* averaging apex values from Gaussian fitted CCS distribution replicates. Associated CCS errors (±) came from the standard deviation of these values. Total CCS distribution plots for proteins were obtained by combining averaged ion CCS distribution plots (normalised for mass spectral peak intensity and CCS distribution area). All CCS distributions produced within this study were constructed using OriginPro 2015/2017 software. The width of an ATD for a rigid ion is comprised of the longitudinal diffusion of the ion pulse in the drift cell as well as other instrumental factors, as described by Marchand *et al.* [32], for more flexible molecules it may be comprised of several unresolved conformers and also may indicate conformational dynamics on the timescale of the experiment.

2.4. Interactive figures

A number of main text and SI figures presented in this article were recreated in an interactive format to enable in-depth interrogation of the presented results. These are deposited online at https://france-ccs-2019.netlify.com/. The interactive figures were created using ORIGAMI$^{\text{ANALYSE}}$ and require the use of a modern internet browser and access to the internet.[33]

3. Results and Discussion

3.1 Tuning ion transmission to preserve structure

Native IM-MS workflows are dependent upon the solvation of biomolecules within non-denaturing, MS compatible solutions which adequately reflect the electrolytic milieu of the cell.[18,34,35] Accordingly, aqueous ammonium acetate adjusted to pH ~7 is the most commonly employed solution for native IM-MS experiments. In order to sample macromolecular structures which most closely resemble those found in physiological solutions, IM-MS instrumentation has to be carefully tuned so as to reduce lab frame energies and in turn, ion internal energies (E_{int}) which promote gas-phase restructuring.[19] Perturbations in protein conformation, *via* ion heating, often have minimal effects upon the observed CSD (Figure 2 insets);[19] as a result, structural conclusions derived solely from protein charge state signatures (i.e CSDs) observed *via* native MS should be addressed with caution.[36,37] To ascertain the degree to which a set of instrument parameters promote ion activation, we use the observed ATD of selected proteins as a measure of transmission 'softness', analogous to the use of fragments from thermometer ions.[22,38,39] Given this approach, suitable ions are those with a well-documented "native" globular state and defined unfolding pathway previously observed with IM-MS. Accordingly, we recommend the [Ubiquitin+6H]$^{6+}$ and [Cytochrome c+7H]$^{7+}$ (Figure 2) ions as suitable.

Post ionisation, optimisation for 'soft' ion transmission is dependent upon: 1) the reduction of accelerating voltages and 2) the modulation of gas pressures, both of which act in synergy to minimise the energy of ion-neutral collisions. In the instance where desirable 'soft' tuning has been achieved, the ATD of the thermometer ion (cytochrome c 7+ in this instance) should present with a comparatively narrow, Gaussian-like peak (indicative of a single conformational population) observed at low arrival times (Figure 2, Top). These observations would likely point to the retention of a folded form of the protein which effectively is a dehydrated solution-phase structure; this hypothesis can be confirmed *via* CCS determination.[40] The associated mass spectrum (Figure 2, Top, inset) presents with a dominant 7+ peak and a small amount of the 6+ ion. This mass spectrum is typical for cytochrome c sprayed from non-denaturing solutions.[41] Critical to our workflow is the observation that when certain ions undergo collisional heating, they first anneal into highly collapsed structures prior to unfolding. These collapsed structures will present in much the same manner as the native-like dehydrated ion, except with lower CCS values. Subsequently, in situations where gas-phase annealing to collapsed structures is suspected, it is instructive to compare the associated CCS with those found within the literature.[42]

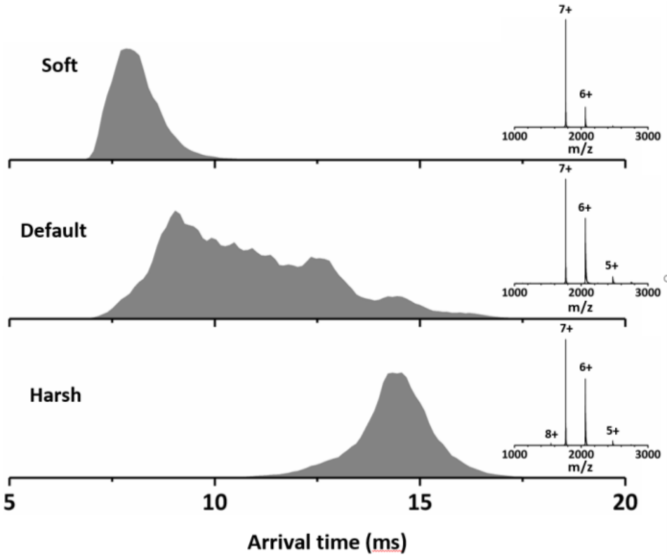

Figure 2. IM conformational landscapes of the [cytochrome c +7H]$^{7+}$ ion obtained from the Synapt G2 (TWIMS) under different tuning conditions. Top) 'soft' settings. Middle) 'Default' settings. Bottom) 'Harsh' settings. Insets) Mass spectra corresponding to each set of tuning conditions.

For many commercial mass spectrometers, the default settings employ greater accelerating voltages in tandem with gas pressures which permit increased gains in ion transmission (~5 fold) and detection efficiency. Often these gains in signal intensity are concomitant with a reduction in salt adducts (observed *via* MS). Under 'default' settings a given flexible ion may undergo a degree of gas-phase restructuring, typically yielding more complicated ATDs (Figure 2, Middle). Interestingly, within the corresponding MS (Figure 2, Middle, Inset), we observe a slight increase in the relative abundance of lower charge states (6 & 5+) when compared to the soft tune, perhaps attributable to the loss of counterions. If accelerating potentials within the instrument are increased further still, then the intermediary conformations largely re-organise to an extended gas-phase form which tends to have one conformer.[5,43] This capability to manipulate the structure of a given ion *in vacuo* is exploited in activated ion mobility (aIM)/ collision-induced unfolding (CIU) experiments, which describe the gas-phase restructuring of an ion, often induced by high energy gas-ion collisions, monitored *via* IM-MS.[33,40] aIM/CIU has long played a pivotal role in the interrogation of protein unfolding mechanisms as well as the effect of ligand/co-factor binding upon protein stability.[44,45] Gas phase unfolding of ions within the G2 instrument can be facilitated by raising the trap bias DC and/or the trap CE (as with aIM experiments), which increases the potential difference between the trap and IM region thus effectively imbuing ions with greater kinetic energies as they enter the IM cell (Figure S2b). Even for stable protein complexes, for example the tetrameric alcohol dehydrogenase, large potential differences applied between the trap and IM regions result in individual subunit unfolding (Figure 3a) prior to the ejection of highly charged monomers.[46,47] When modulating the trap bias DC, it is crucial that a compromise between 'softness' and signal intensity is struck, as this parameter significantly effects ion transmission. For the Synapt G2 (DTIMS configuration), we also found the trap wave height (WH) to have an observable impact upon the conformational landscape sampled for monomeric protein ions. We believe this effect to be due to the increased kinetic energy imparted upon ions within the trap when higher trap WHs are employed. Interestingly, we did not observe this effect on the Synapt G2 (TWIMS configuration). In agreement with Williams *et al.* we did not observe TWIMS wave velocity or wave height to have any observable effect upon the conformational landscape sampled for any of the ions analysed.[22] Voltages at the beginning of the IM cell, namely the IMS entrance voltage and the He cell DC (Figure 3a), were also observed to have a 'fine tuning' effect upon the observed ion ATD (for monomeric proteins), with the latter only impacting the ATD when the G2 was configured for TWIMS. In contrast to the aforementioned pre-IM DC voltages, variation of RF voltages within both instrument configurations were not observed to have any significant effects upon ion ATDs, although they did have a notable impact upon ion transmission.[48] To offset reductions in ion transmission which occur under native IM-MS settings, the IM bias DC, transfer CE and transfer wave velocity can be raised. Increasing the IM bias DC and/or the transfer CE, raises the potential energy difference between the IM and transfer region and thus raises ion kinetic energies post-IMS (Figure S2b).

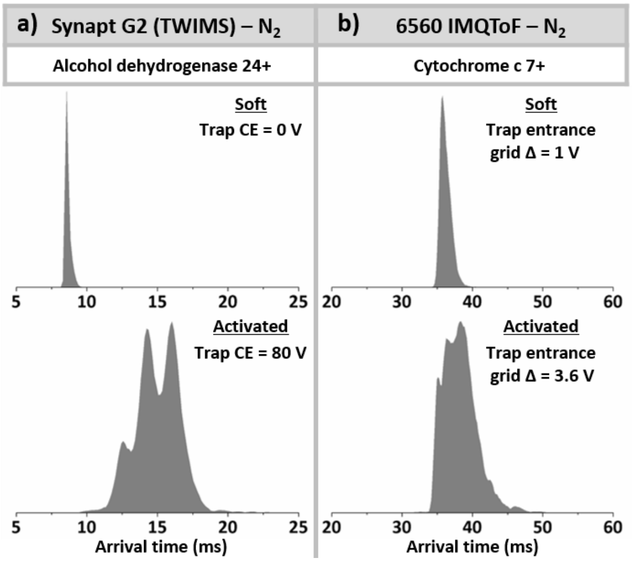

Figure 3. The use of alcohol dehydrogenase and cytochrome c to illustrate the effect of altering instrument parameters a) [Alcohol dehydrogenase + 24H]$^{24+}$, Synapt G2, Top) soft tuning, whereby no trap collision energy is applied. Bottom) activating tuning: trap collision energy has been raised to 80 V. b) [Cytochrome c + 7H]$^{7+}$ 6560 IMQToF, Top) soft tuning parameters: gating height of the trap entrance is +1V. Bottom) using activating tuning parameters: whereby the gating height of the trap entrance is +3.6V.

Optimisation of these three parameters permit favourable gains in ion transmission concomitant with the dissociation of non-volatile salt adducts.

Tuning for 'soft' ion transmission on the Agilent 6560 IMQToF, like the Synapt G2, is largely dependent upon the application of voltages within the trapping region. Most importantly the trap entrance grid delta, which is the potential difference between the trap during filling (low) and during storage and release (high), had a significant effect upon ion activation. This effect was most notable for small monomeric proteins such as cytochrome c (Figure 3b) and was in corroboration with findings from Gabelica *et al*.[23]. Unlike the Synapt G2, we observed tuning of the RF voltages within the 6560 to have a noticeable effect upon ion activation. The most significant of these was the trapping funnel RF which acts to radially confine ions within the trapping funnel prior to gating into the IM cell. In contrast to Gabelica *et al*. and Mclean *et al*., we found that maintaining the trap DC voltages employed across both N_2 and He drift gases (Table S7) did not yield any observable differences in protein conformation (See Figures S7-20, LHS column).[23,41] Within the source region of the instrument we observed minor effects on the conformation of monomeric proteins when the fragmentor voltage, was altered within the 300-400 V range. Lower fragmentor voltages led to losses in signal transmission without gains in transmission 'softness', whilst higher fragmentor voltages did not permit gains in signal intensity yet began to promote ion activation.[23]

3.2 Assessing inter-instrument variation in the CCS distributions for proteins and protein complexes

After 'soft' ion transmission parameters were defined across the three instrumental platforms, we focused upon IM-MS analysis of a range of protein analytes that are well studied and readily available (Table S1). We sought to compare analyte gas-phase CCS distributions, utilising He and N_2 as drift gases, across instruments (Figure S7-20). Figure 4 compares the data obtained for tetrameric concanavalin a with cytochrome c. Concanavalin a presents with a CSD centring on the 20+ species and a Δz of ~5 (although the charge states at either end of the CSD are often barely visible, Figure S17). Across all three instruments, the CCS distributions for the tetrameric species of concanavalin a largely present as unimodal Gaussian-like peaks which yield CCS_{He} values (replicable to within ~0.5%) that differ by ~0.1-0.9% across charge states and <2% across instruments (when comparing like charge states). Our findings suggest that we are probably sampling a single conformational population which is retained across the charge states analysed, as might be expected for a well-structured protein complex. The only exception to this is the [M+22H]$^{22+}$ species which presents as a bimodal CCS distribution with a larger conformer observed at ~6300 Å^2 (Figure S17). Previous aIM experiments on concanavalin a showed a larger species with a drift time which was ~25% higher than the structure sampled prior to activation.[33,49] Regarding the CCS distributions for concanavalin a analysed in He, the charge states sampled on a given instrument possess almost identical CCS peak widths (with the exception of the 19+ species sampled on the 6560 which is notably narrower) (Figure S17).

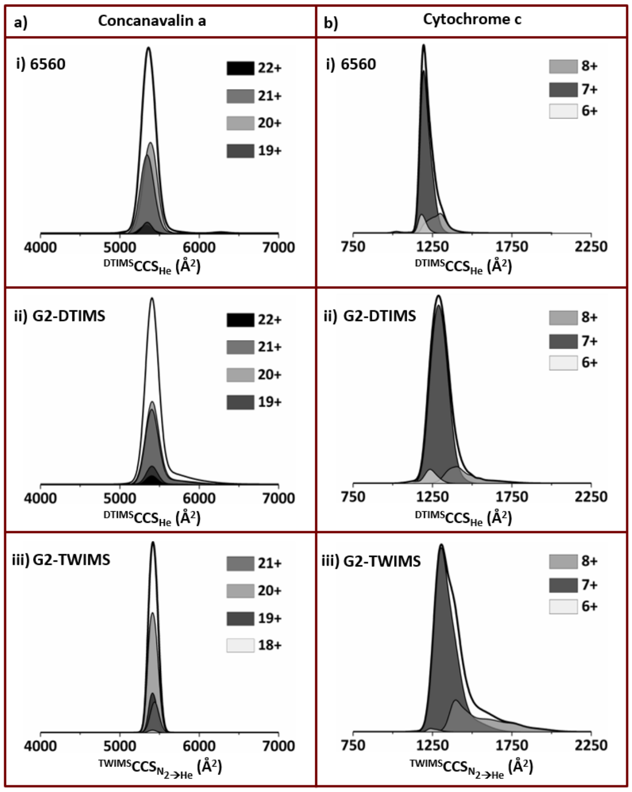

Helium CCS values (Å²) across all platforms

Concanavalin a			
Z	6560	G2-DTIMS	G2-TWIMS
18	-	-	5412 ± 16
19	5340 ± 15	5399 ± 2	5409 ± 8
20	5384 ± 20	5397 ± 1	5412 ± 14
21	5345 ± 29	5401 ± 1	5434 ± 18
22	5335 ± 23 6285 ± 24	5405 ± 1	-

Cytochrome c			
Z	6560	G2-DTIMS	G2-TWIMS
6	1182 ± 4	1234 ± 5	1238 ± 6
7	1196 ± 1	1286 ± 12	1304 ± 6
8	1258 ± 19 1297 ± 2	1373 ± 34 1540 ± 17	1399 ± 6 1625 ± 11 1768 ± 6 1918 ± 12

Figure 4. Total CCS distributions for a flexible protein and rigid protein complex obtained across all instrumental platforms utilised within this study with helium as the drift gas. a) Total CCS distributions obtained when analysing monomeric cytochrome c using parameters tuned for native IM-MS on the i) Agilent 6560 IMQToF, ii) Synapt G2 (DTIMS) and iii) Synapt G2 (TWIMS). b) Total CCS distributions obtained when analysing tetrameric concanavalin a using parameters tuned for native IM-MS on the i) Agilent 6560 IMQToF, ii) Synapt G2 (DTIMS) and iii) Synapt G2 (TWIMS). The total CCS distribution trace encompassing the averaged CCS distributions for each analyte charge state are represented by the thick black lines. The colours of the CCS distributions for each charge state observed correspond to the key at the RHS of each total CCS distribution. The table underneath the total CCS distributions gives the average CCS_{He} values obtained for the observed conformations of concanavalin a (LHS) and cytochrome c (RHS) across the three instrumental configurations employed.

However, across instruments there are observable differences in CCS distribution width. Most notably the CCS distributions obtained from the G2 (TWIMS), both for $N_2 \rightarrow He$ (Figure S17) and N_2 (Figure S18) are ~50% narrower than the corresponding CCS distributions obtained from the 6560 and G2 (DTIMS) respectively, which themselves are very similar to one another (Figure 4a). With nitrogen as the drift gas, we observe predominantly unimodal Gaussian-like CCS distributions (as in He) but with CCS (replicable to within ~0.5%) that differ more significantly across charge states (~0.9-4.3%) but not instruments (<2%) (Figure S18). For clarity, we have provided representative raw ATDs to show the unprocessed gas-phase conformational landscapes we observe by IM in both He (Figure S21) and N_2 (Figure S22), within this study. The most notable variation across CCS_{N_2} values is observed on the G2-TWIMS, where the highest charge state (21+) is ~4.3% bigger than the lowest charge state (18+). This difference is most likely due to the Ω_{Lit} values employed for the $^{TW}CCS_{N_2}$ calibration procedure. In accordance with this hypothesis, a significantly smaller CCS variation across charge states is observed (~0.5%) for the same raw data set calibrated to yield $^{TW}CCS_{N_2 \rightarrow He}$ values. In contrast, the range of CCS_{N_2} values obtained for concanavalin a on the G2 (DTIMS) and 6560 do not vary to the same degree, at ~1.7 and 0.9% respectively.

Cytochrome c also presents as a narrow CSD, with a Δz = 2-3, centring on the $[M+7H]^{7+}$ species (Figure 2 and Figure S9). Across all three instruments, the ATDs for the $[M+6H]^{6+}$ are bimodal, but here the small earlier arriving species can be assigned to a concentration specific coincident dimer whilst the $[M+7H]^{7+}$ ATD is unimodal. Slight tailing toward higher CCS is observed for the $[M+6H]^{6+}$ on the G2 (TWIMS) and the 7+ ion analysed on the 6560 and G2. The CCS distribution of the 7+ ion analysed on the G2 is comparatively broad (Figure 4 & Figure S9). This tailing and broader CCS distribution (7+, G2) may be indicative of a lowly populated, partially unfolded conformer which we were unable to resolve. In contrast to the highest charge states of concanavalin a, the 8+ species of cytochrome c when sampled on the G2 presents as a broad unresolved peak with one dominant, partially resolved apex with a notable tail. This tail likely constitutes numerous unresolved, closely related intermediate conformations resulting from differing degrees of structural activation. The 8+ ion sampled on the 6560 presents as a far narrower, albeit partially resolved peak with minimal tailing. This finding is consistent with what is observed for the highest charge states of the other small proteins (Figure S7-12) and suggests that transmission on the 6560 is softer than that observed on the G2 under the conditions we have employed. Across the three instruments, the CCS_{He} values for the most compact ion conformations observed vary by ~0.3-9%, with the variation rising with increasing charge (Figure 4 & Figure 5). However, most of this variation is due to the CCS_{He} values obtained on the 6560 which are ~4-9% smaller than those obtained on the G2 platform. When comparing CCS_{He} values obtained on the 6560 and G2 we observe the same trend (to differing degrees) for all analytes within this study, except for concanavalin a (Figure 5). Interestingly, the systematically lower CCS measured on the 6560 relative to the G2 are not observed with nitrogen as the drift gas (Figures S7-S20 & S23). Comparing the total CCS distribution plots for cytochrome c across the three instruments employed, we see that the CCS distribution widths, particularly for the 7+ and 8+ ion, are considerably wider on the G2 platform (~50%) than on the 6560. This finding is inconsistent with the total CCS distributions of concanavalin a, where the opposite is observed.

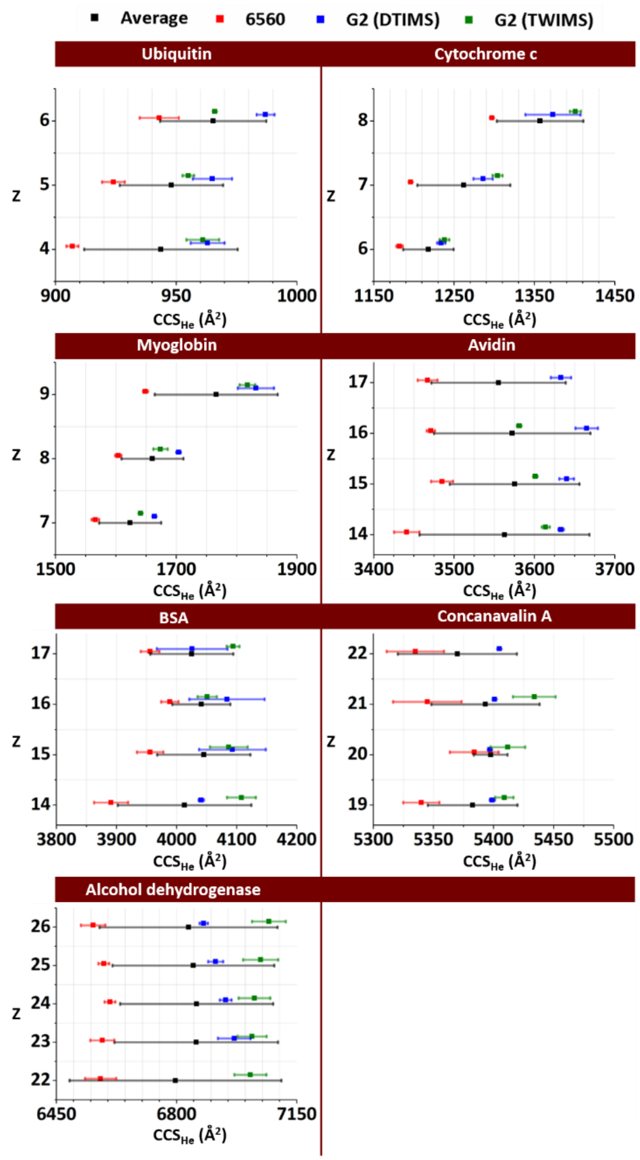

Figure 5. Range of CCS_{He} values obtained for the proteins analysed within this study. In all cases the CCS for the single most abundant conformation for each charge state was compared across the three instruments. The black, red, blue and green squares represent the average CCS_{He} values obtained for single conformations as an average across all the instruments, on the 6560, the G2 (DTIMS) and the G2 (TWIMS) respectively. The associated coloured bars show the standard deviation across the experimental replicates.

3.3 Comparisons with literature

In order to visualise the general spread of conformations for proteins/protein complexes across the literature, as well as this study (as discussed above), we have plotted all of the CCS values we could find, for all the analytes and their charge states observed in this study, as global CCS frequency histogram plots (see Figure 6 for cytochrome c [He & N_2] and Figures S24-35 for the other analytes). These plots, along with their associated tabulated CCS (Tables S9 & S10) may act as a guide for future native IM-MS analyses.

The smallest CCS_{He} values obtained for the 6+ and 7+ ions of cytochrome c within our study range from ~6% smaller to 5% larger than the most compact conformations sampled by Clemmer and co-workers on their 50.6 cm and 7.6 cm long drift tube instruments (Figure 6a & Table S9).[5,50,51] Additionally, our CCS_{He} values for the 6+ and 7+ ion range from ~7% smaller to 2% larger than those measured by Bush *et al*. on a modified Synapt G2 with an RF confining linear cell (Figure 6a & Table S9).[30,53]

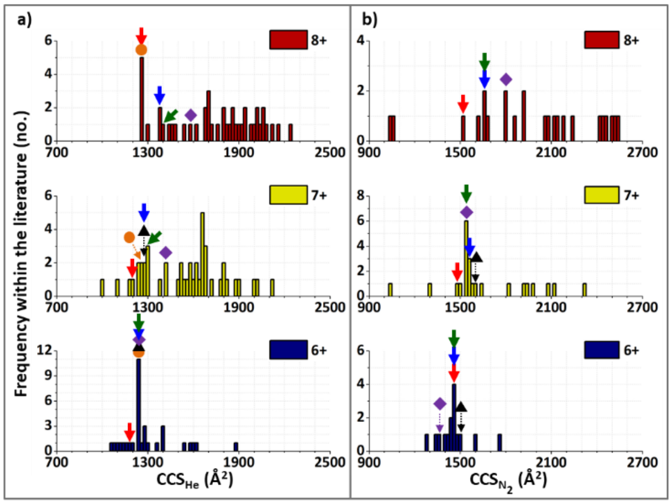

Figure 6. Global histogram plots of cytochrome c. a) Global CCS_{He} histogram plots, b) Global CCS_{N_2} histogram plots, for all the experimentally observed charge states of cytochrome c. Literature as well as our own experimentally obtained CCS values were grouped into 20 Å² bins, whereby the frequency of CCS to the nearest 20 Å² were summed and represented as solid bars within the histograms. Within these stacked histogram, blue, yellow and red bars represent the frequency and size of CCS for the 6+, 7+ and 8+ ions of cytochrome c respectively. Red, blue and green arrows represent the smallest CCS we obtained on the 6560, the G2 (DTIMS) and the G2 (TWIMS) respectively, whilst black triangles, orange circles, and purple diamonds represent the smallest literature CCS values from Clemmer *et al*., Bush *et al*. and McLean *et al*. respectively.[5,30,41,50–52]

Regarding the most compact conformations of the 8+ ion sampled on the G2, our CCS_{He} values range from ~9-12% larger than those reported by Clemmer (Figure 6a & Table S9), whilst the values obtained from the 6560 are <1% larger than the most compact conformation sampled by Clemmer (Figure 6a & Table S9).[5,50,51] Furthermore, our values for the most compact conformations of the 6+, 7+ and 8+ ions sampled across the three instruments range from 0-21% smaller than the most compact conformations sampled by Mclean *et al*. on a 6560 IMQToF (Figure 6a & Table S9).[41] Notably, our values on the 6560 in He, provide the largest source of variation when compared with literature.

The CCS_{He} values measured for concanavalin a within this study are in good agreement (~0.5-3% smaller) with those obtained on a modified Synapt G2 (RF confining linear cell) [30,53], and those measured on a home built VT-IM-MS instrument by Barran *et al*. (Figure S32 & Table S9).[54] In a separate study Barran *et al*. also recorded CCS, on a second home built IMQToF, ~8-18% smaller than those observed here (Figure S32 & Table S9).[42,55] Regarding the small body of published CCS_{N_2}, the values we have obtained are systematically smaller (~0.5-4%) than those reported by Bush and coworkers on a 1st and 2nd gen RF confining drift cell (Figure S33 & Table S10).[30,52]

When comparing our CCS_{N_2} values with those obtained in the literature, our values for the 6+ and 7+ ions of cytochrome c are systematically smaller than the most compact conformers obtained in a series of studies by Bush *et al*. (Figure 6b & Table

S10).[30,52] In comparison to values published by Mclean *et al.*, our smallest values obtained across the three instruments range from 5-13% smaller for the 8+, 4% smaller to 2% larger for the 7+ and 7-8% larger for the 6+ ion (Figure 6b & Table S10).[41] We reason that the most compact conformation measured for the 6+ ion by Mclean *et al*. may actually correspond to a *m/z* coincident dimer. If we discount this signal the most intense smallest conformer (on all platforms) has for us a CCS_{N_2}1460 Å^2 in close agreement with their published CCS_{N_2} value of 1477 ± 6 Å^2.[41] Accordingly, our values for the 6+ ion are <1-2% smaller than the values given for the most abundant conformer they observe, making it likely that this species is indeed the most compact accessible conformation of the 6+ ion. The above information, together with prior EHSS and PSA models (in He) for the native fold of cytochrome c, suggest that for the 6+, 7+ (on all instruments) and 8+ ion (measured on the 6560), we are sampling dehydrated, contracted, native-like structures of cytochrome c.[5,41,56] Regarding the 8+ species, the conformations sampled on the G2 likely represent different intermediates along the unfolding pathway toward more extended structures, as seen previously.[5,57] In contrast, concanavalin a does not show the same degree of charge/instrument dependent CCS distribution variation and CCS increase, likely due to strong inter and intra molecular interactions preserving the fold.

Across all of the proteins analysed, we present CCS_{N_2} values which are reproducible to within <3% across the 6560 and G2 (TWIMS and DTIMS) configurations. Similar variation was observed when comparing CCS_{He} values obtained across both configurations of the G2. However, CCS_{He} values derived from the Agilent 6560 proved significantly different from those obtained on the Synapt G2, with the (notable) exception of concanavalin a. If this difference in CCS was a result of applying an incorrect IM-Trap pressure Δ, then we would expect 1) The CCS_{He} values obtained for the monomorphic test systems utilised to be significantly different from their published values and 2) all of the CCS_{He} values to be systematically larger on the 6560 relative to the G2, as the drift cell would be contaminated with nitrogen gas (if the IM-Trap pressure Δ was too low), which would retard ion motion more than helium, leading to comparatively longer drift times and thus larger CCS.[41] Instead, at a Δ of ~0.13 Torr, we observe the CCS_{He} values for the monomorphic systems to be in close agreement with the average helium CCS derived from previously published data (<0.5%).[20,41,53,58–61] In addition, the CCS_{He} values for the analytes under test were systematically smaller than those observed on the G2, by an average of 4.3% and a maximum of ~10%.

Conclusion and Outlook

Native IM-MS is used to measure a host of proteins across many instrumental platforms. Within this study, we have shown that when parameters are tuned to minimise gas-phase activation *via* the employment of suitable thermometer ions, compact conformations and highly similar structural landscapes can be sampled across three common platforms. These findings in tandem with the body of literature for CCS_{He} values suggests that the instrument parameters employed on the 6560 (when operating in He) permit access to native-like dehydrated solution phase-like structures that are notably smaller than those obtained on the G2 as a result of "softer" pre-IMS conditions. When comparing our 6560 CCS_{He} values with the smallest values from the literature (Table S9), we observe that our values are not systematically smaller, and actually range from ~16% larger to 11% smaller than the smallest $^{DT}CCS_{He}$ values published. As such, we conclude that the smallest CCS_{He} values we observe on the 6560 are most probably dehydrated, native-like solution-phase structures sampled *in vacuo*. Regarding the difference between He and N_2 CCS values across instruments, we propose that the G2 platform facilitates more activation pre-IMS than the 6560, as shown previously by Camacho *et al*.[62]. With He as the drift gas, proteins injected into the IM cell likely undergo negligible annealing, and therefore retain a memory of the more activating source conditions thus leading to the discrepancy between instrument CCS_{He} for all but the most rigid proteins (Con A). However in N_2, injected proteins likely undergo partial annealing, due to collisions with the heavier N_2 atoms, yielding similar CCS_{N_2} across instruments.

Our findings in combination with the range of accessed CCS observed previously show that whilst careful tuning allows reproducible data to be obtained proteins/protein complexes are often conformationally flexible, dynamic structures which can easily undergo unintentional gas-phase restructuring. IM-MS is highly suited to the measurement of flexible systems, but they are less suitable as calibrants. A more ideal set of calibrants would be monomorphic and therefore impervious to gas-phase ion activation, unlike proteins. But similar to the protein 'standards', these calibrants would span a wide range of masses, mobilities, Δz's and effective densities. CCS distributions, or even raw ATDs provide more insights than single CCS values as to the relative population of a given conformer and should be reported along with CCS to allow comparability.

ASSOCIATED CONTENT

Supporting Information

The Supporting Information is available free of charge on the ACS Publications website. Detailed description of the experimental processes and complete CCS/CCS distributions of analytes as well as literature CCS histogram plots and associated tables.

AUTHOR INFORMATION

Corresponding Author

*Perdita Barran perdita.barran@manchester.ac.uk

Author Contributions

The experiments were carried out and the manuscript was written by APF. LGM constructed the online repository and provided advice alongside ES, BB & PEB. All authors edited the manuscript.

ACKNOWLEDGMENT

This research was supported by the BBSRC (awards: BB/L015048/1, BB/K017802/1 and BB/H013636/1 and the BBSRC/EPSRC-funded Manchester Synthetic Biology Research Centre, SYNBIOCHEM (BB/M017702/1)) and the EPSRC Future Biomanufacturing Research Hub EP/S01778X/1, and the Centre for Biocatalytic Manufacture of New Modalities (CBNM) EP/S005226/1. MRC, BBSRC, EPSRC, Waters Corp. Agilent and the Universities of Edinburgh and Manchester are thanked for their support of studentships to APF, LGM, and ES.

REFERENCES

1 D. Smith, T. Knapman, I. Campuzano, R. Malham, J. Berryman, S. Radford and A. Ashcroft, *Eur. J. Mass Spectrom.*, 2009, **15**, 113.

2 K. Breuker and F. W. McLafferty, *Proc. Natl. Acad. Sci.*, 2008, **105**, 18145–18152.

3 J. A. Silveira, K. L. Fort, D. Kim, K. A. Servage, N. A. Pierson,

D. E. Clemmer and D. H. Russell, *J. Am. Chem. Soc.*, 2013, 135, 19147–19153.

4 T. Wyttenbach, G. Von Helden and M. T. Bowers, *J. Am. Chem. Soc.*, 1996, **118**, 8355–8364.

5 K. B. Shelimov, D. E. Clemmer, R. R. Hudgins and M. F. Jarrold, *J. Am. Chem. Soc.*, 1997, **119**, 2240–2248.

6 T. Wyttenbach and M. T. Bowers, *J. Phys. Chem. B*, 2011, **115**, 12266–12275.

7 B. T. Ruotolo, J. L. P. Benesch, A. M. Sandercock, S.-J. Hyung and C. V Robinson, *Nat. Protoc.*, 2008, **3**, 1139–1152.

8 S. C. Wang, A. Politis, N. Di Bartolo, V. N. Bavro, S. J. Tucker, P. J. Booth, N. P. Barrera and C. V. Robinson, *J. Am. Chem. Soc.*, 2010, **132**, 15468–15470.

9 B. Schiffrin, A. N. Calabrese, P. W. A. Devine, S. A. Harris, A. E. Ashcroft, D. J. Brockwell and S. E. Radford, *Nat. Struct. Mol. Biol.*, 2016, **23**, 786–793.

10 R. Beveridge, L. G. L. G. L. G. Migas, K. A. P. P. K. A. P. Payne, N. S. N. S. Scrutton, D. Leys and P. E. P. E. Barran, *Nat. Commun.*, 2016, **7**, 12163.

11 E. S. Baker, S. L. Bernstein, V. Gabelica, E. De Pauw and M. T. Bowers, *Int. J. Mass Spectrom.*, 2006, **253**, 225–237.

12 V. Gabelica, E. S. Baker, M. P. Teulade-Fichou, E. De Pauw and M. T. Bowers, *J. Am. Chem. Soc.*, 2007, **129**, 895–904.

13 S. L. Bernstein, N. F. Dupuis, N. D. Lazo, T. Wyttenbach, M. M. Condron, G. Bitan, D. B. Teplow, J. E. Shea, B. T. Ruotolo, C. V. Robinson and M. T. Bowers, *Nat. Chem.*, 2009, **1**, 326–331.

14 N. F. Dupuis, C. Wu, J. E. Shea and M. T. Bowers, *J. Am. Chem. Soc.*, 2011, **133**, 7240–7243.

15 V. Gabelica, A. A. Shvartsburg, C. Afonso, P. Barran, J. L. P. Benesch, C. Bleiholder, M. T. Bowers, A. Bilbao, M. F. Bush, J. L. Campbell, I. D. G. Campuzano, T. Causon, B. H. Clowers, C. S. Creaser, E. De Pauw, J. Far, F. Fernandez-Lima, J. C. Fjeldsted, K. Giles, M. Groessl, C. J. Hogan, S. Hann, H. I. Kim, R. T. Kurulugama, J. C. May, J. A. McLean, K. Pagel, K. Richardson, M. E. Ridgeway, F. Rosu, F. Sobott, K. Thalassinos, S. J. Valentine and T. Wyttenbach, *Mass Spectrom. Rev.*, 2019.

16 E. A. Mason and E. W. McDaniel, *Transport Properties of Ions in Gases*, Wiley, New York, 1988.

17 E. Jurneczko and P. E. Barran, 2011, 20–28.

18 H. Hernández and C. V. Robinson, *Nat. Protoc.*, 2007, **2**, 715–726.

19 S. H. Chen and D. H. Russell, *J. Am. Soc. Mass Spectrom.*, 2015, **26**, 1433–1443.

20 E. Jurneczko, J. Kalapothakis, I. D. G. I. D. G. Campuzano, M. Morris and P. E. P. E. Barran, *Anal. Chem.*, , DOI:10.1021/ac301260d.

21 S. J. Valentine, A. E. Counterman and D. E. Clemmer, 1997, **8**, 954–961.

22 S. I. Merenbloom, T. G. Flick and E. R. Williams, *J. Am. Soc. Mass Spectrom.*, , DOI:10.1007/s13361-011-0313-7.

23 V. Gabelica, S. Livet, F. Rosu, U. De Bordeaux, I. Européen, D. Chimie and B. Iecb, , DOI:10.1007/s13361-018-2029-4.

24 G. Paglia, J. P. Williams, L. Menikarachchi, J. W. Thompson, R. Tyldesley-Worster, S. Halldórsson, O. Rolfsson, A. Moseley, D. Grant, J. Langridge, B. O. Palsson and G. Astarita, *Anal. Chem.*, 2014, **86**, 3985–3993.

25 G. Paglia, P. Angel, J. P. Williams, K. Richardson, H. J. Olivos, J. W. Thompson, L. Menikarachchi, S. Lai, C. Walsh, A. Moseley, R. S. Plumb, D. F. Grant, B. O. Palsson, J. Langridge, S. Geromanos and G. Astarita, *Anal. Chem.*, 2015, **87**, 1137–1144.

26 S. M. Stow, T. J. Causon, X. Zheng, R. T. Kurulugama, T. Mairinger, J. C. May, E. E. Rennie, E. S. Baker, R. D. Smith, J. A. McLean, S. Hann and J. C. Fjeldsted, *Anal. Chem.*, 2017, **89**, 9048–9055.

27 J. A. Harrison, C. Kelso, T. L. Pukala and J. L. Beck, *J. Am. Soc. Mass Spectrom.*, , DOI:10.1007/s13361-018-2074-z.

28 R. Salbo, M. F. Bush, H. Naver, I. Campuzano, C. V Robinson, I. Pettersson, T. J. D. Jørgensen and K. F. Haselmann, 2012, 1181–1193.

29 A. A. Shvartsburg and R. D. Smith, 2008, **80**, 9689–9699.

30 M. F. Bush, Z. Hall, K. Giles, J. Hoyes, C. V. Robinson and B. T. Ruotolo, *Anal. Chem.*, 2010, **82**, 9557–9565.

31 T. Wyttenbach and M. T. Bowers, *Top. Curr. Chem.*, 2003, **225**, 207–232.

32 A. Marchand, S. Livet, F. Rosu and V. Gabelica, *Anal. Chem.*, 2017, **89**, 12674–12681.

33 L. G. Migas, A. P. France, B. Bellina and P. E. Barran, *Int. J. Mass Spectrom.*, 2017, **427**, 20–28.

34 A. J. R. Heck, *Nat. Methods*, 2008, **5**, 927–933.

35 L. Konermann, *J. Am. Soc. Mass Spectrom.*, 2017, 28, 1827–1835.

36 A. Natalello, C. Santambrogio and R. Grandori, *J. Am. Soc. Mass Spectrom.*, 2017, **28**, 21–28.

37 Z. Hall and C. V. Robinson, *J. Am. Soc. Mass Spectrom.*, 2012, **23**, 1161–1168.

38 D. Morsa, V. Gabelica and E. De Pauw, *J. Am. Soc. Mass Spectrom.*, 2014, **25**, 1384–1393.

39 V. Gabellca and E. De Pauw, *Mass Spectrom. Rev.*, 2005, **24**, 566–587.

40 M. F. Jarrold, *Acc. Chem. Res.*, 1999, **32**, 360–367.

41 J. C. May, E. Jurneczko, S. M. Stow, I. Kratochvil, S. Kalkhof and J. A. McLean, *Int. J. Mass Spectrom.*, 2017, 1–16.

42 R. Beveridge, S. Covill, K. J. Pacholarz, J. M. D. Kalapothakis, C. E. MacPhee and P. E. Barran, *Anal. Chem.*, 2014, **86**, 10979–10991.

43 S. J. Valentine, A. E. Counterman and D. E. Clemmer, *J. Am. Soc. Mass Spectrom.*, 1999, 10, 1188–1211.

44 S. Niu and B. T. Ruotolo, *Protein Sci.*, 2015, **24**, 1272–1281.

45 Y. Zhao, A. Singh, Y. Xu, C. Zong, F. Zhang, G. J. Boons, J. Liu, R. J. Linhardt, R. J. Woods and I. J. Amster, *J. Am. Soc. Mass Spectrom.*, 2017, **28**, 96–109.

46 K. J. Light-Wahl, B. L. Schwartz and R. D. Smith, *J. Am. Chem. Soc.*, 1994, **116**, 5271–5278.

47 B. T. Ruotolo, S. J. Hyung, P. M. Robinson, K. Giles, R. H. Bateman and C. V. Robinson, *Angew. Chemie - Int. Ed.*, 2007, **46**, 8001–8004.

48 S. J. Allen and M. F. Bush, *J. Am. Soc. Mass Spectrom.*, 2016, **27**, 2054–2063.

49 L. Han and B. T. Ruotolo, *Int. J. Ion Mobil. Spectrom.*, 2013, **16**, 41–50.

50 E. R. Badman, C. S. Hoaglund-Hyzer and D. E. Clemmer, *Anal. Chem.*, 2001, **73**, 6000–6007.

51 Q. Zhao, G. M. Schieffer, M. W. Soyk, T. J. Anderson, R. S. Houk and E. R. Badman, *J. Am. Soc. Mass Spectrom.*, 2010, **21**, 1208–1217.

52 S. J. Allen, R. M. Eaton and M. F. Bush, *Anal. Chem.*, 2016, **88**, 9118–9126.

53 S. J. Allen, K. Giles, T. Gilbert and M. F. Bush, *Analyst*, 2016, **141**, 884–891.

54 J. Ujma, K. Giles, M. Morris, P. E. Barran and C. M. Spectrometry, *Anal. Chem.*, 2016, **88**, 9469–9478.

55 K. J. Pacholarz and P. E. Barran, *Anal. Chem.*, 2015, **87**, 6271–6279.

56 Y. Sun, S. Vahidi, M. A. Sowole and L. Konermann, *J. Am. Soc. Mass Spectrom.*, 2016, **27**, 31–40.

57 J. R. Jhingree, R. Beveridge, E. R. Dickinson, J. P. Williams, J. M. Brown, B. Bellina and P. E. Barran, *Int. J. Mass Spectrom.*, , DOI:10.1016/j.ijms.2016.08.006.

58 S. C. Henderson, J. Li, A. E. Counterman and D. E. Clemmer, *J. Phys. Chem. B*, 1999, 103, 8780–8785.

59 M. F. Bush, I. D. G. Campuzano and C. V. Robinson, *Anal. Chem.*, 2012, **84**, 7124–7130.

60 E. S. Baker, B. H. Clowers, F. Li, K. Tang, A. V. Tolmachev, D. C. Prior, M. E. Belov and R. D. Smith, *J. Am. Soc. Mass Spectrom.*, 2007, **18**, 1176–1187.

61 Y. Liu, S. J. Valentine and D. E. Clemmer, (unpublished results).

62 L. A. Díaz-Ramos, L. O. Johannissen, A. R. Jones, J. M. Christie, P. Barran, A. Theisen, I. S. Camacho, G. I. Jenkins and B. Bellina, *Proc. Natl. Acad. Sci.*, , DOI:10.1073/pnas.1813254116.

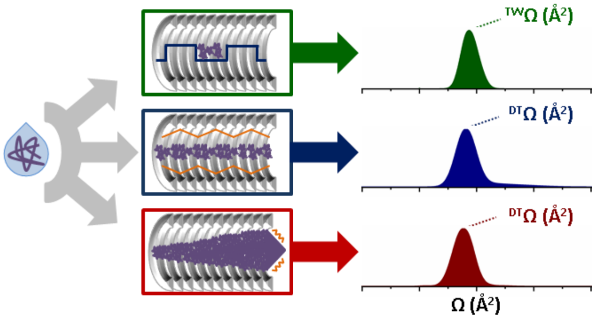
$^{TW}\Omega$ (Å^2)
$^{DT}\Omega$ (Å^2)
$^{DT}\Omega$ (Å^2)
Ω (Å^2)

Supporting Information

Using Collision Cross Section Distributions to Assess the Distribution of Collision Cross Section Values

Aidan P. France, Lukasz G. Migas, Eleanor Sinclair, Bruno Bellina and Perdita E. Barran*

Manchester Institute of Biotechnology, University of Manchester,
131 Princess Street, Manchester, M1 7DN, United Kingdom

* Address correspondence to perdita.barran@manchester.ac.uk

Table of Contents

1. Sample preparation and ionisation

1.1 Sample preparation

For the proteins, ammonium acetate solutions were made by dissolving ammonium acetate (Sigma) in ultrapure water (Merck Milli-Q) to yield ionic buffer concentrations of 50 or 200 mM (SI Table S1). All of these solutions were then adjusted to a pH of 7.4 using ammonium hydroxide solution (Sigma). All seven samples were purchased as lyophilised powders which were dissolved in either 50 or 200 mM ammonium acetate solution, pH 7.4, to form protein stock solutions (typically 100 µM protein concentrations). These stocks were then de-salted twice using Biospin-6 columns (BioRad, USA), aliquoted out, flash frozen and stored at -80 °C until the day of analysis. On the day of analysis, aliquots were thawed at r.t and diluted to their final concentration prior to experimentation (SI Figure S1). A mixture of commercially available phosphazine salts pre-dissolved in a acetonitrile/water solution (95:5, % v:v) (G1969-85020) known as “tunemix” (Agilent technologies, Santa Clara, CA), as well as poly-DL-alanine (Sigma, P9003) and myoglobin (Sigma, G7882) dissolved in water/methanol/formic acid (50:50:0.1, % v:v) were used to optimise the helium IM-Trap differential on the modified Agilent 6560 IMQToF.

1.2 Ionisation

All experiments were performed using nano-electrospray ionisation (nESI) in positive ionisation mode. Samples were infused into emitters prepared in-house from thin walled (O.D. 1.2 mm, I.D. 0.9 mm; WPI, UK) and thick walled (O.D. 1.2 mm, I.D. 0.69 mm; Sutter Instrument Company, USA) fire polished borosilicate glass capillaries using either a Flaming/Brown P-97, Sutter P1000 or P2000/F micropipette puller (Sutter Instrument Company, USA). In order to facilitate more facile spraying, all solution loaded emitters were centrifuged at 5000 rpm for 15 seconds prior to loading into the instrument tip holder. Platinum wire (diamater 0.125 mm, Goodfellow Cambridge Ltd, UK), was inserted into the capillaries to permit efficient ionisation. In order to compensate for the reduction in ion transmission which typically accompanies native IM-MS instrument optimisation, all experiments were carried out in sensitivity mode. Sensitivity mode is a manufacturer setting which may be employed for all instrumentation within this study. Sensitivity mode describes instrument MS operating parameters which maximise ion transmission, at the expense of MS peak resolution.

2. Ion Mobility Mass Spectrometry Measurements

2.1 Waters Synapt G2 (TWIMS)

Travelling wave derived CCS distributions/CCS were obtained on a Synapt G2 (Waters, UK) with nitrogen as the drift gas (SI Figure S2). Within this instrumental configuration, ions can be mass selected in the quadrupole prior to IMS. After navigating the quadrupole, ions enter the “Tri-wave” region which encompasses: 1) an argon filled trap cell, where ions are periodically stored and gated into the helium cell, 2) a helium cell held at a comparatively high pressure to the trap cell, where ions experience “collisional cooling” prior to IM separation, 3) an ~25 cm long TWIMS cell filled with nitrogen, whereby propagating DC waves enable the mobility separation of ions based upon their size, charge and conformation and 4) a transfer cell which acts to ferry ions toward the ToF analyser for *m/z* quantitation. For all the TWIMS experiments within this study, IM wave velocities of 100-300 ms^{-1} and wave heights of 9.5-19.5 V were employed. General parameters employed for native TWIMS experiments are outlined in Table S2. For a more detailed description of the Synapt G2 (TWIMS), see Giles *et al.*[1].

2.2 Waters Synapt G2 (DTIMS)

The Synapt G2 was modified *via* substitution of the travelling-wave IM cell (incorporating the helium cell) with an ~25 cm long RF-confining drift cell (Waters, UK) (SI Figure S3).[2]

Helium/nitrogen gas was introduced into the RF cell using a gas inlet system positioned in the centre of the cell to promote pressure homogeneity (SI Figure S4). Absolute IM cell pressure readouts were enabled by the installation of a baratron (model 626C, MKS, UK). Drift gases could be switched by toggling the "He" (for helium) or "IMS" (for nitrogen) tabs, whilst the RF confining drift cell could also be operated using the original instrument software (MassLynx V4.1) (SI Figure S4). The static potential gradient required for IMS was applied across the RF cell using a combination of four DC voltages (SI Figure S3). For all the experiments outlined in this study, six drift voltages separated by 25 V increments were employed to obtain ion dead times (t_0) and subsequent CCS/CCS distributions. It is important to note that the RF cell pressure was left to equilibrate for >30 minutes after gas initiation/switching prior to data acquisition. General parameters employed for native DTIMS experiments performed on the modified G2 are outlined in SI Table S3.

2.3 Agilent 6560 IMQToF

The setup employed for helium and nitrogen experiments carried out on the 6560 is described in SI Figure S5. For experiments undertaken on the 6560, an orthogonally configured nESI source (G1988-60000 Nanospray, Agilent) was utilised. The source drying gas flow (nitrogen), which was observed to have a large impact upon the observed analyte charge state distributions (CSDs) (SI Figure S6), was adjusted to below 2 L min^{-1} by a manual flow controller (Porter instrument company, USA) fitted to the drying gas outlet and source inlet. Post source, ions were transferred through a heated capillary into a two-stage ion funnel, the first of which focuses ions *via* the use of elevated pressures, whilst the latter operates as an ion funnel trap which enables the release of discrete ion pulses into the IM cell. The IM region comprises an ~78 cm long static field drift tube with an absolute pressure capacitance gauge (CDG 500, Agilent) positioned at the far end of the cell and a thermocouple (Type K, Omega engineering) positioned above the middle of the cell. The instrument configuration employed for measurements taken with nitrogen and helium drift gases is depicted in SI Figure S5. For measurements taken in nitrogen, a positive IM cell pressure differential of 0.15 Torr relative to the preceding trapping funnel was utilised, as described previously.[3] The pressure differential was maintained within 0.01 Torr *via* the inclusion of a drift gas kit (G2582A, Agilent) fitted with a precision flow controller (640B 10 Torr range, MKS) which regulated drift tube pressure by responding to the absolute pressure capacitance gauge (CDG 500, Agilent). However, we found the precision flow controller to be unable to maintain pressure differentials when the instrument was operated with helium as the drift gas. As such, we modified the gas inlets into the trap and IM cell so as to bypass the flow controller and permit manual control of the gas pressures using needle valves (Swagelok) (See SI Figure S5). After carrying out pressure differential optimisation experiments in helium using tunemix (SI Table S4), polyalanine (SI Table S5) and myoglobin (SI Table S6), we settled on an optimum helium IM-Trap differential of ~0.13 Torr. This differential prevented nitrogen contamination in the IM cell, resulting in $^{DT}CCS_{He}$ values closest to those previously published. It is important to note that all gases pass through a gas purifier trap (nitrogen and helium; RMSN and RMSH, Agilent) prior to entering the instrument in both of the instrumental configurations employed. Data was recorded using the MassHunter Data Acquisition software (Agilent) using the stepped-field method, whereby incremental variation of the electric field (five 100 V steps) across the drift cell permitted enumeration of the CCS distributions for a given ion. General parameters employed for native experiments performed on the 6560 IMQToF are outlined in SI Table S7.

3. Creating CCS distributions from ATDs

a) Extract ATD chromatogram list for a given *m/z* (ion of interest).

b) Convert the drift time axis into a CCS axis (in Å^2) using either a TWIMS calibration procedure (for TWIMS data)[4] or the Mason-Schamp equation (for DTIMS data).[5]

c) Take the normalised ion intensity across each triplicate measurement and plot against their corresponding CCS axes in Origin.

d) This will yield three CCS distribution plots (one for each replicate). Using the Peak Analyser tool accurately fit Gaussian distributions to best reflect the experimental data. It is imperative that replicates are fitted using a consistent number of data points (e.g. 1000) across a fixed CCS range (e.g. 2500-4500).

e) After fitting take the CCS range for the fitted peaks, which in the exemplary case would be 1000 data points across a CCS range of 2500-4500 Å^2, you will obtain the x axis of your averaged CCS distribution plot. Then take the ion intensity across each fitted replicate and average the intensity of each replicate to give a representative y-axis intensity and standard deviation across the replicates.

Table S1. Analyte sources and final solution conditions.

Protein	Source	Supplier	Catalogue #	Solution conditions
Ubiquitin *(8.6 kDa)*	Bovine erythrocytes	Sigma	U6253	50 mM AmAc pH 7.4
Cytochrome c *(12.4 kDa)*	Horse heart	Sigma	C2506	50 mM AmAc pH 7.4
Myoglobin *(17.6 kDa)*	Horse heart	Sigma	G7882	50 mM AmAc pH 7.4
Avidin *(64 kDa)*	Chicken egg white	Sigma	A9275	200 mM AmAc pH 7.4
Serum albumin (BSA) *(66 kDa)*	Bovine	Bio-rad labs	500-0007	200 mM AmAc pH 7.4
Concanavalin a *(103 kDa)*	Jack bean	Sigma	C2010	200 mM AmAc pH 7.4
Alcohol dehydrogenase *(148 kDa)*	Yeast	Sigma	A7011	200 mM AmAc pH 7.4

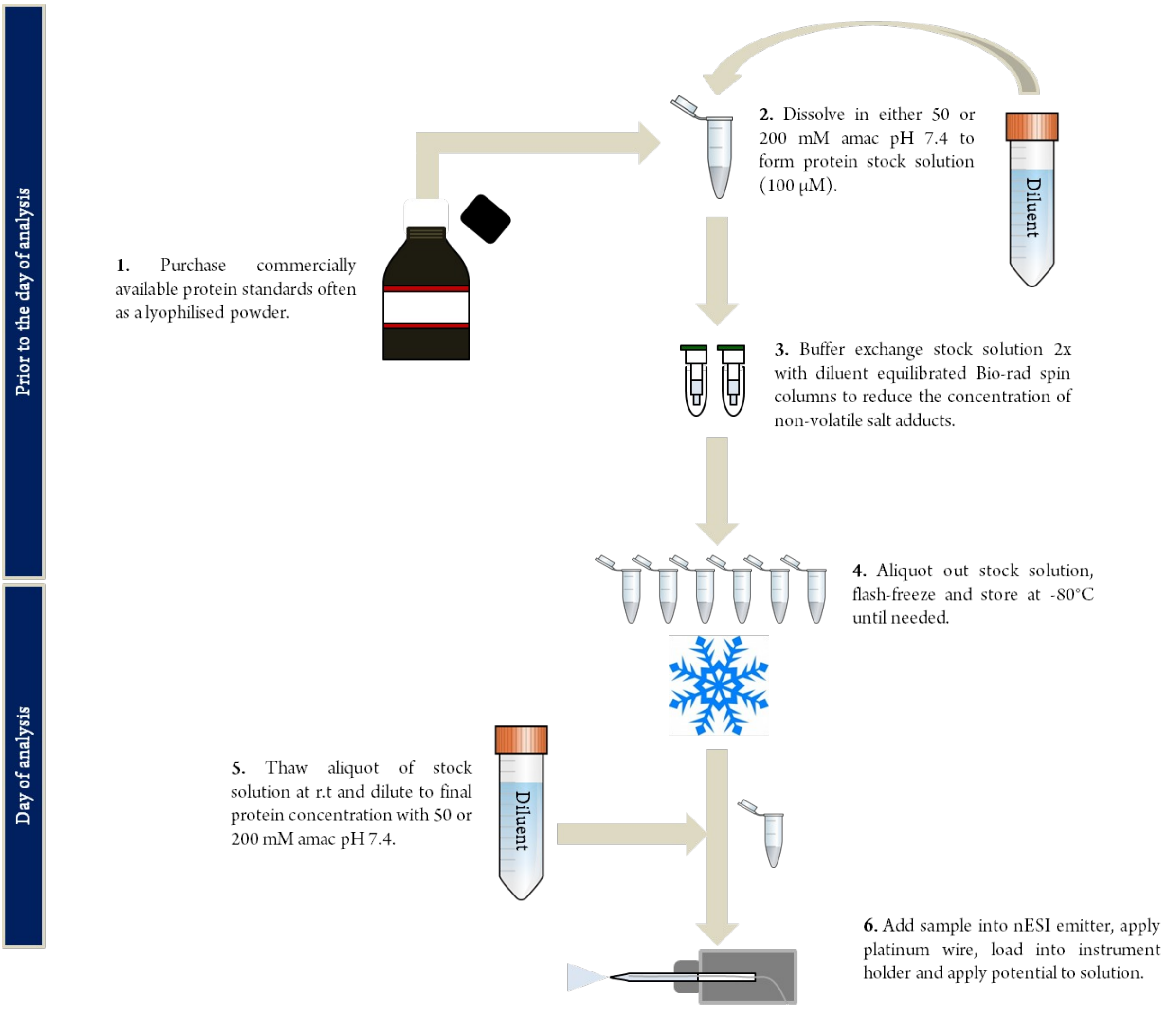

1. Purchase commercially available protein standards often as a lyophilised powder.

2. Dissolve in either 50 or 200 mM amac pH 7.4 to form protein stock solution (100 μM).

3. Buffer exchange stock solution 2x with diluent equilibrated Bio-rad spin columns to reduce the concentration of non-volatile salt adducts.

4. Aliquot out stock solution, flash-freeze and store at -80°C until needed.

5. Thaw aliquot of stock solution at r.t and dilute to final protein concentration with 50 or 200 mM amac pH 7.4.

6. Add sample into nESI emitter, apply platinum wire, load into instrument holder and apply potential to solution.

Figure S1. Schematic of standard protein/protein complex preparative procedure. Samples were purchased as lyophilised powders. Samples were then dissolved in 50 mM AmAc (monomeric proteins < 20 kDa) or 200 mM AmAc pH 7.4 (proteins/protein complexes > 20 kDa) to a stock concentration of ~ 100 μM. Stock solutions were then desalted using two equilibrated Bio-rad spin columns. After this process the buffer exchanged stock solutions were aliquoted out, flash-frozen in liquid nitrogen and then stored at -80 °C until the day of analysis. On the day of analysis aliquots were thawed at r.t., diluted to their final concentrations, loaded into nESI borosilicate emitters, centrifuged for 15 seconds and loaded onto an IM-MS holder prior to voltage application. Final analyte concentrations utilised for experiments within this study were between 1.25 – 10 μM.

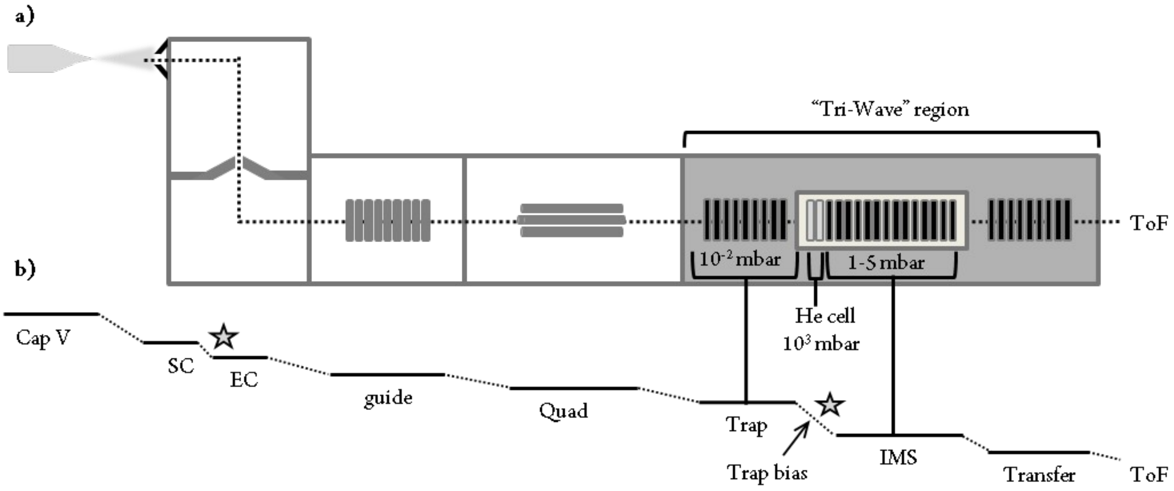

Figure S2. Schematic of the Synapt G2 (TWIMS) and its corresponding potential landscape. a) Schematic of the Synapt G2 (TWIMS). Ions travel through the instrument as follows: 1) droplets produced from nESI undergo continuous evaporation/fission processes whilst navigating a z-spray ion source via a favourable potential gradient and pressure differential, 2) ions are then transferred through a T-wave ion guide into a quadrupole mass analyser (which permits ion selection up to 32,000 m/z), after which they enter the "Tri-wave" region, 3) an argon filled trap cell encompasses the first 9 cm of this region. Within the trap cell ions are "axially focussed" by gas-ion collisions, whilst a transient DC gating field permits regular ion pulses into the next stage of the instrument[6], 4) post gating, the ion pulse travels through a 4 cm travelling wave ion guide into a 7 mm cell pressurised with helium gas. A comparatively high pressure in this region acts to permit the use of greater pressures in the downstream IM region whilst "collisionally cooling" ions prior to IM separation, 5) ions then enter the 25.2 cm long IM region (consisting of 168 stacked ring electrodes) whereby mobility separation is permitted by the application of a DC potential to sequential plate pairs in single plate pair steps. This effectively creates a propagating wave which separates ions based upon their charge and their propensity to interact with the drift gas,[1] 6) following mobility separation, ions traverse a 9 cm transfer region pressurised in the same fashion as the trap cell. The application of low velocity, high amplitude travelling waves in this region acts to ferry ions toward the ToF analyser (for m/z detection) without further activation and IM separation. b) Schematic of the potential gradient along the instrument. Voltages which impart the greatest energy upon ions, thus promoting their gas-phase activation, are highlighted by grey stars. The voltage gradient from the sample cone (SC) to the extractor cone (EC) can be utilised to promote in-source ion activation. Furthermore, the trap bias voltage, which acts to accelerate ions (analogous to an injection voltage in DTIMS) from a comparatively low pressure environment (the trap cell) to a higher pressure one (the Helium and IM cell) can also significantly perturb ion structures if not tuned. Similar representations of a) and b) are present in Chen *et al.*[7].

Source voltages (V) and gas flows (mL/min)	
Capillary voltage (kV)	0.7 – 1.2
Source temperature (°C)	40.0
Sample cone	10.0 – 20.0
Extractor cone	1.0
Trap gas flow	2.0
Helium cell gas flow	200
IMS gas flow	75.0
DC voltages	
Trap cell energy (V)	0.0 – 6.0
Trap DC entrance	4.0
Trap DC bias	40.0
Trap DC	-2.2
Trap DC exit	5.0
Trap height (V)	10-15
IMS DC entrance	27.0
Helium cell DC	30.0
Helium cell exit	-5.0
IMS bias	2.0
IMS DC exit	0.0
Transfer cell energy (V)	0.0 – 6.0
Transfer DC entrance	4.0
Transfer DC exit	15.0
RF voltages (V)	
Source	350
Trap	300
IMS	300
IMS mobility	250
Transfer	350
Wave velocities (ms^{-1}) and heights (V)	
Source wave velocity	8
Source wave height	0.0
Trap wave velocity	450
Trap wave height	0.5
IMS wave velocity	100 – 300
IMS wave height	9 – 19.5
Transfer wave velocity	100-600
Transfer wave height	10
Pressures (mbar)	
Backing	2.90
Trap	$2.81e^{-2}$
Helium cell	$1.41e^{3}$
IM cell	4.26
Transfer	$2.96e^{-2}$
ToF	$1.04e^{-6}$

Table S2. Synapt G2 (TWIMS) tuning parameters. For proteins/protein complex ions >60 kDa, backing pressure and trap cell pressures were raised to ~4-7 and ~4e-2 mbar respectively in order to maximise ion transmission. Furthermore, larger protein complexes were analysed using higher source and pre-IM voltages which permitted greater transmission without notable structural alteration.

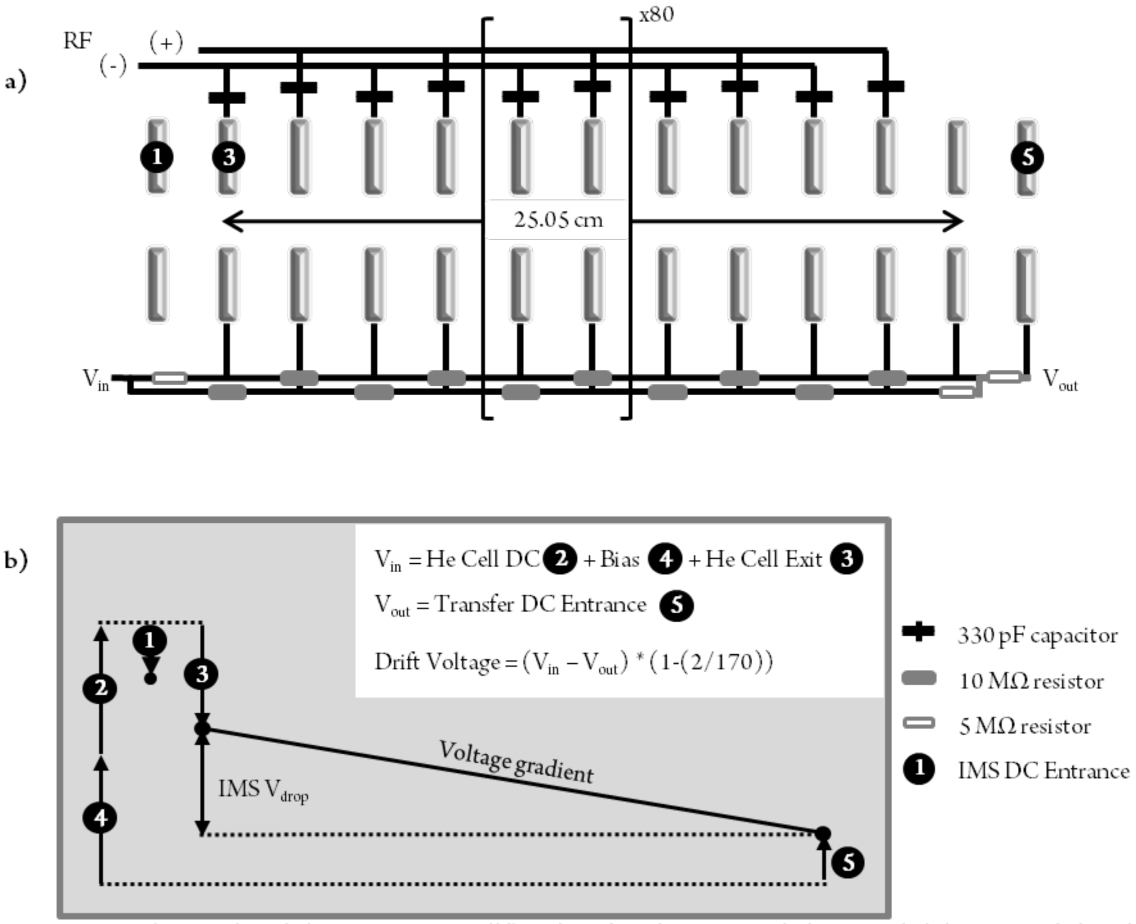

Figure S3. Schematic of the RF cell modification for the G2 and the establishment of the drift voltage within the RF cell. a) Schematic of the RF cell modification for the G2. The DC drift voltage applied across the cell is established by the resistor series which are parallel to one another. The presence of two 330 pF capacitor series running along the length of the cell acts to promote ion transmission via radial confinement of the ion beam. b) Schematic showing how the drift voltage is applied across the RF cell. The entrance drift voltage (V_{in}) is established using the He cell DC (2), IM Bias (4) and He cell exit (3) voltages. The IMS DC entrance (1) controls the helium exit plate and thus does not affect the drift voltage. Within our study (1) was set at approximately a quarter of the value of (3). The effective drift voltage is calculated by subtracting V_{out} from V_{in} and correcting for two individual resistors (one before V_{in} and one between the RF-confining drift cell exit plate and (5)). As such, the effective drift length (25.05 cm) is slightly shorter than the cell length (25.2 cm) as the drift voltage is only applied from the first electrode to the exit plate of the cell. Drift voltages utilised for the experiments described in this study ranged from 325 to 75 V. Similar representations of a) and b) are present in Allen *et al.*[2].

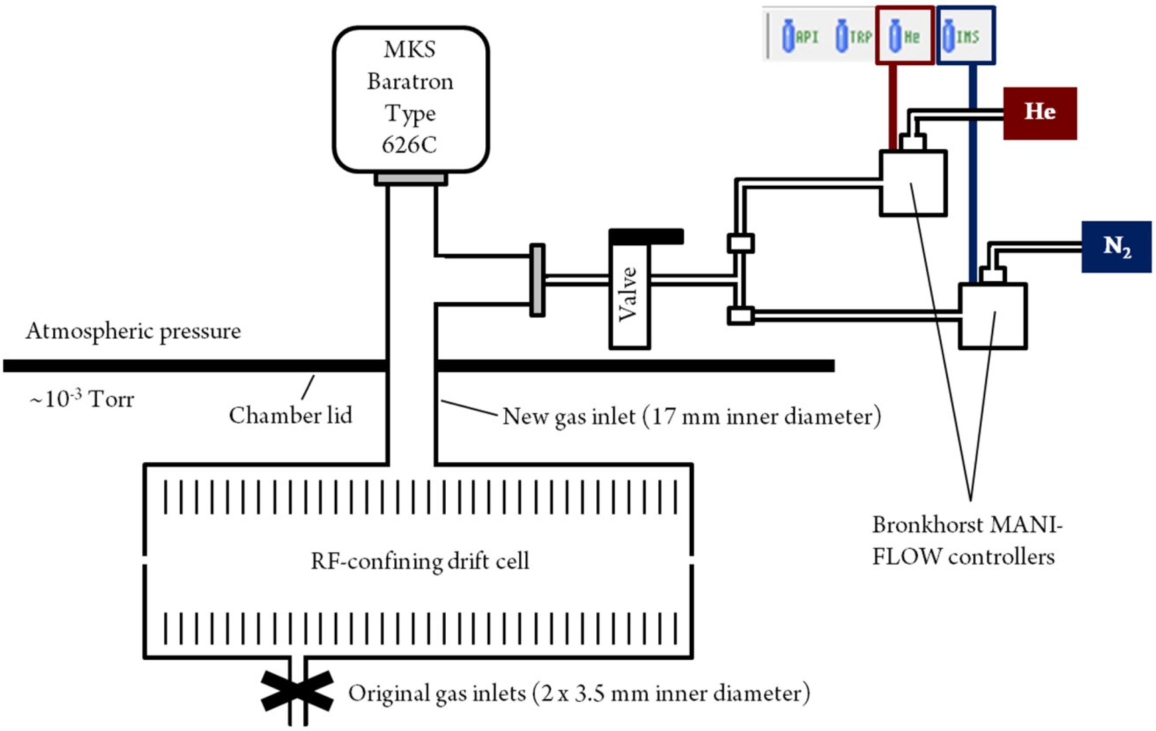

Figure S4. Schematic of the RF cell configuration and gas inlet system. Drift gas composition was controlled using the original MassLynx V4.1 software, where the “IMS” tab permitted nitrogen gas flow and the “He” tab permitted helium gas flow. Gas pressures within the drift cell were controlled via Bronkhorst MANI-FLOW controllers which responded to controls on the original MassLynx V4.1 software, whereby “IMS gas” regulated the amount of nitrogen in the cell and “Helium cell gas” regulated the amount of helium in the cell. Drift gas pressures were measured via a capacitance manometer (MKS Baratron type 626C) placed above the centre of the drift cell which permitted absolute pressure measurements. A similar representative figure is present in Allen *et al.*[2].

Source voltages (V) and gas flows (mL/min)		
Capillary voltage (kV)	0.7 – 1.2	
Source temperature (°C)	40.0	
Sample cone	10.0 – 20.0	
Extractor cone	1.0	
Trap gas flow	2.0	
Helium gas flow (for experiments in He)	100.0	
Nitrogen gas flow (for experiments in N_2)	41.0	
DC voltages		
Trap cell energy (V)	0.0 – 4.0	
Trap DC entrance	1.0	
Trap DC bias	1.0	
Trap DC	0.0	
Trap DC exit	1.0	
Trap height (V)	10-15	
IMS DC entrance	-6.5	
Helium cell DC	← altered incrementally (25 V steps) to establish Drift Voltages	
Helium cell exit	-40	
IMS bias	← altered incrementally (25 V steps) to establish Drift Voltages	
IMS DC exit	0.0	
Transfer cell energy (V)	0.0 – 6.0	
Transfer DC entrance	4.0	
Transfer DC exit	15.0	
RF voltages (V)		
Source	350	
Trap	300	
IMS	300	
IMS mobility	250	
Transfer	350	
Wave velocities (ms^{-1}) and heights (V)		
Source wave velocity	200	
Source wave height	0.2	
Trap wave velocity	313	
Trap wave height	2.0	
IMS wave velocity	650	
IMS wave height	0	
Transfer wave velocity	300	
Transfer wave height	4	
Pressures		
	He	**N_2**
Backing (mbar)	2.7	2.7
Trap (mbar)	$1.3e^{-2}$	$1.1e^{-2}$
IM (Torr)	1.94	1.98
Transfer (mbar)	$1.4e^{-2}$	$1.1e^{-2}$
ToF (mbar)	$7.4e^{-7}$	$7.5e^{-7}$

Table S3. Synapt G2 (DTIMS) tuning parameters. For proteins/protein complex ions >60 kDa, the backing pressure and trap cell pressure was raised to ~ 4-7 and ~ 4e-2 mbar respectively in order to maximise ion transmission. Furthermore, larger protein complexes were analysed using higher source and pre-IM voltages as no notable structural alterations occurred whilst significant increases in transmission were observed.

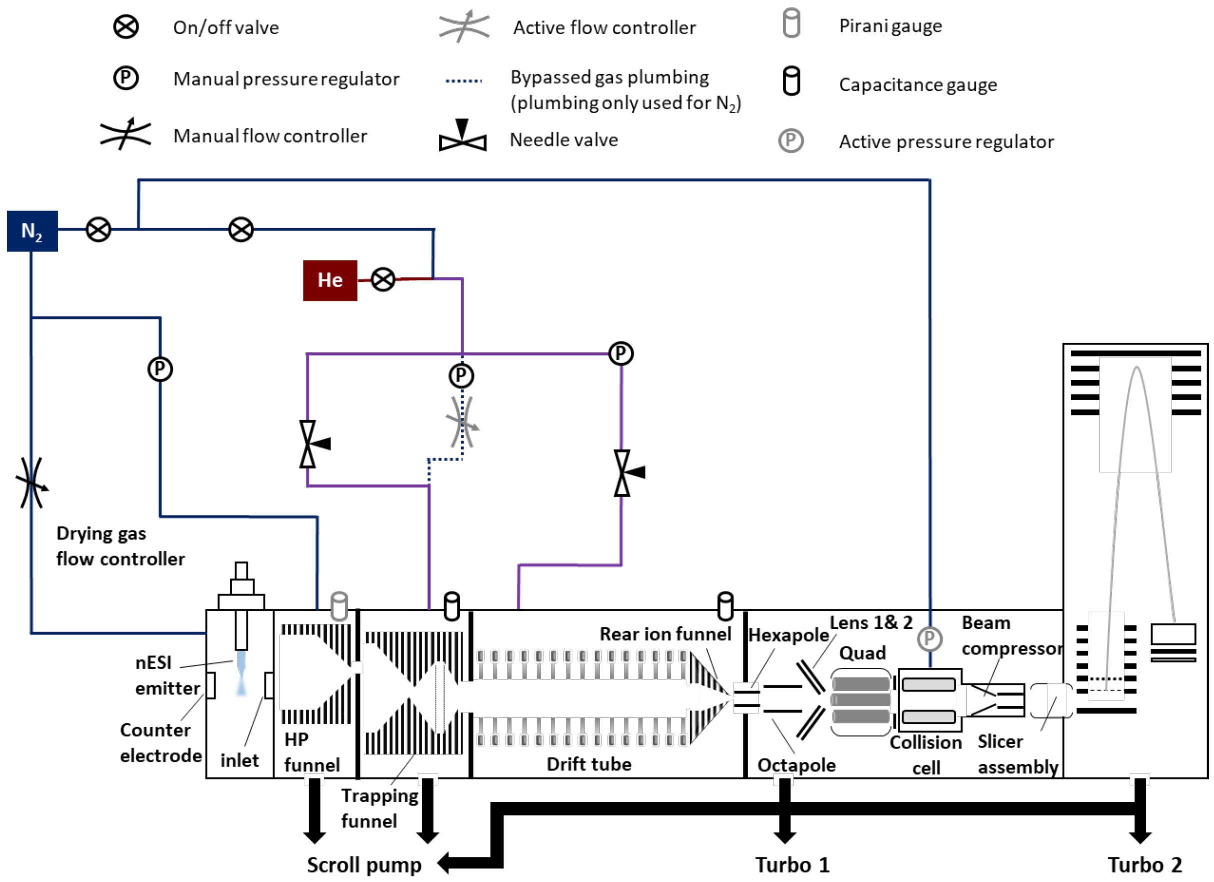

Figure S5. Schematic of the Agilent 6560 IMQToF and gas inlet system. Schematic of the Agilent 6560 IMQToF (with a nESI source) with nitrogen gas inlets (blue), helium gas inlets (red) and inlets which can be configured to allow either nitrogen or helium gas in (purple). In all configurations the internal structure of the instrument remains unchanged. In both configurations nitrogen is pumped into the source (as drying gas), HP funnel region, and collision cell (back end of the instrument post IM). Drying gas flow into the source is regulated by a manually adjustable flow controller (Porter instrument company, USA). For all of the experiments carried out with nitrogen as the drift gas, a mass flow controller (installed as part of the Agilent gas kit upgrade) was utilised to actively regulate the pressure differential between the IM cell and the trapping funnel. In this configuration, manually adjustable pressure regulators prior to the drift cell and HP funnel were also used to help establish the IM pressure and IM-Trap pressure differential. However, for all the experiments done in helium the mass flow controller was bypassed, as pressure stabilisation was not possible. As such, we installed pressure regulators and needle valves which we positioned prior to the IM cell and trap funnel to permit manual control of IM cell and trap funnel pressures. Pressures at the front end of the 6560 are maintained by a single scroll pump (Edwards) whilst at the back end of the instrument the scroll pump works in synergy with two turbo pumps to maintain the low pressures required in the QToF region. Absolute pressure measurements for the trapping funnel and drift tube are recorded by CDG 500 capacitance gauges positioned at the end of the aforementioned regions (black and white cylinders). The HP funnel pressure is recorded via a pirani gauge (grey and white cylinder) which yields a relative pressure measurement. A similar representative figure is present in May *et al.*[8].

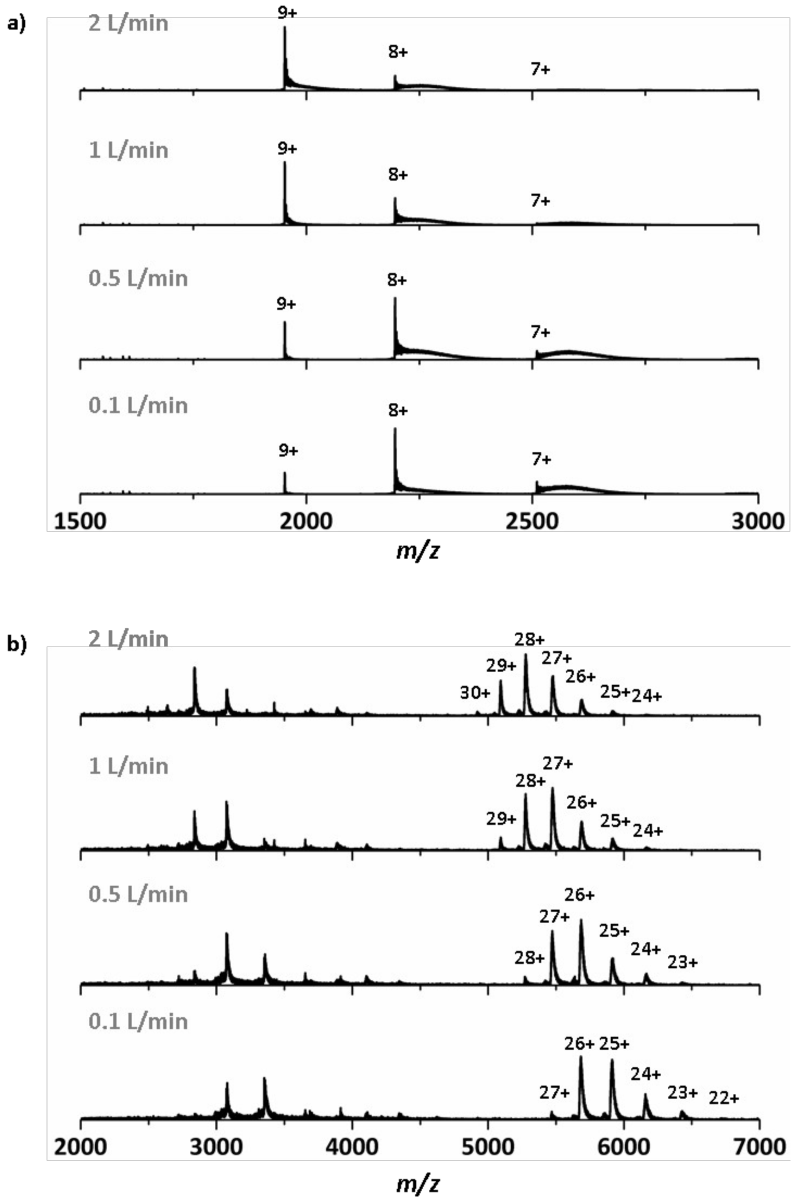

Figure S6. Impact of drying gas flow rates upon protein/protein complex CSDs. Mass spectra of myoglobin and alcohol dehydrogenase obtained using different drying gas flow rates on the Agilent 6560 IMQToF. a) Mass spectra of myoglobin obtained when employing drying gas flow rates of 0.1, 0.5, 1 and 2 L/min. No parameters except drying gas flow rate were altered between the acquisition of the mass spectra. The CSD centres on the 8+ ion of myoglobin at the lowest drying gas flow rate employed and is observed to shift in favour of the 9+ ion as the drying gas flow rate is increased. b) Mass spectra of alcohol dehydrogenase obtained when employing drying gas flow rates of 0.1, 0.5, 1 and 2 L/min. No parameters except drying gas flow rate were altered between the acquisition of the mass spectra. The CSD centres on the 25 and 26+ ions of alcohol dehydrogenase at the lowest drying gas flow rate employed and is observed to shift in favour of higher charge states (eventually centring on the 28+ ion) as the drying gas flow rate is increased. As such, the CSD of protein/protein complex ions can be seen to shift in favour of higher charge states with greater drying gas flow rates. Interestingly, this affect appears to be more significant for larger protein complexes (which present with larger Δz values) in comparison to smaller proteins (which present with smaller Δz values). No parameters except drying gas flow rate were altered between the acquisition of the mass spectra shown above Both myoglobin and alcohol dehydrogenase were sprayed from 50 mM and 200 mM AmAc solutions (pH 7.4) respectively. It is important to note that the associated IM landscape of each ion (peak apexes, ATD morphology and widths) did not noticeably alter with differing drying gas flow rates.

Table S4. Establishing the helium IM-Trap differential on the modified Agilent 6560 IMQToF using Agilent tune mix. a) Average $^{DT}CCS_{He}$ literature values and our experimental $^{DT}CCS_{He}$ values for the 622, 922 & 1222 1+ ions of tune mix obtained under helium IM-Trap differentials of 0.109, 0.130, 0.134, 0.138 & 0.143 Torr. b) Relative differences (%) between the average literature values and our experimental $^{DT}CCS_{He}$ values obtained from the aforementioned helium IM-Trap differentials.

a)

	helium IM-Trap differential (Torr)					
		0.109	**0.130**	**0.134**	**0.138**	**0.143**
Tune mix (m/z)	**Avg of Literature & DTIMS (G2) $^{DT}CCS_{He}$ values[9,10]**	**$^{DT}CCS_{He}$ DTIMS (6560)**	**$^{DT}CCS_{He}$ DTIMS (6560)**	**$^{DT}CCS_{He}$ DTIMS (6560)**	**$^{DT}CCS_{He}$ DTIMS (6560)**	**$^{DT}CCS_{He}$ DTIMS (6560)**
622	139.5	142.4	138.7	137.8	137.2	136.9
922	174.6 ± 1.1	180.2	175.9	176	173.3	173.2
1222	208.2 ± 1.4	214.2	207.4	207.9	205.6	205.3

b)

	helium IM-Trap differential (Torr)				
	0.109	**0.130**	**0.134**	**0.138**	**0.143**
Tune mix (m/z)	**ΔExp vs Ref (%)**	**ΔExp vs Ref (%)**	**ΔExp vs Ref (%)**	**ΔExp vs Ref (%)**	**ΔExp vs Ref (%)**
622	2.04	-0.58	-1.23	-1.68	-1.90
922	3.23	0.76	0.82	-0.73	-0.78
1222	2.88	-0.38	-0.14	-1.25	-1.39
Average	2.72 ± 0.61	-0.07 ± 0.72	-0.18 ± 1.03	-1.22 ± 0.48	-1.36 ± 0.56

Table S5.

a)

		helium IM-Trap differential (Torr)			
		0.128	**0.132**	**0.135**	**0.140**
Polyalanine	**Avg of Literature $^{DT}CCS_{He}$ values[2,11]**	**$^{DT}CCS_{He}$ DTIMS (6560)**	**$^{DT}CCS_{He}$ DTIMS (6560)**	**$^{DT}CCS_{He}$ DTIMS (6560)**	**$^{DT}CCS_{He}$ DTIMS (6560)**
z = 1+					
7	140.8 ± 0.4	144.1	142.6	140.3	141.1
8	156.3 ± 1.1	158	157	157.6	156.3
9	169.0 ± 1.5	168.5	169	169.2	168.2
10	178.7 ± 3.3	180.5	179.1	179.4	178.9
11	193.1 ± 1.3	191.6	192.6	190.6	190.6
12	204.2 ± 2.5	202	203.2	203.2	200.4
13	216.0 ± 1.5	215.3	213	220	210.8
14	226.5 ± 2.2	225	221.4	214.1	220.8
z = 2+					
12	208	209.9	207	208.5	206.7
13	220	220.4	221.4	222.5	220
14	232	232.6	232.5	233.6	229.6
15	243	243.4	242.3	242.5	242
16	255	255.7	254.2	254.8	252.5
17	265	267.5	264.4	265.2	264.6
18	276	277.5	273.2	275.8	275.1
19	287	287.9	285.6	285	284.9
20	297	298.7	297.5	295.7	295.3
21	308	306.8	307.1	306.6	305.6
22	317	319.3	314.2	313.3	315.9
23	327	330.2	324.7	326.4	326.2
24	337	336.4	336.8	332.4	334.8
25	348	351.8	347.2	344	346.7
26	358	356.8	359.5	362.2	355.4
z = 3+					
22	373	369.5	371.1	375.2	373.3
23	386	384	388.8	388.4	386.1
24	399	401.6	401.8	400.1	398.6
25	412	415.3	407	410.4	408.7
26	425	427.6	424.9	423.5	424.3
27	438	437.9	436.8	432.6	436.7
28	452	451	449.5	448.4	451.2
29	465	465.4	463.3	460.7	461.7
30	479	475.5	474.8	473.2	473.8
31	490	486	482.6	482.7	487.9
32	502	498.3	495.7	499.2	501.4
33	516	508.5	511.9	503.8	513.3

Establishing the helium IM-Trap differential on the modified Agilent 6560 IMQToF using polyalanine. a) Average $^{DT}CCS_{He}$ literature values and our experimental $^{DT}CCS_{He}$ values for a series of 1+, 2+ & 3+ ions of polyalanine obtained under helium IM-Trap differentials of 0.128, 0.132, 0.135 & 0.140 Torr. b) Relative differences (%) between the average literature values and our experimental $^{DT}CCS_{He}$ values obtained from the aforementioned helium IM-Trap differentials.

b)	**helium IM-Trap differential (Torr)**			
	0.128	**0.132**	**0.135**	**0.14**
Polyalanine	**ΔExp vs Ref (%)**	**ΔExp vs Ref (%)**	**ΔExp vs Ref (%)**	**ΔExp vs Ref (%)**
z = 1+				
7	1.31	-0.32	0.25	2.38
8	0.48	0.86	0.03	1.12
9	0.03	0.15	-0.44	-0.27
10	0.25	0.42	0.14	1.04
11	-0.26	-1.29	-1.29	-0.78
12	-0.49	-0.49	-1.86	-1.08
13	-1.37	1.88	-2.38	-0.30
14	-2.23	-5.45	-2.50	-0.64
z = 2+				
12	-0.48	0.24	-0.63	0.91
13	0.64	1.14	0.00	0.18
14	0.22	0.69	-1.03	0.26
15	-0.29	-0.21	-0.41	0.16
16	-0.31	-0.08	-0.98	0.27
17	-0.23	0.08	-0.15	0.94
18	-1.01	-0.07	-0.33	0.54
19	-0.49	-0.70	-0.73	0.31
20	0.17	-0.44	-0.57	0.57
21	-0.29	-0.45	-0.78	-0.39
22	-0.88	-1.17	-0.35	0.73
23	-0.70	-0.18	-0.24	0.98
24	-0.06	-1.36	-0.65	-0.18
25	-0.23	-1.15	-0.37	1.09
26	0.42	1.17	-0.73	-0.34
z = 3+				
22	-0.51	0.59	0.08	-0.94
23	0.73	0.62	0.03	-0.52
24	0.70	0.28	-0.10	0.65
25	-1.21	-0.39	-0.80	0.80
26	-0.02	-0.35	-0.16	0.61
27	-0.27	-1.23	-0.30	-0.02
28	-0.55	-0.80	-0.18	-0.22
29	-0.37	-0.92	-0.71	0.09
30	-0.88	-1.21	-1.09	-0.73
31	-1.51	-1.49	-0.43	-0.82
32	-1.25	-0.56	-0.12	-0.74
33	-0.79	-2.36	-0.52	-1.45
Average	0.12 ± 0.80	-0.34 ± 0.72	-0.42 ± 1.24	-0.58 ± 0.64

Table S6. Establishing the helium IM-Trap differential on the modified Agilent 6560 IMQToF using apo-myoglobin. a) Average $^{DT}CCS_{He}$ literature values and our experimental $^{DT}CCS_{He}$ values for a series of monomorphic ions (18-26+) of apo-myoglobin obtained under helium IM-Trap differentials of 0.125, 0.130, 0.135 & 0.140 Torr. b) Relative differences (%) between the average literature values and our experimental $^{DT}CCS_{He}$ values obtained from the aforementioned helium IM-Trap differentials.

a)	**helium IM-Trap differential (Torr)**				
		0.125	**0.130**	**0.135**	**0.140**
Apo-myoglobin (z)	**Avg of Literature $^{DT}CCS_{He}$ values**[12-15]	**$^{DT}CCS_{He}$ DTIMS (6560)**	**$^{DT}CCS_{He}$ DTIMS (6560)**	**$^{DT}CCS_{He}$ DTIMS (6560)**	**$^{DT}CCS_{He}$ DTIMS (6560)**
18+	3488 ± 38	3534	3487	3499	3476
19+	3578 ± 18	3646	3587	3610	3578
20+	3671 ± 26	3749	3686	3698	3669
21+	3760 ± 27	3824	3770	3774	3733
22+	3816 ± 21	3881	3829	3821	3795
23+	3893 ± 32	3913	3874	3848	3828
24+	3952 ± 45	3936	3897	3881	3847
25+	3995 ± 49	3966	3933	3908	3891
26+	4034 ± 47	4008	3968	3948	3928

b)	**0.125**	**0.130**	**0.135**	**0.140**
Apo-myoglobin (z)	**ΔExp vs Ref (%)**	**ΔExp vs Ref (%)**	**ΔExp vs Ref (%)**	**ΔExp vs Ref (%)**
18+	1.35	-0.02	0.33	-0.34
19+	1.92	0.25	0.92	0.03
20+	2.12	0.40	0.74	-0.04
21+	1.70	0.26	0.38	-0.71
22+	1.70	0.36	0.14	-0.55
23+	0.53	-0.46	-1.14	-1.67
24+	-0.41	-1.38	-1.80	-2.65
25+	-0.71	-1.55	-2.18	-2.60
26+	-0.63	-1.63	-2.11	-2.61
Average	-0.84 ± 1.16	-0.42 ± 0.87	-0.53 ± 1.27	-1.24 ± 1.15

Table S7. Agilent 6560 IMQToF tuning parameters. The Quad AMU was set at 500 for ubiquitin, cytochrome c and myoglobin, at 1000 for Avidin and BSA and 2000 for concanavalin a and alcohol dehydrogenase. These settings were observed to be optimal for the transmission of the different analyte ions analysed during this study. For proteins/protein complexes < 70 kDa, the collision cell flow was maintained at 22. However, for protein complexes > 100 kDa the collision cell flow was increased to 25 in order to aid transmission of these larger ions.

Source voltages (V) and gas flows (L/min)		
Capillary voltage (kV)	0.9 – 1.4	
Source temperature (°C)	50.0	
Drying gas flow	0.1-0.3	
Fragmentor	300-375	
DC voltages		
HP Funnel delta	120-180	
Trap entrance grid delta	1	
Trap entrance grid low	97	
Trap entrance grid high	98	
Trap entrance	91	
Trap exit	90	
Trap exit grid 1 delta	4	
Trap exit grid 1 low	87.6	
Trap exit grid 1 high	91.6	
Trap exit grid 2 delta	7.1	
Trap exit grid 2 low	87.5	
Trap exit grid 2 high	94.6	
Trap Funnel delta	180	
IM Hexapole delta	-8	
IM Hexapole entrance	41	
Rear Funnel entrance	240	
Rear Funnel exit	45	
RF voltages (V)		
Octapole	750	
High Pressure Funnel	100-140	
Trap Funnel	100-160	
IM Hexapole	300	
Rear Funnel	200	
Other parameters		
Trap fill time (µs)	5000	
Trap release time (µs)	150	
Pressures (Torr)		
	He	**N_2**
HP Funnel	4.50-4.80	4.30-4.70
Drift tube	3.89-3.93	3.95
Trap Funnel	3.76-3.80	3.80

Table S8. Calibrants employed for TWIMS experiments and their associated Pearson coefficients. Note that for ubiquitin, cytochrome c and myoglobin, there was not a complete selection of calibrant ions with previously published $^{DT}CCS_{N2}$ values. In these instances we utilised our own $^{DT}CCS_{N2}$ values (denoted by *), derived from our RF confining drift cell (to remain consistent with our other literature CCS origins), as calibrant literature CCS for the calibration procedure. The WVs and WHs employed for analytes were selected from three different WV/WH combinations: 1) 100/9.5; 2) 200/14 and; 3) 300/18 (or 19.5 for larger ions, to prevent mobility wrap around) based upon which WV/WH combination gave the highest pearson coefficient for each calibrant set.

Protein	**n**	**TWIMS calibrants**	**Calibrant literature Ω source**	**TWIMS WV (ms^{-1})**	**TWIMS WH (V)**	**Average r^2 $N_2 \rightarrow He$**	**Average r^2 N_2**
Ubiquitin *(8.6 kDa)*	1	Melittin Insulin (1n) Cytochrome C	Bush *et al.*[2,15,16] *Our RF CCS	300	18	0.9951 (±0.0016)	*0.9872 (±0.0002)
Cytochrome C *(12.4 kDa)*	1	Ubiquitin Lysozyme β-Lactoglobulin A (1n)	Bush *et al.*[2,15] *Our RF CCS	200	14	0.9931 (±0.0006)	*0.9940 (±0.0035)
Myoglobin *(17.6 kDa)*	1	Lysozyme Cytochrome C β-Lactoglobulin A (1n)	Bush *et al.*[2,15] *Our RF CCS	300	18	0.9824 (±0.0012)	*0.9969 (±0.0011)
Avidin *(64 kDa)*	4	TTR Concanavalin A	Bush *et al.*[2,15]	300	19.5	0.9932 (±0.0025)	0.9994 (±0.0005)
Serum albumin (BSA) *(66 kDa)*	1	Avidin Concanavalin A	Bush *et al.*[2,15]	100	9.5	0.9956 (±0.0011)	0.9956 (±0.0014)
Concanavalin A *(103 kDa)*	4	Avidin Alcohol dehydrogenase	Bush *et al.*[2,15]	100	9.5	0.9951 (±0.0036)	0.9706 (±0.0102)
Alcohol dehydrogenase *(148 kDa)*	4	Concanavalin A Pyruvate kinase	Bush *et al.*[2,15]	300	19.5	0.9977 (±0.0004)	0.9851 (±0.0043)

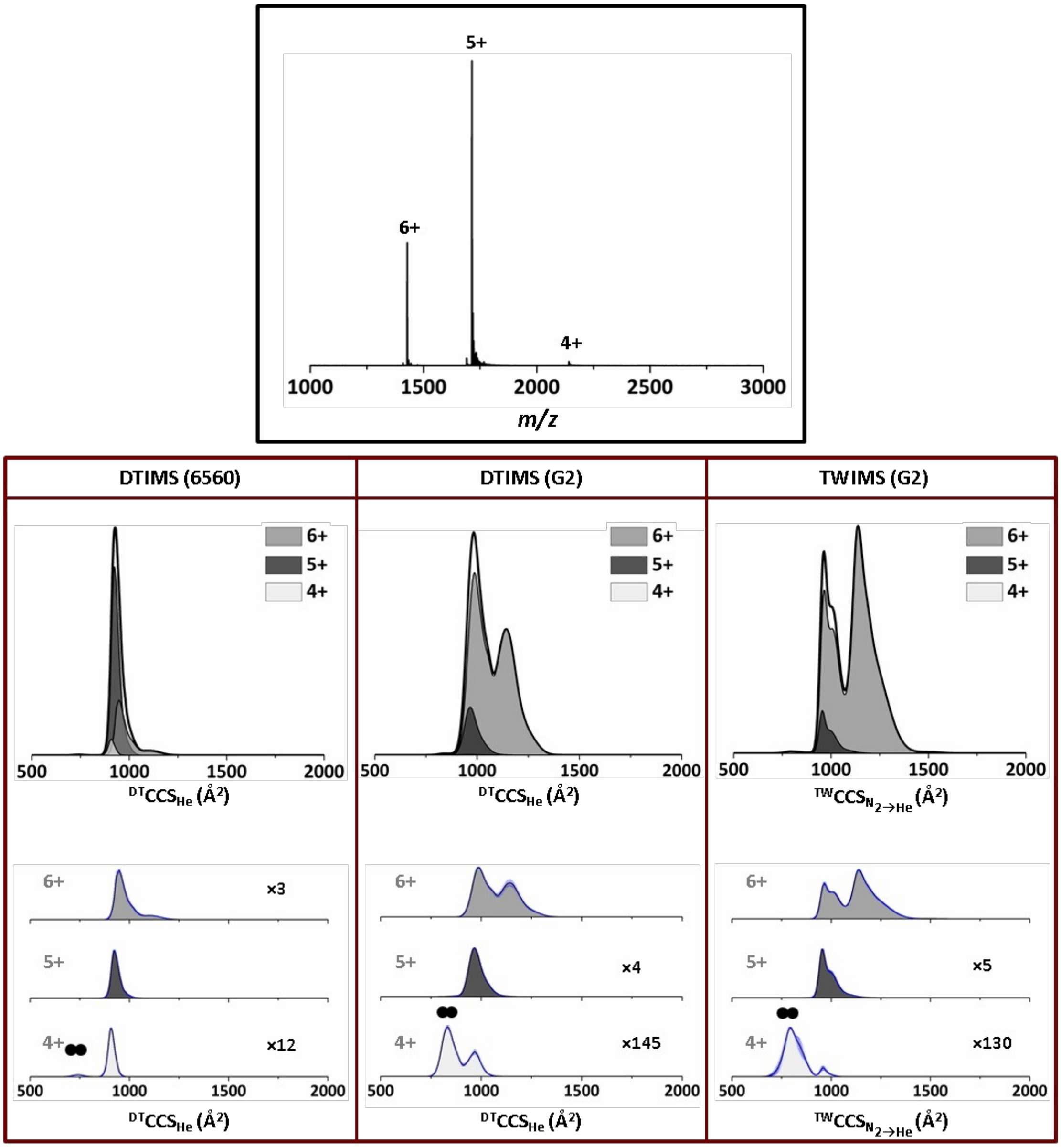

Protein			Helium Drift Gas					
Ubiquitin (8566 Da)			6560-DTIMS		G2-DTIMS		G2-TWIMS	
Z_{Avg}	Species	#	$^{DT}CCS_{He}$ (Å^2)	%RSD	$^{DT}CCS_{He}$ (Å^2)	%RSD	$^{TW}CCS_{He}$ (Å^2)	%RSD
5.41 ± 0.29	$[M+4H]^{4+}$	1	907 ± 2	0.27	963 ± 7	0.72	961 ± 7	0.71
	$[M+5H]^{5+}$	1	924 ± 5	0.51	965 ± 8	0.84	955 ± 2	0.25
		2	-	-	-	-	1003 ± 2	0.22
	$[M+6H]^{6+}$	1	943 ± 8	0.86	987 ± 4	0.37	966 ± 0.2	0.02
		2	1113 ± 10	0.85	1143 ± 2	0.14	1006 ± 9	0.88
		3	-	-	-	-	1143 ± 4	0.35

Figure S7. Ubiquitin helium CCS & CCS distributions. Top) Mass spectrum of Ubiquitin sprayed from 50 mM AmAc solution at pH 7.4, where charge states are denoted by z+. Upper middle) Total CCS distributions of Ubiquitin. Lower middle) Stacked CCS distribution plots for each ion normalised to the same intensity with magnification factors applied. Two black circles denote the presence of coincident dimer. Table) Average CCS_{He} values with replicate (n=3) standard deviations (±) and associated RSDs (%) for Ubiquitin obtained across the instrument platforms utilised.

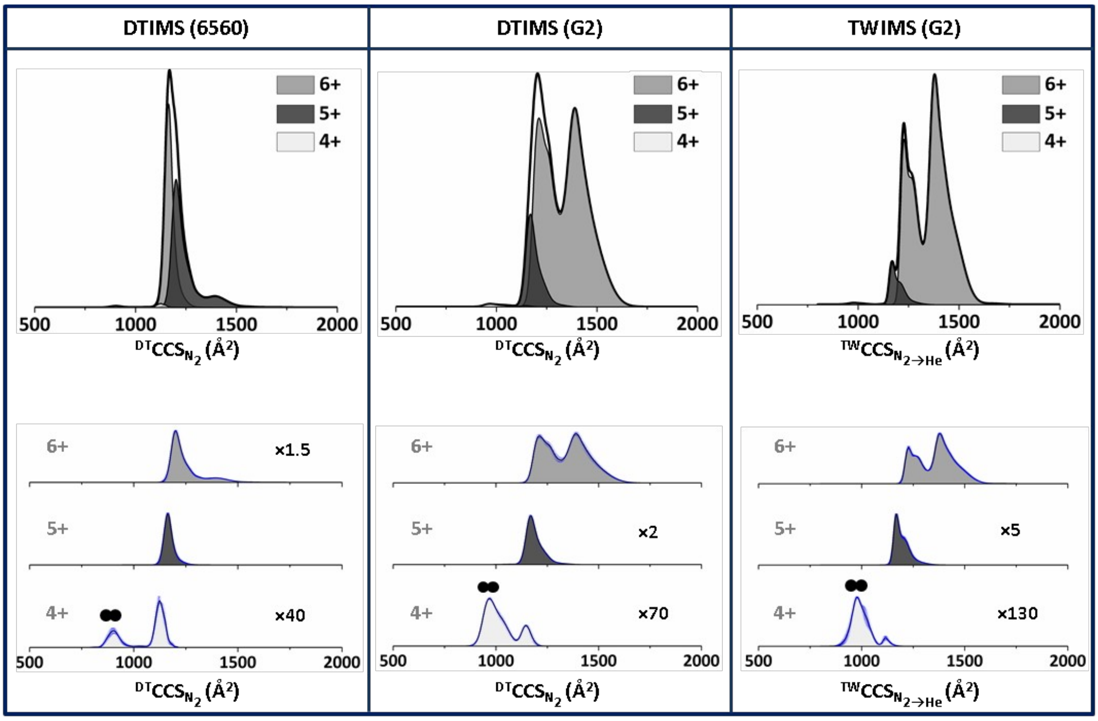

Protein			Nitrogen Drift Gas					
Ubiquitin (8566 Da)			6560-DTIMS		G2-DTIMS		G2-TWIMS	
Z_{Avg}	Species	#	$^{DT}CCS_{N_2}$ (Å^2)	%RSD	$^{DT}CCS_{N_2}$ (Å^2)	%RSD	$^{TW}CCS_{N_2}$ (Å^2)	%RSD
5.43 ± 0.18	$[M+4H]^{4+}$	1	1128 ± 13	1.15	1148 ± 10	0.90	1118 ± 3	0.45
	$[M+5H]^{5+}$	1	1163 ± 4	0.31	1166 ± 6	0.54	1167 ± 1	0.08
		2	-	-	1208 ± 4	0.35	1208 ± 3	0.28
	$[M+6H]^{6+}$	1	1199 ± 5	0.38	1209 ± 13	1.05	1229 ± 0.3	0.03
		2	1401 ± 2	0.11	1386 ± 4	0.32	1268 ± 2	0.15
		3	-	-	1466 ± 13	0.91	1382 ± 1.4	0.10

Figure S8. Ubiquitin nitrogen CCS & CCS distributions. Upper) Total CCS distributions of Ubiquitin. Lower) Stacked CCS distribution plots for each ion normalised to the same intensity with magnification factors applied. Two black circles denote the presence of coincident dimer. Table) Average CCS_{N2} values with replicate (n=3) standard deviations (±) and associated RSDs (%) for Ubiquitin obtained across the instrument platforms utilised. Interactive versions of Figures S7 & S8 are available online at https://france-ccs-2019.netlify.com/assets/ubi_s7&s8.

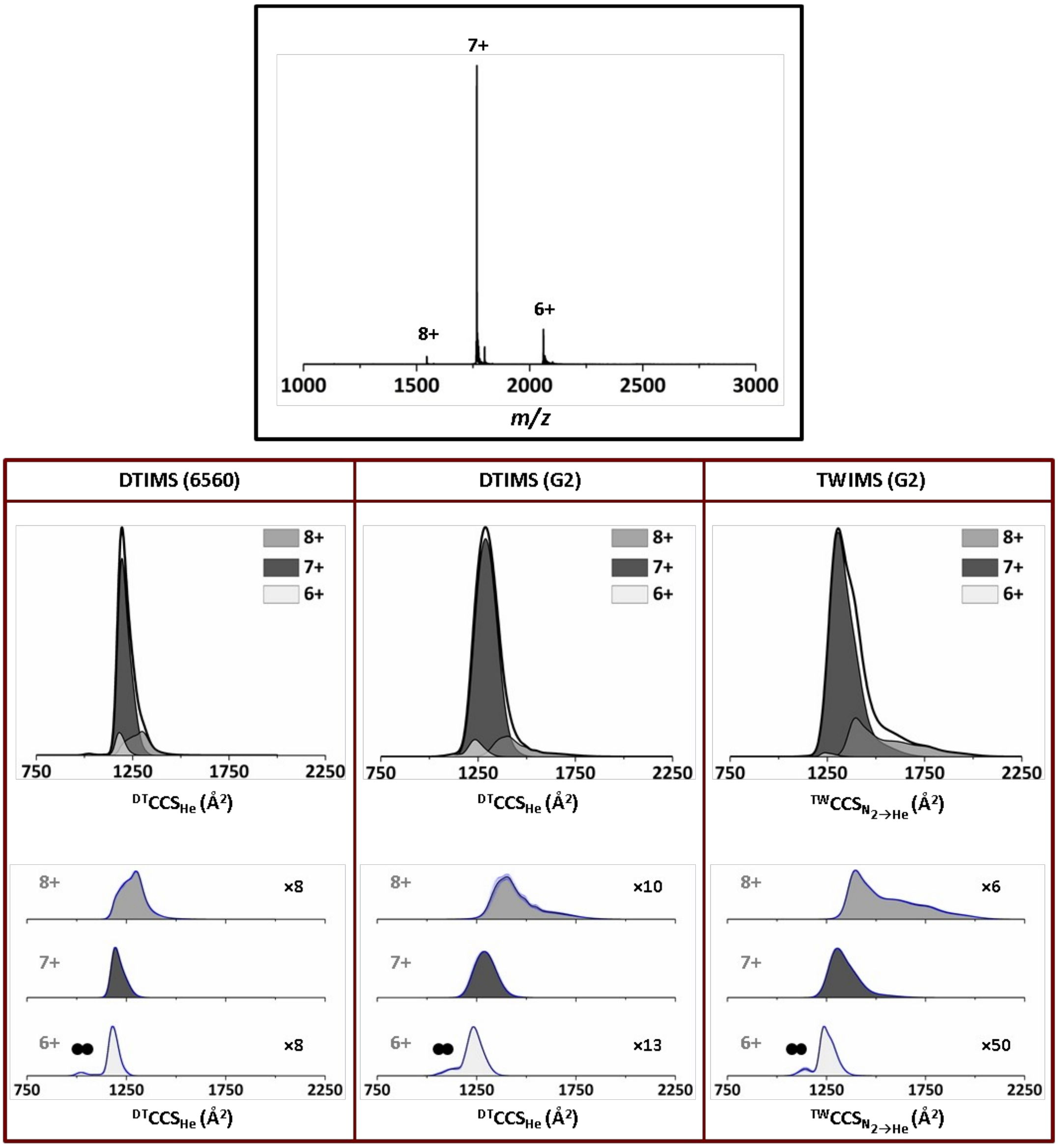

Protein			Helium Drift Gas					
Cytochrome c (12,358 Da)			6560-DTIMS		G2-DTIMS		G2-TWIMS	
Z_{Avg}	Species	#	$^{DT}CCS_{He}$ (Å²)	%RSD	$^{DT}CCS_{He}$ (Å²)	%RSD	$^{TW}CCS_{He}$ (Å²)	%RSD
6.96 ± 0.01	$[M+6H]^{6+}$	1	1182 ± 4	0.33	1234 ± 5	0.41	1238 ± 6	0.48
	$[M+7H]^{7+}$	1	1196 ± 1	0.09	1286 ± 12	0.93	1304 ± 6	0.49
		2	-	-	-	-	-	
	$[M+8H]^{8+}$	1	1258 ± 19	1.47	1373 ± 34	2.49	1399 ± 6	0.46
		2	1297 ± 2	0.14	1540 ± 17	1.12	1625 ± 11	0.67
		3	-	-	-	-	1768 ± 6	0.36
		4	-	-	-	-	1918 ± 12	0.62

Figure S9. Cytochrome c helium CCS & CCS distributions. Top) Mass spectrum of cytochrome c sprayed from 50 mM AmAc solution at pH 7.4, where charge states are denoted by z+. Upper middle) Total CCS distributions of Ubiquitin. Lower middle) Stacked CCS distribution plots for each ion normalised to the same intensity with magnification factors applied. Two black circles denote the presence of coincident dimer. Table) Average CCS_{He} values with replicate (n=3) standard deviations (±) and associated RSDs (%) for cytochrome c obtained across the instrument platforms utilised.

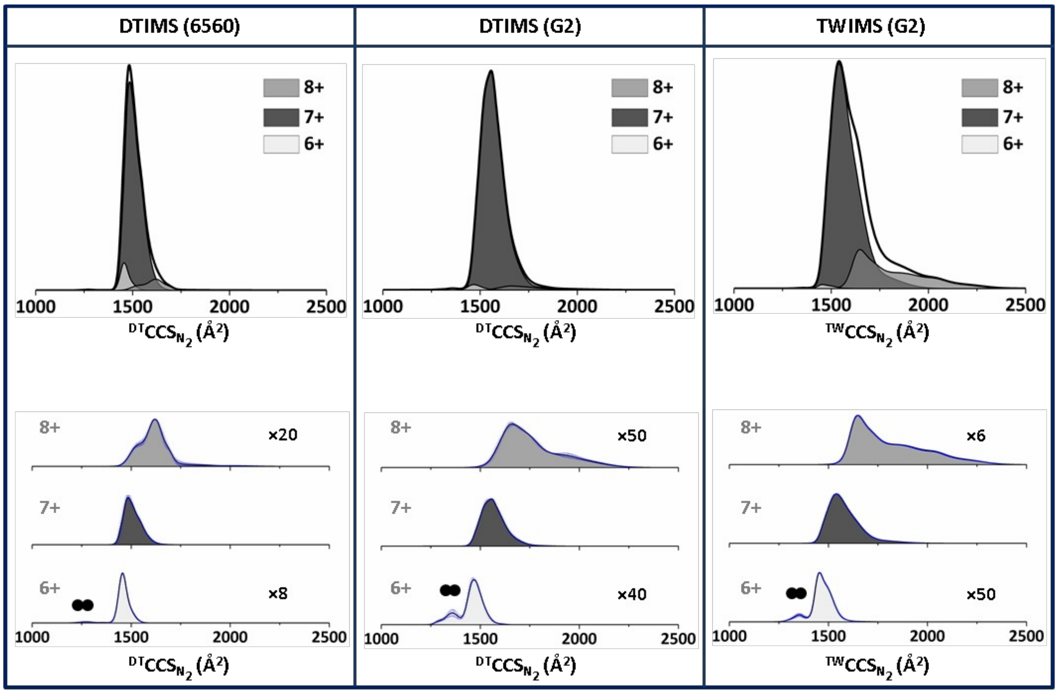

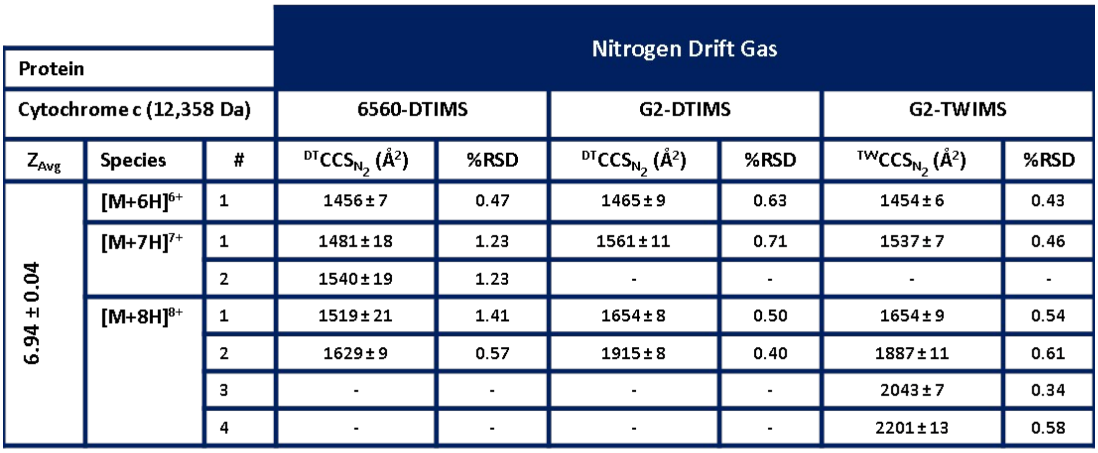

Protein			Nitrogen Drift Gas					
Cytochrome c (12,358 Da)			6560-DTIMS		G2-DTIMS		G2-TWIMS	
Z_{Avg}	Species	#	$^{DT}CCS_{N_2}$ (Å^2)	%RSD	$^{DT}CCS_{N_2}$ (Å^2)	%RSD	$^{TW}CCS_{N_2}$ (Å^2)	%RSD
6.94 ± 0.04	$[M+6H]^{6+}$	1	1456 ± 7	0.47	1465 ± 9	0.63	1454 ± 6	0.43
	$[M+7H]^{7+}$	1	1481 ± 18	1.23	1561 ± 11	0.71	1537 ± 7	0.46
		2	1540 ± 19	1.23	-	-	-	-
	$[M+8H]^{8+}$	1	1519 ± 21	1.41	1654 ± 8	0.50	1654 ± 9	0.54
		2	1629 ± 9	0.57	1915 ± 8	0.40	1887 ± 11	0.61
		3	-	-	-	-	2043 ± 7	0.34
		4	-	-	-	-	2201 ± 13	0.58

Figure S10. Cytochrome c nitrogen CCS & CCS distributions. Upper) Total CCS distributions of cytochrome c. Lower) Stacked CCS distribution plots for each ion normalised to the same intensity with magnification factors applied. Two black circles denote the presence of coincident dimer. Table) Average CCS_{N2} values with replicate (n=3) standard deviations (±) and associated RSDs (%) for cytochrome c obtained across the instrument platforms utilised. Interactive versions of Figures S9 & S10 are available online at https://france-ccs-2019.netlify.com/assets/cytc_s9&s10.

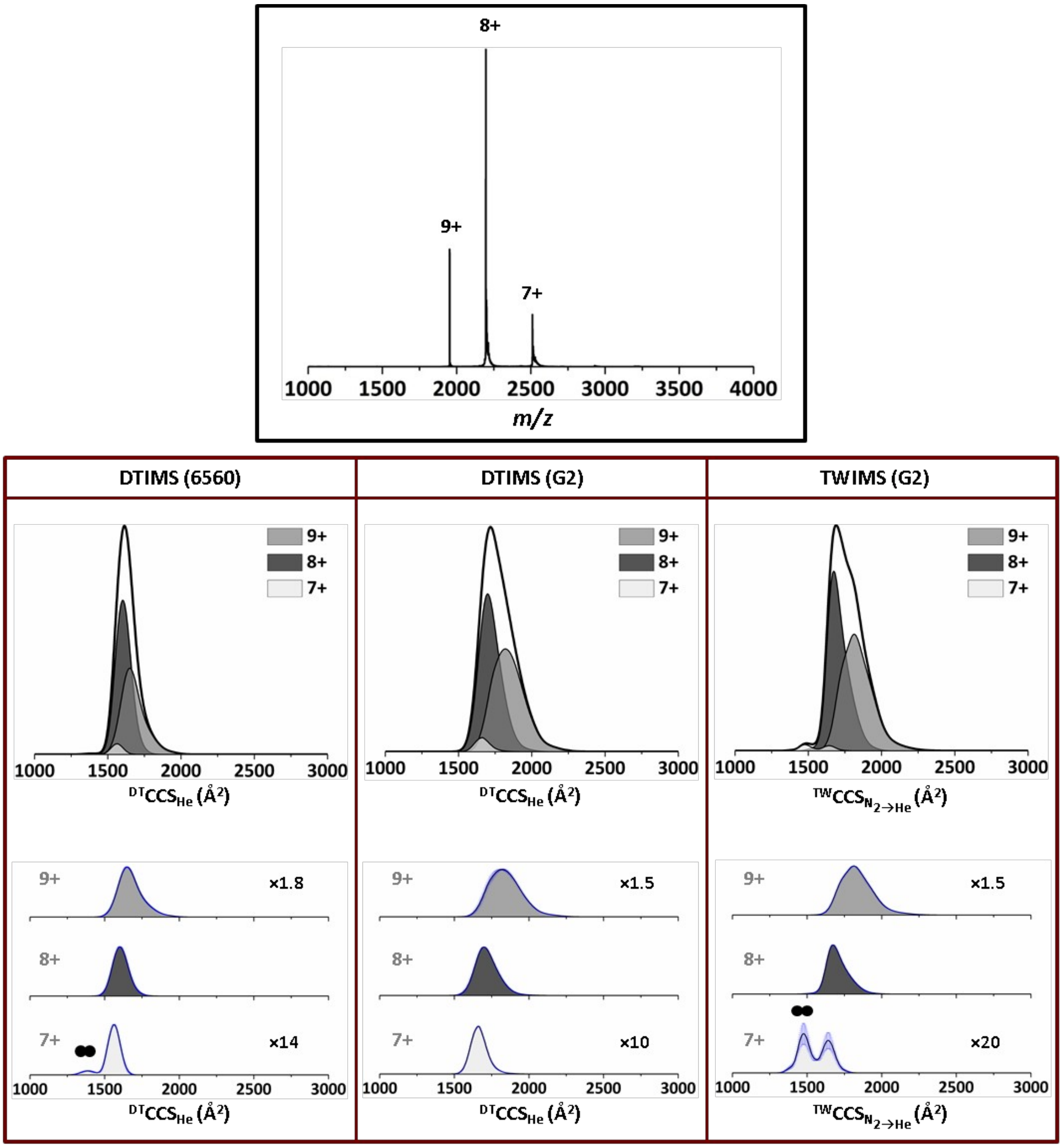

Protein			Helium Drift Gas					
Myoglobin (17,567 Da)			6560-DTIMS		G2-DTIMS		G2-TWIMS	
Z_{Avg}	Species	#	$^{DT}CCS_{He}$ (Å^2)	%RSD	$^{DT}CCS_{He}$ (Å^2)	%RSD	$^{TW}CCS_{He}$ (Å^2)	%RSD
8.13 ± 0.10	$[M+7H]^{7+}$	1	1566 ± 6	0.25	1664 ± 1	0.07	1641 ± 2	0.14
	$[M+8H]^{8+}$	1	1604 ± 5	0.33	1704 ± 4	0.21	1674 ± 12	0.71
	$[M+9H]^{9+}$	1	1649 ± 4	0.39	1832 ± 30	1.63	1713 ± 17	0.72
		2	-	-	-	-	1818 ± 13	0.98

Figure S11. Myoglobin helium CCS & CCS distributions. Top) Mass spectrum of myoglobin sprayed from 50 mM AmAc solution at pH 7.4, where charge states are denoted by z+. Upper middle) Total CCS distributions of myoglobin. Lower middle) Stacked CCS distribution plots for each ion normalised to the same intensity with magnification factors applied. Two black circles denote the presence of coincident dimer. Table) Average CCS_{He} values with replicate (n=3) standard deviations (±) and associated RSDs (%) for myoglobin obtained across the instrument platforms utilised.

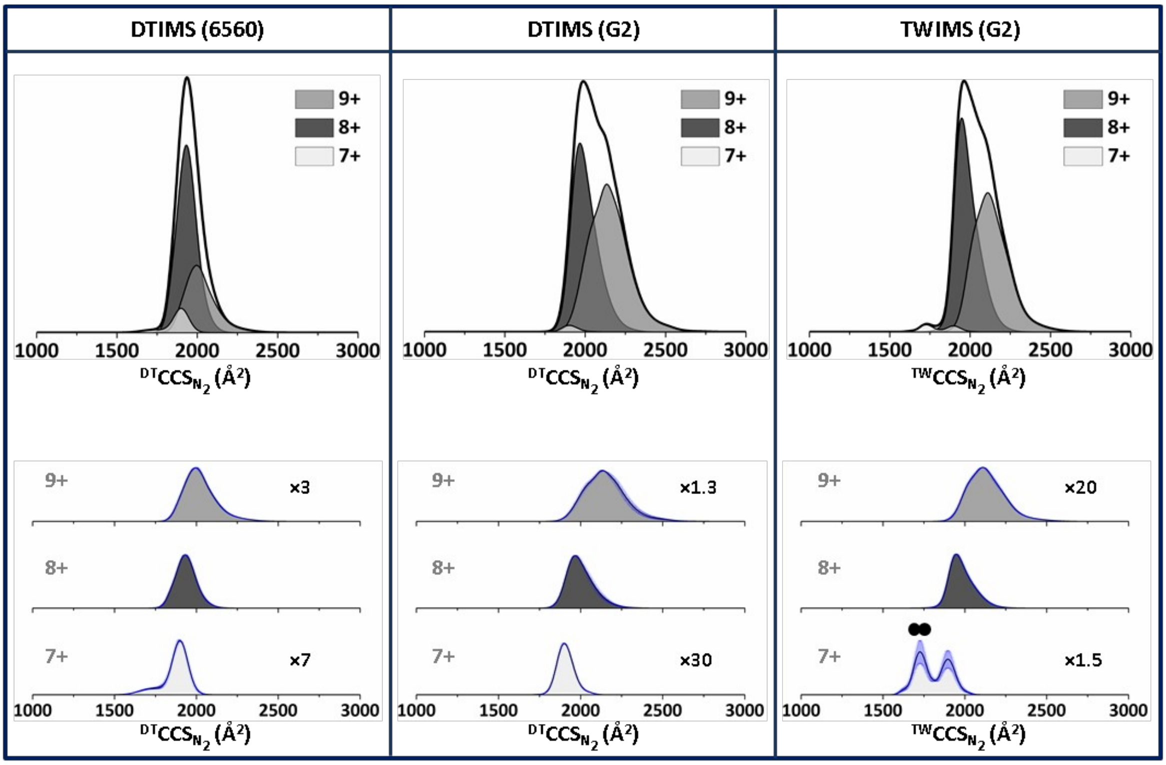

Protein			Nitrogen Drift Gas					
Myoglobin (17,567 Da)			6560-DTIMS		G2-DTIMS		G2-TWIMS	
Z_{Avg}	Species	#	$^{DT}CCS_{N_2}$ (Å^2)	%RSD	$^{DT}CCS_{N_2}$ (Å^2)	%RSD	$^{TW}CCS_{N_2}$ (Å^2)	%RSD
8.11 ± 0.09	$[M+7H]^{7+}$	1	1899 ± 12	0.62	1903 ± 8	0.40	1896 ± 3	0.17
	$[M+8H]^{8+}$	1	1934 ± 2	0.11	1972 ± 9	0.44	1949 ± 10	0.51
	$[M+9H]^{9+}$	1	1995 ± 13	0.63	2040 ± 17	0.85	2003 ± 16	0.43
		2	-	-	2149 ± 26	1.19	2114 ± 14	0.94

Figure S12. Myoglobin nitrogen CCS & CCS distributions. Upper) Total CCS distributions of myoglobin. Lower) Stacked CCS distribution plots for each ion normalised to the same intensity with magnification factors applied. Two black circles denote the presence of coincident dimer. Table) Average CCS_{N2} values with replicate (n=3) standard deviations (±) and associated RSDs (%) for myoglobin obtained across the instrument platforms utilised. Interactive versions of Figures S11 & S12 are available online at https://france-ccs-2019.netlify.com/assets/myo_s11&s12.

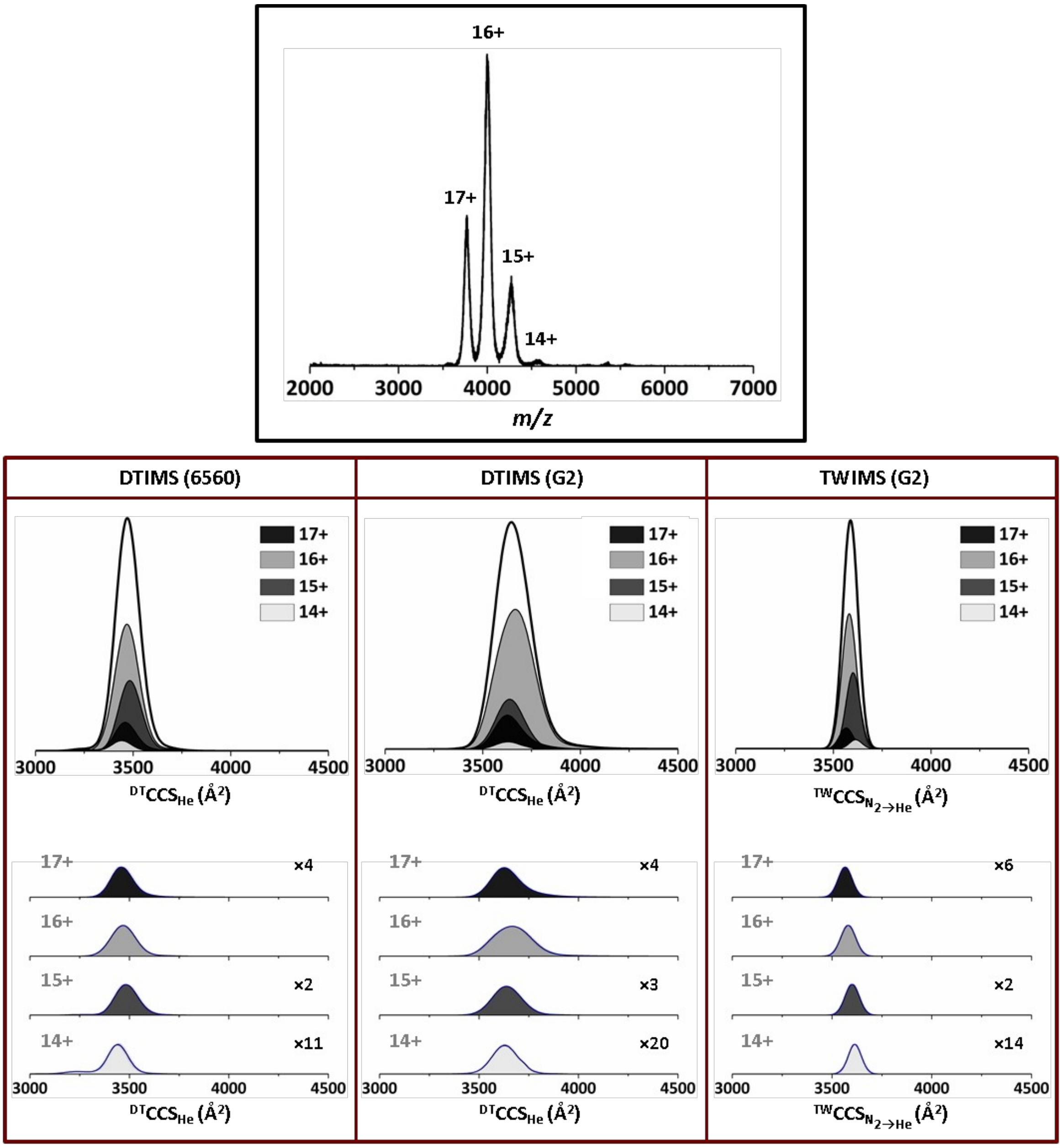

Protein			Helium Drift Gas					
Avidin (4n = 63,933 Da)			6560-DTIMS		G2-DTIMS		G2-TWIMS	
Z_{avg}	Species	#	$^{DT}CCS_{He}$ (Å^2)	%RSD	$^{DT}CCS_{He}$ (Å^2)	%RSD	$^{TW}CCS_{He}$ (Å^2)	%RSD
15.75 ± 0.07	$[4M+14H]^{14+}$	1	3441 ± 16	0.45	3633 ± 3	0.35	3614 ± 5	0.13
	$[4M+15H]^{15+}$	1	3485 ± 14	0.39	3640 ± 9	0.25	3601 ± 2	0.07
	$[4M+16H]^{16+}$	1	3471 ± 5	0.14	3665 ± 14	0.38	3581 ± 3	0.08
	$[4M+17H]^{17+}$	1	3467 ± 12	0.35	3633 ± 13	0.35	3566 ± 2	0.06

Figure S13. Avidin helium CCS & CCS distributions. Top) Mass spectrum of avidin sprayed from 200 mM AmAc solution at pH 7.4, where charge states are denoted by z+. Upper middle) Total CCS distributions of avidin. Lower middle) Stacked CCS distribution plots for each ion normalised to the same intensity with magnification factors applied. Table) Average CCS_{He} values with replicate (n=3) standard deviations (±) and associated RSDs (%) for avidin obtained across the instrument platforms utilised.

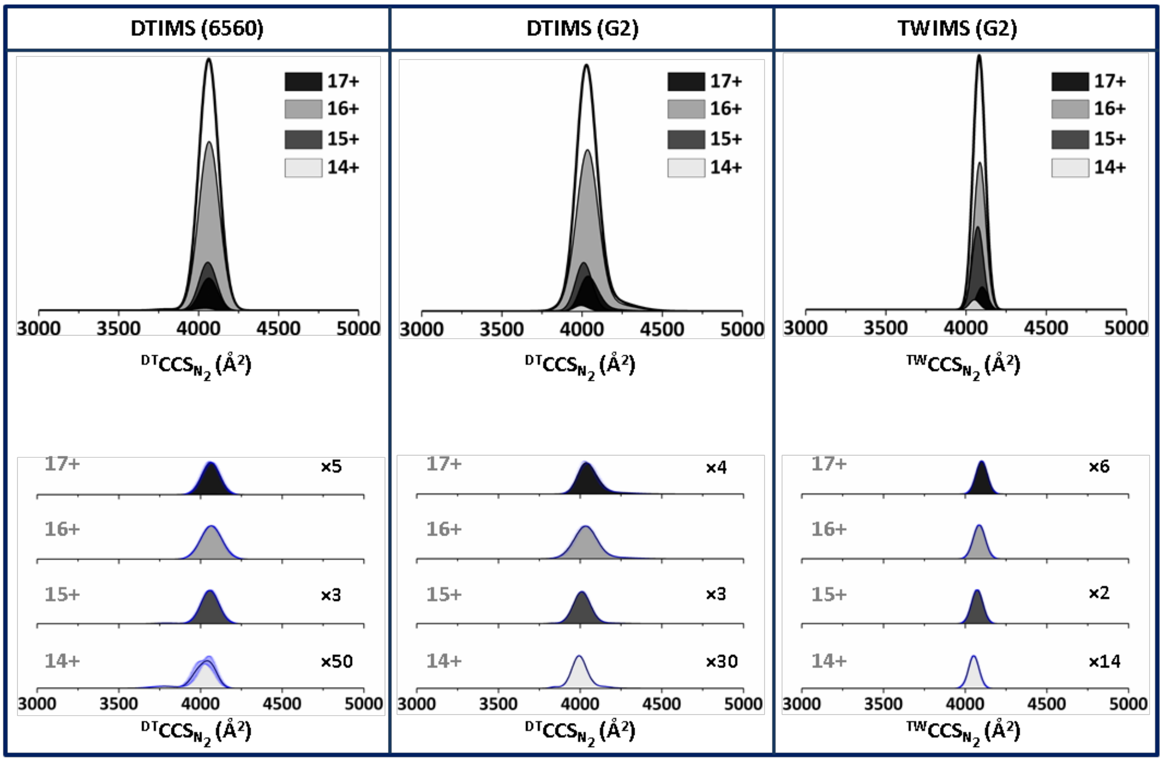

Protein			Nitrogen Drift Gas					
Avidin (4n = 63,933 Da)			6560-DTIMS		G2-DTIMS		G2-TWIMS	
Z_{avg}	Species	#	$^{DT}CCS_{N_2}$ (Å^2)	%RSD	$^{DT}CCS_{N_2}$ (Å^2)	%RSD	$^{TW}CCS_{N_2}$ (Å^2)	%RSD
15.83 ± 0.12	$[4M+14H]^{14+}$	1	4029 ± 46	1.14	3996 ± 6	0.15	4053 ± 5	0.12
	$[4M+15H]^{15+}$	1	4057 ± 13	0.33	4008 ± 14	0.34	4073 ± 2	0.05
	$[4M+16H]^{16+}$	1	4066 ± 11	0.26	4038 ± 14	0.34	4086 ± 3	0.07
	$[4M+17H]^{17+}$	1	4063 ± 23	0.56	4041 ± 31	0.77	4101 ± 2	0.06

Figure S14. Avidin nitrogen CCS & CCS distributions. Upper) Total CCS distributions of avidin. Lower) Stacked CCS distribution plots for each ion normalised to the same intensity with magnification factors applied. Table) Average CCS_{N_2} values with replicate (n=3) standard deviations (±) and associated RSDs (%) for avidin obtained across the instrument platforms utilised. Interactive versions of Figures S13 & S14 are available online at https://france-ccs-2019.netlify.com/assets/avi_s13&s14.

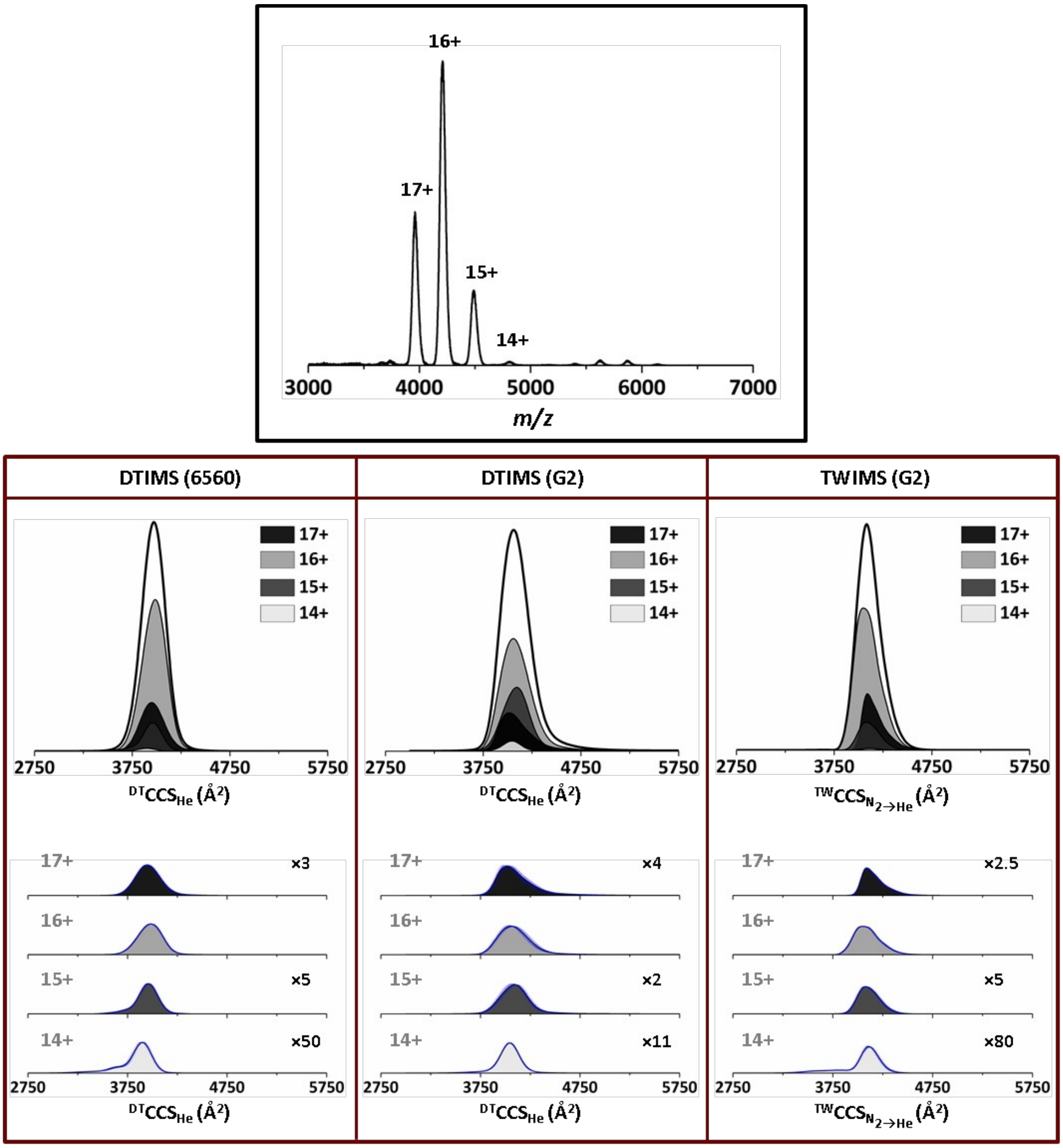

Protein			Helium Drift Gas					
BSA (66,433 Da)			6560-DTIMS		G2-DTIMS		G2-TWIMS	
Z_{avg}	Species	#	$^{DT}CCS_{He}$ (Å^2)	%RSD	$^{DT}CCS_{He}$ (Å^2)	%RSD	$^{TW}CCS_{He}$ (Å^2)	%RSD
15.95 ± 0.22	$[4M+14H]^{14+}$	1	3891 ± 28	0.73	4041 ± 4	0.11	4108 ± 24	0.59
	$[4M+15H]^{15+}$	1	3956 ± 22	0.56	4093 ± 55	1.35	4087 ± 31	0.76
	$[4M+16H]^{16+}$	1	3989 ± 15	0.36	4084 ± 63	1.53	4051 ± 16	0.39
	$[4M+17H]^{17+}$	1	3956 ± 15	0.39	4026 ± 59	1.44	4094 ± 11	0.26

Figure S15. BSA helium CCS & CCS distributions. Top) Mass spectrum of BSA sprayed from 200 mM AmAc solution at pH 7.4, where charge states are denoted by z+. Upper middle) Total CCS distributions of BSA. Lower middle) Stacked CCS distribution plots for each ion normalised to the same intensity with magnification factors applied. Table) Average CCS_{He} values with replicate (n=3) standard deviations (±) and associated RSDs (%) for BSA obtained across the instrument platforms utilised.

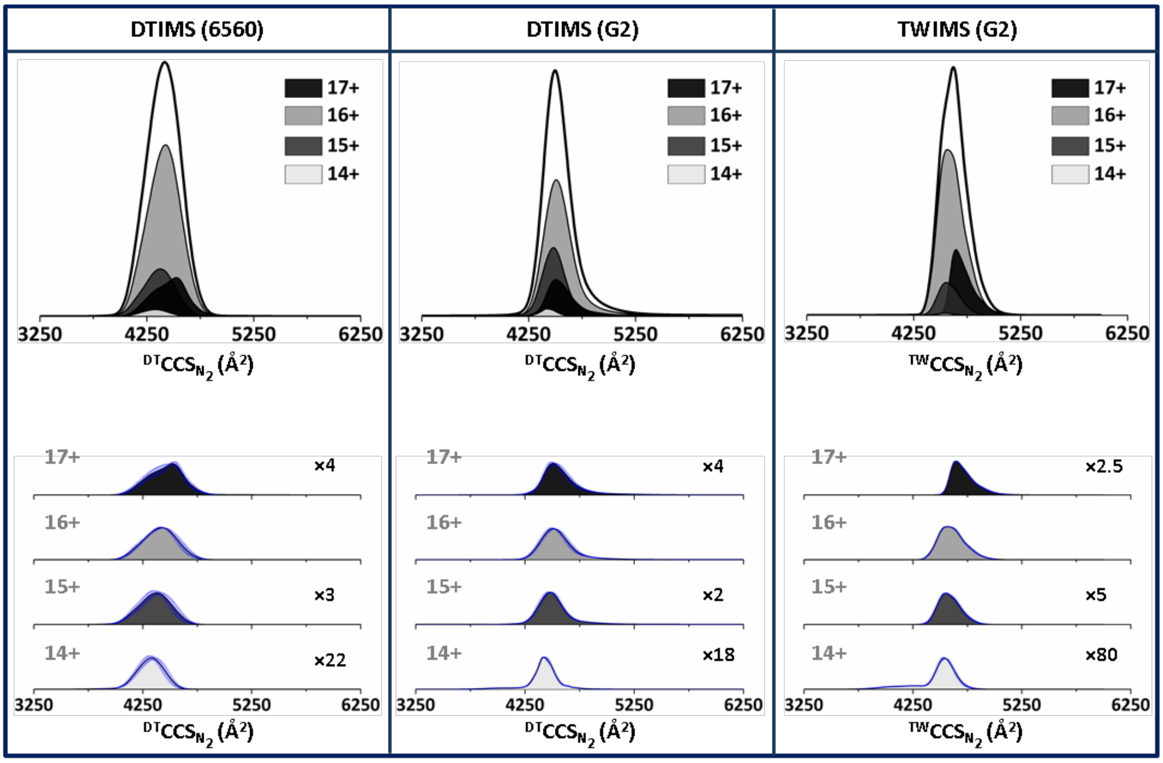

Protein			Nitrogen Drift Gas					
BSA (66,433 Da)			6560-DTIMS		G2-DTIMS		G2-TWIMS	
Z_{avg}	Species	#	$^{DT}CCS_{N_2}$ (Å^2)	%RSD	$^{DT}CCS_{N_2}$ (Å^2)	%RSD	$^{TW}CCS_{N_2}$ (Å^2)	%RSD
15.85 ± 0.12	$[M+14H]^{14+}$	1	4349 ± 74	1.70	4425 ± 19	0.43	4535 ± 23	0.50
	$[M+15H]^{15+}$	1	4392 ± 96	2.18	4478 ± 35	0.79	4548 ± 20	0.44
	$[M+14H]^{16+}$	1	4445 ± 68	1.53	4514 ± 51	1.14	4567 ± 18	0.40
	$[M+17H]^{17+}$	1	4506 ± 80	1.77	4523 ± 54	1.18	4648 ± 10	0.22

Figure S16. BSA nitrogen CCS & CCS distributions. Upper) Total CCS distributions of BSA. Lower) Stacked CCS distribution plots for each ion normalised to the same intensity with magnification factors applied. Table) Average CCS_{N2} values with replicate (n=3) standard deviations (±) and associated RSDs (%) for BSA obtained across the instrument platforms utilised. Interactive versions of Figures S15 & S16 are available online at https://france-ccs-2019.netlify.com/assets/bsa_s15&s16.

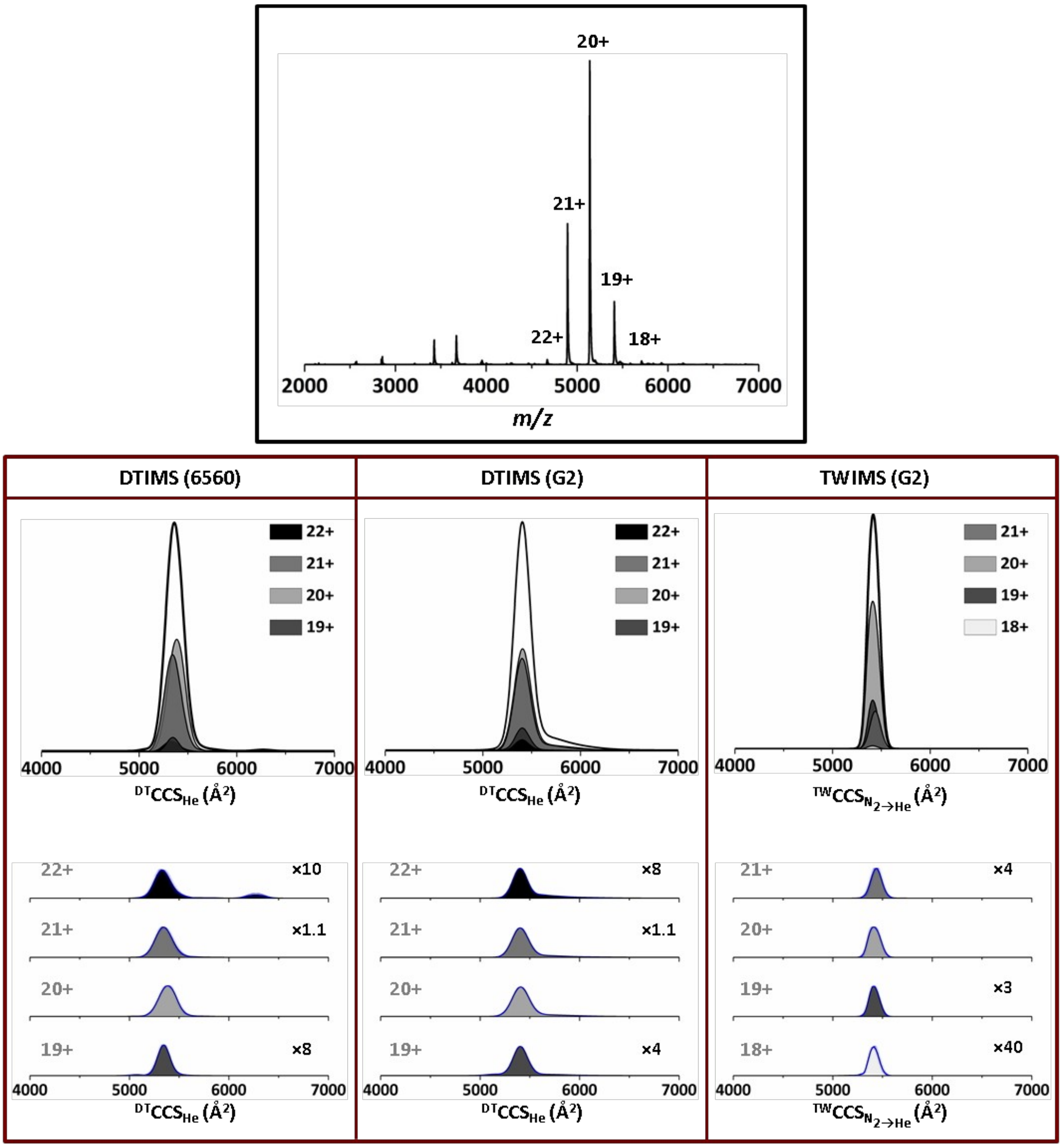

Protein			Helium Drift Gas					
Concanavalin A (4n = 102,393 Da)			6560-DTIMS		G2-DTIMS		G2-TWIMS	
Z_{avg}	Species	#	$^{DT}CCS_{He}$ (Å²)	%RSD	$^{DT}CCS_{He}$ (Å²)	%RSD	$^{TW}CCS_{He}$ (Å²)	%RSD
20.20 ± 0.30	$[4M+18H]^{18+}$	1	-	-	-	-	5412 ± 16	0.30
	$[4M+19H]^{19+}$	1	5340 ± 15	0.28	5399 ± 2	0.04	5409 ± 8	0.14
	$[4M+20H]^{20+}$	1	5384 ± 20	0.38	5397 ± 1	0.03	5412 ± 14	0.27
	$[4M+21H]^{21+}$	1	5345 ± 29	0.53	5401 ± 1	0.01	5434 ± 18	0.33
	$[4M+22H]^{22+}$	1	5335 ± 23	0.45	5405 ± 1	0.01	-	-
		2	6285 ± 24	0.38	-	-	-	-

Figure S17. Concanavalin a helium CCS & CCS distributions. Top) Mass spectrum of concanavalin a sprayed from 200 mM AmAc solution at pH 7.4, where charge states are denoted by z+. Upper middle) Total CCS distributions of concanavalin a. Lower middle) Stacked CCS distribution plots for each ion normalised to the same intensity with magnification factors applied. Table) Average CCS_{He} values with replicate (n=3) standard deviations (±) and associated RSDs (%) for concanavalin a obtained across the instrument platforms utilised.

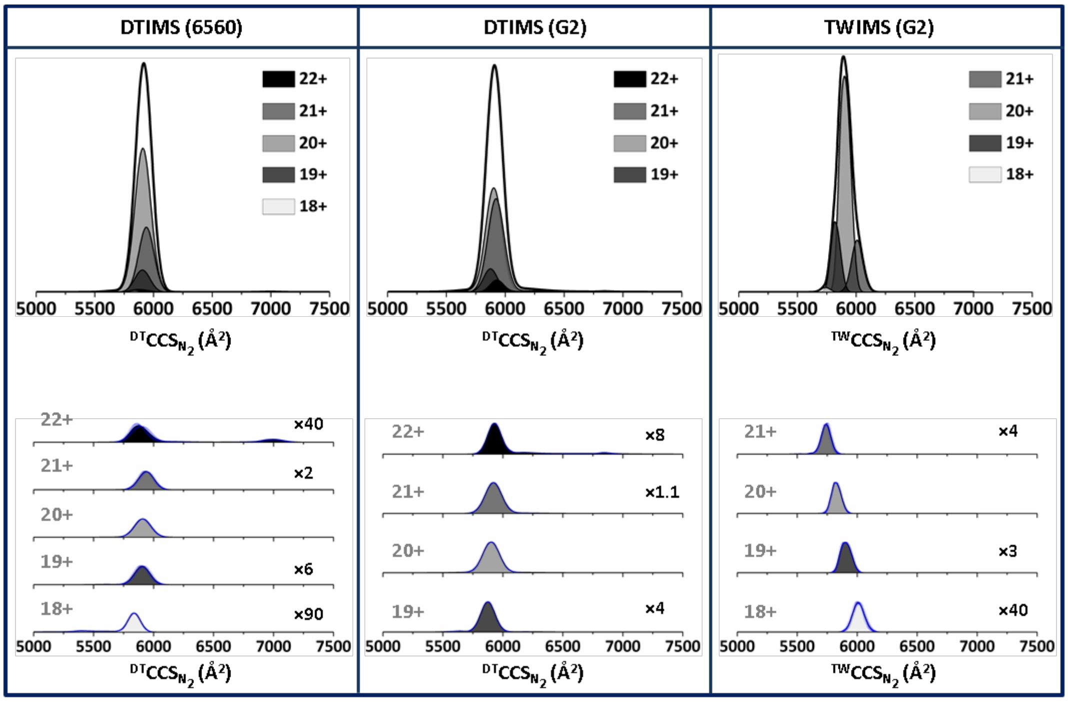

Protein			Nitrogen Drift Gas					
Concanavalin A (4n = 102,393 Da)			6560-DTIMS		G2-DTIMS		G2-TWIMS	
Z_{avg}	Species	#	$^{DT}CCS_{N_2}$ (Å²)	%RSD	$^{DT}CCS_{N_2}$ (Å²)	%RSD	$^{TW}CCS_{N_2}$ (Å²)	%RSD
20.13 ± 0.25	$[4M+18H]^{18+}$	1	5838 ± 7	0.11	-	-	5740 ± 15	0.27
	$[4M+19H]^{19+}$	1	5905 ± 32	0.54	5879 ± 13	0.22	5820 ± 5	0.09
	$[4M+20H]^{20+}$	1	5913 ± 5	0.09	5902 ± 9	0.15	5900 ± 11	0.18
	$[4M+21H]^{21+}$	1	5937 ± 25	0.42	5921 ± 9	0.16	5997 ± 14	0.24
	$[4M+22H]^{22+}$	1	5890 ± 34	0.58	5930 ± 9	0.16	-	
		2	7011 ± 38	0.55	6846 ± 36	0.52	-	

Figure S18. Concanavalin a nitrogen CCS & CCS distributions. Upper) Total CCS distributions of concanavalin a. Lower) Stacked CCS distribution plots for each ion normalised to the same intensity with magnification factors applied. Table) Average CCS_{N_2} values with replicate (n=3) standard deviations (±) and associated RSDs (%) for concanavalin a obtained across the instrument platforms utilised. Interactive versions of Figures S17 & S18 are available online at https://france-ccs-2019.netlify.com/assets/cona_s17&s18.

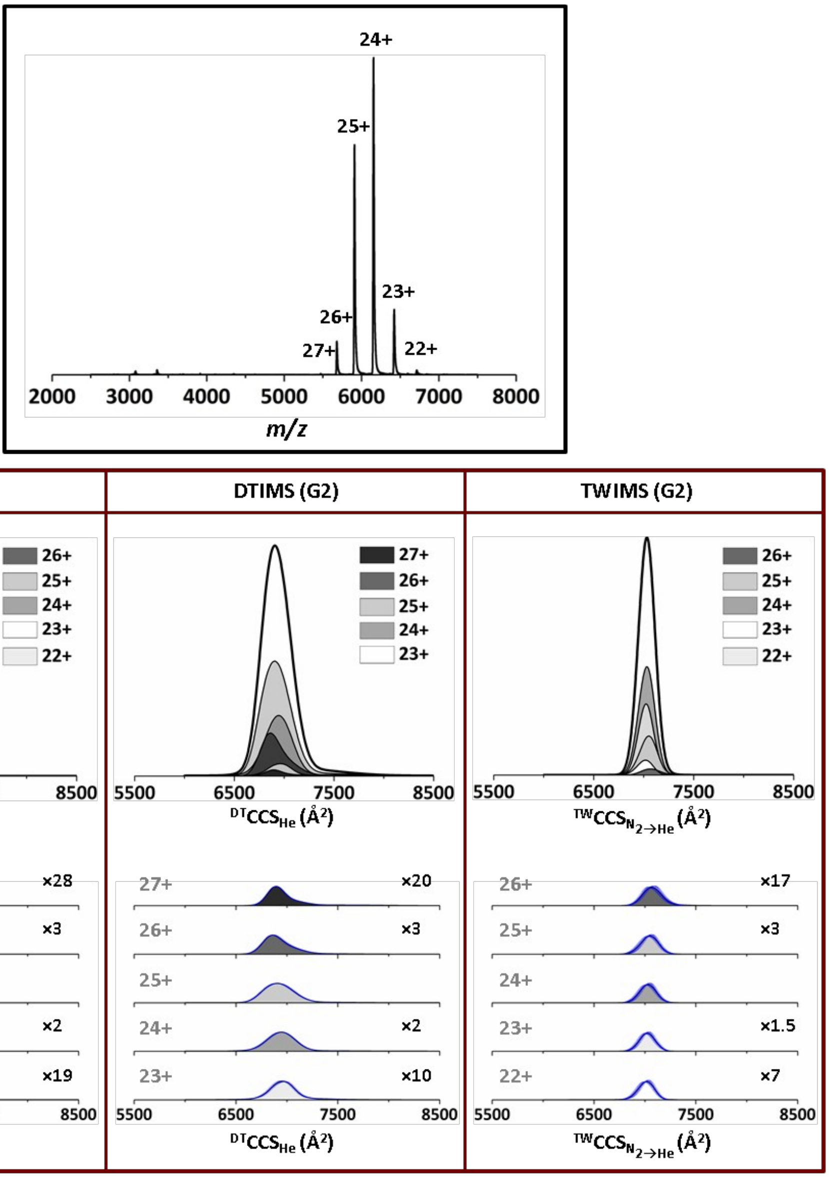

Protein			Helium Drift Gas					
Alcohol Dehydrogenase (4n = 147,659 Da)			6560-DTIMS		G2-DTIMS		G2-TWIMS	
Z_{Avg}	Species	#	$^{DT}CCS_{He}$ (Å^2)	%RSD	$^{DT}CCS_{He}$ (Å^2)	%RSD	$^{TW}CCS_{He}$ (Å^2)	%RSD
24.20 ± 0.54	$[4M+22H]^{22+}$	1	6579 ± 45	0.69	-	-	7015 ± 47	0.66
	$[4M+23H]^{23+}$	1	6584 ± 35	0.53	6968 ± 48	0.68	7020 ± 42	0.60
	$[4M+24H]^{24+}$	1	6606 ± 16	0.24	6943 ± 17	0.24	7027 ± 46	0.65
	$[4M+25H]^{25+}$	1	6588 ± 16	0.23	6914 ± 22	0.32	7045 ± 51	0.72
	$[4M+26H]^{26+}$	1	6557 ± 36	0.54	6879 ± 12	0.17	7069 ± 49	0.70
	$[4M+27H]^{27+}$	1	-	-	6908 ± 5	0.05	-	-

Figure S19. Alcohol dehydrogenase helium CCS & CCS distributions. Top) Mass spectrum of alcohol dehydrogenase sprayed from 200 mM AmAc solution at pH 7.4, where charge states are denoted by z+. Upper middle) Total CCS distributions of alcohol dehydrogenase. Lower middle) Stacked CCS distribution plots for each ion normalised to the same intensity with magnification factors applied. Table) Average CCS_{He} values with replicate (n=3) standard deviations (±) and associated RSDs (%) for alcohol dehydrogenase obtained across the instrument platforms utilised.

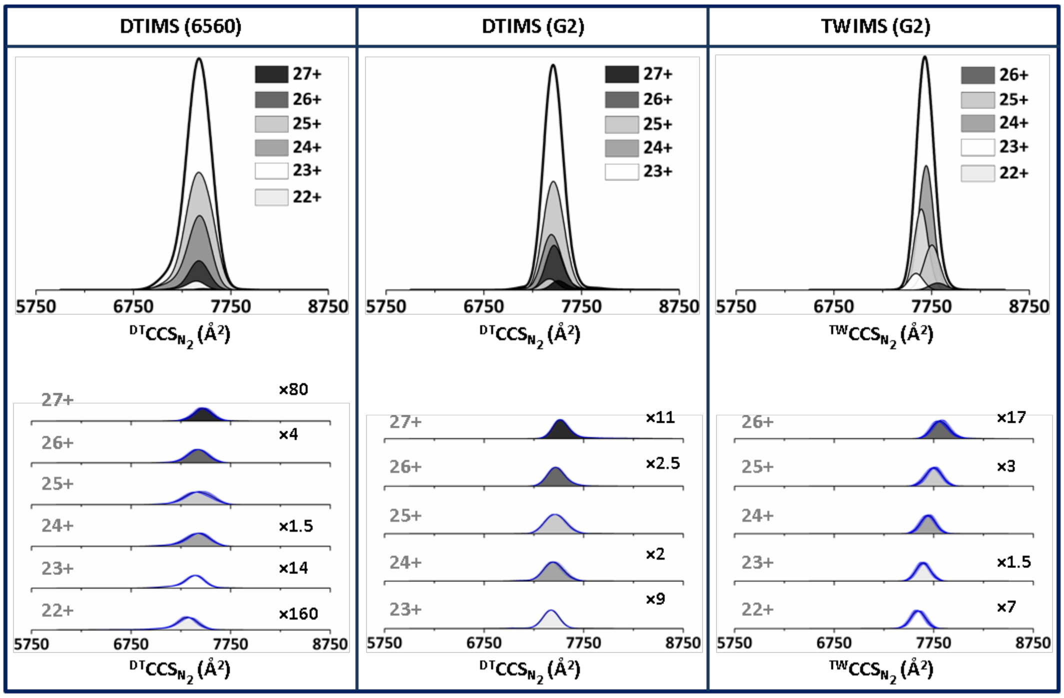

Protein			Nitrogen Drift Gas					
Alcohol Dehydrogenase (4n = 147,659 Da)			**6560-DTIMS**		**G2-DTIMS**		**G2-TWIMS**	
Z_{avg}	**Species**	**#**	**$^{DT}CCS_{N_2}$ (Å^2)**	**%RSD**	**$^{DT}CCS_{N_2}$ (Å^2)**	**%RSD**	**$^{TW}CCS_{N_2}$ (Å^2)**	**%RSD**
24.45 ± 0.62	$[4M+22H]^{22+}$	1	7330 ± 70	0.70	-	-	7594 ± 44	0.58
	$[4M+23H]^{23+}$	1	7399 ± 32	0.43	7422 ± 4	0.06	7640 ± 33	0.44
	$[4M+24H]^{24+}$	1	7427 ± 52	0.71	7447 ± 37	0.50	7693 ± 41	0.54
	$[4M+25H]^{25+}$	1	7429 ± 70	0.94	7465 ± 22	0.30	7750 ± 47	0.60
	$[4M+26H]^{26+}$	1	7424 ± 36	0.49	7473 ± 16	0.21	7814 ± 45	0.58
	$[4M+27H]^{27+}$	1	7470 ± 51	0.68	7520 ± 18	0.24	-	-

Figure S20. Alcohol dehydrogenase nitrogen CCS & CCS distributions. Upper) Total CCS distributions of alcohol dehydrogenase. Lower) Stacked CCS distribution plots for each ion normalised to the same intensity with magnification factors applied. Table) Average CCS$_{N2}$ values with replicate (n=3) standard deviations (±) and associated RSDs (%) for alcohol dehydrogenase obtained across the instrument platforms utilised. Interactive versions of Figures S19 & S20 are available online at https://france-ccs-2019.netlify.com/assets/alcdehy_s19&s20**.**

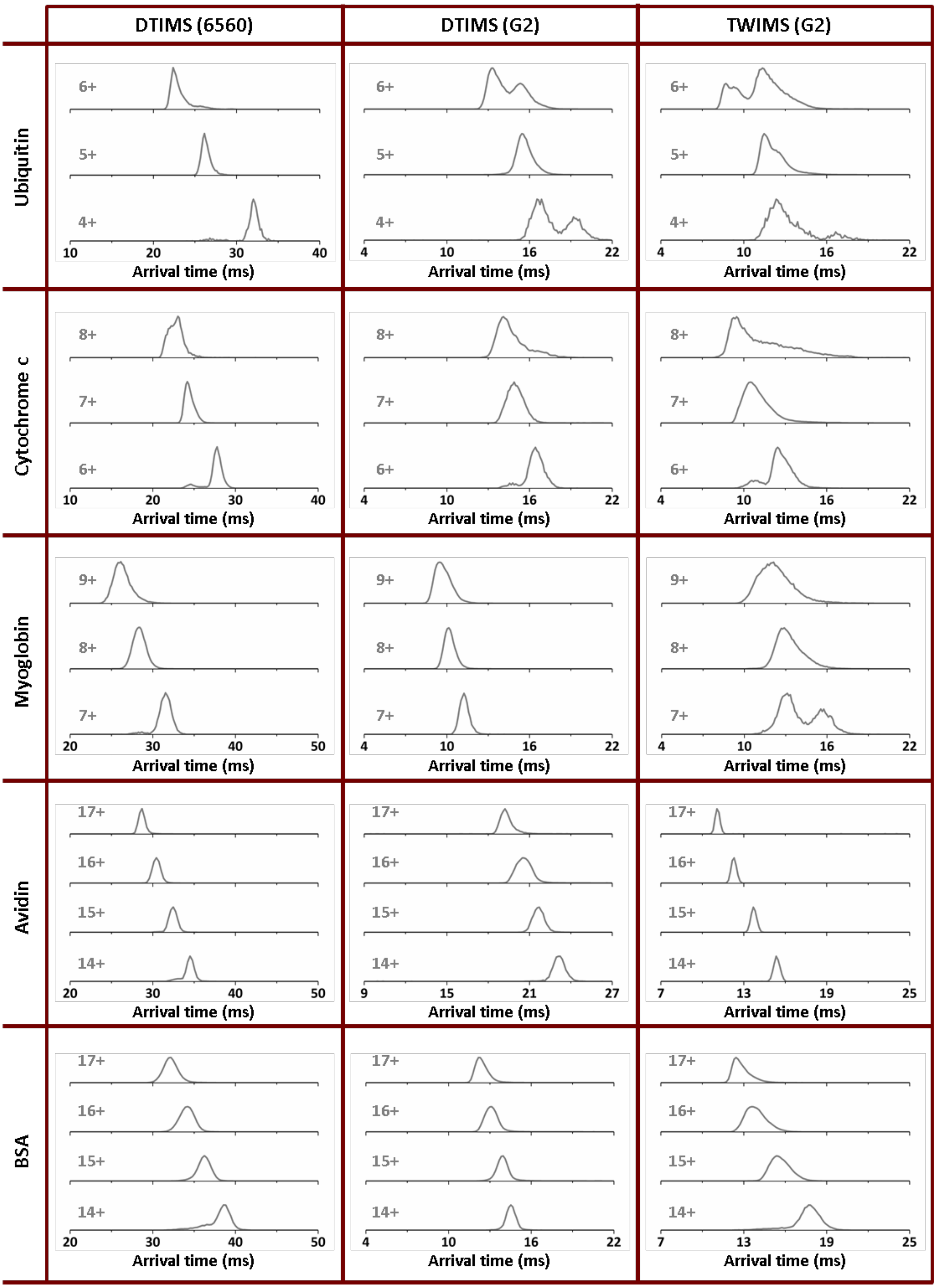
DTIMS (6560)
DTIMS (G2)
TWIMS (G2)
Ubiquitin
6+
5+
4+
Cytochrome c
8+
7+
6+
Myoglobin
9+
8+
7+
Avidin
17+
16+
15+
14+
BSA
17+
16+
15+
14+
10 20 30 40
20 30 40 50
4 10 16 22
9 15 21 27
7 13 19 25
Arrival time (ms)

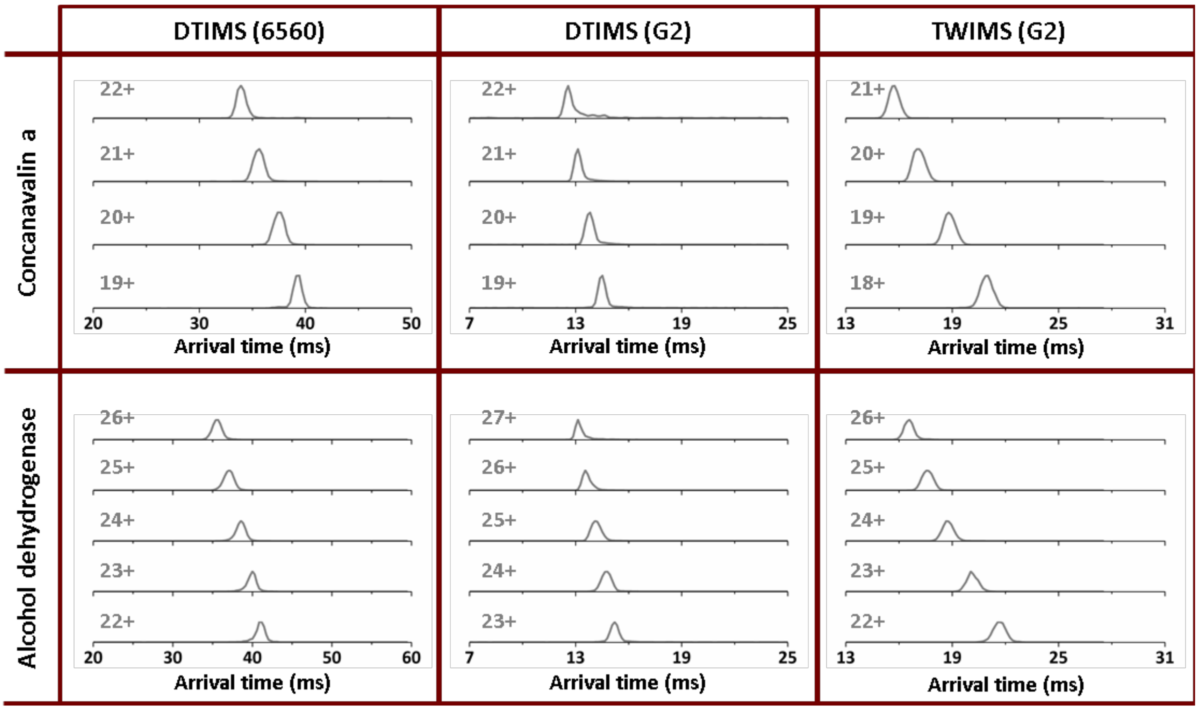

Figure S21. Raw ATDs (He).Raw single replicate ATDs, obtained with He as the drift gas, for all of the protein/protein complex ions analysed across the instruments utilised within this study.

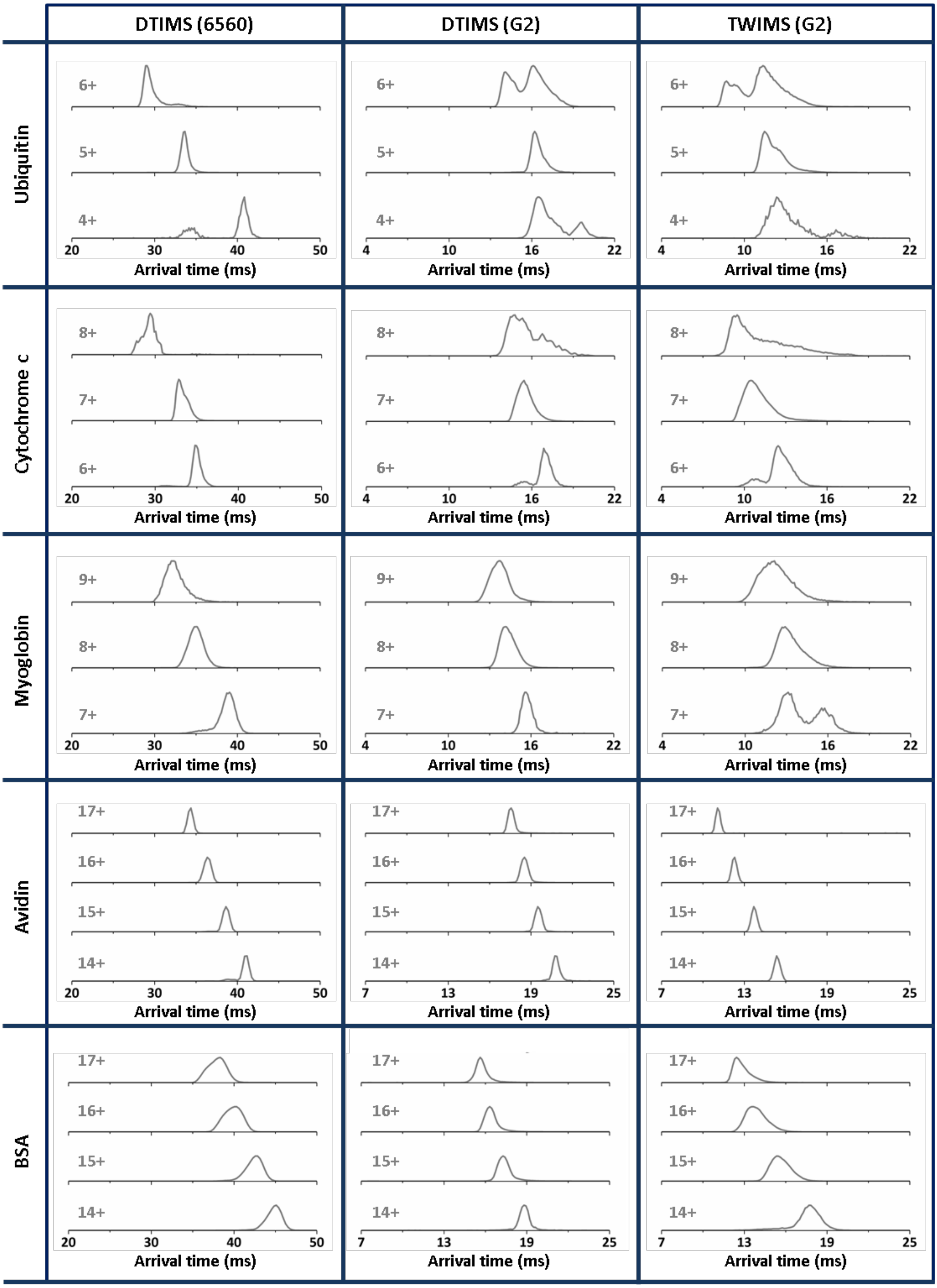
DTIMS (6560)
DTIMS (G2)
TWIMS (G2)
Ubiquitin
6+
5+
4+
Cytochrome c
8+
7+
6+
Myoglobin
9+
8+
7+
Avidin
17+
16+
15+
14+
BSA
17+
16+
15+
14+
20
30
40
50
4
10
16
22
7
13
19
25
Arrival time (ms)

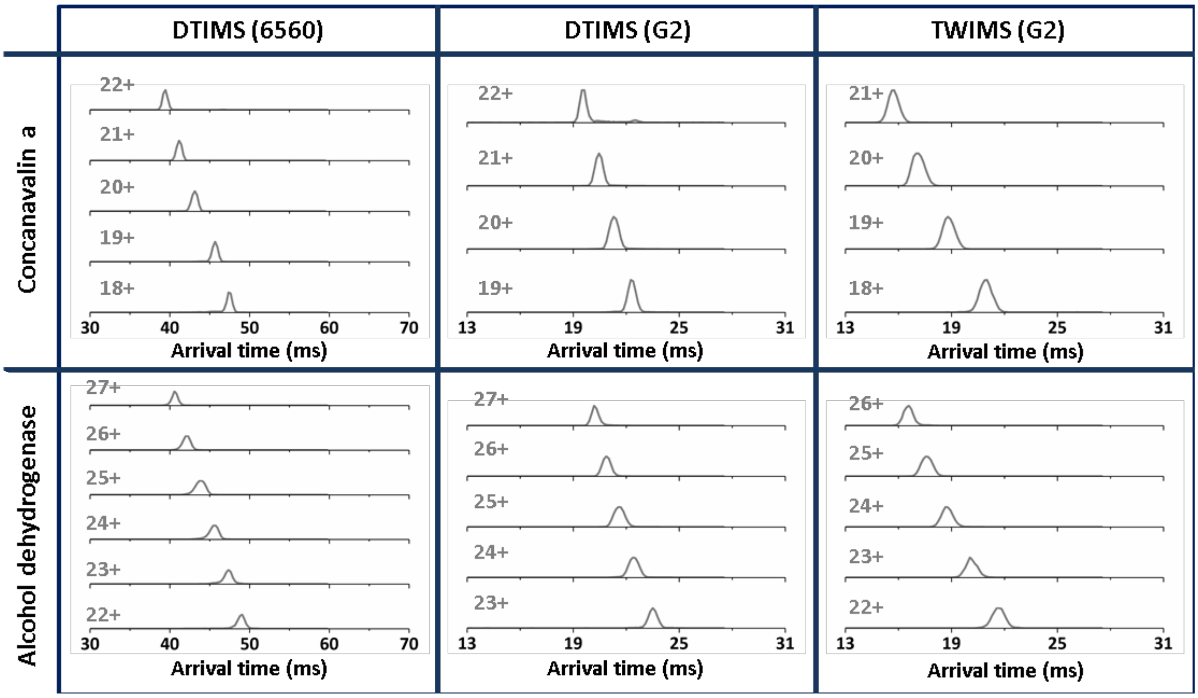

Figure S22. ATDs (N_2). Raw single replicate ATDs, obtained with N_2 as the drift gas, for all of the protein/protein complex ions analysed across the instruments utilised within this study. Interactive versions of Figures S21 & S22 are available online at: 1) https://france-ccs-2019.netlify.com/assets/ubi_s21&s22, 2) https://france-ccs-2019.netlify.com/assets/cytc_s21&s22, 3) https://france-ccs-2019.netlify.com/assets/myo_s21&s22, 4) https://france-ccs-2019.netlify.com/assets/avi_s21&s22, 5) https://france-ccs-2019.netlify.com/assets/bsa_s21&s22, 6) https://france-ccs-2019.netlify.com/assets/cona_s21&s22, 7) https://france-ccs-2019.netlify.com/assets/alcdehy_s21&s22.

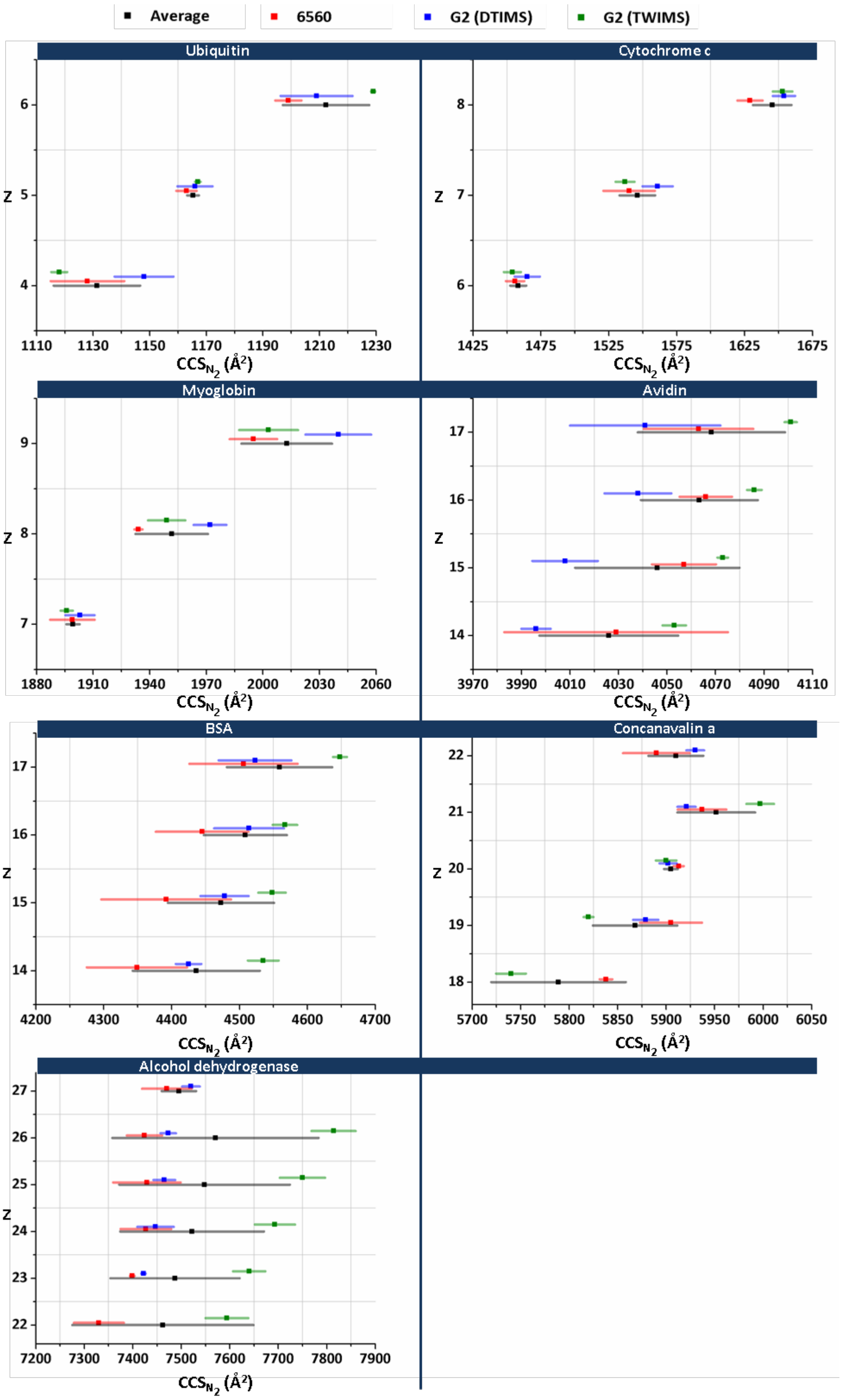

Figure S23. Scatter plots showing the range of CCS$_{N_2}$ values taken for the protein/protein complexes analysed within this study across the instrumental platforms utilised. In all cases the CCS for the single most abundant conformation for each charge state was compared across the three instruments. The black, red, blue and green squares represent the average CCS$_{N_2}$ values obtained for single conformations as an average across all the instruments, on the 6560, the G2 (DTIMS) and the G2 (TWIMS) respectively. The associated coloured bars show the standard deviation across the experimental replicates.

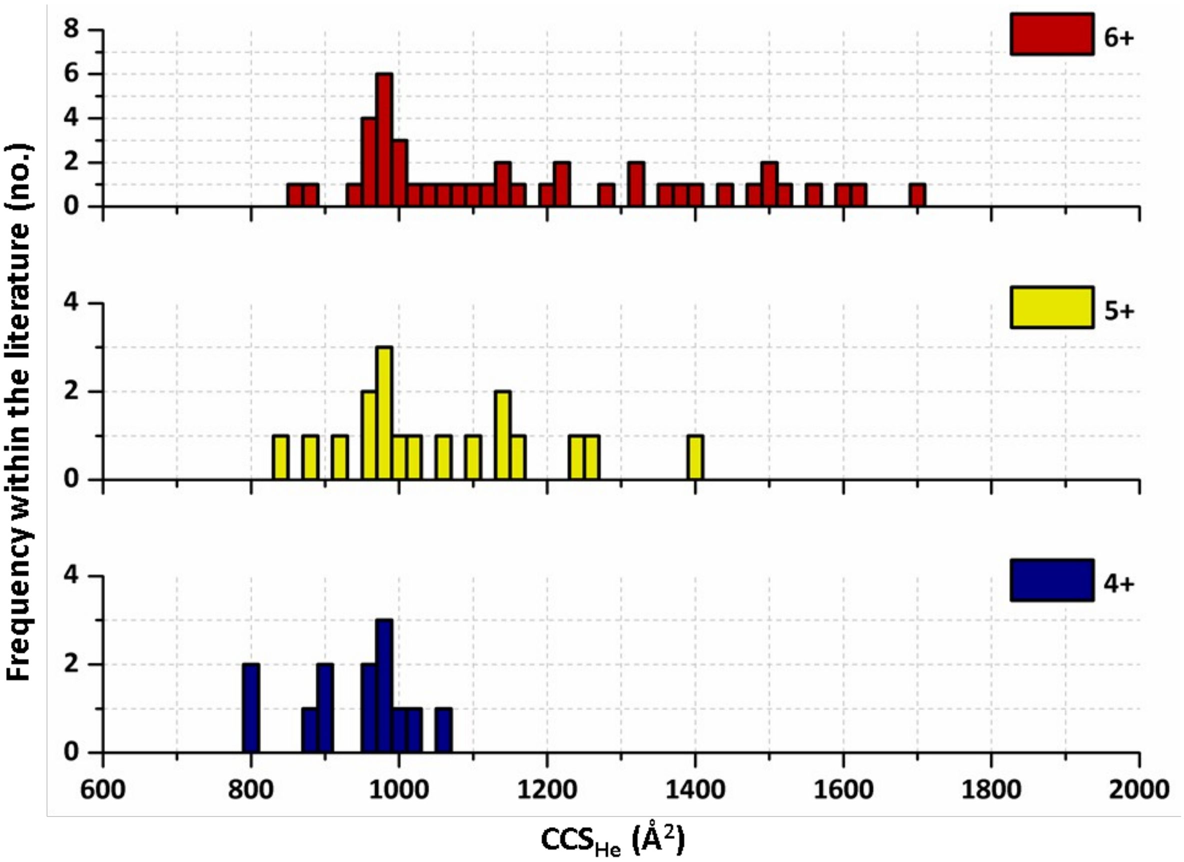

Figure S24. Global CCS$_{He}$ histogram plots for the charge states of ubiquitin observed across the experiments outlined in this study. Literature as well as our own experimentally obtained CCS were grouped into 20 Å^2 bins, whereby the frequency of CCS to the nearest 20 Å^2 increment were summed and represented as solid bars within the histogram plots. Within these stacked histogram plots, blue, yellow and red bars represent the frequency and size of CCS values for the 4+, 5+ and 6+ ions of ubiquitin respectively.

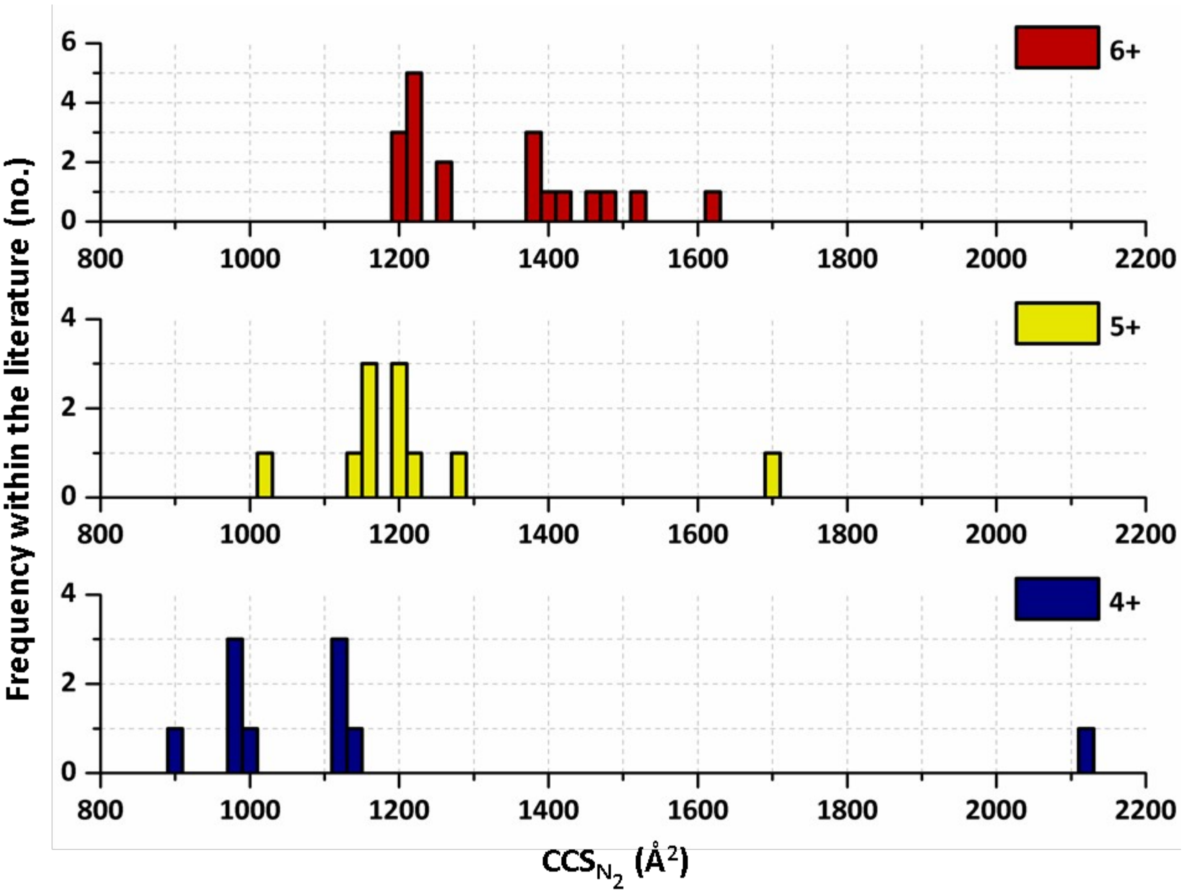

Figure S25. Global CCS_{N_2} histogram plots for the charge states of ubiquitin observed across the experiments outlined in this study. Literature as well as our own experimentally obtained CCS were grouped into 20 Å^2 bins, whereby the frequency of CCS to the nearest 20 Å^2 increment were summed and represented as solid bars within the histogram plots. Within these stacked histogram plots, blue, yellow and red bars represent the frequency and size of CCS values for the 4+, 5+ and 6+ ions of ubiquitin respectively.

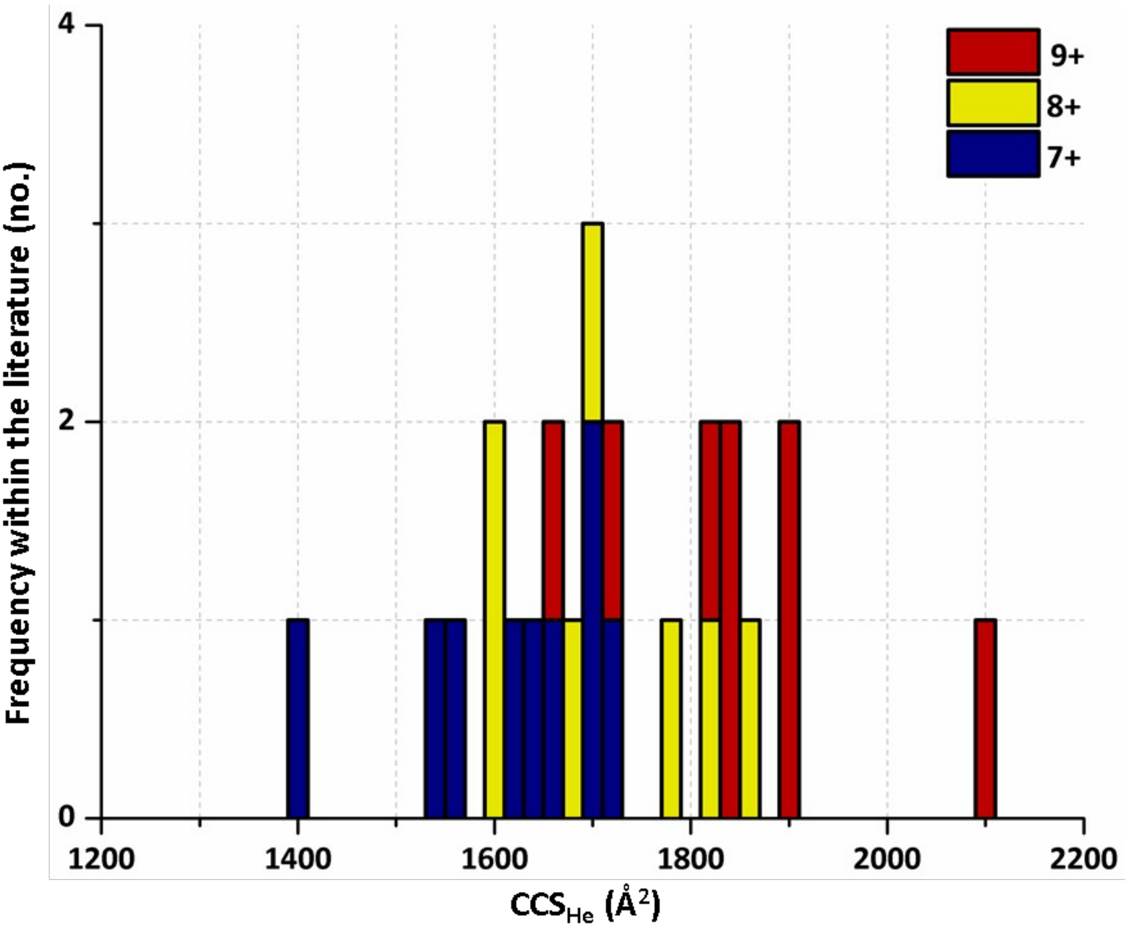

Figure S26. Global CCS$_{He}$ histogram plot for the charge states of myoglobin observed across the experiments outlined in this study. Literature as well as our own experimentally obtained CCS were grouped into 20 Å^2 bins, whereby the frequency of CCS to the nearest 20 Å^2 increment were summed and represented as solid bars within the histogram plot. Within the histogram plot, blue, yellow and red bars represent the frequency and size of CCS values for the 7+, 8+ and 9+ ions of myoglobin respectively.

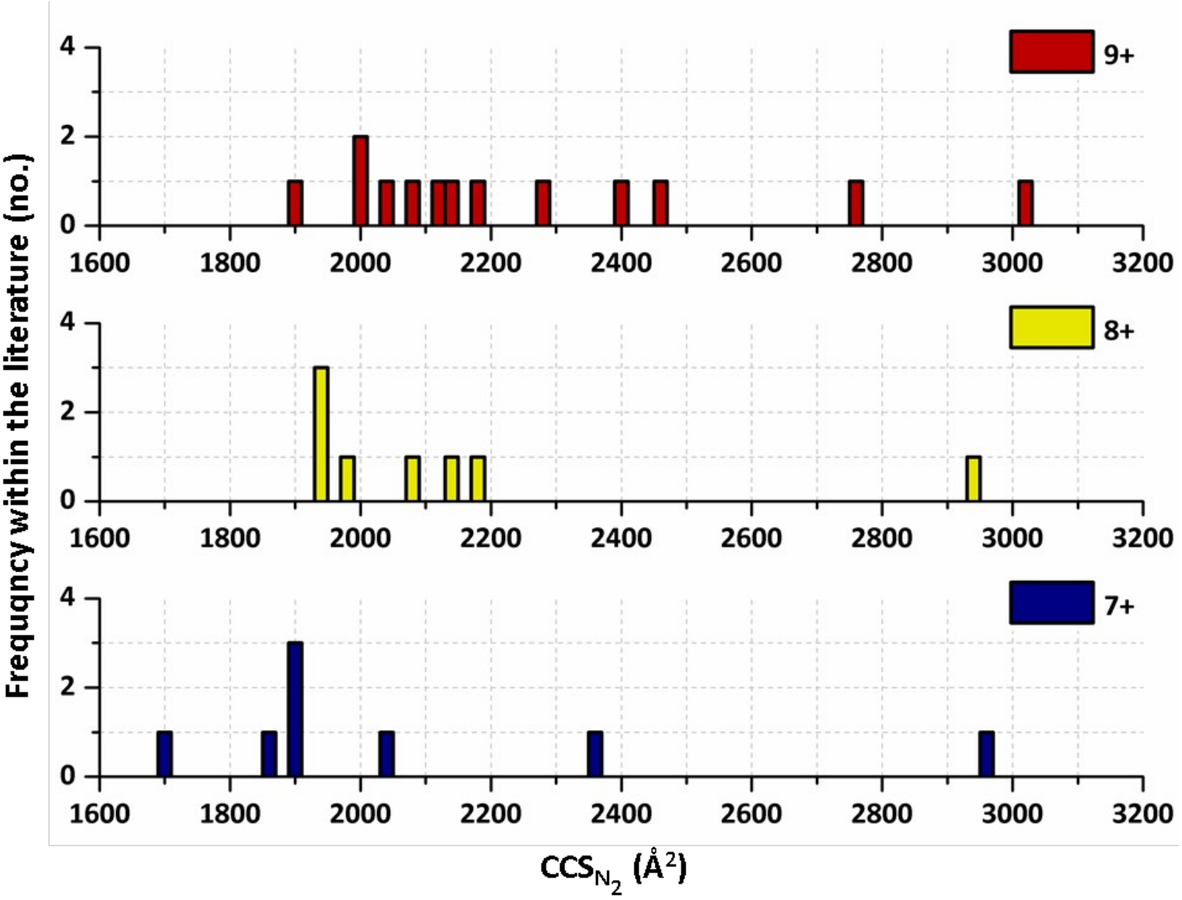

Figure S27. Global CCS_{N_2} histogram plots for the charge states of myoglobin observed across the experiments outlined in this study. Literature as well as our own experimentally obtained CCS were grouped into 20 Å^2 bins, whereby the frequency of CCS to the nearest 20 Å^2 increment were summed and represented as solid bars within the histogram plots. Within these stacked histogram plots, blue, yellow and red bars represent the frequency and size of CCS values for the 7+, 8+ and 9+ ions of myoglobin respectively.

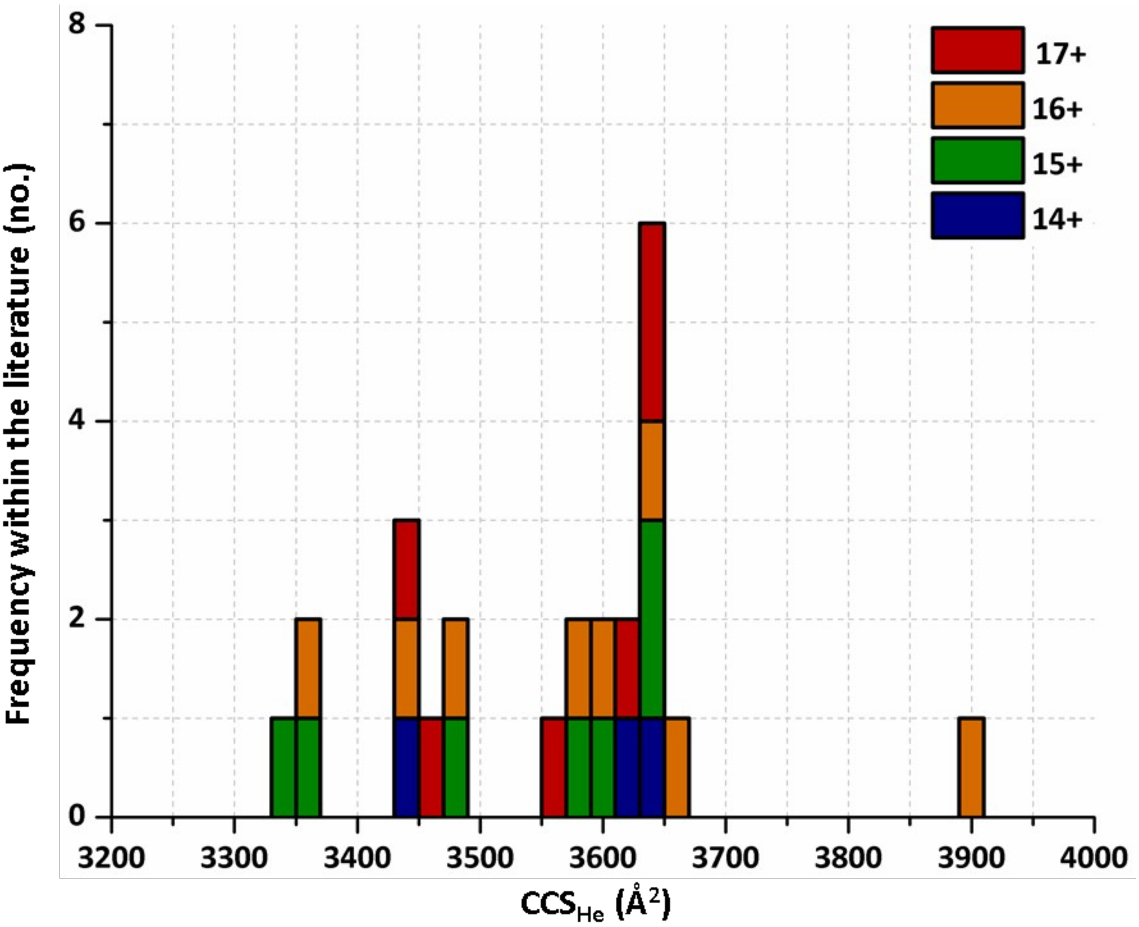

Figure S28. Global CCS$_{He}$ histogram plot for the charge states of avidin observed across the experiments outlined in this study. Literature as well as our own experimentally obtained CCS were grouped into 40 Å^2 bins, whereby the frequency of CCS to the nearest 40 Å^2 increment were summed and represented as solid bars within the histogram plot. Within the histogram plot, blue, green, orange and red bars represent the frequency and value of CCS for the 14+, 15+, 16+ and 17+ ions of avidin respectively.

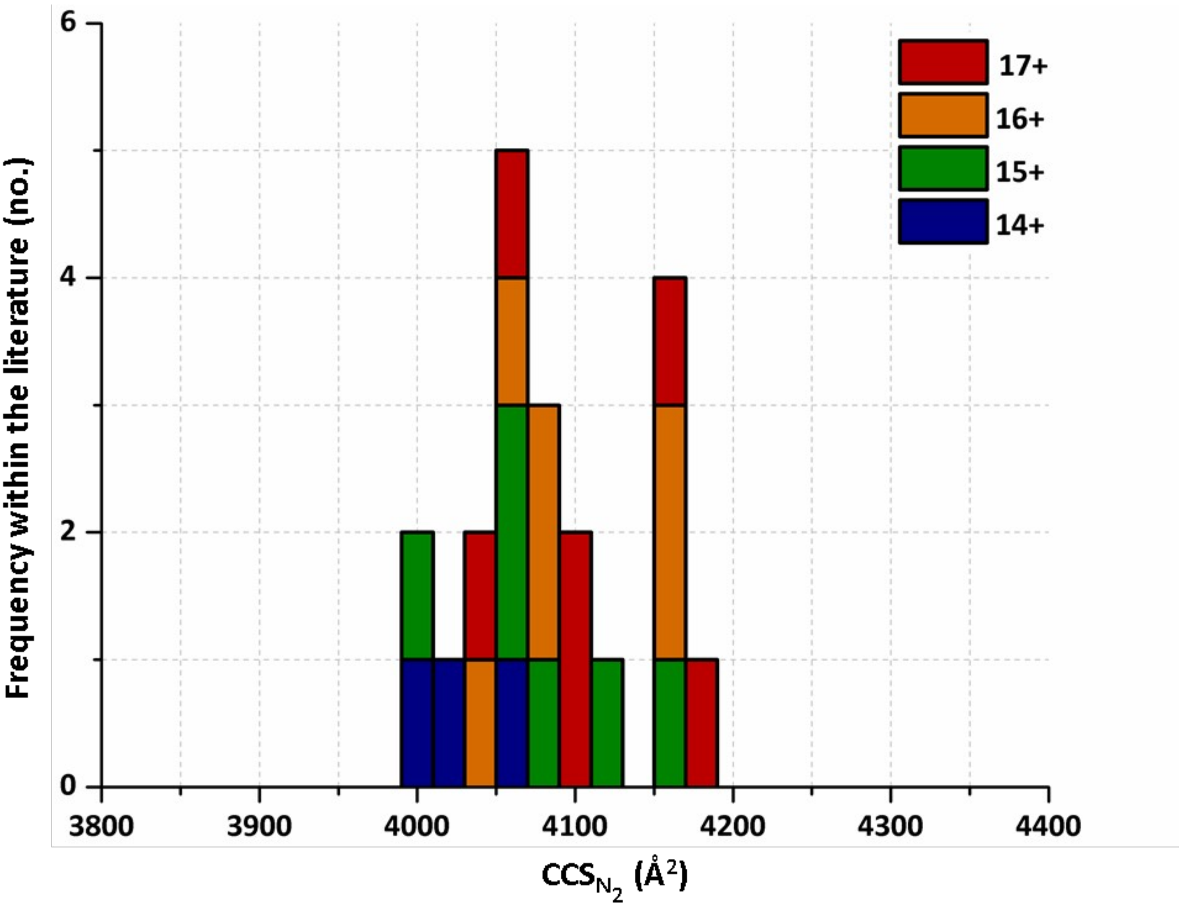

Figure S29. Global CCS_{N2} histogram plot for the charge states of avidin observed across the experiments outlined in this study. Literature as well as our own experimentally obtained CCS were grouped into 40 Å^2 bins, whereby the frequency of CCS to the nearest 40 Å^2 increment were summed and represented as solid bars within the histogram plot. Within the histogram plot, blue, green, orange and red bars represent the frequency and value of CCS for the 14+, 15+, 16+ and 17+ ions of avidin respectively.

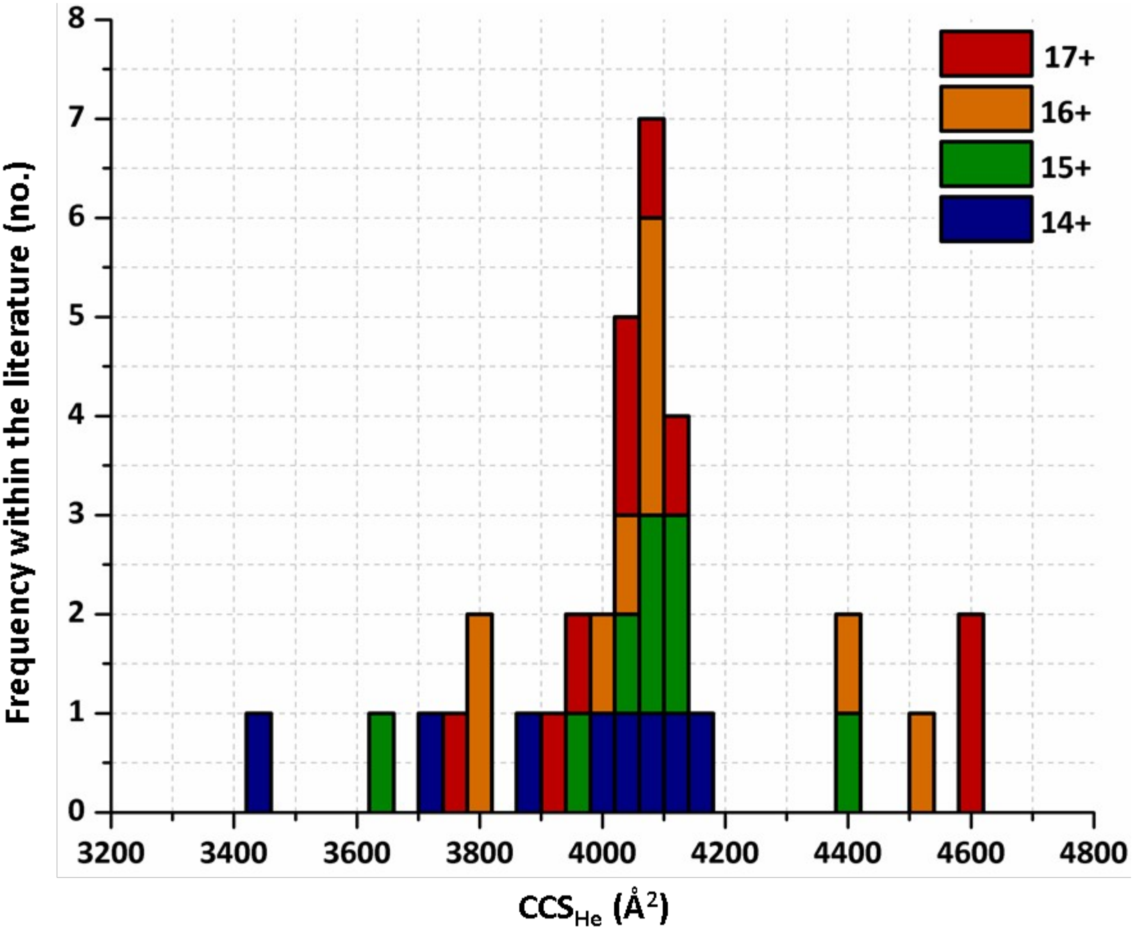

Figure S30. Global CCS$_{He}$ histogram plot for the charge states of BSA observed across the experiments outlined in this study. Literature as well as our own experimentally obtained CCS were grouped into 40 Å^2 bins, whereby the frequency of CCS to the nearest 40 Å^2 increment were summed and represented as solid bars within the histogram plot. Within the histogram plot, blue, green, orange and red bars represent the frequency and value of CCS for the 14+, 15+, 16+ and 17+ ions of BSA respectively.

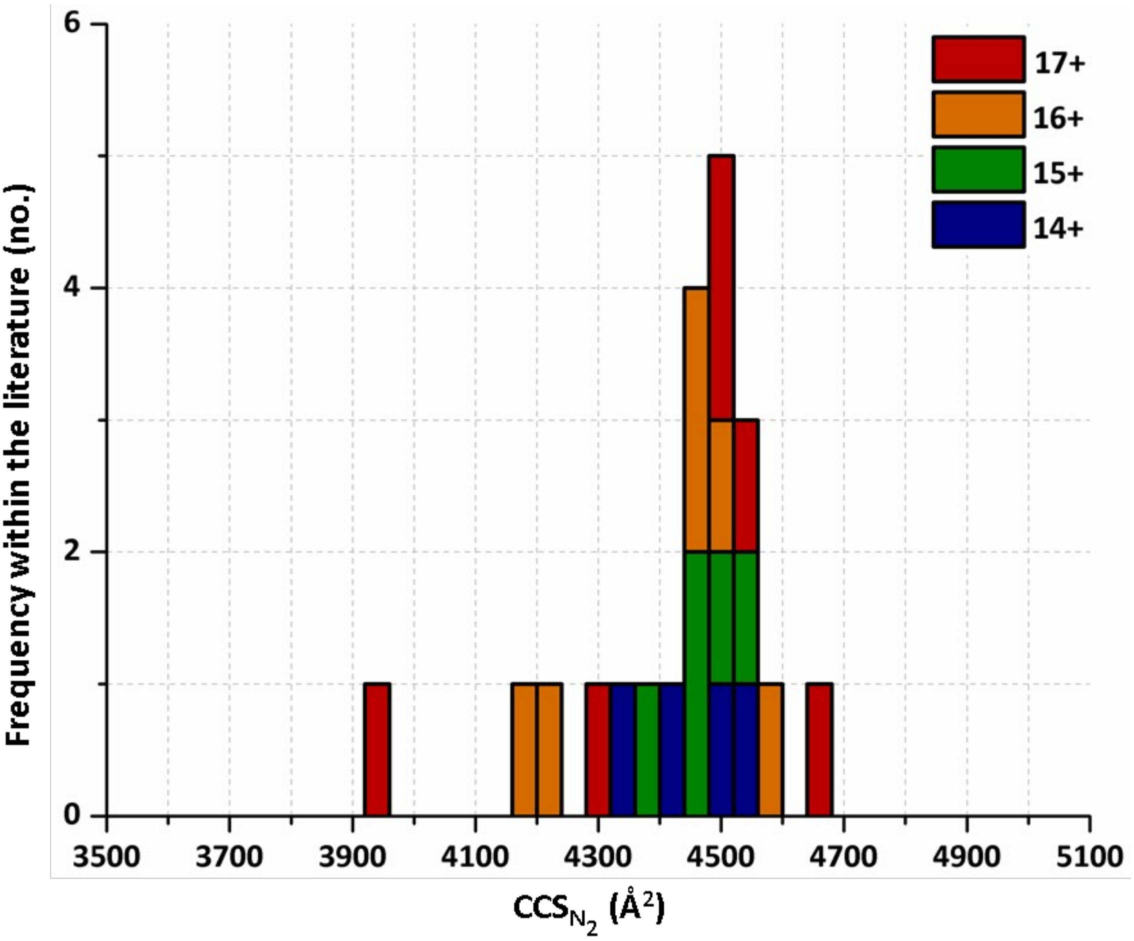

Figure S31. Global CCS_{N_2} histogram plot for the charge states of BSA observed across the experiments outlined in this study. Literature as well as our own experimentally obtained CCS were grouped into 40 Å^2 bins, whereby the frequency of CCS to the nearest 40 Å^2 increment were summed and represented as solid bars within the histogram plot. Within the histogram plot, blue, green, orange and red bars represent the frequency and value of CCS for the 14+, 15+, 16+ and 17+ ions of BSA respectively.

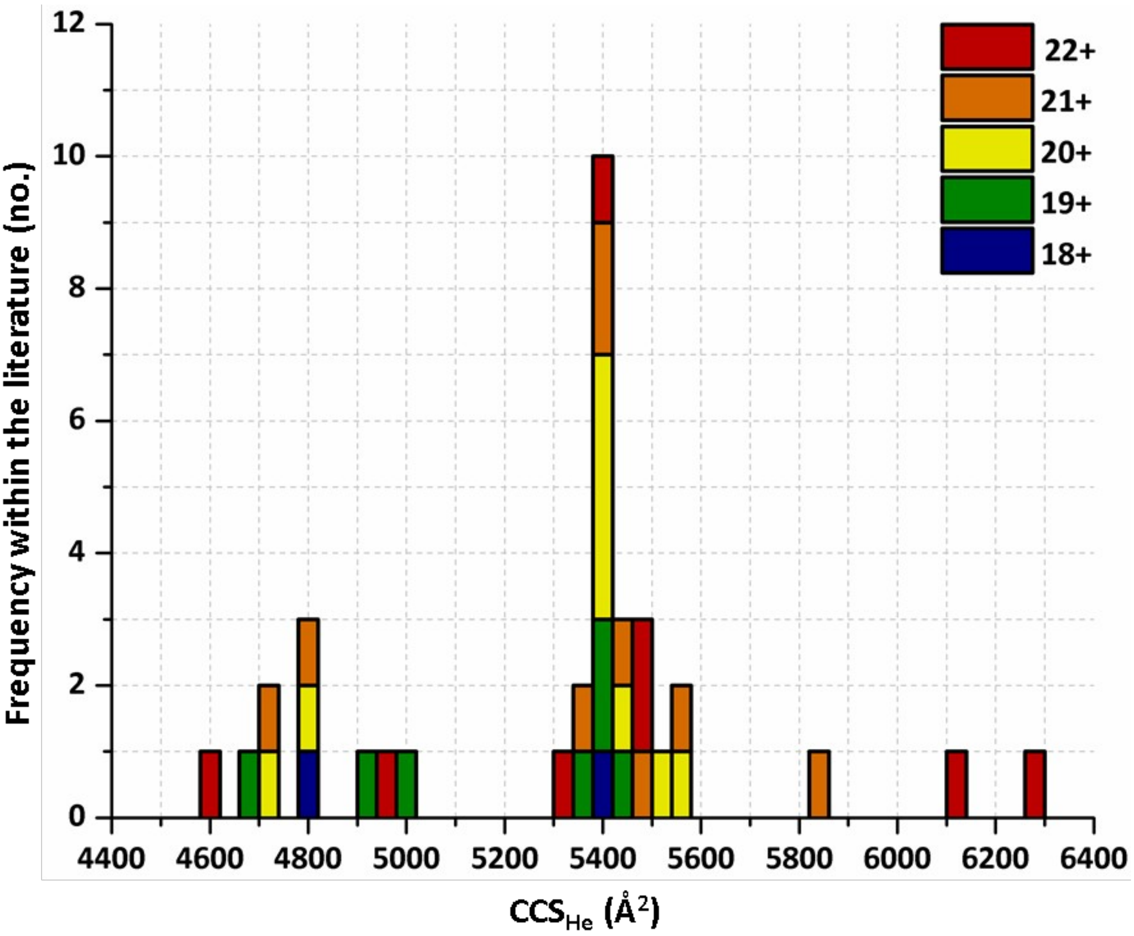

Figure S32. Global CCS$_{He}$ histogram plot for the charge states of concanavalin a observed across the experiments outlined in this study. Literature as well as our own experimentally obtained CCS were grouped into 40 Å^2 bins, whereby the frequency of CCS to the nearest 40 Å^2 increment were summed and represented as solid bars within the histogram plot. Within the histogram plot, blue, green, yellow, orange and red bars represent the frequency and value of CCS for the 18+, 19+, 20+, 21+ and 22+ ions of concanavalin a respectively.

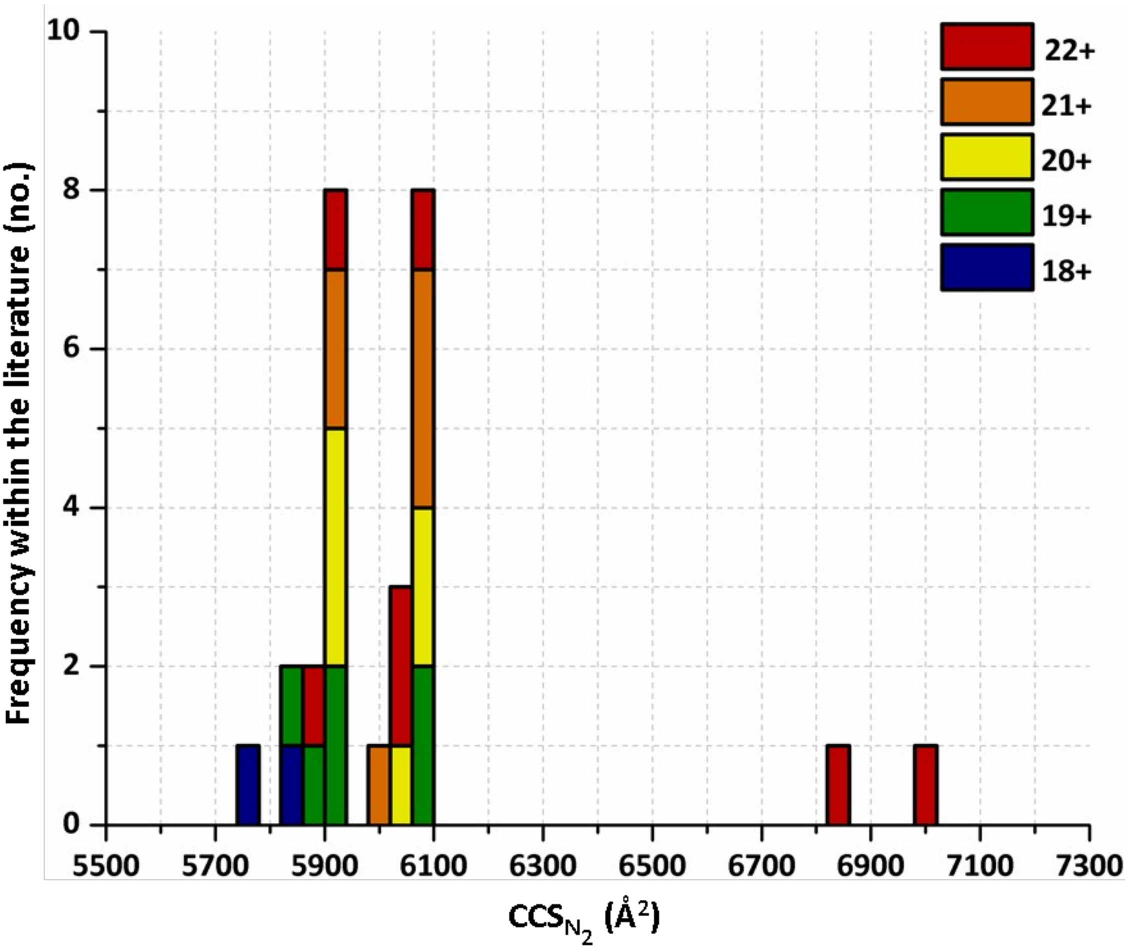

Figure S33. Global CCS_{N_2} histogram plot for the charge states of concanavalin a observed across the experiments outlined in this study. Literature as well as our own experimentally obtained CCS were grouped into 40 Å^2 bins, whereby the frequency of CCS to the nearest 40 Å^2 increment were summed and represented as solid bars within the histogram plot. Within the histogram plot, blue, green, yellow, orange and red bars represent the frequency and value of CCS for the 18+, 19+, 20+, 21+ and 22+ ions of concanavalin a respectively.

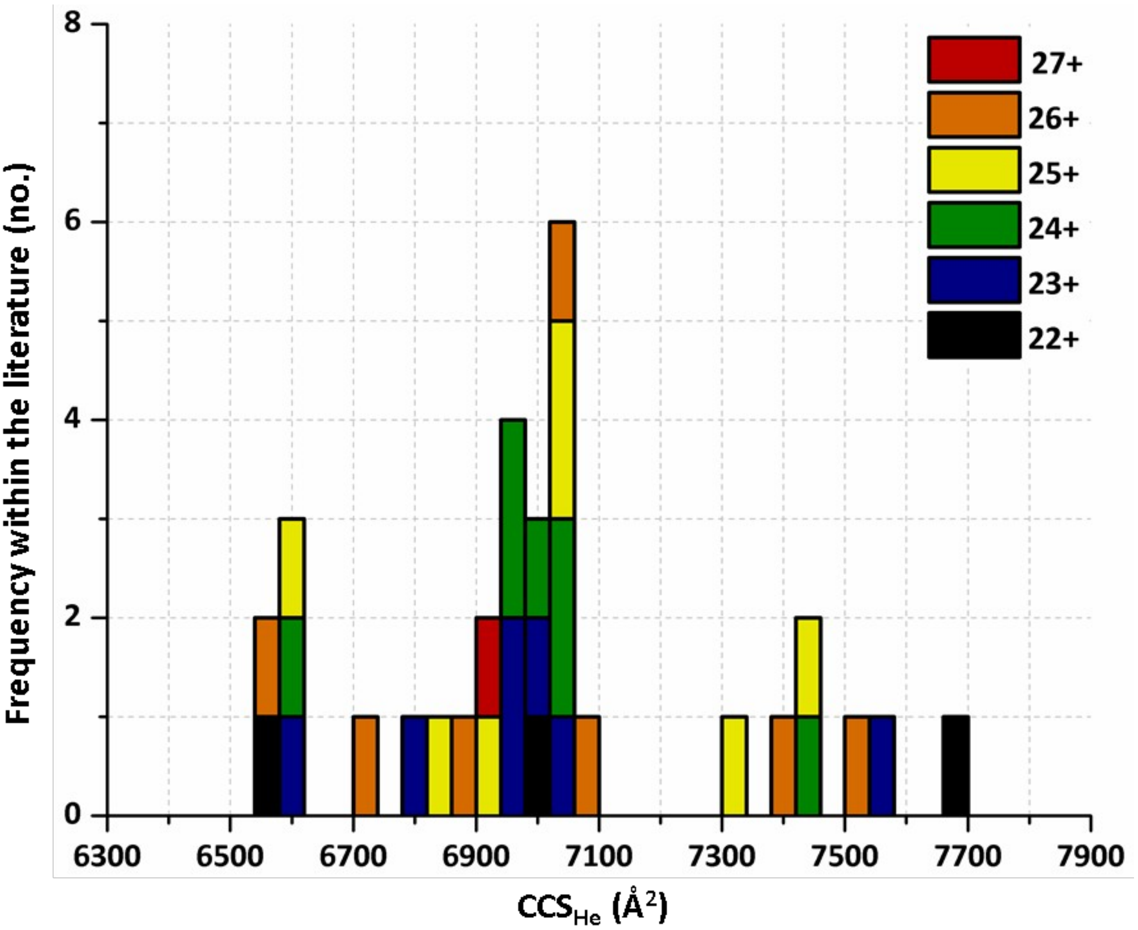

Figure S34. Global CCS_{He} histogram plot for the charge states of alcohol dehydrogenase observed across the experiments outlined in this study. Literature as well as our own experimentally obtained CCS were grouped into 40 Å^2 bins, whereby the frequency of CCS to the nearest 40 Å^2 increment were summed and represented as solid bars within the histogram plot. Within the histogram plot, black, blue, green, yellow, orange and red bars represent the frequency and value of CCS for the 22+, 23+, 24+, 25+, 26+ and 27+ ions of alcohol dehydrogenase respectively.

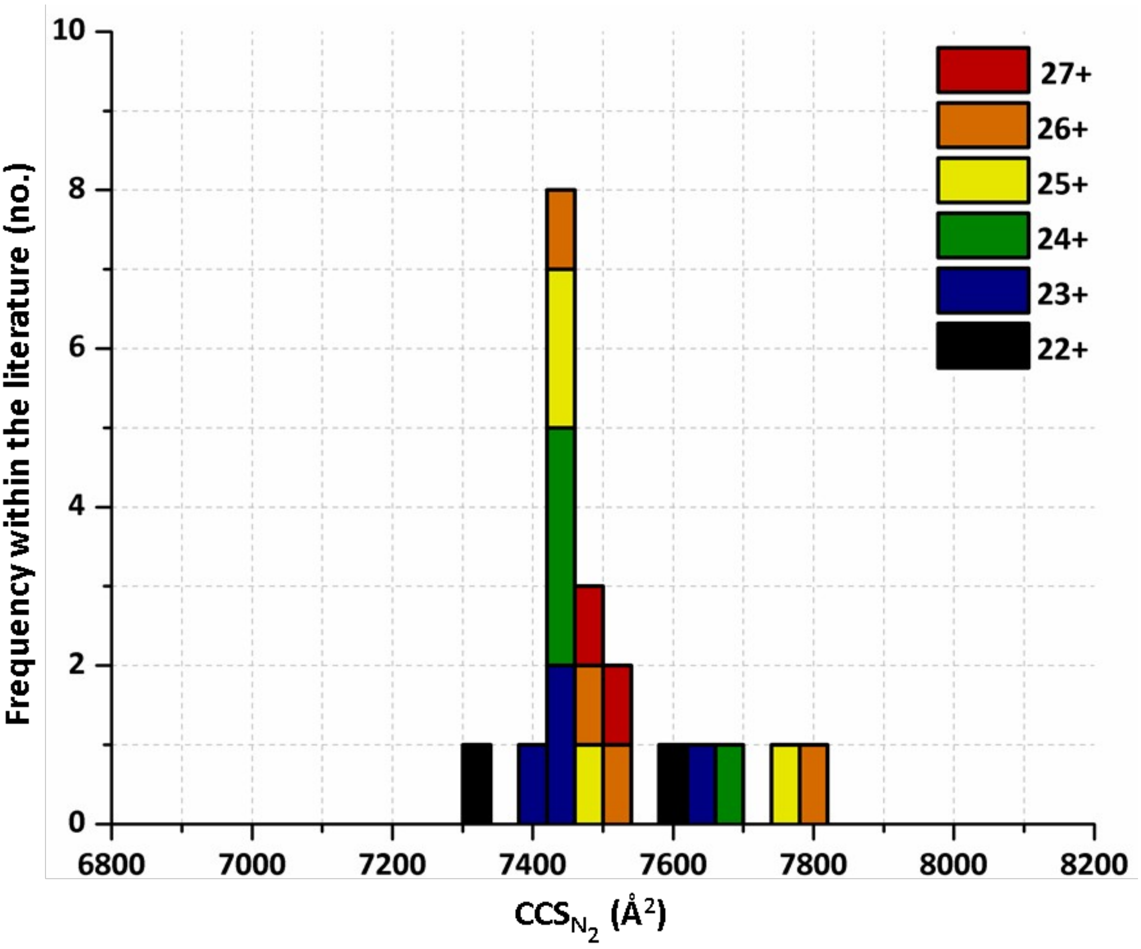

Figure S35. Global CCS_{N2} histogram plot for the charge states of alcohol dehydrogenase observed across the experiments outlined in this study. Literature as well as our own experimentally obtained CCS were grouped into 40 Å^2 bins, whereby the frequency of CCS to the nearest 40 Å^2 increment were summed and represented as solid bars within the histogram plot. Within the histogram plot, black, blue, green, yellow, orange and red bars represent the frequency and value of CCS for the 22+, 23+, 24+, 25+, 26+ and 27+ ions of alcohol dehydrogenase respectively.

Table S9. Literature and experimentally determined CCS$_{He}$ values obtained for the protein/protein complex ions described within this study. Within this table ‘n’ represents the multimeric state of the protein, ‘z’ denotes the protein charge state and the ‘Source’ column highlights the references from which the CCS$_{He}$ values were found, where the ‘#’ denotes CCS$_{He}$ values that were obtained experimentally within this study. Abbreviated versions of the IM techniques employed to obtain the corresponding CCS$_{He}$ values are noted in the ‘IM technique’ column. CCS$_{He}$ values highlighted in red were obtained from graphs within the associated references and as such will likely not be completely accurate. The ‘**’ after some CCS denotes the high likelihood that these values actually correspond to misidentified coincident dimer species and not more compact monomeric conformations.

Analyte	**n**	**Z (+)**	**CCS$_{He}$**	**IM technique**	**Source**
Ubiquitin	1	4	791	TWIMS	[17]
			800	TWIMS	[18]
			889**	DTIMS	[12]
			904	DTIMS	[19]
			907	DTIMS	#
			961	TWIMS	#
			963	DTIMS	#
			971	DTIMS	[12]
			972	DTIMS	[2]
			972	DTIMS	[13]
			1004	DTIMS	[20]
			1020	DTIMS	[21]
			1059	DTIMS	[20]
	1	5	840	TWIMS	[18]
			872	DTIMS	[19]
			924	DTIMS	#
			955	TWIMS	#
			965	DTIMS	#
			979	DTIMS	[19]
			982	DTIMS	[2]
			983	DTIMS	[13]
			1003	TWIMS	#
			1027	DTIMS	[20]
			1053	DTIMS	[12]
			1100	TWIMS	[22]
			1135	TWIMS	[23]
			1137	DTIMS	[20]
			1150	DTIMS	[21]
			1239	DTIMS	[20]
			1260	TWIMS	[22]
			1390	ROMIAC	[24]
	1	6	863	DTIMS	[19]
			870	TWIMS	[18]
			943	DTIMS	#
			950	TWIMS	[18]

			950	DTIMS	25
			950	TWIMS	7
			966	TWIMS	#
			970	DTIMS	26
			970	DTIMS	27
			970	DTIMS	28
			980	TWIMS	7
			980	TWIMS	29
			987	DTIMS	#
			1000	DTIMS	13
			1000	DTIMS	25
			1006	TWIMS	#
			1020	DTIMS	21
			1041	DTIMS	20
			1056	DTIMS	19
			1080	DTIMS	30
			1103	DTIMS	12
			1110	TWIMS	7
			1113	DTIMS	#
			1143	DTIMS	#
			1143	TWIMS	#
			1160	DTIMS	30
			1200	TWIMS	7
			1220	DTIMS	20
			1220	DTIMS	21
			1280	DTIMS	30
			1311	TWIMS	22
			1314	DTIMS	19
			1368	DTIMS	12
			1380	DTIMS	30
			1400	TWIMS	7
			1440	DTIMS	30
			1480	DTIMS	30
			1500	DTIMS	21
			1500	TWIMS	7
			1525	DTIMS	20
			1553	TWIMS	23
			1590	DTIMS	30
			1613	ROMIAC	24
			1700	TWIMS	22
Cytochrome C	1	6	1050	TWIMS	18
			1080 **	DTIMS	31
			1120	TWIMS	32
			1130	TWIMS	33
			1150	TWIMS	32

			1182	DTIMS	#
			1190	TWIMS	[32]
			1230	DTIMS	[31]
			1230	TWIMS	[32]
			1234	DTIMS	#
			1238	TWIMS	#
			1238	DTIMS	[12]
			1240	DTIMS	[2]
			1240	DTIMS	[15]
			1240	TWIMS	[17]
			1240	DTIMS	[31]
			1243	DTIMS	[34]
			1244	DTIMS	[35]
			1254	DTIMS	[36] (found in [31])
			1270	TWIMS	[32]
			1270	TWIMS	[33]
			1280	TWIMS	[32]
			1290	TWIMS	[17]
			1360	TWIMS	[37]
			1393	DTIMS	[35]
			1400	DTIMS	[36] (found in [31])
			1402	DTIMS	[12]
			1530	TWIMS	[32]
			1571	TWIMS	[38]
			1602	DTIMS	[35]
			1611	DTIMS	[36] (found in [31])
			1880	DTIMS	[31]
	1	7	1000	DTIMS	[39]
			1100	TWIMS	[18]
			1170	TWIMS	[33]
			1196	DTIMS	#
			1230	TWIMS	[32]
			1247	DTIMS	[35]
			1250	TWIMS	[32]
			1257	DTIMS	[36] (found in [31])
			1280	DTIMS	[15]
			1286	DTIMS	#
			1290	TWIMS	[33]
			1300	DTIMS	[2]
			1304	TWIMS	#
			1338	DTIMS	[40]
			1380	DTIMS	[31]
			1418	DTIMS	[12]
			1426	DTIMS	[36] (found in [31])
			1500	TWIMS	[32]

			1520	TWIMS	[33]
			1520	TWIMS	[17]
			1546	DTIMS	[34]
			1550	TWIMS	[32]
			1579	TWIMS	[38]
			1580	TWIMS	[17]
			1600	DTIMS	[39]
			1620	DTIMS	[35]
			1629	DTIMS	[36] (found in [31])
			1640	TWIMS	[32]
			1650	DTIMS	[31]
			1650	TWIMS	[32]
			1650	TWIMS	[33]
			1650	TWIMS	[37]
			1660	DTIMS	[31]
			1670	TWIMS	[17]
			1680	TWIMS	[32]
			1685	DTIMS	[12]
			1720	TWIMS	[38]
			1785	DTIMS	[35]
			1790	TWIMS	[37]
			1792	DTIMS	[36] (found in [31])
			1826	DTIMS	[12]
			1870	TWIMS	[33]
			1900	DTIMS	[31]
			2007	DTIMS	[35]
			2018	DTIMS	[36] (found in [31])
			2120	TWIMS	[38]
	1	8	1250	DTIMS	[35]
			1250	TWIMS	[18]
			1250	TWIMS	[32]
			1258	DTIMS	#
			1260	DTIMS	[36] (found in [31])
			1297	DTIMS	#
			1370	TWIMS	[18]
			1373	DTIMS	#
			1399	TWIMS	#
			1430	TWIMS	[18]
			1450	TWIMS	[33]
			1477	DTIMS	[36] (found in [31])
			1540	DTIMS	#
			1583	DTIMS	[12]
			1625	TWIMS	#
			1670	TWIMS	[32]
			1680	TWIMS	[32]

			1700	TWIMS	[33]
			1702	DTIMS	[35]
			1709	DTIMS	[36] (found in [31])
			1710	TWIMS	[17]
			1768	TWIMS	#
			1796	DTIMS	[12]
			1802	TWIMS	[38]
			1820	TWIMS	[37]
			1845	DTIMS	[35]
			1854	DTIMS	[36] (found in [31])
			1863	DTIMS	[34]
			1875	TWIMS	[38]
			1918	TWIMS	#
			1940	TWIMS	[32]
			1940	TWIMS	[33]
			1980	TWIMS	[17]
			2000	TWIMS	[17]
			2020	TWIMS	[32]
			2020	TWIMS	[17]
			2040	TWIMS	[32]
			2053	DTIMS	[12]
			2061	DTIMS	[35]
			2071	DTIMS	[36] (found in [31])
			2114	DTIMS	[12]
			2150	TWIMS	[38]
			2230	TWIMS	[37]
Myoglobin	1	7	1398	TWIMS	[38]
			1546 **	DTIMS	[12]
			1566	DTIMS	#
			1613	TWIMS	[38]
			1641	TWIMS	#
			1664	DTIMS	#
			1695	DTIMS	[41]
			1700	TWIMS	[37]
			1716	DTIMS	[12]
	1	8	1593	TWIMS	[38]
			1604	DTIMS	#
			1674	TWIMS	#
			1704	DTIMS	#
			1788	DTIMS	[41]
			1824	DTIMS	[12]
			1850	TWIMS	[37]
	1	9	1650	DTIMS	#
			1713	TWIMS	#
			1818	TWIMS	#
			1832	DTIMS	#

			1835	DTIMS	41
			1900	TWIMS	37
			1907	DTIMS	12
			2106	DTIMS	41
Avidin	4	14	3441	DTIMS	#
			3614	TWIMS	#
			3633	DTIMS	#
	4	15	3347	DTIMS	42
			3350	DTIMS	43
			3485	DTIMS	#
			3570	DTIMS	2
			3601	TWIMS	#
			3640	DTIMS	#
			3640	DTIMS	15
	4	16	3350	DTIMS	43
			3434	DTIMS	42
			3471	DTIMS	#
			3581	TWIMS	#
			3590	DTIMS	2
			3640	DTIMS	15
			3665	DTIMS	#
			3900	DTIMS	43
	4	17	3446	DTIMS	42
			3467	DTIMS	#
			3566	TWIMS	#
			3610	DTIMS	2
			3633	DTIMS	#
			3640	DTIMS	15
BSA	1	14	3433	DTIMS	42
			3700	TWIMS	33
			3891	DTIMS	#
			4010	DTIMS	2
			4041	DTIMS	#
			4090	DTIMS	15
			4108	TWIMS	#
			4167	DTIMS	42
	1	15	3653	DTIMS	42
			3956	DTIMS	#
			4030	DTIMS	2
			4087	TWIMS	#
			4093	DTIMS	#
			4100	DTIMS	15
			4100	TWIMS	33
			4419	DTIMS	42
	1	16	3788	DTIMS	42
			3800	TWIMS	18
			3989	DTIMS	#
			4051	TWIMS	#

			4060	DTIMS	15
			4070	DTIMS	2
			4084	DTIMS	#
			4400	TWIMS	33
			4535	DTIMS	42
	1	17	3766	DTIMS	42
			3900	TWIMS	18
			3956	DTIMS	#
			4026	DTIMS	#
			4040	DTIMS	15
			4094	TWIMS	#
			4110	DTIMS	2
			4600	TWIMS	33
			4613	DTIMS	42
Concanavalin A	4	18	4800	TWIMS	33
			5412	TWIMS	#
	4	19	4681	DTIMS	42
			4900	DTIMS	43
			5000	TWIMS	33
			5340	DTIMS	#
			5399	DTIMS	#
			5409	TWIMS	#
			5440	DTIMS	2
	4	20	4713	DTIMS	42
			4800	DTIMS	43
			5384	DTIMS	#
			5397	DTIMS	#
			5400	DTIMS	9
			5412	TWIMS	#
			5450	DTIMS	2
			5500	TWIMS	33
			5550	DTIMS	15
	4	21	4700	DTIMS	43
			4804	DTIMS	42
			5345	DTIMS	#
			5401	DTIMS	#
			5434	TWIMS	#
			5460	DTIMS	2
			5550	DTIMS	15
			5850	TWIMS	33
	4	22	4600	DTIMS	43
			4977	DTIMS	42
			5335	DTIMS	#
			5405	DTIMS	#
			5460	DTIMS	2
			5480	DTIMS	15
			6100	TWIMS	33

			6285	DTIMS	#
Alcohol Dehydrogenase	4	22	6579	DTIMS	#
			7015	TWIMS	#
			7696	TWIMS	[44]
	4	23	6584	DTIMS	#
			6800	TWIMS	[33]
			6940	DTIMS	[15]
			6968	DTIMS	#
			6990	DTIMS	[2]
			7020	TWIMS	#
			7545	TWIMS	[44]
	4	24	6606	DTIMS	#
			6940	DTIMS	[15]
			6943	DTIMS	#
			7000	TWIMS	[33]
			7020	DTIMS	[2]
			7027	TWIMS	#
			7457	TWIMS	[44]
	4	25	6588	DTIMS	#
			6830	DTIMS	[15]
			6914	DTIMS	#
			7020	DTIMS	[2]
			7045	TWIMS	#
			7300	TWIMS	[33]
			7428	TWIMS	[44]
	4	26	6557	DTIMS	#
			6720	DTIMS	[15]
			6879	DTIMS	#
			7020	DTIMS	[2]
			7069	TWIMS	#
			7388	TWIMS	[44]
			7500	TWIMS	[33]
	4	27	6908	DTIMS	#

Table S10. Literature and experimentally determined CCS_{N_2} values obtained for the protein/protein complex ions described within this study. Within this table 'n' represents the multimeric state of the protein, 'z' denotes the protein charge state and the 'Source' column highlights the references from which the CCS_{N_2} values were found, where the '#' denotes CCS_{N_2} values that were obtained experimentally within this study. Abbreviated versions of the IM techniques employed to obtain the corresponding CCS_{N_2} values are noted in the 'IM technique' column. CCS_{N_2} values highlighted in red were obtained from graphs within the associated references and as such will likely not be completely accurate. The '**' after some CCS denotes the high likelihood that these values actually correspond to misidentified coincident dimer species and not more compact monomeric conformations.

Analyte	**n**	**Z (+)**	**CCS_{N_2}**	**IM technique**	**Source**
Ubiquitin	1	4	949**	DTIMS	[12]
			967	DTIMS	[45]
			1116	DTIMS	[12]
			1118	TWIMS	#
			1128	DTIMS	#
			1148	DTIMS	#
			2125	TIMS	[46]
	1	5	1011	DTIMS	[12]
			1116	DTIMS	[45]
			1139	DTIMS	[45]
			1149	TIMS	[46]
			1163	DTIMS	#
			1166	DTIMS	#
			1167	TWIMS	#
			1204	SLIM	[47]
			1208	DTIMS	#
			1208	TWIMS	#
			1221	DTIMS	[12]
			1271	OrbiCCS	[48]
			1700	TIMS	[46]
	1	6	1196	DTIMS	[45]
			1199	DTIMS	#
			1200	DTIMS	[28]
			1209	DTIMS	#
			1217	TIMS	[49]
			1222	DTIMS	[12]
			1229	TIMS	[46]
			1229	TWIMS	#
			1258	SLIM	[47]
			1268	TWIMS	#
			1380	DTIMS	[28]
			1382	TWIMS	#
			1386	DTIMS	#
			1401	DTIMS	#
			1417	TIMS	[46]

			1466	DTIMS	#
			1474	DTIMS	[12]
			1517	OrbiCCS	[48]
			1628	DTIMS	[12]
Cytochrome C	1	6	1289	TIMS	[46]
			1330	DTIMS	[45]
			1360**	DTIMS	[12]
			1398	TWIMS	[45]
			1413	OrbiCCS	[48]
			1438	TIMS	[46]
			1449	DTIMS	[45]
			1450	SLIM	[47]
			1454	TWIMS	#
			1456	DTIMS	#
			1465	DTIMS	#
			1477	DTIMS	[12]
			1490	DTIMS	[15]
			1590	DTIMS	[47]
			1769	TIMS	[46]
	1	7	1030	TMIMS	[50] interpolated from [35]
			1307	TIMS	[46]
			1481	DTIMS	#
			1508	DTIMS	[45]
			1533	TWIMS	[45]
			1536	DTIMS	[12]
			1537	TWIMS	#
			1540	DTIMS	#
			1540	TMIMS	[50] interpolated from [34]
			1548	TIMS	[46]
			1550	SLIM	[51]
			1560	SLIM	[47]
			1561	DTIMS	#
			1574	TIMS	[46]
			1590	DTIMS	[15]
			1636	TMIMS	[50] interpolated from [35]
			1810	OrbiCCS	[48]
			1922	TIMS	[46]
			1948	TMIMS	[50] interpolated from [35]
			1970	DTIMS	[47]
			2083	TIMS	[46]
			2115	DTIMS	[12]
			2326	TMIMS	[50] interpolated from [35]
	1	8	1036	TMIMS	[50] interpolated from [35]
			1053	TMIMS	[50] interpolated from [52]
			1519	DTIMS	#
			1629	DTIMS	#

			1654	TWIMS	#
			1654	DTIMS	#
			1686	TIMS	[46]
			1793	DTIMS	[12]
			1806	TMIMS	[50] interpolated from [35]
			1887	TWIMS	#
			1915	DTIMS	#
			1925	TIMS	[46]
			2043	TWIMS	#
			2050	TMIMS	[50] interpolated from [35]
			2084	TMIMS	[50] interpolated from [34]
			2114	DTIMS	[12]
			2146	OrbiCCS	[48]
			2201	TWIMS	#
			2249	TIMS	[46]
			2418	TMIMS	[50] interpolated from [35]
			2441	DTIMS	[12]
			2468	TIMS	[46]
			2496	TIMS	[46]
			2528	DTIMS	[12]
			2543	TMIMS	[50] interpolated from [52]
Myoglobin	1	7	1697**	DTIMS	[12]
			1709	DTIMS	[45]
			1788	TWIMS	[45]
			1863	DTIMS	[12]
			1896	TWIMS	#
			1899	DTIMS	#
			1903	DTIMS	#
			1908	DTIMS	[45]
			2037	DTIMS	[41]
			2353	DTIMS	[41]
			2952	DTIMS	[41]
	1	8	1839	TWIMS	[45]
			1934	DTIMS	#
			1937	DTIMS	[12]
			1949	TWIMS	#
			1953	DTIMS	[45]
			1972	DTIMS	#
			2089	OrbiCCS	[48]
			2147	TIMS	[46]
			2187	TIMS	[53]
			2939	DTIMS	[41]
	1	9	1908	TIMS	[46]
			1995	DTIMS	#
			2003	TWIMS	#
			2010	TWIMS	[45]

			2038	DTIMS	[45]
			2040	DTIMS	#
			2085	DTIMS	[12]
			2114	TWIMS	#
			2149	DTIMS	#
			2187	TIMS	[46]
			2280	OrbiCCS	[48]
			2399	TIMS	[53]
			2465	TIMS	[53]
			2756	DTIMS	[41]
			3027	DTIMS	[41]
Avidin	4	14	3996	DTIMS	#
			4029	DTIMS	#
			4053	TWIMS	#
	4	15	4008	DTIMS	#
			4057	DTIMS	#
			4060	DTIMS	[47]
			4073	TWIMS	#
			4120	SLIM	[47]
			4150	DTIMS	[15]
	4	16	4038	DTIMS	#
			4066	DTIMS	#
			4080	DTIMS	[47]
			4086	TWIMS	#
			4150	SLIM	[47]
			4150	DTIMS	[15]
	4	17	4041	DTIMS	#
			4063	DTIMS	#
			4100	DTIMS	[47]
			4101	TWIMS	#
			4160	DTIMS	[15]
			4170	SLIM	[47]
BSA	1	14	4349	DTIMS	#
			4425	DTIMS	#
			4490	DTIMS	[15]
			4535	TWIMS	#
	1	15	4392	DTIMS	#
			4467	TIMS	[46]
			4478	DTIMS	#
			4490	DTIMS	[15]
			4548	TWIMS	#
	1	16	4188	TIMS	[46]
			4200	TIMS	[46]
			4445	DTIMS	#
			4470	DTIMS	[15]
			4514	DTIMS	#
			4567	TWIMS	#
	1	17	3941	TIMS	[46]

			4291	TIMS	[46]
			4490	DTIMS	[15]
			4506	DTIMS	#
			4523	DTIMS	#
			4648	TWIMS	#
Concanavalin A	4	18	5740	TWIMS	#
			5838	DTIMS	#
	4	19	5820	TWIMS	#
			5879	DTIMS	#
			5905	DTIMS	#
			5920	SLIM	[47]
			6060	DTIMS	[15]
			6060	DTIMS	[47]
	4	20	5900	TWIMS	#
			5902	DTIMS	#
			5913	DTIMS	#
			6020	SLIM	[47]
			6060	DTIMS	[47]
			6080	DTIMS	[15]
	4	21	5921	DTIMS	#
			5937	DTIMS	#
			5997	TWIMS	#
			6060	DTIMS	[47]
			6070	SLIM	[47]
			6090	DTIMS	[15]
	4	22	5890	DTIMS	#
			5930	DTIMS	#
			6030	SLIM	[47]
			6050	DTIMS	[15]
			6070	DTIMS	[47]
			6846	DTIMS	#
			7011	DTIMS	#
Alcohol Dehydrogenase	4	22	7330	DTIMS	#
			7594	DTIMS	#
	4	23	7399	DTIMS	#
			7420	DTIMS	[15]
			7422	DTIMS	#
			7640	TWIMS	#
	4	24	7427	DTIMS	#
			7447	DTIMS	#
			7450	DTIMS	[15]
			7693	TWIMS	#
	4	25	7429	DTIMS	#
			7440	DTIMS	[15]
			7465	DTIMS	#
			7750	TWIMS	#
	4	26	7424	DTIMS	#
			7473	DTIMS	#
			7500	DTIMS	[15]
			7814	TWIMS	#

	4	27	7470	DTIMS	#
			7520	DTIMS	#

References

1 K. Giles, J. P. Williams and I. D. G. Campuzano, in *Rapid Communications in Mass Spectrometry*, 2011, vol. 25, pp. 1559–1566.

2 S. J. Allen, K. Giles, T. Gilbert and M. F. Bush, *Analyst*, 2016, **141**, 884–891.

3 J. C. May, J. N. Dodds, R. T. Kurulugama, G. C. Stafford, J. C. Fjeldsted and J. A. McLean, *Analyst*, 2015, **140**, 6824–6833.

4 B. T. Ruotolo, J. L. P. Benesch, A. M. Sandercock, S.-J. Hyung and C. V Robinson, *Nat. Protoc.*, 2008, **3**, 1139–1152.

5 H. E. Revercomb and E. A. Mason, *Anal. Chem.*, 1975, **47**, 970–983.

6 Y. Zhong, S.-J. Hyung and B. T. Ruotolo, *Analyst*, 2011, **136**, 3534.

7 S. H. Chen and D. H. Russell, *J. Am. Soc. Mass Spectrom.*, 2015, **26**, 1433–1443.

8 J. C. May, C. R. Goodwin, N. M. Lareau, K. L. Leaptrot, C. B. Morris, R. T. Kurulugama, A. Mordehai, C. Klein, W. Barry, E. Darland, G. Overney, K. Imatani, G. C. Stafford, J. C. Fjeldsted and J. A. McLean, *Anal. Chem.*, 2014, **86**, 2107–2116.

9 J. Ujma, K. Giles, M. Morris and P. E. Barran, *Anal. Chem.*, 2016, **88**, 9469–9478.

10 R. T. Kurulugama, E. Darland, F. Kuhlmann, G. Stafford and J. Fjeldsted, *Analyst*, 2015, **140**, 6834–6844.

11 S. C. Henderson, J. Li, A. E. Counterman and D. E. Clemmer, *J. Phys. Chem. B*, 1999, **103**, 8780–8785.

12 J. C. May, E. Jurneczko, S. M. Stow, I. Kratochvil, S. Kalkhof and J. A. McLean, *Int. J. Mass Spectrom.*, 2017, **429**, 79–90.

13 E. S. Baker, B. H. Clowers, F. Li, K. Tang, A. V. Tolmachev, D. C. Prior, M. E. Belov and R. D. Smith, *J. Am. Soc. Mass Spectrom.*, 2007, **18**, 1176–1187.

14 C. S. Hoaglund-Hyzer, A. E. Counterman and D. E. Clemmer, *Chem. Rev.*, 2002, **99**, 3037–3080.

15 M. F. Bush, Z. Hall, K. Giles, J. Hoyes, C. V. Robinson and B. T. Ruotolo, *Anal. Chem.*, 2010, **82**, 9557–9565.

16 R. Salbo, M. F. Bush, H. Naver, I. Campuzano, C. V. Robinson, I. Pettersson, T. J. D. Jørgensen and K. F. Haselmann, *Rapid Commun. Mass Spectrom.*, 2012, **26**, 1181–1193.

17 D. Smith, T. Knapman, I. Campuzano, R. Malham, J. Berryman, S. Radford and A. Ashcroft, *Eur. J. Mass Spectrom.*, 2009, **15**, 113.

18 Y. Zhong, L. Han and B. T. Ruotolo, *Angew. Chemie Int. Ed.*, 2014, **53**, 9209–9212.

19 Q. Zhao, M. W. Soyk, G. M. Schieffer, K. Fuhrer, M. M. Gonin, R. S. Houk and E. R. Badman, *J. Am. Soc. Mass Spectrom.*, 2009, **20**, 1549–1561.

20 S. J. Valentine, A. E. Counterman and D. E. Clemmer, *J. Am. Soc. Mass Spectrom.*, 1997, **8**, 954–961.

21 Y. Guo, J. Wang, G. Javahery, B. A. Thomson and K. W. M. Siu, *Anal. Chem.*, 2005, **77**, 266–275.

22 S. I. Merenbloom, T. G. Flick and E. R. Williams, *J. Am. Soc. Mass Spectrom.*, 2012, **23**, 553–562.

23 B. Shrestha and A. Vertes, *Anal. Chem.*, 2014, **86**, 4308–4315.

24 W. Mui, D. A. Thomas, A. J. Downard, J. L. Beauchamp, J. H. Seinfeld and R. C. Flagan, *Anal. Chem.*, 2013, **85**, 6319–6326.

25 J. Li, J. A. Taraszka, A. E. Counterman and D. E. Clemmer, *Int. J. Mass Spectrom.*, 1999, **185**, 37–47.

26 T. J. El-Baba, D. W. Woodall, S. A. Raab, D. R. Fuller, A. Laganowsky, D. H. Russell and D. E. Clemmer, *J. Am. Chem. Soc.*, 2017, **139**, 6306–6309.

27 T. Wyttenbach and M. T. Bowers, *J. Phys. Chem. B*, 2011, **115**, 12266–12275.

28 C. Bleiholder, N. R. Johnson, S. Contreras, T. Wyttenbach and M. T. Bowers, *Anal. Chem.*, 2015, **87**, 7196–203.

29 N. D. Wagner, D. Kim and D. H. Russell, *Anal. Chem.*, 2016, **88**, 5934–5940.

30 A. A. Shvartsburg, F. Li, K. Tang and R. D. Smith, *Anal. Chem.*, 2007, **79**, 1523–1528.

31 Q. Zhao, G. M. Schieffer, M. W. Soyk, T. J. Anderson, R. S. Houk and E. R. Badman, *J. Am. Soc. Mass Spectrom.*, 2010, **21**, 1208–1217.

32 T. W. Knapman, N. M. Valette, S. L. Warriner and a E. Ashcroft, *Curr. Anal. Chem.*, 2013, **9**, 181–191.

33 G. N. Sivalingam, J. Yan, H. Sahota and K. Thalassinos, *Int. J. Mass Spectrom.*, 2013, **345**–**347**, 54–62.

34 P. A. Faull, K. E. Korkeila, J. M. Kalapothakis, A. Gray, B. J. McCullough and P. E. Barran, *Int. J. Mass Spectrom.*, 2009, **283**, 140–148.

35 K. B. Shelimov, D. E. Clemmer, R. R. Hudgins and M. F. Jarrold, *J. Am. Chem. Soc.*, 1997, **119**, 2240–2248.

36 E. R. Badman, C. S. Hoaglund-Hyzer and D. E. Clemmer, *Anal. Chem.*, 2001, **73**, 6000–6007.

37 C. A. Scarff, K. Thalassinos, G. R. Hilton and J. H. Scrivens, *Rapid Commun. Mass Spectrom.*, 2008, **22**, 3297–3304.

38 J. R. Jhingree, R. Beveridge, E. R. Dickinson, J. P. Williams, J. M. Brown, B. Bellina and P. E. Barran, *Int. J. Mass Spectrom.*, 2017, **413**, 43–51.

39 E. R. Dickinson, E. Jurneczko, K. J. Pacholarz, D. J. Clarke, M. Reeves, K. L. Ball, T. Hupp, D. Campopiano, P. V. Nikolova and P. E. Barran, *Anal. Chem.*, 2015, **87**, 3231–3238.

40 M. F. Jarrold, *Acc. Chem. Res.*, 1999, **32**, 360–367.

41 E. Jurneczko, J. Kalapothakis, I. D. G. Campuzano, M. Morris and P. E. Barran, *Anal. Chem.*, 2012, **84**, 8524–8531.

42 R. Beveridge, S. Covill, K. J. Pacholarz, J. M. D. D. Kalapothakis, C. E. MacPhee and P. E. Barran, *Anal. Chem.*, 2014, **86**, 1–24.

43 K. J. Pacholarz and P. E. Barran, *Anal. Chem.*, 2015, **87**, 6271–6279.

44 I. Campuzano, *Waters, Tech. Note*, 2008, 1–4.

45 J. A. Harrison, C. Kelso, T. L. Pukala and J. L. Beck, *J. Am. Soc. Mass Spectrom.*, 2018, **30**, 256–267.

46 P. Benigni, R. Marin, J. C. Molano-Arevalo, A. Garabedian, J. J. Wolff, M. E. Ridgeway, M. A. Park and F. Fernandez-Lima, *Int. J. Ion Mobil. Spectrom.*, 2016, **19**, 95–104.

47 S. J. Allen, R. M. Eaton and M. F. Bush, *Anal. Chem.*, 2016, **88**, 9118–9126.

48 J. D. Sanders, D. Grinfeld, K. Aizikov, A. A. Makarov, D. D. Holden and J. S. Brodbelt, *Anal. Chem.*, 2018, **90**, 5896–5902.

49 F. C. Liu, S. R. Kirk and C. Bleiholder, *Analyst*, 2016, **141**, 3722–3730.

50 N. A. Meyer, K. Root, R. Zenobi and G. Vidal-De-Miguel, *Anal. Chem.*, 2016, **88**, 2033–2040.

51 S. J. Allen, R. M. Eaton and M. F. Bush, *Anal. Chem.*, 2017, **89**, 7527–7534.

52 S. J. Valentine and D. E. Clemmer, *J. Am. Chem. Soc.*, 1997, **119**, 3558–3566.

53 E. R. Schenk, R. Almeida, J. Miksovska, M. E. Ridgeway, M. A. Park and F. Fernandez-Lima, *J. Am. Soc. Mass Spectrom.*, 2015, **26**, 555–563.

	Nitrogen		
	Rep1	Rep 2	Rep 3
Ubiquitin	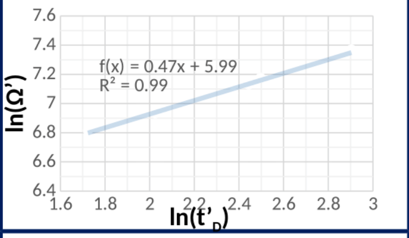	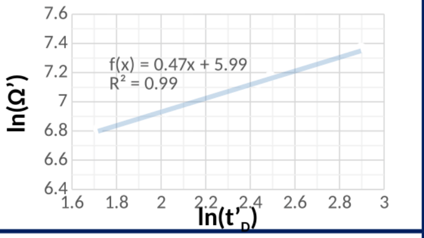	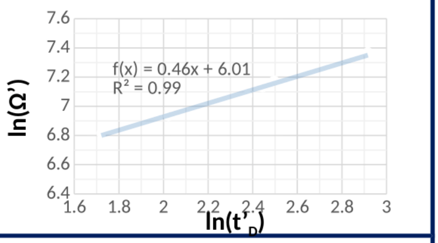
Cytochrome c	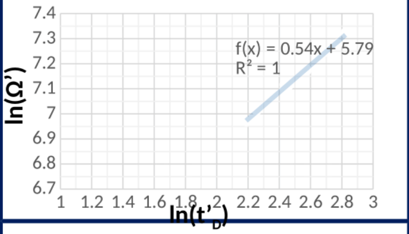	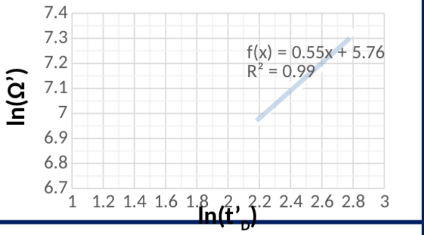	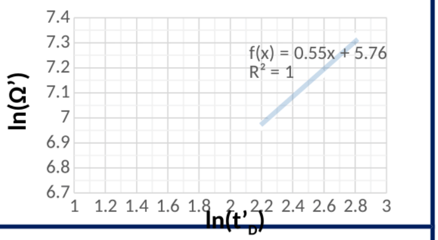
Myoglobin	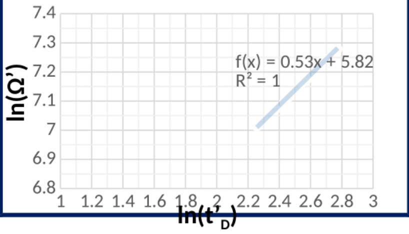	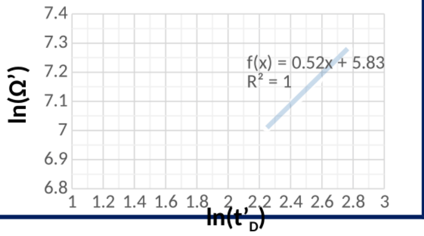	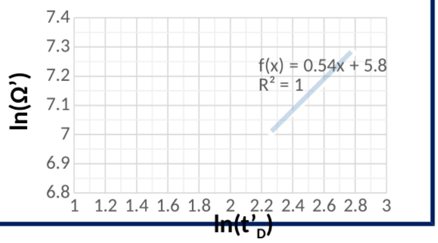

	Rep1	Rep 2	Rep 3
Avidin	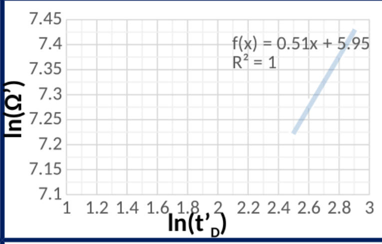	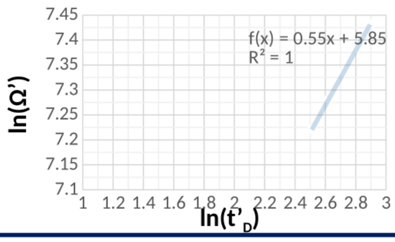	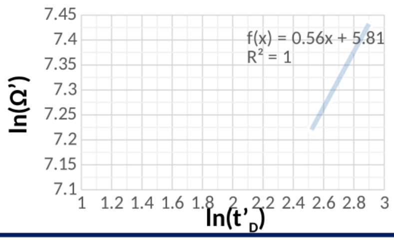
BSA	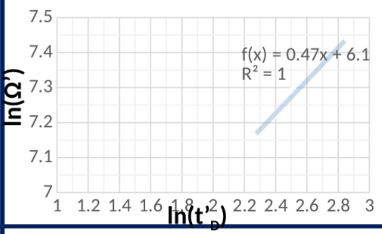	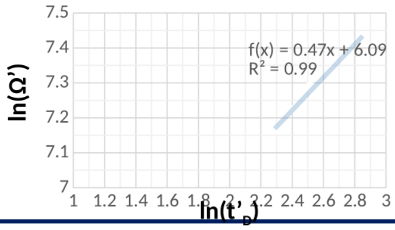	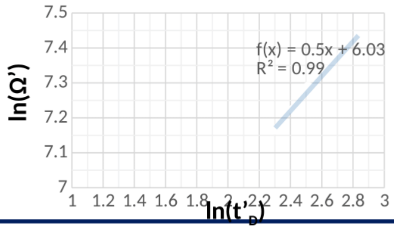
Concanavalin A	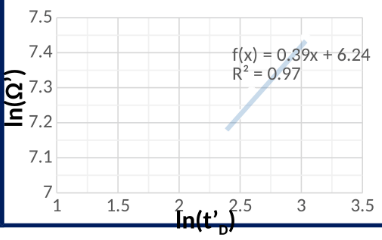	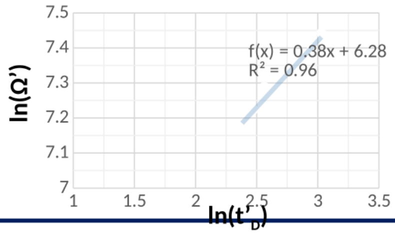	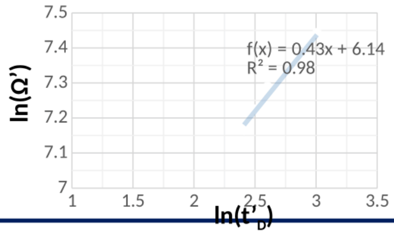

<table>
<tr><th></th><th>Rep1</th><th>Rep 2</th><th>Rep 3</th></tr>
<tr><td>Alcohol dehydrogenase</td><td>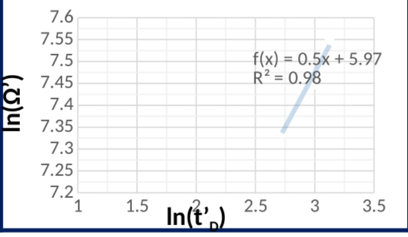 </td><td>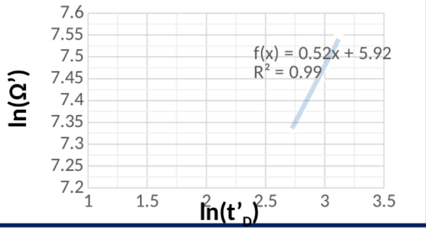 </td><td>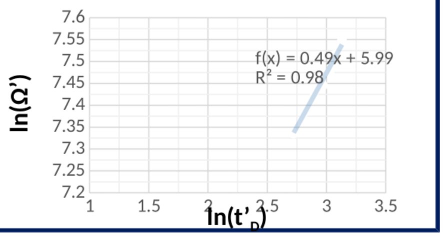 </td></tr>
</table>

	Helium		
	Rep1	Rep 2	Rep 3
Ubiquitin	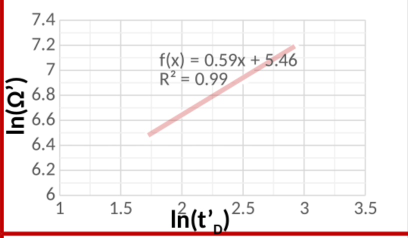	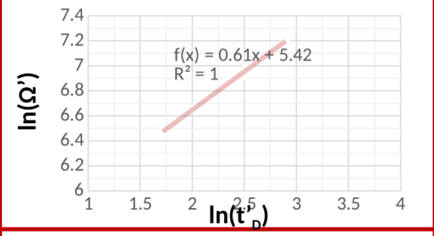	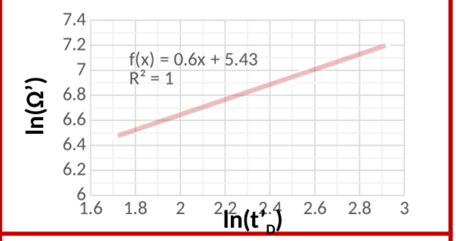
Cytochrome c	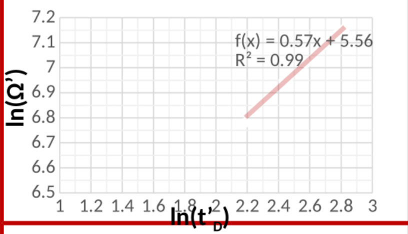	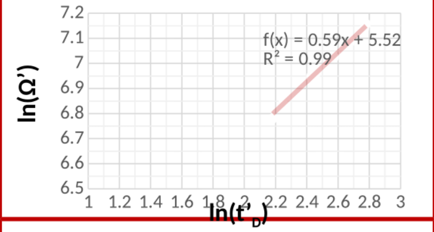	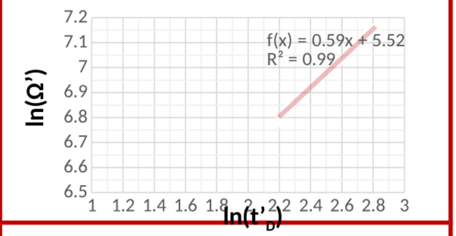
Myoglobin	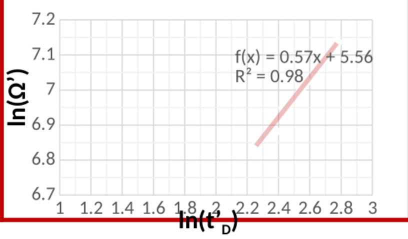	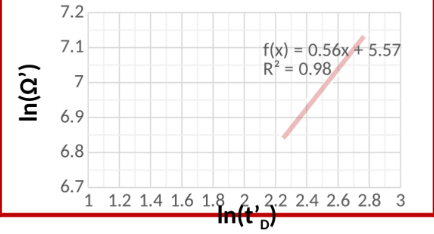	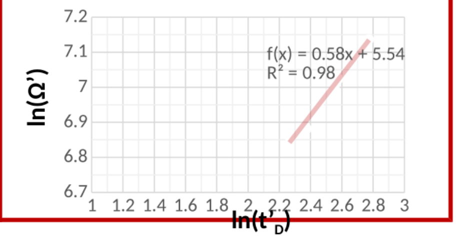

	Rep1	Rep 2	Rep 3
Avidin	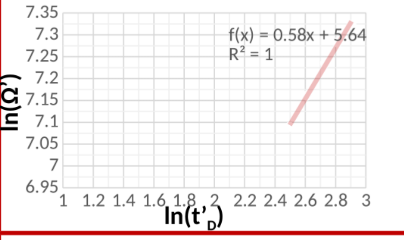	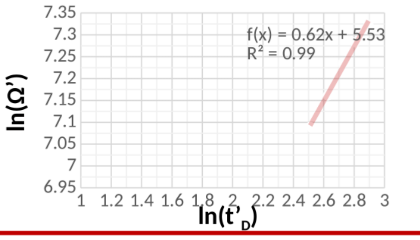	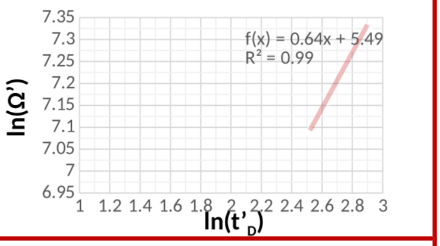
BSA	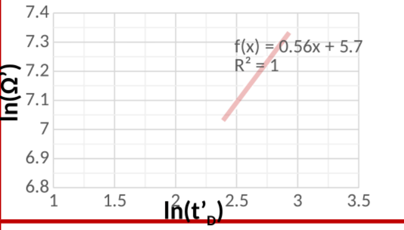	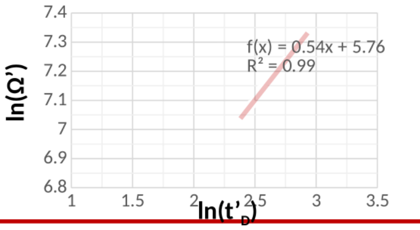	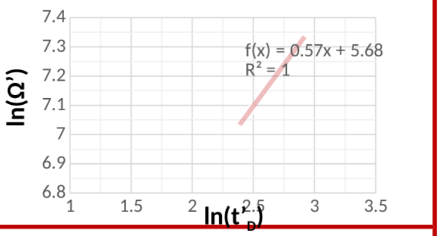
Concanavalin A	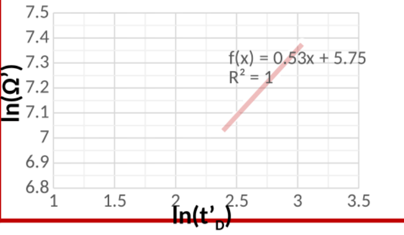	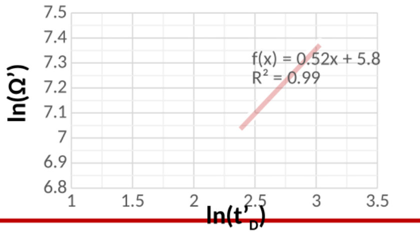	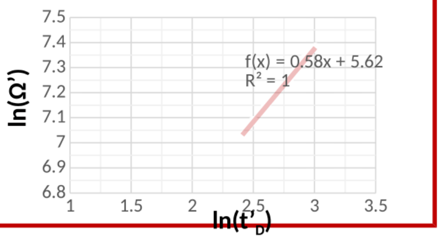

	Rep1	Rep 2	Rep 3
Alcohol dehydrogenase